



Faculteit Wetenschappen  
Departement Fysica

---

---

Quantitative atom detection from atomic-resolution  
transmission electron microscopy images

*Kwantitatieve atoomdetectie uit atomaire resolutie  
transmissie elektronenmicroscopische beelden*

---

---

Proefschrift voorgelegd tot het  
behalen van de graad van  
**Doctor in de Wetenschappen**  
aan de Universiteit Antwerpen,  
te verdedigen door

**Jarmo Fatermans**

**Promotors:**

Prof. dr. S. Van Aert  
Dr. ir. A.J. den Dekker

Antwerpen, 2019

## **Doctoral Committee**

### **Chairman**

Prof. dr. Jacques Tempere, University of Antwerp, Belgium

### **Promotors**

Prof. dr. Sandra Van Aert, University of Antwerp, Belgium

Dr. ir. Arnold J. den Dekker, University of Antwerp, Belgium

### **Members**

Prof. dr. Sabine Van Doorslaer, University of Antwerp, Belgium

Prof. dr. Martin Hÿtch, CEMES-CNRS and Université de Toulouse, France

Prof. dr. Knut Müller-Caspary, Forschungszentrum Jülich, Germany

Dr. Joris De Ridder, KU Leuven, Belgium



This research was financially supported by the FWO, the Research Foundation Flanders.



### **Contact Information**

Jarmo Fatermans

University of Antwerp - Department of Physics

EMAT - Electron Microscopy for Materials Science

Groenenborgerlaan 171, 2020 Antwerp

imec-Vision Lab

Universiteitsplein 1, 2610 Wilrijk

Belgium

[jarmo.fatermans@uantwerpen.be](mailto:jarmo.fatermans@uantwerpen.be)

# Samenvatting

Nanomaterialen ondervinden steeds meer wetenschappelijke interesse omdat hun precieze atomaire structuur kan leiden tot interessante en onverwachte fysische en chemische eigenschappen die heel verschillend kunnen zijn van de eigenschappen van bulkmaterialen op een grotere schaal. Daarom is het nodig om de relatie tussen de structuur en eigenschappen van deze materialen volledig te begrijpen opdat nieuwe materialen met uitstekende eigenschappen kunnen ontwikkeld worden op de nanoschaal. Door verschillende belangrijke ontwikkelingen in aberratie correctie technologie is transmissie elektronenmicroscopische beeldvorming uitgegroeid tot een uitstekende techniek om nanomaterialen te visualiseren met subangstrom resolutie waardoor uitdagende problemen binnen materiaalonderzoek kunnen opgelost worden. Echter is het zo dat slechts een visuele interpretatie van zulke beelden onvoldoende is om nauwkeurige structuurinformatie te bekomen. Het nauwkeurig meten van de atomaire schikking van geprojecteerde atoomkolommen of individuele atomen is wel degelijk belangrijk omdat kleine veranderingen in de lokale atoomstructuur significante veranderingen kunnen teweegbrengen op het vlak van de eigenschappen. Daarom is een kwantitatieve aanpak aanbevolen die op een betrouwbare manier de structuurparameters, zoals de posities van de atomen, het type van de atomen, en het aantal atomen, kan kwantificeren. Een belangrijke veronderstelling in deze kwantitatieve aanpak is dat het aantal atoomkolommen gekend is. Gewoonlijk wordt dit aantal visueel bepaald wat mogelijk is voor beelden met atomaire resolutie van bundelstabiele materialen waarvoor een hoge inkomende elektronendosis kan gebruikt worden wat resulteert in beelden die een hoge signaal-ruisverhouding (SNR) vertonen. Bundelgevoelige materialen en materialen bestaande uit lichte elementen daarentegen moeten belicht worden met een voldoende lage elektronendosis om schade door de elektronenbundel te voorkomen. Als gevolg hiervan vertonen deze beelden een lage SNR en zwak contrast en dus ook een lage contrast-ruisverhouding (CNR). Dit veroorzaakt een onbetrouwbare visuele bepaling van het aantal atoomkolommen in het beeld wat leidt tot systematische fouten in de structuurbepaling. Om dit probleem te overwinnen wordt in deze thesis een alternatieve, kwantitatieve methode voorgesteld die het aantal atoomkolommen bepaalt waarvoor er het meeste bewijs is in de beeldgegevens.

Door de aanwezigheid van ruis fluctueren experimentele observaties rond hun verwachtingswaarden. De constructie van een parametrisch (fysisch gebaseerd) model dat de verwachtingswaarden van de observaties beschrijft als functie van ongekende parameters vormt het startpunt van een kwantitatieve analyse. Hierbij worden beelden met atomaire resolutie beschouwd als datavlakken waar de observaties overeenkomen met de pixelwaarden van het beeld waaruit ongekende parameters geschat moeten worden. Op die manier is kwantitatieve structuurbepaling gereduceerd tot een statistisch parameterschattingsprobleem. Omdat beeldintensiteiten scherp gepiekt zijn op de atoomkolomposities kunnen de geprojecteerde atoomkolommen van beelden met atomaire resolutie, die bekeken worden langs een belangrijke zone-as, gemodelleerd worden als Gaussische pieken die gesuperponeerd zijn op een constante achtergrond. Nauwkeurige structuurinformatie

kan dan bekomen worden door dit model te fitten aan de geobserveerde beeldpixelwaarden met betrekking tot de ongekende parameters waarbij een modelaanpassingscriterium gebruikt wordt om de gelijkaardigheid tussen het beeld en het model te kwantificeren.

Bovendien is het mogelijk om parameterschattingstheorie te combineren met modelselectie. Hierbij wordt naast het schatten van de ongekende parameters van het verwachtingswaardenmodel ook het aantal parameters bepaald, dat het dichtst het onderliggende proces dat de experimentele observaties genereerde, benadert. Voor ringvormige donkerveld (ADF) rastertransmissie elektronenmicroscopie (STEM) is een methode die statistische parameterschattingstheorie combineert met modelselectie volledig uitgewerkt in deze thesis gebruik makend van Bayesiaanse waarschijnlijkheidstheorie. Naar deze methode wordt verwezen als de maximum a posteriori (MAP) waarschijnlijkheidsregel die toestaat om atoomkolommen en zelfs individuele atomen te detecteren uit ADF STEM beelden met atomaire resolutie op een automatische en objectieve manier. De geldigheid en bruikbaarheid van deze methode voor beeldgegevens met lage kwaliteit werd aangetoond door experimentele en gesimuleerde ADF STEM beelden te analyseren van nanomaterialen van verschillende vorm, grootte, en atoomtype.

Naast het detecteren van atoomkolommen van ADF STEM beelden biedt de MAP waarschijnlijkheidsregel ook een manier aan om de relatie tussen beeldkwaliteitsmaten, zoals SNR and CNR, te evalueren t.o.v. atoomdetecteerbaarheid welke gedefinieerd is als de waarschijnlijkheid om een atoom te detecteren uit een beeld. In het algemeen is atoomdetecteerbaarheid inderdaad gerelateerd aan beeldkwaliteit omdat men bijvoorbeeld verwacht dat de detecteerbaarheid van atoomkolommen in een beeld toeneemt met toenemende beeldkwaliteit. Op deze manier is de waarschijnlijkheid om een atoomkolom te detecteren uit ADF STEM beeldgegevens, welke bepaald kan worden door de MAP waarschijnlijkheidsregel, gecorreleerd met de kwaliteit van het beeld. Zo wordt in deze thesis een nieuwe beeldkwaliteitsmaat voor ADF STEM beelden voorgesteld, de zogenaamde geïntegreerde CNR (ICNR), die beter correleert met atoomdetecteerbaarheid dan conventionele beeldkwaliteitsmaten.

Verder wordt in deze thesis bevestigd dat de MAP waarschijnlijkheidsregel gerelateerd is aan het concept van modelselectie. In het bijzonder is deze methode nauw verwant met het Bayesiaans Informatie Criterium (BIC), omdat beide methoden afgeleid worden middels een Bayesiaanse aanpak. Het interessante aan de MAP waarschijnlijkheidsregel is dat deze rekening houdt met meer dimensies van modelcomplexiteit in vergelijking met andere veel gebruikte modelselectie criteria. Dit laat een superieure prestatie toe voor het detecteren van het juiste aantal atoomkolommen uit ADF STEM beelden. Bovendien zorgt de MAP waarschijnlijkheidsregel voor een duidelijke en flexibele opname van voorafgaande kennis, wat vaak niet het geval is voor andere modelselectie methodes.

Tot slot wordt in deze thesis getoond dat de methodologie van de MAP waarschijnlijkheidsregel uitgebreid kan worden om simultaan verkregen ringvormige helderveld (ABF) en ADF STEM beelden te analyseren. Deze techniek combineert de betere visualisatie van lichte elementen via ABF STEM met het gemakkelijk interpreteerbare beeldcontrast van ADF STEM. Verder kan ook voor ABF STEM beelden de ICNR worden gebruikt als een toereikende beeldkwaliteitsmaat die goed correleert met atoomdetecteerbaarheid. De voordelen van simultaan model fitten in vergelijking met het combineren van kwantitatieve metingen uit het apart analyseren van ABF en ADF STEM beelden worden uitgebreid besproken als functie van ICNR. In deze thesis wordt aangetoond dat een simultane analyse de atoomdetecteerbaarheid verbetert alsook de nauwkeurigheid waarmee atoomposities geschat kunnen worden. Verder wordt geïllustreerd

---

dat door gebruik te maken van de MAP waarschijnlijkheidsregel om experimentele ABF en ADF STEM gegevens te onderzoeken een betrouwbare schatting van atoomkolomposities kan bekomen worden zonder rekening te houden met voorafgaande kennis over de verwachte posities van deze kolommen.

De ontwikkeling van de MAP waarschijnlijkheidsregel in deze thesis als een nieuwe kwantitatieve methode heeft kwantitatieve elektronenmicroscopie naar een meer objectieve interpretatie gebracht. De methode veralgemeent de karakterisatie van nanomaterialen op de atomaire schaal in STEM met het oog op het bekomen van nauwkeurige structuurinformatie van een materiaal.



# Summary

Nanomaterials have attracted increasing scientific interest, because their exact atomic structure may lead to interesting and unexpected physical and chemical properties, which may be very different than the properties that arise from bulk materials at a larger scale. Therefore, in order to develop new materials with outstanding properties at the nanoscale, one needs to fully understand the structure-properties relation of these nanomaterials. Because of several important developments in aberration correction technology, transmission electron microscopy imaging has become an excellent technique to visualize nanomaterials down to sub-angstrom resolution and thereby solving challenging problems in materials science. However, a merely visual interpretation of such images is inadequate to obtain precise structure information. Precisely measuring the atomic arrangement of projected atomic columns or individual atoms, though, is important since small changes in the local atomic structure may induce significant changes in their properties. Therefore, a quantitative approach is required which can reliably quantify structure parameters, such as the positions of the atoms, the type of the atoms, and the number of atoms. An important assumption in this quantitative approach is that the number of atomic columns is known. Usually, this number is determined visually, which is possible for atomic-resolution images of beam-stable materials where a high incoming electron dose can be used resulting in images exhibiting high signal-to-noise ratio (SNR). However, beam-sensitive and light-element materials should be imaged with a sufficiently low electron dose to avoid beam damage. As a consequence, these images exhibit low SNR and low contrast, and hence low contrast-to-noise ratio (CNR). This causes poor visual determination of the number of atomic columns in the image leading to biased structure information. To overcome this problem, an alternative, quantitative method is proposed in this thesis to determine the number of atomic columns for which there is most evidence in the image data.

Due to the presence of noise, experimental observations fluctuate around their expectation values. The starting point of a quantitative analysis is the construction of a parametric (physics-based) model describing the expectations of the observations as a function of unknown parameters. Here, atomic-resolution images are considered as data planes where the observations are the pixel values of the image from which unknown structure parameters need to be estimated. In this way, quantitative structure determination can be reduced to a statistical parameter estimation problem. Since image intensities are sharply peaked at the atomic column positions, the projected atomic columns of atomic-resolution images viewed along a major zone axis can be modelled as Gaussian peaks superimposed on a constant background. Accurate and precise structure information is then obtained by fitting this model to the observed image pixel values with respect to the unknown parameters using a criterion of goodness of fit quantifying the similarity between the image and the model.

Moreover, it is possible to combine parameter estimation with model-order selection. Hereby, besides estimating the unknown parameters of the expectation model, also the number of pa-

rameters that most closely represents the underlying process that generated the experimental observations needs to be determined. For annular dark-field (ADF) scanning transmission electron microscopy (STEM), a method which combines statistical parameter estimation and model-order selection has been fully derived in this thesis by using Bayesian probability theory. This method is referred to as the maximum a posteriori (MAP) probability rule, which allows to detect atomic columns and even single atoms from atomic-resolution ADF STEM images in an automatic and objective manner. The validity and usefulness of this method to low-quality image data have been demonstrated by analyzing experimental and simulated ADF STEM images of samples of different shape, size, and atom type.

Besides detecting atomic columns from ADF STEM images, the MAP probability rule also offers a way to evaluate the relation between image quality measures, such as SNR and CNR, and atom detectability, which is defined as the probability to detect an atom from an image. In general, atom detectability is indeed related to image quality, as, for example, one expects the detectability of atomic columns in an image to increase with increasing image quality. In this way, the probability to detect an atomic column from ADF STEM image data, which can be provided by the MAP probability rule, is correlated with the quality of the image. As such, for ADF STEM images, a new image quality measure, the so-called integrated CNR (ICNR), has been proposed in this thesis that better correlates with atom detectability than conventional image quality measures.

Furthermore, in this thesis, it is confirmed that the MAP probability rule is related to the concept of model selection. In particular, it is closely related to the Bayesian Information Criterion (BIC), as both methods are derived using a Bayesian approach. Interestingly, the MAP probability rule takes into account more dimensions of model complexity as compared to other commonly used model-selection criteria. This allows for a superior performance to detect the correct number of atomic columns from ADF STEM images. In addition, the MAP probability rule allows for a clear and flexible incorporation of prior knowledge, which is often not the case for other model-selection methods.

Finally, it is shown in this thesis that the methodology of the MAP probability rule can be extended for analyzing simultaneously acquired annular bright-field (ABF) and ADF STEM images. This technique combines the improved light-element visualization of ABF STEM with the easily interpretable image contrast of ADF STEM. Furthermore, also for ABF STEM images the ICNR can be used as a valid image quality measure correlating well with atom detectability. The advantages of simultaneous model fitting, as compared to combining quantitative measurements from analyzing the ABF and ADF STEM images separately, have been thoroughly discussed as a function of ICNR. It has been demonstrated in this thesis that a simultaneous analysis improves atom detectability, as well as atom position accuracy and precision. Furthermore, it has been illustrated that by using the MAP probability rule to investigate experimental ABF and ADF STEM data, a reliable estimation of atomic column locations can be obtained without including prior information about the expected positions of these columns.

The development of the MAP probability rule in this thesis as a new quantitative method has pushed quantitative electron microscopy towards a more objective interpretation. The method generalizes the characterization of nanomaterials at the atomic scale in STEM in order to obtain accurate and precise structure information about a material.

# Contents

<b>Samenvatting</b>	<b>iii</b>
<b>Summary</b>	<b>vii</b>
<b>1 Introduction</b>	<b>1</b>
1.1 The importance of data . . . . .	1
1.2 Model selection . . . . .	2
1.3 Materials science and technology . . . . .	5
1.4 Electron beam damage . . . . .	7
1.5 What to expect in this thesis? . . . . .	9
<b>2 Scanning transmission electron microscopy</b>	<b>13</b>
2.1 Introduction . . . . .	13
2.2 Electron-specimen interaction . . . . .	19
2.3 Electron probe . . . . .	22
2.4 Specimen potential . . . . .	24
2.5 Multislice method . . . . .	25
2.6 Image formation . . . . .	29
2.7 STEM detector . . . . .	32
2.8 Conclusions . . . . .	34
<b>3 Quantitative atomic-resolution electron microscopy</b>	<b>35</b>
3.1 Introduction . . . . .	35
3.2 Model-based parameter estimation . . . . .	37
3.3 Maximum likelihood estimator . . . . .	42
3.4 Bias and variance . . . . .	46
3.4.1 Fisher information . . . . .	48
3.4.2 Cramér-Rao lower bound . . . . .	48
3.5 Model-order selection . . . . .	50
3.6 Conclusions . . . . .	51
<b>4 Atom column detection from ADF STEM images</b>	<b>53</b>
4.1 Introduction . . . . .	53
4.2 Bayes' theorem . . . . .	55
4.3 Maximum a posteriori probability . . . . .	57
4.3.1 Bayesian approach . . . . .	57

4.3.2	Algorithm . . . . .	62
4.4	Experimental examples . . . . .	64
4.4.1	SrTiO <sub>3</sub> . . . . .	64
4.4.2	Graphene . . . . .	66
4.4.3	Gold nanorod . . . . .	68
4.4.4	Ultrasmall nanoclusters . . . . .	72
4.5	Conclusions . . . . .	75
<b>5</b>	<b>The maximum a posteriori probability rule for atom column detection</b>	<b>77</b>
5.1	Introduction . . . . .	77
5.2	Atom detectability . . . . .	78
5.2.1	SNR and CNR . . . . .	80
5.2.2	Integrated CNR . . . . .	82
5.3	Relation to model selection . . . . .	83
5.3.1	Performance in detecting atoms . . . . .	85
5.3.2	Relation between MAP and BIC . . . . .	87
5.3.3	Influence of prior density . . . . .	89
5.4	Conclusions . . . . .	90
<b>6</b>	<b>Atom column detection from ABF-ADF STEM images</b>	<b>93</b>
6.1	Introduction . . . . .	93
6.2	Model-based parameter estimation . . . . .	95
6.3	Maximum a posteriori probability . . . . .	98
6.4	Advantages of simultaneous model fitting . . . . .	100
6.4.1	Atom detectability . . . . .	100
6.4.2	Spatial deviation and precision . . . . .	103
6.5	Experimental examples . . . . .	105
6.5.1	SrTiO <sub>3</sub> . . . . .	105
6.5.2	LiMn <sub>2</sub> O <sub>4</sub> . . . . .	107
6.6	Conclusions . . . . .	108
<b>7</b>	<b>General conclusions and future perspectives</b>	<b>111</b>
	<b>Bibliography</b>	<b>115</b>
	<b>List of Symbols and Abbreviations</b>	<b>145</b>
	Roman characters . . . . .	145
	Greek characters . . . . .	148
	Abbreviations . . . . .	151
	<b>List of publications</b>	<b>153</b>
	Contributions to scientific journals . . . . .	153
	Contributions to scientific meetings . . . . .	153
	<b>Acknowledgements - Dankwoord</b>	<b>155</b>

# 1

## Introduction

### 1.1 The importance of data

Nowadays, data collection has become common practice due to the increased digitalisation of our world. A new term of datafication has risen which covers the fact that almost every phenomenon is now being observed and stored [Cukier 2013]. Devices and people are more than ever constantly connected with each other through the web where every click and movement is monitored. The information that is captured within this data can be considered as a new form of value or resource [O'Neil 2013].

Data can be broadly defined as anything that is recorded and may exist in many different forms [Maheshwari 2015]. Data could be an unordered collection of values, which means that there exists no intrinsic ordering in the data. The available set of colors of shirts in a shop is an example of such nominal data. On the other hand, the sizes of these shirts, like small, medium, and large, possess a certain intrinsic ordering as one size is bigger than another. Such data is called ordinal data. Often, people may immediately relate data to consist of numeric values. The prices of the aforementioned shirts would be an example of such ratio data. This kind of data allows for further advanced mathematical analysis. An example of this is the possibility to combine measurements of temperature, air pressure, and humidity into a mathematical framework to predict future weather. When the data is restricted to only discrete numeric values defined in a certain range, like for example a 10-point scale measuring customer satisfaction, one can speak of interval data. Another kind of data is data such as audio, video, and graphics files which may be described based on emotions they evoke, which does not have a clear quantitative nature. Data can originate from basically any source. It can come from records inside an organisation or it can be collected by industry or government institutions. There exists even metadata, which is data about data. This includes, for example, the time when a piece of data has been collected. These days, one might automatically relate data with digital files on a computer or other device, but data may appear as well in paper form of which numerous historical documents are examples. In addition, data may be of public or private nature. Currently, there is an ongoing debate on

whether the vast amounts of personal data which are available through social media can be considered to be private and whether this personal data can be collected by large digital media companies and used for commercial purposes.

The importance of data collection lies in the statement that there is hidden value in data. It is the task of data science to extract knowledge and innovative insights from data. This can be done by unifying statistical concepts and processing with data analysis [Hayashi 1998, Dhar 2013]. Hereby, it is required that relevant features, patterns, and information can be reliably detected and extracted from the data. This is not a straightforward task and depends on the quality of the data. In principle, one can consider data to consist of signal and noise [Silver 2012]. The goal of data science is to find the signal which can be seen as the underlying truth. The noise, on the other hand, is a nuisance that distracts from the truth. It is needless to say that nowadays data collection and data analysis play an important role in many fields of science with a growing need for methods which point out interesting and relevant features of the data.

## 1.2 Model selection

Statistical model selection is an essential part of data analysis. More information about model-selection procedures and their applications can be found in [McQuarrie 1998, Zucchini 2000, Burnham 2002, Claeskens 2008, Konishi 2008, Claeskens 2016]. Model selection consists of the task of selecting a statistical model from a set of candidate models which most closely describes the underlying process that generated the data. The constructed model should be complex enough to explain relations that are hidden within the data, but, on the other hand, simple enough so that no overinterpretation of the data occurs. Statistical model selection provides a framework for handling this balance. It supports the search for good models and for determining which variables are relevant and need to be included when analysing data.

There are some general concepts related with statistical model selection [Claeskens 2008]. Firstly, in almost all situations it is not possible to find the strictly correct or true model that generated the data. This true model is often simply too complex and is almost always unknown. In practice, one works with a slightly simpler model which is almost as good. Secondly, an important concept in statistics is the balance and interplay between bias and variance [Geman 1992, Sammut 2011]. When a model consists of parameters that need to be estimated from the data, the bias-variance tradeoff manifests itself in the form of balancing simplicity against complexity [Myung 2000]. A simple model, with for example a low number of estimated parameters, is often associated with low variability and large bias. Increasing the number of parameters, though, increases the complexity of the model which leads to a higher degree of variability but smaller bias. The key of statistical model selection lies in this balance where both overfitting and underfitting preferably need to be avoided [Burnham 2002, Everitt 2010, Lever 2016]. Overfitting refers to the fact that a model consists of too many parameters, hereby overinterpreting the data. Underfitting, on the other hand, is quite the opposite where a model has too few parameters, which disables it from capturing relevant information. In addition, statistics often relies on the principle of parsimony, or Ockham's razor, which may be of relevance as well in other domains. It states that when several theories exist to describe some phenomenon, the simplest one consistent with the empirical evidence is preferred [Sivia 1992a, Hoffman 1997, Myung 1997, Gauch 2003, Schaffer 2015]. In statistical modelling, this statement could be translated by claiming that

only parameters that really matter should be included in the selected model. Furthermore, data analysis is dependent on the scientific context and for what purpose it is investigated. In statistics, it can also be that certain quantities or functions of parameters are more important than others. Interestingly, model-selection methods have been developed that are aimed on focusing specifically on the most important quantities [Claeskens 2003, Hjort 2006]. An important note on model selection is that different selection methods might end up offering different results, even when the data and list of candidate models is the same. These conflicting recommendations do not necessarily form a contradiction, but indicate the importance of understanding the working principle of model-selection methods and in what context and for what aim they are relevant. Lastly, it is noted that most model-selection strategies work by assigning a score to each of the candidate models. In certain cases, it might be advantageous to perform a multi-modal approach where all fitted models are averaged in a weighted manner according to their scores [Stoica 2004b].

An important application of model-selection procedures is to detect and extract relevant features or peaks from noisy data [Knuth 2015]. As already stated in the previous section, noise is a nuisance and the goal is to find the underlying signal in possibly heavily distorted data. Model selection may, for example, be used to estimate the degree of a polynomial from a noisy data sample [Mana 2014]. Furthermore, model selection can be applied as well on the problem of signal detection where the question is whether a certain signal is present or absent [Mubeen 2013]. In addition, model selection has been used to determine the model order of a Gaussian mixture model of the spatial sensitivity function of a light sensor used in a robotics application [Malakar 2013]. Further examples concern exoplanet detection by determining the importance of various photometric effects in an exoplanetary system [Knuth 2012, Placek 2014] and force field selection in biomolecular structure determination from nuclear magnetic resonance (NMR) data [Habeck 2011]. In X-ray photoelectron spectroscopy (XPS), model selection has been applied to detect spectral peaks from noisy data [Armstrong 2009]. In order to highlight the importance and difficulty of correctly detecting peaks from noisy data, an example from

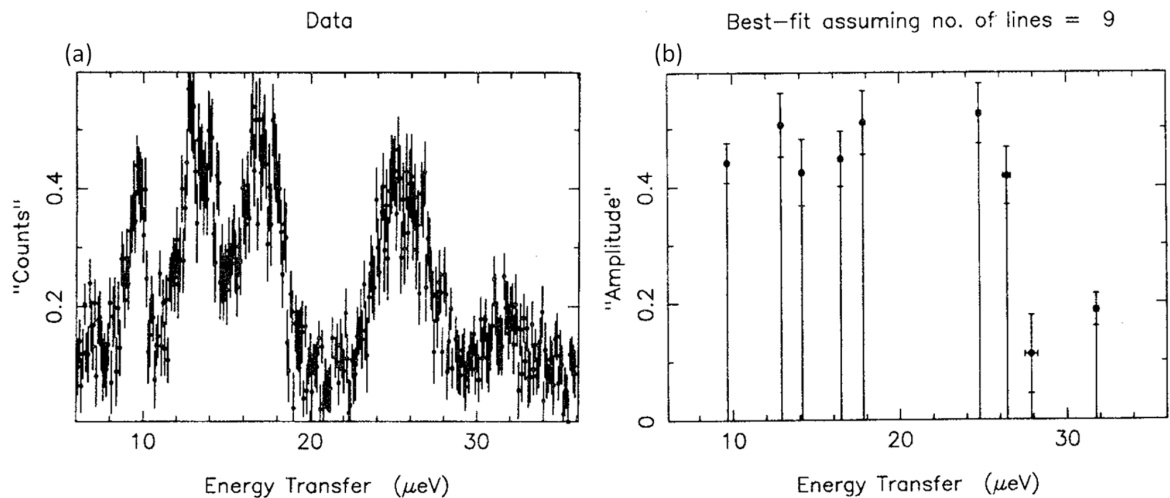


**Figure 1.1:** (a) Experimental neutron diffraction spectrum of lutidine. (b) Best estimate of peaks, including amplitudes and positions, extracted from (a) [Sivia 1992a].

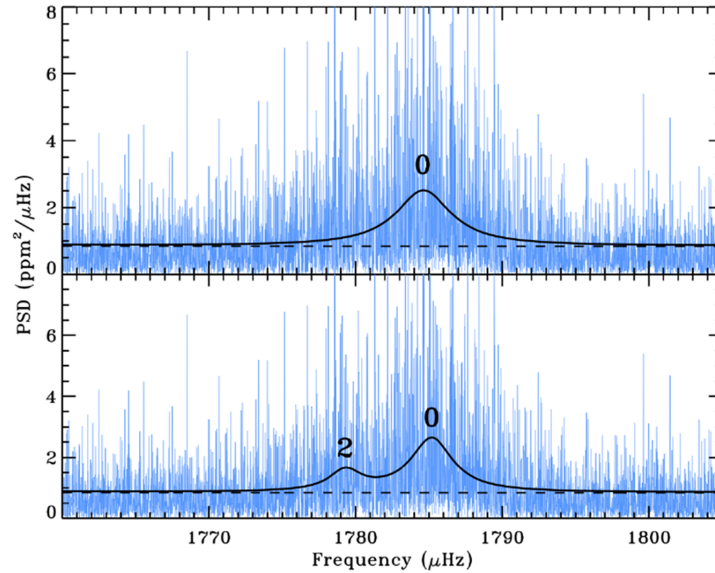


**Figure 1.2:** Detection of oscillation peaks from the PSD of star KIC 9139163. Upper panel: model fit consisting of one peak with angular degree equal to 0. Lower panel: favored model fit assessing the presence of two peaks with angular degrees 2 and 0 [Corsaro 2014].

experimental molecular spectroscopy has been shown in Fig. 1.1. The spectrum of Fig. 1.1(a) has been obtained by examining the sample being placed in a beam of neutrons, allowing the recording of a diffraction pattern that provides information of the structure of the material under investigation. The spectrum, though, consists of very noisy data which hampers a visual determination of the locations of spectral peaks that are present. The technique of model selection can be successfully applied to this spectrum, answering the question of how many peaks the spectrum consists [Sivia 1992a, Sivia 1992b, Sivia 1993, Monserrat 2015]. Fig. 1.1(b) shows the best estimate of the amplitudes and positions of the excitations peaks. The analysis by model selection has revealed that there are 9 peaks present in the data shown in Fig. 1.1(a). This clearly shows the importance of model selection since it is not straightforward to detect these peaks from only visually interpreting the data of Fig. 1.1(a).

Another example of the importance of model selection is illustrated in Fig. 1.2 which shows the power spectral density (PSD) of a star. The example stems from the domain of asteroseismology where stellar physics and stellar evolution is investigated through oscillations that occur in stars [García 2013]. Since oscillations are related to the internal structure of a star, information can be gained about a star's interior. From the data in Fig. 1.2, oscillation peaks need to be reliably detected in order to be able to extract stellar structural information. Two competing models are shown in Fig. 1.2 where the upper one contains only one oscillation peak, whereas the lower one contains two peaks. By applying model selection, it has been shown that the model containing two peaks is strongly favored [Corsaro 2014]. As for the example of neutron diffraction in Fig. 1.1, a visual interpretation of the noisy data in Fig. 1.2 is insufficient to reliably detect the possible presence of peaks. Therefore, a quantitative model-selection method is required which is able to disentangle signal from noise.

## 1.3 Materials science and technology

Model selection is not restricted to the examples described in the previous section, but can play an important role as well in materials science. Nowadays, the field of materials science has evolved from micro-to nanoscience covering the study of objects, structures and phenomena at dimensions of less than 100 nanometers [Demetzos 2004]. There exists a great variety of nanomaterials, including metals, ceramics, polymers, semiconductors, magnetic materials, biomaterials and energy materials for applications such as transistors, sensors, catalysts, batteries, contrast agents, and biomedical drugs [Klabunde 2002, Liz-Marzán 2003, Callister 2007, Wang 2015, Wu 2015, Tan 2017]. During the last few decades, nanotechnology, which is the branch of technology that deals with nanometer-scale dimensions and, in particular, with the manipulation of individual atoms and molecules, has grown substantially in the field of materials science for developing applications in physics, chemistry, biology, and engineering. Nanomaterials have gained great interest because their properties may vary significantly as compared to the properties of their bulk counterparts [Nebel 2003, Roduner 2006, Huang 2010, Alshamari 2012, Husain 2016]. This phenomenon can be traced back to the fact that the properties of nanomaterials depend strongly on their size and shape, which is defined by their exact atomic arrangement. Nanostructures may consist of only a few up to several millions of atoms or molecules [Ferrando 2008]. Nanoparticles that consist of a very low amount of atoms and yield only very few stable geometric configurations can be referred to as atomic clusters. Such nanoclusters can be considered as a bridge between atoms and nanoparticles. Today, materials science is mainly aimed on discovering new nanomaterials with outstanding properties. For this, one needs to fully understand the relation between properties and structure [Yang 2012]. This is important since, for example, the physical properties of nanomaterials can already be significantly altered by only small local changes in the structure [Zambelli 1996, Nørskov 2009, Qi 2010, Alem 2011, Mazzucco 2012, Van Aert 2012a, Tang 2014] or composition [Tedsree 2011, Huang 2012].

In particular, the concept of model selection can play a crucial role in reliably detecting the presence of atoms of nanomaterials. This is important, since it is well known that the exact surface morphology of nanomaterials can influence their physical properties. Also for ultrasmall nanoclusters, the detection of single atoms is crucial. Such atomic clusters can be thought of as fundamental building blocks leading to metamaterials with physical and chemical properties that are not available in nature [Binns 2001, Claridge 2009]. The growth mechanisms for small nanoclusters are much more exotic than for bulk materials and, therefore, they possess more complex structures, providing the need of applying model-selection techniques to study their exact atomic arrangements. Model selection in materials science is not limited to detecting single atoms. It may also be applied to detect signals of light elements that are present in materials. Light atoms, such as hydrogen, lithium, and oxygen, play a key-role in modern technology. In hydrogen storage applications, hydrogen is used as a medium to store energy [Schlapbach 2001, von Colbe 2019]. For example, energy created by intermittent energy sources, such as wind and solar energy, can be stored during periods of high availability and low demand. As such, the fluctuating nature of intermittent energy sources can be addressed. An important application of lithium is that of lithium batteries, which are commonly used for portable electronics and electric vehicles. As compared to other types of batteries, lithium batteries are light weight and possess higher energy densities [Tarascon 2001, Du Pasquier 2003, Lee 2011]. In order to develop lithium-based batteries with improved charging rate, capacity, and life time, it is essential to

study the movement of lithium ions during charging and discharging processes [Levi 1999, Morcrette 2003, Nishimura 2008]. Furthermore, oxygen appears in a wide range of technologically interesting materials. Oxide materials have been reported to possess a whole range of fascinating phenomena [Martin 2010, MacLaren 2014]. For example, at oxide interfaces novel electrical transport properties may arise [Ohtomo 2002, Ohtomo 2004, Seidel 2009, Shah 2010, Yu 2010]. In all of the aforementioned examples, it is crucial that signals from light elements can be detected in order to understand the role of the light atoms on the physical and chemical properties of the material.

Through the years, different characterisation techniques have been developed to analyse material structures down to the atomic level. X-ray and neutron diffraction techniques enable revealing the lattice structure with high resolution [Zanchet 2001]. Such techniques typically only provide spatially averaged structural information, losing information at the local scale. For this reason, X-ray and neutron diffraction are applicable to characterise materials exhibiting a periodic structure, whereas nanomaterials are usually aperiodic. Local scale structural information is available through scanning probe techniques, such as scanning tunneling microscopy (STM), and atomic force microscopy (AFM). However, these techniques only provide surface or near-surface information [Wiesendanger 1994, Hofer 2003, Tseng 2011]. By using transmission electron microscopy (TEM), though, both the local and internal structure of materials can be examined at the atomic scale, because of the strong interaction of electrons with matter [Henderson 1995]. Interestingly, since electrons are also charged, observations in TEM are not only sensitive to the atomic structure, but can also provide information about the type and the ionisation state of the atoms. As such, TEM has become a widely used technique to visualise nanomaterials with high resolution. Nowadays, electron microscopes can be operated in conventional transmission electron microscopy (CTEM) mode, where the specimen is illuminated by a parallel incoming electron beam, and in scanning transmission electron microscopy (STEM) mode, where the beam is focused onto the specimen and scanned in a two-dimensional (2D) raster.

Ever since the construction of the first electron microscope, the field of TEM has been mainly focused on the microscope itself for improving the image quality. For this, the quality of the lenses and stability of the acceleration voltage and lens currents need to be sufficient in order to obtain atomic-resolution electron microscopy images [De Graef 2003]. By increasing the acceleration voltage, the point resolution, representing the smallest detail which is directly interpretable from the recorded images, can be improved [Egerton 2014]. In this manner, a resolution of 43 pm has been achieved by using a TEM working at 1.2 MV [Akashi 2015]. However, the downside of using such a high acceleration voltage is the occurrence of radiation damage, which is especially problematic for, for example, light-element nanostructures. The introduction of aberration corrected electron optics [Haider 1995, Rose 2009, Hawkes 2015], though, pushed the directly interpretable resolution down to the atomic level for moderate acceleration voltages. State-of-the-art electron microscopes are often equipped with aberration correctors, allowing for analysing materials down to the atomic level. In the CTEM mode, a point resolution of about 75 to 100 pm can be achieved at moderate acceleration voltages [Haider 1998a, Haider 1998b, Jia 2004, Ricolleau 2012]. The interpretable resolution can be improved towards 50 pm by considering the image of the exit wave [Kisielowski 2001, Kisielowski 2008, Haider 2010, Alem 2011], which can, for example, be obtained from a focal or tilt series of CTEM images [Van Dyck 1993, Miedema 1994, Thust 1996, Zandbergen 2000, Hsieh 2004, Allen 2004]. Sub-angstrom resolution has been achieved earlier in

STEM than in CTEM for intermediate accelerating voltages [Batson 2002, Nellist 2004]. The directly interpretable resolution has reached sub-50 pm for aberration-corrected STEM imaging [Kisielowski 2008, Erni 2009, Sawada 2009, Walther 2013, MacLaren 2014, Krivanek 2015]. The improved resolution of STEM as compared to CTEM is related to the fact that the resolution that is attainable is higher for incoherent imaging than for coherent imaging [Rayleigh 1896].

## 1.4 Electron beam damage

Nowadays, due to instrument developments, TEM enables to routinely image specimens at atomic resolution with high signal-to-noise ratio (SNR). This is only viable for specimens that can withstand high-energy electron irradiation meaning that they do not show significant signs of damage due to the electron beam. For biological samples and for samples which are composed predominantly of low atomic number elements, though, large radiation doses have a destructive effect [Tach 1971, Egerton 2004]. The primary damage mechanisms from exposure to high-energy electrons are knock-on damage and radiolysis [Ugurlu 2011, Williams 2009]. For both mechanisms, inelastic scattering occurs in which part of the incident electron energy is transferred during the collision event. Knock-on damage manifests itself as the displacement of atoms in the sample, due to a direct interaction with the nucleus where enough energy is transferred from the incoming electrons that is able to even eject atoms from the specimen. In general, knock-on damage is a significant damaging mechanism for inorganic samples, but is less significant for biological samples. By using lower incident electron energies, knock-on damage can be mitigated when the energy transferred during inelastic scattering events is below the threshold energy for displacement of a certain kind of atom. Decreasing the incident energy of the imaging electrons decreases the likelihood of a knock-on damage event, but can increase the frequency of radiolysis [Csencsits 1987], which is an important damaging mechanism for biological samples. Here, damage arises due to ionizations by the incident electrons interacting with valence electrons and breaking chemical bonds.

In order to limit the occurrence of beam damage due to the electron beam, beam-sensitive materials, such as light-element nanostructures, need to be investigated with a limited incoming electron dose. In this thesis, individual atomic-resolution STEM images have been imaged using electron doses limited to the order of  $10^3 - 10^5 e^-/\text{\AA}^2$ . Several techniques are available which reduce the incident dose on the sample in different imaging modes. A first example is the possibility of acquiring TEM images at cryogenic temperatures since low temperatures increase the tolerance to radiation damage [Knapek 1980, Newmark 1982, Chiu 1987]. Imaging specimens at liquid nitrogen or liquid helium temperatures falls within the domain of transmission electron cryomicroscopy (CryoTEM) [Adrian 1984]. Here, a specimen holder is used which maintains the specimen at cryogenic temperatures. This allows one to study specimens prepared in vitreous, or amorphous, ice, which is advantageous to image individual molecules or molecular assemblies in the field of structural biology [Li 2009b, Wolf 2014, Callaway 2015], since it preserves the internal structure of small tissue or cells, or to image materials that are prone to sublimation at room temperature [Levin 2017]. Due to advances in detector technology and software algorithms, CryoTEM has enabled structure determination with angstrom resolution of molecules including enzymes, proteins, ribosomes and viruses [Dellisanti 2015, Campbell 2015,

Bartesaghi 2015, Merk 2016, Sirohi 2016, Khoshouei 2017, Vonck 2017, Cheng 2018]. It is noted that such resolutions are achieved by combining many individual particle images. As a result, the resolution of the reconstruction of a particle depends on the homogeneity of the sample and on the accuracy of the image alignment. Alternatively, electron diffraction can be used, where bright spots corresponding to repetitive crystal spacings in Fourier or diffraction space are recorded [Downing 2001, Hadermann 2011, Hadermann 2012, Karakulina 2018]. Since unit cell information within the crystal is amplified, enough signal can be generated [Unwin 1975]. In real-space imaging, using a lower acceleration voltage limits the effect of knock-on damage [Egerton 2004, Girit 2009]. In addition, in STEM, the effects of beam damage can be further limited by reducing the pixel dwell time and beam current while recording the image [Buban 2010]. Another interesting option to physically limit the amount of electrons reaching the specimen is compressed sensing [Binev 2012, Saghi 2015, B  ch   2016]. Here, the electron dose is reduced by measuring image intensities for a few pixels only. In electron tomography, the total dose can be reduced by acquiring the series of images in a fast way [Migunov 2015, Koneti 2019], or by limiting the number of images in the series to only a few number of projections, for example by performing discrete tomography [Herman 2007].

Since there is a direct relationship between the incident dose and detected signal, imaging specimens in STEM with a limited incoming electron dose of around  $10^3 - 10^5 \text{ e}^-/\text{ }^2$  results

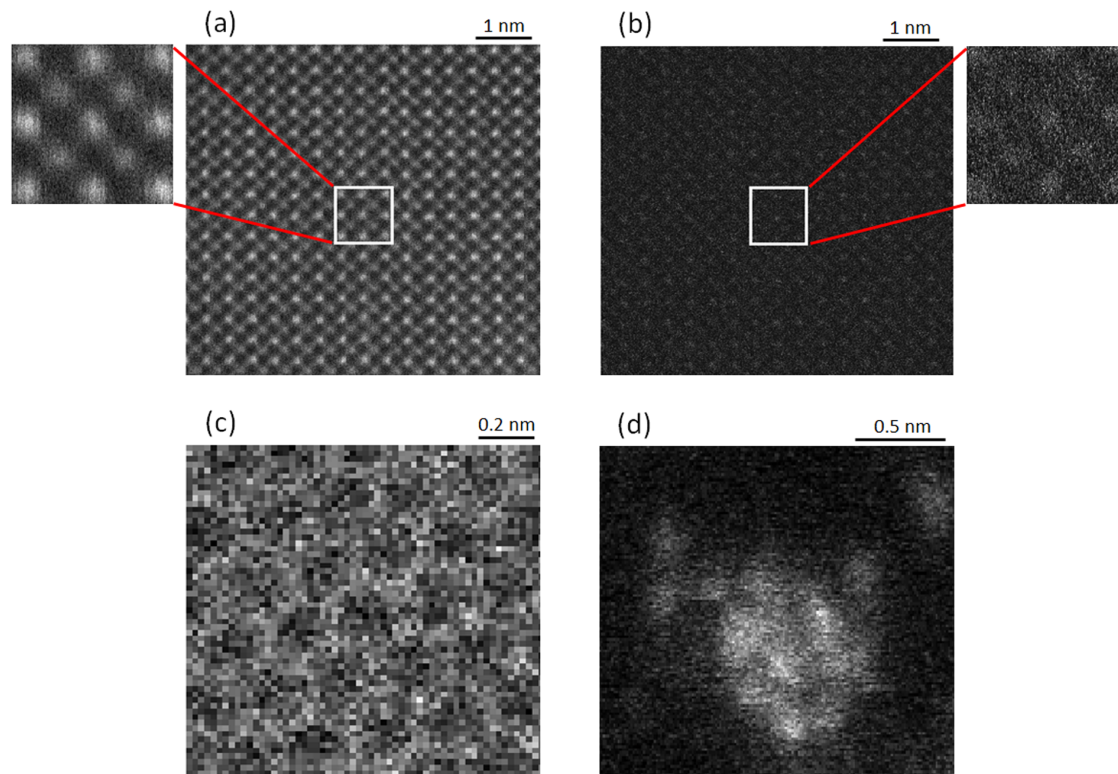


**Figure 1.3:** (a) Atomic-resolution electron microscopy image of  $\text{SrTiO}_3$  using a high incoming electron dose of almost  $10^6 \text{ e}^-/\text{ }^2$ . (b), (c), and (d) Images of  $\text{SrTiO}_3$ , graphene, and a small Ge cluster, respectively, using a limited incoming electron dose of the order of  $10^4 - 10^5 \text{ e}^-/\text{ }^2$ , resulting into a detected electron dose of the order of  $10^2 \text{ e}^-/\text{ }^2$ .

in images exhibiting low intensities of the order of  $10^2$  detected electrons/ $\text{\AA}^2$ . Recognising structural features or even atomic columns from such images by just a visual inspection is unreliable and might lead to biased structural information. Usually, for beam-stable materials, the number of atomic columns can be determined visually due to the high incoming electron dose, typically of the order of more than  $10^6 - 10^8$   $e^-/\text{\AA}^2$  [Williams 2009], that can be used to image these materials. This results into images containing a high number of detected electrons, roughly of the order of  $10^4$  electrons/ $\text{\AA}^2$ , leading to images exhibiting high quality. This is illustrated in Fig. 1.3(a) for an atomic-resolution image of  $\text{SrTiO}_3$  where the atomic columns can be easily recognised. For beam-sensitive and light-element materials, though, the incoming electron dose should be limited in order to avoid beam damage, resulting into low-quality images. Visual inspection of such images may lead to biased results. Figs. 1.3(b), (c) and (d) show images recorded with a limited incoming electron dose of the order of  $10^4 - 10^5$   $e^-/\text{\AA}^2$  of  $\text{SrTiO}_3$ , graphene, and a small Ge cluster, respectively [Fatermans 2018]. Although some features can be recognised from these images, it is not straightforward to visually indicate the presence or absence of atomic columns, especially when no prior knowledge about the material's structure is available. Therefore, often imaging processing techniques are necessary in order to interpret low-dose images and to obtain reliable structural information. Several noise-reduction techniques exist which are aimed to remove noise from images and to highlight relevant features [Westin 2000, Vieira 2013]. Nowadays, deep-learning techniques making use of neural networks are also being developed to remove noise or other image artefacts from images and to perform image restoration [Madsen 2018]. In case of a series of low-dose images, a higher signal can be obtained by combining the individual images in the series by using image registration or image alignment algorithms [Goshtasby 2005, Jones 2015]. An alternative way is to use template matching where parts of an image are matched with a template which can be a smaller area of the image or a separate image [Brunelli 2009, Altantzis 2016]. A drawback of the techniques of image registration and template matching is that only average structure information can be obtained, losing information on the local level which might have an important effect on the physical properties of nanomaterials. Alternatively, also statistical techniques are available for detecting atoms or the number of atoms in a column and to recover information about the structure of the material under investigation [Meyer 2014, Gonniissen 2014, De Backer 2015b, Gonniissen 2016b, Kramberger 2016, Kramberger 2017, Van Aert 2019].

In this thesis, a new method, based on Bayesian model selection, will be developed and applied which is capable of quantifying the available image information and detecting the atomic columns that are present in STEM images. In this manner, the most probable atomic structure of unknown nanomaterials can be determined in an automatic and objective manner.

## 1.5 What to expect in this thesis?

Nowadays, powerful image quantification procedures in atomic-resolution TEM are available which enable the possibility to obtain structural information with high accuracy and precision. Often, in such techniques, it is important that the atomic columns in the image can be recognised. As discussed in the previous section, visually determining the number of columns is not straightforward for materials which are sensitive to the electron beam. This is due to the use of a limiting incoming electron dose which causes images to exhibit low intensities, hampering

visual interpretation. Therefore, in this thesis, a new method is developed which brings both image quantification and atom detection together in one framework.

After describing the image formation theory of TEM imaging, this thesis will start by introducing statistical parameter estimation theory. This framework is widely applicable in different fields of science and consists of the estimation of unknown parameters from an available set of experimental observations. The starting point is the construction of a parametric (physics-based) model describing the expectations of the experimental observations as a function of the unknown parameters. In TEM, atomic-resolution images are considered as data planes where the observations are characterised by a set of image pixel values from which unknown parameters need to be estimated, such as the atomic column positions and their widths and heights, and image background. Accurate and precise structure information is then obtained by fitting the parametric model to the observed image pixel values with respect to the unknown structure parameters using a criterion of goodness of fit, quantifying the similarity between the image and the model. Recently, an open source program called StatSTEM has been developed to facilitate model-based quantitative electron microscopy [De Backer 2016].

Interestingly, the framework of parameter estimation theory can be combined with model-order selection. Hereby, besides estimating the unknown structure parameters of the expectation model, also the number of parameters need to be determined, most closely representing the underlying process that generated the experimental observations. Typical model-selection methods perform a tradeoff between high goodness of fit and low model complexity, since model fit can be easily improved by increased model complexity without necessarily bearing any interpretable relationship with the underlying data-generating process. In this thesis, it will be shown that for annular dark-field (ADF) STEM, model selection can be used to automatically and objectively determine the number of atomic columns which are present in the image data. This method is referred to as the maximum a posteriori (MAP) probability rule. As a result, atomic columns and even single atoms can be reliably detected and the most probable atomic structure of unknown nanomaterials can be determined. This is especially relevant for analysing the structure of beam-sensitive nanomaterials, as such materials need to be imaged in STEM with limited incoming electron doses, varying in this thesis from around  $10^3$  to around  $10^5$   $e^-/\text{\AA}^2$  leading to images consisting of low intensities, which makes visual inspection unreliable. The validity and usefulness of this method will be demonstrated to experimental and simulated images of samples of different shape, size, and atom type.

In principle, atom detection from STEM images can be performed with any model-selection criterion. Therefore, the thesis continues with comparing the performance of the MAP probability rule in correctly detecting atoms from ADF STEM images to that of other model-selection criteria. It will be shown that the MAP probability rule takes into account more dimensions of model complexity as compared to other commonly used model-selection criteria. This allows for a superior performance to detect the correct number of atomic columns from ADF STEM images. In addition, the MAP probability rule offers a more flexible way to detect atoms from images than other criteria. This is due to the fact that the prior information can be tuned, resulting into a different value for the complexity of the model under consideration. Moreover, by using the MAP probability rule, it is clear what prior knowledge has been taken into account during the analysis, which is not always straightforward for other model-selection criteria. Besides detecting atomic columns from ADF STEM images, the MAP probability rule also offers a way to evaluate the relation between STEM image quality measures, such as SNR and contrast-to-noise ratio (CNR),

and atom detectability, which is defined as the probability to detect an atom from an image. In general, atom detectability is indeed related to image quality, since, for example, one expects the detectability of atomic columns in an image to increase with increasing image quality. In this way, the probability to detect an atomic column from STEM image data, which can be provided by the MAP probability rule, is correlated with the quality of the image. As such, for STEM images, a new image quality measure, the so-called integrated CNR (ICNR), will be proposed that better correlates with atom detectability than conventional image quality measures.

In the last part of this thesis, the concept of the MAP probability rule, which has initially been developed for analysing ADF STEM images, is extended in order to analyse simultaneously acquired ADF and annular bright-field (ABF) STEM images. Such a simultaneous acquisition from these detector geometries is of relevance since this technique combines the improved light-element visualisation of ABF STEM with the easily interpretable image contrast of ADF STEM. Although a combined ADF and ABF STEM acquisition allows to better visualise atoms of materials consisting of both light and heavy atoms, studying and interpreting such images in a visual way is not necessarily straightforward since light-element nanostructures are typically sensitive to the electron beam, limiting the incoming electron dose resulting into images with low intensities. Therefore, a reliable quantitative method to detect the atomic columns from the image data is required.

The outline of this thesis is as follows. In Chapter 2, the electron-specimen interaction in STEM is described together with methods to characterise the number of electrons being collected by the annular STEM detector. In Chapter 3, model-based parameter estimation theory, which aims to extract structure parameters from the image data, and model-order selection, which aims to determine the optimal number of parameters needed in a parametric model, are introduced. Next, in Chapter 4, the combination of parameter estimation with model selection is discussed. This method is referred to as the MAP probability rule and aims to detect atomic columns and single atoms in an automatic and objective manner from ADF STEM images. This is followed by Chapter 5, where the performance of the MAP probability rule is compared to other selection criteria. In addition, it is shown that the MAP probability rule can also be used to evaluate atom detectability as a function of image quality. In Chapter 6, the methodology of the MAP probability rule for ADF STEM is extended to analyse simultaneously acquired ADF and ABF STEM images. Finally, in Chapter 7, conclusions are drawn and future perspectives are considered.



# 2

## Scanning transmission electron microscopy

### 2.1 Introduction

In the beginning of the 1930s, physicist Ernst Ruska and electrical engineer Max Knoll designed the first electron microscope [Knoll 1932], an instrument capable of exceeding the resolution attainable by an optical microscope. For this, in 1986, Ernst Ruska was awarded the Nobel Prize. Although, the first electron microscopes were very primitive as compared to today's highly sophisticated machines, they still form the basis of modern-day electron illumination techniques. The original design was similar to that of the optical microscope where a broad beam is used to image the specimen. By the late 1930s, though, already alternative ways of illumination were investigated by using a fine probe being scanned over the specimen [Knoll 1935, Von Ardenne 1938]. In principle, by using such a fine probe, the specimen is incoherently illuminated [Cowley 1969], which results into a higher attainable resolution as compared to the coherent illumination of a broad beam [Nellist 2000]. Only in the 1970s, the technique of STEM was further developed [Crewe 1966, Crewe 1968], demonstrating the visualisation of single atoms [Crewe 1970].

In Fig. 2.1, CTEM is schematically illustrated. More details on this imaging mode can be found in [Van Dyck 2002, De Graef 2003, Williams 2009]. In CTEM, the specimen is illuminated by a parallel incident electron beam. The electrons of the incident plane wave propagate through the specimen while interacting with the electrostatic potential of the atoms, resulting into a complex wave function that leaves the specimen, i.e. the exit wave. When the specimen is oriented along a major zone axis and when the distance between neighbouring atomic columns is not too small, there exists a one-to-one correspondence between the exit wave and the projected atomic structure [Van Dyck 1996, Van Dyck 1999, Geuens 2002]. Through a set of objective apertures and electromagnetic lenses, a virtual image of the exit wave is created, which is further magnified by the projector lenses. Since, in practice, the electromagnetic lenses

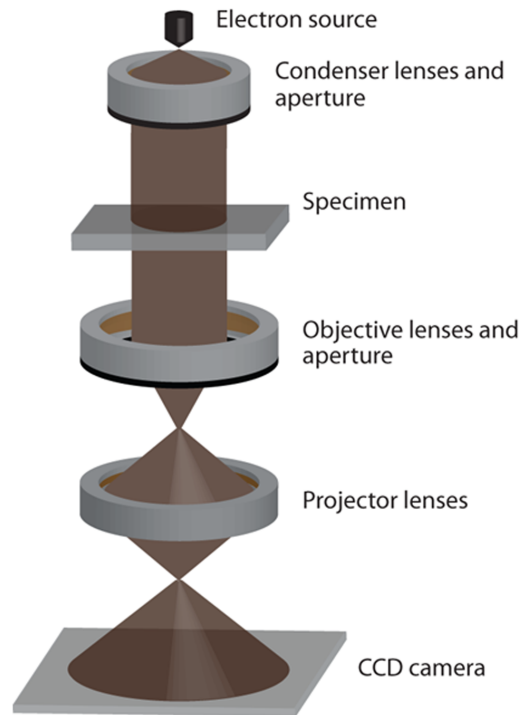


**Figure 2.1:** Schematic drawing of CTEM [Van Aert 2016], where the specimen is illuminated by a plane wave after which an image is formed by using a set of electromagnetic lenses.

in the microscope are not perfect, the exit wave is distorted by aberrations [Rose 2009], such as spherical aberration, defocus, and chromatic aberration. Finally, the wave is recorded in the detector plane with a charge-coupled device (CCD) camera, detecting the electron counts reaching the camera. In this process, only intensities are recorded, losing the information about the phase of the exit wave. The technique of CTEM is a coherent imaging technique. As such, contrast reversals may appear due to the specimen and lens aberrations, which causes CTEM image interpretation to be not straightforward and possibly even complicated.

Details about the STEM technique, which is schematically displayed in Fig. 2.2, can be found in [Nellist 2000, Pennycook 2011]. As shown in Fig. 2.2(a), in STEM, a focused electron beam with convergence semi-angle  $\alpha$  is scanned in a 2D raster across the specimen. Hereby, for each probe position, the electrons propagate through and interact with the specimen, causing them to scatter towards the detector which has an annular shape with inner and outer collection angles  $\beta_1$  and  $\beta_2$ , respectively. The detector integrates the collected electrons as a function of probe position. As a result, an image is built up during the scanning of the specimen. Nowadays, different detector geometries in STEM are available depending on the collection angles of the annular detector [Shibata 2010, Hovden 2012, Yang 2015b]. These geometries are depicted in Fig. 2.2(b). The atomic number dependence of the contrast and the SNR differs depending on what collection angles are chosen. The most commonly used imaging mode in STEM is ADF imaging, where the inner collection angle  $\beta_1$  of the detector is larger than the probe convergence semi-angle  $\alpha$ . The electrons scattered to the ADF detector are mainly

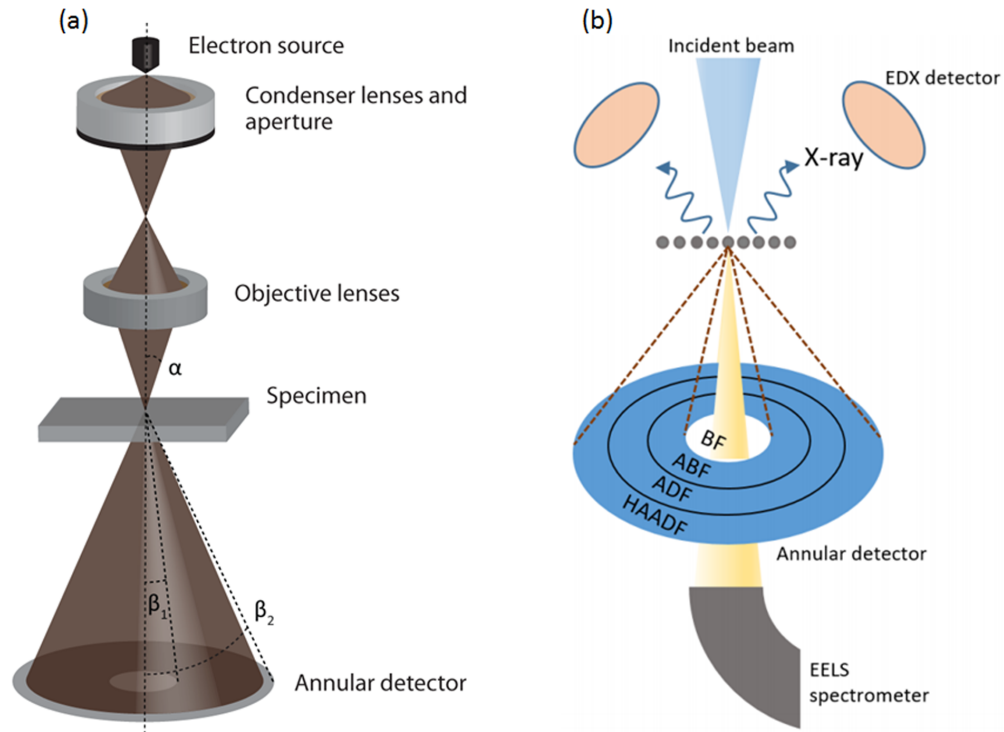


**Figure 2.2:** (a) Schematic drawing of STEM [Van Aert 2016], where a focused electron beam with convergence semi-angle  $\alpha$  is scanned over the specimen. The scattered electrons are collected on an annular detector with inner and outer angles  $\beta_1$  and  $\beta_2$ , respectively. (b) Simplified schematic of STEM [Korneychuk 2018], highlighting the different detector geometries and the ability of collecting EDX and EELS signals simultaneously with STEM images.

inelastically scattered electrons [Hartel 1996, Pennycook 2011]. The image contrast in ADF STEM is easily interpretable due to the fact that it is an incoherent imaging mode which strongly depends on the atomic number  $Z$ . Especially for a high inner detector angle  $\beta_1$ , the image contrast is approximately proportional to  $Z^2$ . Therefore, high-angle annular dark-field (HAADF) STEM imaging is often referred to as  $Z$ -contrast imaging. Alternative ADF set-ups using smaller inner collection angles are referred to as low-angle ADF (LAADF) and medium-angle ADF (MAADF), respectively. Another configuration is bright-field (BF) imaging. Here, use is made of a circular detector that lies within the illumination cone of the electron probe ( $\beta_1 = 0$  and  $\beta_2 \leq \alpha$ ). Interestingly, by the concept of reciprocity, which states that the electron intensities and ray paths in the microscope remain the same if their direction is reversed and the source and detector are interchanged, it can be shown that BF STEM is equivalent with CTEM [Kirkland 2010]. Placing an annular detector within the illumination cone of the electron probe results into ABF STEM imaging, where  $\beta_1 > 0$  and  $\beta_2 \leq \alpha$ . This imaging mode suffers less from contrast reversals than BF STEM, resulting into images which are more easily interpretable over a large range of thicknesses [Findlay 2009, Okunishi 2009, Findlay 2010]. As compared to ADF STEM imaging, ABF STEM is more suitable to visualise both light and heavy elements simultaneously, since image contrast is less dependent on atomic number  $Z$ . Recently, detectors have been developed for STEM that enable to record a complete convergent beam electron diffraction (CBED) pattern

at every pixel during the scanning of the sample. These detectors are referred to as pixelated detectors [Ryll 2016, Tate 2016, Mir 2017, Faruqi 2018]. As such, four-dimensional (4D) STEM data can be acquired, consisting of 2D diffraction patterns recorded at every 2D probe position. From the 4D data, so-called synthetic STEM images can be obtained which are equivalent to images obtained by the conventional annular geometry, but with the benefit that the detector collection angles can be tuned in a flexible manner.

Currently, modern-day electron microscopes are also capable of simultaneously acquiring STEM images and spectral signals. This allows for performing energy-dispersive X-ray spectroscopy (EDX) and electron energy loss spectroscopy (EELS), whose detector geometries are schematically drawn in Fig. 2.2(b). The possibility of collecting spectral signals allows for more robust chemical characterisation, especially for nanomaterials consisting of almost identical atomic numbers. X-rays in the electron microscope occur due to the high energy of the electrons, possibly exciting the atoms in the sample to a higher energy level followed by the emission of X-rays when falling back to their ground states. The technique of recording such X-rays is referred to as EDX. The EDX signal provides direct information about the atomic composition of a material since the energy of the emitted X-ray is related to the electron shell structure of an atom. Hereby, relative quantification methods have been developed for low-magnification images [Cliff 1975, Watanabe 2006]. Recently, new methods have been proposed which have enabled to perform a compositional determination at the atomic scale [MacArthur 2016a, MacArthur 2016b]. In order to be able to directly compare measured experimental EDX spectra with simulations, it is crucial to describe the generation of X-rays correctly [Dwyer 2005, d'Alfonso 2010, Allen 2012] and to take into account the detector geometry and efficiency in image simulations [Xu 2016]. As a result, thickness and composition measurements can be performed in bulk materials [Kothleitner 2014, Chen 2015]. Historically, EDX has suffered from low SNR, but due the implementation of a new recording system composed of 4 detectors, improving the SNR significantly [Schlossmacher 2010], interest in EDX has been regained. EELS, at the other hand, consists of measuring the energy loss of the incident electrons due to interaction with the specimen. Such energy losses are related to the energy transfer required to excite an electron in the atomic electron shell to a higher energy level. When the excited electron falls back to a lower energy level an X-ray might be produced. As such, EDX is a secondary process which only occurs after an EELS event. The technique of EELS can be used to measure the atomic composition of a specimen [Egerton 1996, Egerton 2008]. As compared to EDX, with EELS, also information about chemical bonding, and valence and conduction band electronic properties can be obtained. In order to optimise the analysis of EELS data, model-based methods have been developed [Verbeeck 2004, Verbeeck 2006].

Lastly, it is noted that TEM images are typically acquired in a vacuum system to reduce the collision frequency of the electrons with gas atoms to negligible levels. Nowadays, there is an increasing interest in performing environmental, or in situ, TEM or STEM, where the sample is brought in a liquid environment [de Jonge 2011, Ievlev 2015, Ross 2015, Unocic 2016] or gaseous environment [Boyes 2013, Li 2015] by using specialised specimen holders. Conducting in situ experiments is of great importance for studying nanoparticles, biological samples or chemical reactions in their natural environment [Crozier 2014, Kosasih 2018].

Although TEM imaging has become a standard technique to study the structure of nanomaterials with atomic resolution, a TEM image merely provides a 2D projection of a three-dimensional (3D) atomic structure which might be misleading. For example, as morphology is one of the

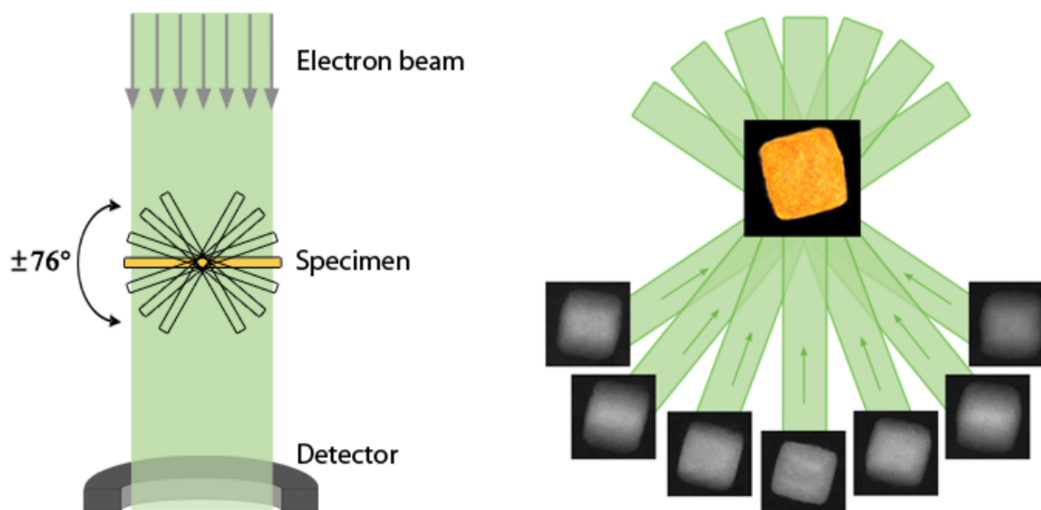


**Figure 2.3:** Schematic showing the principle of electron tomography [Winckelmans 2018a], in which the specimen is tilted over a large angular range while acquiring images at certain tilt increments. Then, the series of projection images is aligned and reconstructed to a 3D representation of the object under investigation.

main factors which influences the properties of a nanoparticle, different techniques which are able to reveal the exact 3D structure have been suggested in the field of electron microscopy. The best known method is electron tomography, where a series of 2D projection images are acquired at different tilt angles, i.e. at incremental degrees of rotation around the specimen [Midgley 2009, Bals 2013]. After carefully aligning the recorded images [Houben 2011, Scott 2012], a 3D reconstruction of the specimen can be obtained. The principle of electron tomography is schematically presented in Fig. 2.3. In order to successfully perform an electron tomography experiment, it is important that the sample is sufficiently stable under illumination of the electron beam during the acquisition of the tilt series. Also, it is assumed that image intensities show a monotonic relationship with the thickness or density of the structure [Weyland 2004]. In addition, electron tomography suffers from the so-called missing wedge problem which causes artefacts in the 3D reconstruction [Midgley 2003]. This is due to the design of the electron microscope where the tilt range of the specimen holder is limited, restricting the acquisition of images from certain tilt angles. Electron tomography reconstructions used to be obtained at the nanoscale [Bals 2007, Ke 2010, Biermans 2010], but the development of new advanced reconstruction algorithms [Goris 2012b, Leary 2013, Goris 2013b] has enabled 3D characterisation to evolve from the nanoscale to the atomic scale [Scott 2012, Goris 2012a, Goris 2013a, Xu 2015, Goris 2015, Yang 2017]. Recently, multimodal tomography has been introduced where spectral imaging by EDX and EELS have been introduced in a tomographic framework [Möbus 2003, Bals 2014, Goris 2014b, Goris 2014a, Yedra 2014, Slater 2016, Zanaga 2016] or where multiple STEM detector geometries are combined [Winckelmans 2018b]. A similar technique to electron tomography is discrete tomography. Here, atom-counting results are obtained from only a few zone-axis orientations. By combining the results from different viewing directions, a 3D reconstruction of the material at the atomic level is achievable

[Van Aert 2011, Bals 2011, van den Bos 2016]. Even from a single projection image, 3D atomic models can be obtained [De Backer 2017]. Furthermore, the 3D dynamical behaviour could be investigated from a single viewing direction by performing *ab initio* or molecular dynamics calculations [Bals 2012, Jones 2014]. The benefit of discrete tomography as compared to conventional electron tomography is that the sample is less exposed to the electron beam as no large series of images is recorded, which offers a more optimal way of imaging beam-sensitive nanoparticles that might otherwise be damaged. Another possible technique for 3D structure characterisation is depth-sectioning by HAADF STEM [van Benthem 2005, Einspahr 2006, van Benthem 2006]. In this technique, it is possible to slice through the specimen from a single viewing direction by acquiring a focal series of images [Van den Broek 2010]. Depth sectioning is useful for obtaining information about 3D surface morphology, thickness, top/surface atomic structures or dislocations [Hirsch 2013, Yang 2015a, Alania 2017b]. Despite advances in aberration correction technology, the resolution obtained by depth sectioning remains insufficient to reach atomic-depth resolution [Borisevich 2006, Cosgriff 2007, Alania 2017b]. In CTEM, a 3D reconstruction at the atomic scale can be provided by an advanced analysis of the exit wave, which is closely related to the object structure. The exit wave can be reconstructed by a series of CTEM images acquired at different focal values [Wang 2010, Wang 2012].

In this chapter, the image formation process of STEM will be described. More details concerning the topic can be found in [Van Dyck 1989, Broeckx 1995, Van Dyck 1996, Kirkland 2010]. In particular, the derivations in this chapter have been based on [Kirkland 2010]. The description of the electron interactions in the electron microscope is important for understanding the observed image contrast in images. Furthermore, knowledge about the image formation process can be used to simulate realistic electron microscopy images which can be directly compared to experimental images. In STEM, the electron probe is focused onto the specimen by a set of lenses and scanned in a 2D raster across the specimen, as depicted in Fig. 2.2. When the electrons interact with the sample, many types of reactions such as electron backscattering, production of X-rays and Auger electrons, and cathodoluminescence can occur, whose signals can be captured to gain information about the specimen under investigation. In this thesis, the focus will lie on the transmitted electrons which, in STEM, are collected by an annular detector. In section 2.2, the electron-specimen interaction is discussed, which forms the most important part of the image formation process. Mathematically describing this interaction involves introducing the Schrödinger equation. The remaining of this chapter discusses the electron interactions according to their trajectory in the electron microscope, as shown in Fig. 2.2, starting with the mathematical description of the electron-probe formation in section 2.3, including the aberrations and compensations of the magnetic lenses. Then, in section 2.4, the specimen potential is introduced. In order to understand the mechanisms behind the interactions of the electrons with the specimen, the Schrödinger equation needs to be solved. In principle, this comes down to describing a dynamical scattering process, in which the electrons are scattered multiple times while propagating through the specimen [Van Dyck 1985, Cowley 1995]. When a scattering event occurs only once, the scattering is referred to as being kinematical. The dynamical scattering problem can be solved from an optics point of view [Cowley 1957]. In this method, which is referred to as the multislice method [Lynch 1972, Allpress 1972, Allpress 1973], the specimen is divided into thin 2D slices along the propagation direction of the electron beam. Hereby, the electron beam alternately transverses a slice and propagates then to the next slice. The multislice method is thoroughly described in section 2.5. Hereby, in order

to obtain realistic quantitative image simulations, it is also important to take into account the thermal behaviour of the atoms in the specimen. Nowadays, the multislice method has been incorporated in several software packages for the simulation of high-resolution images of which STEMsim [Rosenauer 2008b] and MULTEM [Lobato 2015, Lobato 2016] are two examples. After interaction with the specimen, it can be seen from Fig. 2.2 that the transmitted electrons are transferred to the detector plane forming an image of the specimen which is described in section 2.6. In section 2.7, the behaviour of the detector is discussed and methods for converting the recorded intensities into physical electron counts are described. Finally, conclusions will be drawn in section 2.8.

## 2.2 Electron-specimen interaction

In the electron microscope, electrons should be treated relativistically as they are travelling at high speeds with energies ranging typically from 50-300 keV. For example, an electron with an energy of 100 keV travels approximately with half the speed of light. This means that quantities such as mass, velocity, and wavelength need to be calculated relativistically. The total energy  $E_0$  of a charged particle with charge  $e$  and rest mass  $m_0$  accelerated through a potential  $V_0$  is given by

$$E_0^2 = (m_0c^2 + eV_0)^2 = p^2c^2 + m_0^2c^4 = m^2c^4, \quad (2.1)$$

where  $c$  is the speed of light in vacuum (299792458 m/s),  $p = mv$  the particle's momentum where  $v$  is its velocity and  $m$  its mass. Hereby,  $m_0c^2 = 511$  keV. From Eq. (2.1), it follows that the ratio of the electron's mass to its rest mass becomes

$$\frac{m}{m_0} = \gamma = \frac{1}{\sqrt{1 - v^2/c^2}} = 1 + \frac{eV_0}{m_0c^2}. \quad (2.2)$$

From this expression, it follows that the velocity of the electron relative to the velocity of light is given by

$$\frac{v}{c} = \sqrt{1 - \left(\frac{m_0c^2}{m_0c^2 + eV_0}\right)^2}. \quad (2.3)$$

The movement of the electrons in the electron microscope and their interaction with the specimen under investigation is a quantum mechanical process. Under such conditions, the electrons can be described not only as particles, but also as waves. This phenomenon is called the wave-particle duality. As a result, the de-Broglie wavelength of the electron can be calculated as:

$$\lambda = h/p, \quad (2.4)$$

where  $h$  is Planck's constant being  $6.62607015 \cdot 10^{-34}$  J·s. Substituting Eq. (2.4) into Eq. (2.1) yields

$$(m_0c^2 + eV_0)^2 = \left(\frac{hc}{\lambda}\right)^2 + m_0^2c^4, \quad (2.5)$$

from which follows that

$$\lambda = \frac{hc}{\sqrt{eV_0(2m_0c^2 + eV_0)}}. \quad (2.6)$$

The wave-particle duality invokes that all the information about an electron in the electron microscope is encoded in a wavefunction. During the electron-specimen interaction, the wavefunction evolves according to the Schrödinger equation. Due to the beam energies in electron microscopy, typically 50-300 keV, the electrons behave in a relativistic way. In principle, the Schrödinger equation is not the correct wave equation for relativistic electrons. Instead, the relativistic Dirac equation should be used. This equation, though, is mathematically significantly more difficult to work with. Traditionally, the Schrödinger equation is still applied using the relativistically correct electron mass and wavelength, as given by Eqs. (2.2) and (2.6), respectively. For the range of energies of the electrons in the microscope, this approach is accurate enough to describe electron scattering [Fujiwara 1961, Ferwerda 1986b, Ferwerda 1986a, Jagannathan 1989, Jagannathan 1990]. Only at energies of the order of 1000 keV or higher, small errors may be introduced [Kirkland 2010].

For describing the electron-specimen interaction the time-independent Schrödinger equation may be used since the electrons move very fast through the specimen which causes the interaction with the crystal to be extremely short. Therefore, the electrons only see a snapshot of the crystal, validating the approximation of using a stationary potential. As such, the Schrödinger equation for the full wave function  $\psi_f(x, y, z)$  as a function of three spatial coordinates  $(x, y, z)$  in the electrostatic potential  $V(x, y, z)$  of the specimen is:

$$\left[ -\frac{\hbar^2}{2m} \Delta - eV(x, y, z) \right] \psi_f(x, y, z) = E\psi_f(x, y, z), \quad (2.7)$$

where  $\hbar = h/2\pi$  and  $m$  is the relativistic mass of the electron, which can be derived from Eq. (2.2). The 3D Laplace operator is given by  $\Delta = \partial^2/\partial x^2 + \partial^2/\partial y^2 + \partial^2/\partial z^2$  and  $e$  denotes the charge of the electron. The total kinetic energy of the electron is denoted by  $E$ . Since in the electron microscope the energy of the incident electrons is much larger than the additional energy they gain inside the specimen, the electron motion will be predominantly in the forward  $z$  direction, thus along the optic axis of the microscope. Therefore, it is useful to separate the large velocity in the  $z$  direction from other small effects due to the specimen [Kirkland 2010, Lobato 2014]:

$$\psi_f(x, y, z) = \psi(x, y, z) e^{2\pi iz/\lambda}. \quad (2.8)$$

Hereby, the full wave function  $\psi_f(x, y, z)$  has been written as the product of two factors, one of which is a plane wave traveling in the  $z$  direction, whereas the other factor  $\psi(x, y, z)$  is the portion of the wave function that varies slowly with position  $z$ . In Eq. (2.8),  $\lambda$  is the electron wavelength given by Eq. (2.6), for which holds that  $k^2 = k_x^2 + k_y^2 + k_z^2 = 1/\lambda^2$ , where  $k^2$  denotes the squared magnitude of the wave vector  $\mathbf{k}$ . For elastic processes, the kinetic energy of the electron is given by

$$E = \frac{\hbar^2 k^2}{2m} = \frac{\hbar^2}{2m\lambda^2}. \quad (2.9)$$

From Eq. (2.7), it follows that the following derivative needs to be calculated:

$$\begin{aligned} \Delta\psi_f(x, y, z) &= \left[ \frac{\partial^2}{\partial x^2} + \frac{\partial^2}{\partial y^2} + \frac{\partial^2}{\partial z^2} \right] \psi_f(x, y, z) \\ &= \left[ \Delta_{x,y} + \frac{\partial^2}{\partial z^2} \right] \psi_f(x, y, z), \end{aligned} \quad (2.10)$$

where  $\Delta_{x,y}$  is the 2D Laplace operator in  $x$  and  $y$ . Substituting Eq. (2.8) into Eq. (2.10) gives the following expression:

$$\Delta\psi_f(x, y, z) = e^{2\pi iz/\lambda} \Delta_{x,y} \psi(x, y, z) + \frac{\partial^2}{\partial z^2} [\psi(x, y, z) e^{2\pi iz/\lambda}]. \quad (2.11)$$

An expression for the second term at the right-hand side of Eq. (2.11) can be found. The first derivative with respect to  $z$  becomes

$$\frac{\partial}{\partial z} [\psi e^{2\pi iz/\lambda}] = e^{2\pi iz/\lambda} \left[ \frac{\partial \psi}{\partial z} + \frac{2\pi i}{\lambda} \psi \right]. \quad (2.12)$$

From this, it follows that the second derivative is:

$$\frac{\partial^2}{\partial z^2} [\psi e^{2\pi iz/\lambda}] = e^{2\pi iz/\lambda} \left[ \frac{\partial^2 \psi}{\partial z^2} + \frac{4\pi i}{\lambda} \frac{\partial \psi}{\partial z} \right] - \frac{4\pi^2}{\lambda^2} \psi_f. \quad (2.13)$$

By substitution of Eqs. (2.11) and (2.13) in Eq. (2.7), the Schrödinger equation can be written as:

$$-\frac{\hbar^2}{2m} \left[ \Delta_{x,y} + \frac{\partial^2}{\partial z^2} + \frac{4\pi i}{\lambda} \frac{\partial}{\partial z} + \frac{2meV(x, y, z)}{\hbar^2} \right] \psi(x, y, z) = 0. \quad (2.14)$$

Since the electrons have high energies, the specimen will only give a minor perturbation on the electron's motion which is predominantly in the forward  $z$  direction. This means that  $\psi$  changes slowly with  $z$  and  $\lambda$  is very small [Kirkland 2010, Lobato 2014]. Therefore,

$$\left| \frac{\partial^2 \psi(x, y, z)}{\partial z^2} \right| \ll \left| \frac{4\pi i}{\lambda} \frac{\partial \psi(x, y, z)}{\partial z} \right|, \quad (2.15)$$

which means that the Schrödinger equation in Eq. (2.14) can be reduced to:

$$\left[ \Delta_{x,y} + \frac{4\pi i}{\lambda} \frac{\partial}{\partial z} + \frac{2meV(x, y, z)}{\hbar^2} \right] \psi(x, y, z) = 0. \quad (2.16)$$

The error introduced by neglecting the second order derivative term consists of two parts. The first part arises from the omission of backscattered electrons, which is shown to be negligible [Van Dyck 1975]. The second part is due to a slight modification of the wave vector of the transmitted electrons which becomes important for highly dynamical diffraction in thicker crystals. As a consequence of the latter, the approximation is only valid for relatively thin crystals, not exceeding thicknesses of a few tens of nanometers [Lobato 2014]. It follows from Eq. (2.16) that the Schrödinger equation for fast electrons traveling in the  $z$  direction may be written as a first order differential equation in  $z$  as:

$$\frac{\partial \psi(x, y, z)}{\partial z} = \left[ \frac{i\lambda}{4\pi} \Delta_{x,y} + i\sigma_i V(x, y, z) \right] \psi(x, y, z), \quad (2.17)$$

where

$$\sigma_i = \frac{2\pi m e \lambda}{h^2} \quad (2.18)$$

is called the interaction parameter which describes the amount of interaction between the specimen and the incident electrons. It is noted that the interaction parameter drops rapidly with

increasing electron energy. In computational electron microscopy, the first order differential equation in Eq. (2.17) is solved in order to determine the electron wave function after interaction with the specimen. Before being able to solve the time-independent Schrödinger equation, the entrance wave function and the specimen potential are described as they are necessary inputs in Eq. (2.17) for determining the exit wave function.

## 2.3 Electron probe

In STEM, the objective lens is situated before the specimen and forms a focused probe on the specimen, as illustrated by Fig. 2.2. An image is built up by scanning this focused probe over the specimen and by recording the transmitted intensity at each position of the probe. In order to solve the differential equation given by Eq. (2.17), the incident wave function of the probe that interacts with the specimen needs to be introduced. This wave function is given by  $\psi(x, y, 0) = \psi_0(\mathbf{x})$ , where  $\mathbf{x} = (x, y)$  is the 2D coordinate vector. In the ideal case, when no aberrations are present, this wave function is given by an integration over the objective aperture as:

$$\psi_0(\mathbf{x}, \mathbf{x}_0) = A_0 \int_0^{\mathbf{k}_{MAX}} e^{2\pi i \mathbf{k} \cdot (\mathbf{x} - \mathbf{x}_0)} d\mathbf{k}, \quad (2.19)$$

where  $\mathbf{x}_0 = (x_0, y_0)$  is the electron probe position and where  $\mathbf{k} = (\mathbf{k}_x, \mathbf{k}_y)$  is the 2D wave vector,  $\lambda|\mathbf{k}_{MAX}| = \alpha_{MAX}$  is the maximum angle in the objective aperture, and  $A_0$  is a normalisation constant chosen to yield

$$\int |\psi_0(\mathbf{x}, \mathbf{x}_0)|^2 d\mathbf{x} = 1. \quad (2.20)$$

With this normalization, the total incident intensity in the electron probe is equal to unity. By making use of the fact that the forward and inverse 2D Fourier transform of the arbitrary functions  $g(\mathbf{x})$  and  $g(\mathbf{k})$  are given by

$$FT[g(\mathbf{x})] = \int g(\mathbf{x}) e^{-2\pi i \mathbf{k} \cdot \mathbf{x}} d\mathbf{x} \quad (2.21)$$

and

$$FT^{-1}[g(\mathbf{k})] = \int g(\mathbf{k}) e^{2\pi i \mathbf{k} \cdot \mathbf{x}} d\mathbf{k}, \quad (2.22)$$

respectively, Eq. (2.19) can be written as

$$\psi_0(\mathbf{x}, \mathbf{x}_0) = A_0 FT^{-1} [A(\mathbf{k}) e^{-2\pi i \mathbf{k} \cdot \mathbf{x}_0}], \quad (2.23)$$

where  $A(\mathbf{k})$  is the aperture function given by

$$A(\mathbf{k}) = \begin{cases} 1, & \lambda|\mathbf{k}| \leq \alpha_{MAX} \\ 0, & \text{otherwise} \end{cases} \quad (2.24)$$

defining the opening of the aperture through which the electrons travel.

In reality, though, lens aberrations are present which characterise the deviation of the electron wave function from an ideal spherical incoming wave [Kirkland 2011]. As compared to their optical counterparts, magnetic lenses suffer from much larger aberrations, limiting them to the use of only small aperture angles. As a result, aberrations cause the wave function of the incident

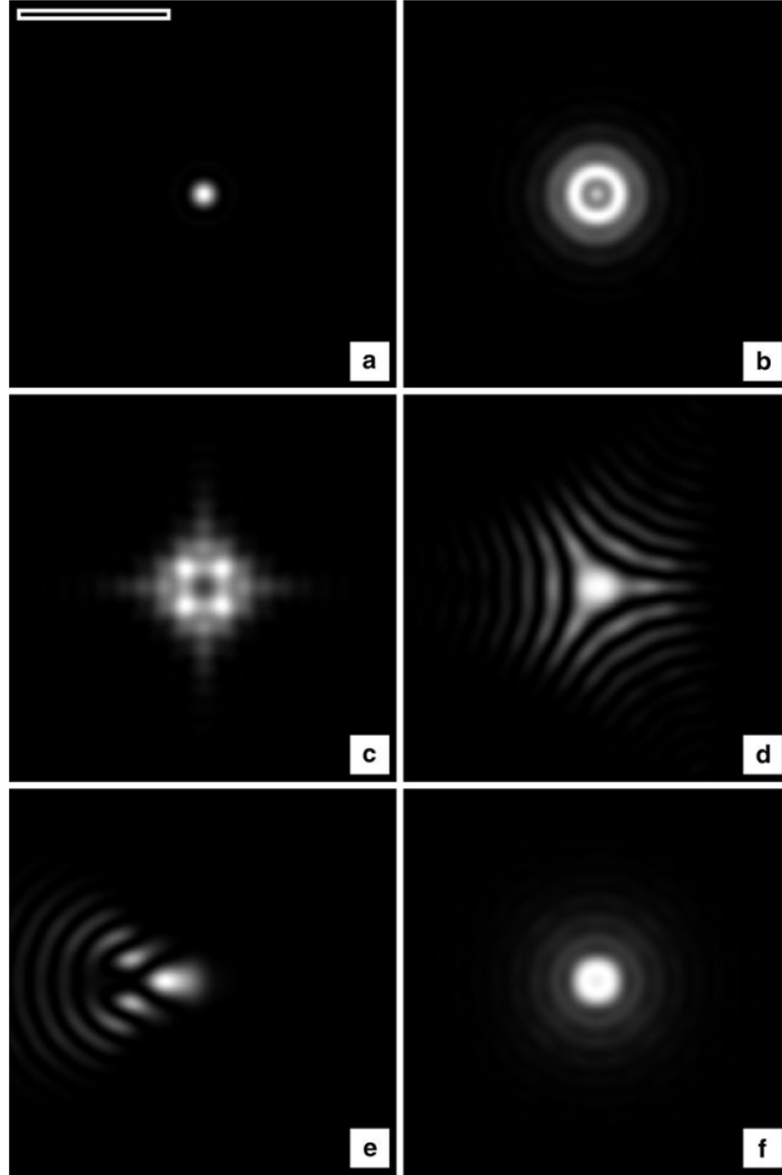


**Figure 2.4:** Qualitative illustration of various single aberrations by images of an electron probe [Kirkland 2010]. (a) no aberrations (scale bar 5 Å), (b) defocus, (c) twofold astigmatism, (d) threefold astigmatism, (e) coma, and (f) spherical aberration.

electrons to be modified by the transfer function  $H_0(\mathbf{k})$  of the objective lens. As a result, Eq. (2.23) can be written as:

$$\begin{aligned}
 \psi_0(\mathbf{x}, \mathbf{x}_0) &= A_0 FT^{-1} \left[ A(\mathbf{k}) H_0(\mathbf{k}) e^{-2\pi i \mathbf{k} \cdot \mathbf{x}_0} \right] \\
 &= A_0 FT^{-1} \left[ A(\mathbf{k}) e^{-i\chi(\mathbf{k}) - 2\pi i \mathbf{k} \cdot \mathbf{x}_0} \right] \\
 &= A_0 \int_0^{\mathbf{k}_{MAX}} e^{-i\chi(\mathbf{k}) + 2\pi i \mathbf{k} \cdot (\mathbf{x} - \mathbf{x}_0)} d\mathbf{k},
 \end{aligned} \tag{2.25}$$

where  $H_0(\mathbf{k}) = e^{-i\chi(\mathbf{k})}$ , containing the aberration function  $\chi(\mathbf{k})$  defined by:

$$\chi(\mathbf{k}) = \pi\lambda C_1 k^2 + \frac{\pi}{2}\lambda^3 C_3 k^4 + \frac{\pi}{3}\lambda^5 C_5 k^6 + \dots \quad (2.26)$$

In Eq. (2.26),  $C_n$  indicates the  $n$ th-order spherical aberration expressed in units of length. The 1st-order spherical aberration is equal to the defocus value,  $C_1 = -\epsilon$ , and the 3rd-order spherical aberration is often denoted as  $C_3 = C_s$ . The 5th-order spherical aberration is indicated by  $C_5$ . In principle, Eq. (2.26) consists further of an infinite number of higher-order terms. It should be noted that in Eq. (2.26) also non-spherical aberrations can be included [Kirkland 2010]. These kind of aberrations can be related to deviations of rotational symmetry which are inevitable due to small errors in the magnetic lenses and small mis-alignment between the lenses. The lowest order effect is the additional aberration of astigmatism and possibly coma. In Fig. 2.4, the typical forms of aberrations are illustrated and compared to the situation of the absence of aberrations. Typically, aberration correctors involve a rather sophisticated combination of multipole focussing elements aimed for correcting the unavoidable 3rd-order spherical aberration  $C_3$  of a rotationally symmetric round lens. Unfortunately, in this process, the multipoles at their turn produce new aberrations, which, ideally, should also be corrected [Kirkland 2016]. As such, one can never fully get rid of aberrations, as removing one aberration invokes another.

## 2.4 Specimen potential

In electron microscopy, the primary interaction between the specimen and the incident electrons arises from the electrostatic Coulomb potential of the specimen and the charge of the electron. As the incoming electrons have high velocities, their relativistic wavelengths are given by Eq. (2.6), from which it follows that

$$\frac{1}{\lambda} = \frac{\sqrt{eV_0(2m_0c^2 + eV_0)}}{hc} \quad (2.27)$$

Typically, the incident electrons pass through the specimen with only a small deviation in their path, which can be described as a small change in wavelength. Since the positive electrostatic potential of the specimen,  $V(x, y, z)$ , accelerates the incident electrons, their wavelength while inside the specimen becomes:

$$\begin{aligned} \frac{1}{\lambda_s} &= \frac{\sqrt{(eV_0 + eV(x, y, z))(2m_0c^2 + eV_0 + eV(x, y, z))}}{hc} \\ &= \frac{1}{\lambda} \sqrt{1 + \frac{eV(x, y, z)(2m_0c^2 + 2eV_0 + eV(x, y, z))}{eV_0(2m_0c^2 + eV_0)}} \approx \frac{1}{\lambda} \left[ 1 + \frac{\lambda\sigma_i V(x, y, z)}{2\pi} \right], \end{aligned} \quad (2.28)$$

where, in the last step, the square root is approximated by a first order Taylor expansion where only the lowest order terms in  $V(x, y, z)/V_0$  are kept. This approximation is validated by the large kinetic energy of the incident electrons as compared to the electrostatic potential of the specimen. In Eq. (2.28),  $\sigma_i$  represents the interaction parameter as given by Eq. (2.18) [Kirkland 2010]. As a changing wavelength is equivalent with a phase shift in the electron wave function, an approximation of the electron wave function while passing through the specimen is:

$$\psi_t(\mathbf{x}) = \psi_0(\mathbf{x}) e^{2\pi iz/\lambda} e^{i\sigma_i V(x, y, z)z} \quad (2.29)$$

In case the specimen is very thin, neglecting the effect of dynamical scattering, then the electron wave function accumulates a total phase change while passing through the specimen that is just the integral of the specimen potential along the optical axis  $z$  [Cowley 1972], which is given by:

$$v_z(\mathbf{x}) = v_z(x, y) = \int_{-\infty}^{\infty} V(x, y, z) dz. \quad (2.30)$$

As a result, the electron wave function in Eq. (2.29) can be written as

$$\psi_t(\mathbf{x}) = \psi_0(\mathbf{x}) e^{2\pi iz/\lambda} e^{i\sigma_i v_z(\mathbf{x})}. \quad (2.31)$$

Here, the total potential of the specimen can be obtained by combining the atomic potentials of the individual atoms which are contained in the specimen:

$$v_z(\mathbf{x}) = \sum_{n=1}^N v_{z,n}(\mathbf{x} - \mathbf{x}_n), \quad (2.32)$$

where  $v_{z,n}(\mathbf{x} - \mathbf{x}_n)$  is the projected potential of the  $n$ th atom at position  $\mathbf{x}_n = (x_n, y_n)$  in a plane perpendicular to the optical axis of the microscope. For single atoms separated by a distance that is large as compared to the atom size, the interaction between the atoms is negligible. As such, the potential of each atom can be approximated as being equal to the potential of an isolated atom and, in this case, the linear superposition approximation in Eq. (2.32) would be exact. For obtaining the potential of an isolated atom, numerical methods can be used [Coulthard 1967, Fischer 1977], where the potential and the charge distribution of a single atom is found by determining the wave functions of all electrons of an atom. However, in reality, atoms in a solid specimen are bound together, causing their outer valence electrons to be rearranged slightly. The interaction resulting in the scattering of the electrons to high angles is mainly due to the interaction between the atomic nuclei and the incident electrons. The bonding effect, though, primarily affects electrons that are scattered to relatively low angles.

## 2.5 Multislice method

In order to find the scattered wave function, given the incident wave function and the specimen's potential, the Schrödinger equation given by Eq. (2.17) needs to be solved. A solution for this equation is provided by the multislice approach [Cowley 1957]. The starting point of this approach states that the 3D atomic potential of the specimen can be approximated by a set of 2D projections. Hereby, the specimen's potential is divided into many slices along the beam-propagation direction in which the atomic potentials of the different atoms in each slice are projected. As such, each slice only modifies the phase of the electron wave. For calculating the exit wave function, the electron wave function gets alternately transmitted through a slice and propagated to the next slice. This process continues until the electron wave function reaches the specified thickness of the specimen. In Fig. 2.5, the multislice decomposition of a thick specimen is illustrated. In the multislice method, the wave function after interaction with a slice of the specimen of thickness  $d_z$  is found by using the general solution to Eq. (2.17):

$$\psi(x, y, z + dz) = \exp \left[ \int_z^{z+dz} \left( \frac{i\lambda}{4\pi} \Delta_{x,y} + i\sigma_i V(x, y, z') \right) dz' \right] \psi(x, y, z). \quad (2.33)$$

When the projected potential of the specimen between  $z$  and  $z + dz$  is written as:

$$v_{dz}(x, y, z) = \int_z^{z+dz} V(x, y, z') dz', \quad (2.34)$$

Eq. (2.35) becomes:

$$\psi(x, y, z + dz) = \exp\left[\frac{i\lambda}{4\pi} dz \Delta_{x,y} + i\sigma_i v_{dz}(x, y, z)\right] \psi(x, y, z). \quad (2.35)$$

By making use of the fact that  $dz$  is small, this expression can be rewritten by making use of a Taylor expansion and factorisation [Goodman 1974, Kirkland 2010]:

$$\psi(x, y, z + dz) = \exp\left[\frac{i\lambda}{4\pi} dz \Delta_{x,y}\right] \exp[i\sigma_i v_{dz}(x, y, z)] \psi(x, y, z) + O(dz^2), \quad (2.36)$$

where  $O(dz^2)$  denotes the higher order terms in the Taylor expansion. The second exponential term at the right-hand side of Eq. (2.36) may be regarded as the transmission function  $t(x, y, z)$  for the portion of the specimen between  $z$  and  $z + dz$ , which is defined as:

$$t(x, y, z) = \exp\left[i\sigma_i \int_z^{z+dz} V(x, y, z') dz'\right]. \quad (2.37)$$

Note that  $t(x, y, z)$  is equal to the phase change of the electron wave function while passing through the specimen in the phase object approximation presented in Eq. (2.31). From Eqs.

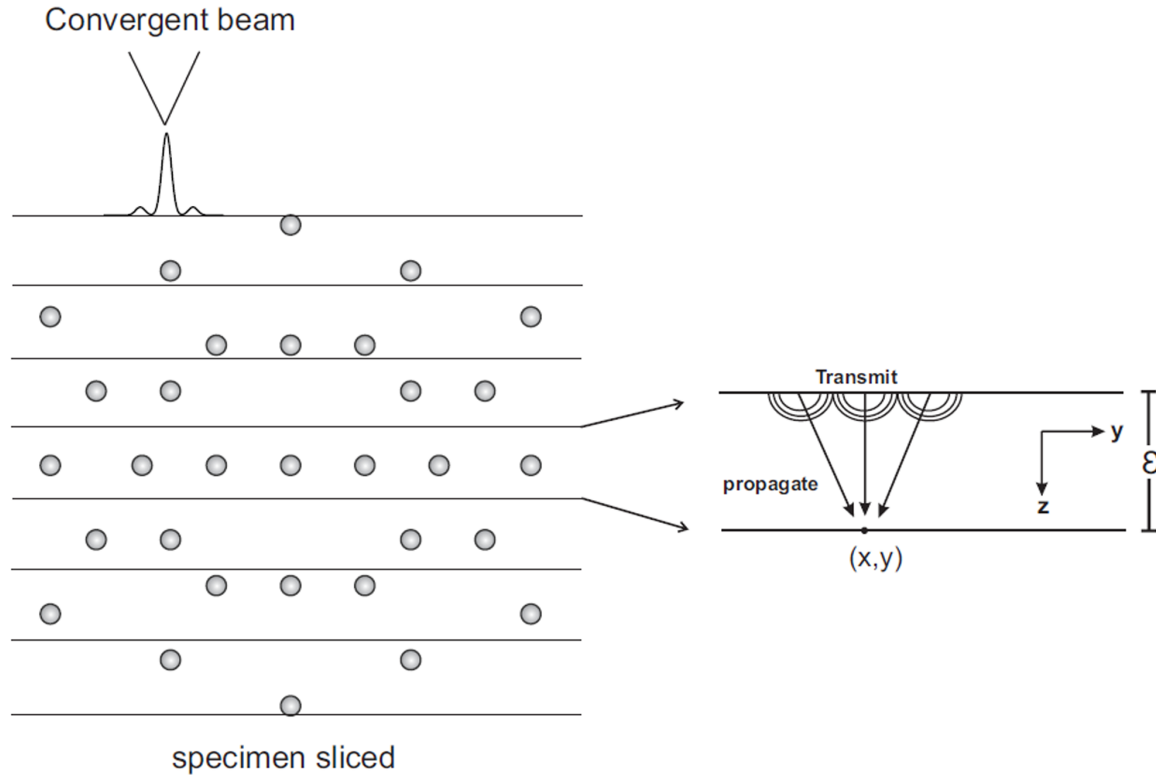


**Figure 2.5:** Schematic illustration of the multislice decomposition of a thick specimen [Alania 2017a].

(2.34) and (2.37), Eq. (2.36) can be written as:

$$\psi(x, y, z + dz) = \exp\left[\frac{i\lambda}{4\pi} dz \Delta_{x,y}\right] t(x, y, z) \psi(x, y, z) + O(dz^2). \quad (2.38)$$

In order to provide an interpretation for the first exponential term in Eq. (2.38) a 2D Fourier transform is performed [Kirkland 2010]:

$$\begin{aligned} FT\left[\exp\left[\frac{i\lambda}{4\pi} dz \Delta_{x,y}\right] t(x, y, z) \psi(x, y, z)\right] &= \exp\left[-i\pi\lambda dz (k_x^2 + k_y^2)\right] FT[t(x, y, z) \psi(x, y, z)] \\ &= P(k_x, k_y, dz) FT[t(x, y, z) \psi(x, y, z)]. \end{aligned} \quad (2.39)$$

The function  $P(k_x, k_y, dz)$  is the propagator function of the electron wave for a distance  $dz$ . Since a multiplication in Fourier space is equal to a convolution in real space, where a convolution between two functions is defined as

$$f(\mathbf{r}) \otimes g(\mathbf{r}) = \int f(\mathbf{r}') h(\mathbf{r} - \mathbf{r}') d\mathbf{r}', \quad (2.40)$$

it follows from Eqs. (2.38) and (2.39) that the wave function after interaction with a slice of thickness  $dz$  becomes

$$\psi(x, y, z + dz) = p(x, y, dz) \otimes t(x, y, z) \psi(x, y, z) + O(dz^2), \quad (2.41)$$

in which  $p(x, y, dz)$  is the propagator function in real space. The multislice equation given by Eq. (2.41) can still be written in a more compact form. For this, the slices in the specimen are labeled  $n = 0, 1, 2, \dots$  with a corresponding depth  $z_n$ . When slices of equal thickness  $dz$  are considered, it holds that  $z_n = ndz$ . The wave function at the top of each slice is labeled  $\psi_n(x, y)$  and the propagator and transmission functions for each slice are labeled as  $p_n(x, y, dz)$  and  $t_n(x, y)$ , respectively. Then, it follows that Eq. (2.41) becomes:

$$\psi_{n+1}(x, y) = p_n(x, y, dz) \otimes t_n(x, y) \psi_n(x, y) + O(dz^2). \quad (2.42)$$

In order to solve this equation, the initial wave function as defined in section 2.3 can be used together with the projected specimen potential discussed in section 2.4. The higher order terms denoted by  $O(dz^2)$  in Eq. (2.42) are usually neglected to speed up calculations. As such, when calculating the wave function after one slice, small errors of the order  $dz^2$  may be present. This error is referred to as the local error. The multislice equation, though, needs to be applied for every slice while advancing all the way through the specimen. The number of slices typically scales with  $1/dz$ . Therefore, the error term of the final result is of the order  $dz$ , which is around one order of magnitude less than the local error. This final error is referred to as the global error. Since this error depends on the slice thickness, decreasing this thickness will improve the accuracy of the calculated exit wave function.

In the derivation of the multislice equation, the specimen has been treated to be completely static and rigid with the atoms located at their ideal positions. In reality, though, atoms are thermally vibrating which causes them to be displaced. The thermal movements of the atoms, although much smaller than the typical interatomic distances [Kirkland 2010], cause the intensities of the diffracted beams to change. In addition, these movements can also lead to a

small diffuse background in between the Bragg peaks, which is referred to as thermal diffuse scattering (TDS). This effect is related to the fact that, due to the thermal vibrations, the crystal lattice is slightly disordered, causing some electrons to be scattered away from the Bragg reflections, which only appear at certain angles and which give rise to a specimen dependent diffraction pattern [De Graef 2003, Williams 2009]. The appearance of a diffuse background mainly influences the recorded intensities in ADF STEM images. Therefore, it is important that TDS is incorporated into multislice calculations. Scattering due to thermal vibrations can be taken into account by considering that the atomic vibrations are quantised in a quantum of energy, which is referred to as a phonon [Kirkland 2010]. As such, scattering by thermal vibrations is also called electron-phonon scattering. In principle, electron-phonon scattering should be treated by a many-body quantum mechanical framework, which treats the thermal scattering as a quantum excitation of the crystal [Yoshioka 1957]. It has been shown, though, that such a rigorous quantum mechanical description is equivalent to the so-called frozen phonon model [Van Dyck 2009]. This model is based on the idea that the time that the electrons in the microscope interact with the specimen is much shorter than the vibration period of an atom. Typically, the frequency of the phonons will not exceed  $10^{12} - 10^{13}$  Hz [Kittel 2004]. For example, for a typical acceleration voltage of 300 kV, resulting in electrons travelling at almost 80% of the speed of light [De Graef 2003], it takes about  $4 \cdot 10^{-16}$  seconds to traverse a specimen of 100 nm thickness, which is relatively thick in TEM. As such, the time of interaction between the incident electrons and the specimen is much smaller than the phonon oscillations. Therefore, when the imaging electron is inside the specimen, it sees only a snapshot of the specimen where the atoms are frozen at their displaced positions. In addition, the current in the microscope is small enough such that the time between two successive incident electrons passing through the specimen is long as compared to the oscillation period of the thermal phonons in the specimen. For example, for an electron current of around 50 pA, 1 electron is emitted per 3 ns. Therefore, each successive imaging electron sees a different atom displacement configuration in the specimen. Since the different phonon configurations are uncorrelated, the resulting exit wave function should be obtained by adding all different configurations incoherently. When enough random uncorrelated phonon configurations are taken into account, a representative equilibrium potential can be obtained [Loane 1991, Muller 2001]. In most multislice based image simulation software packages, the frozen lattice approach is implemented in order to account for TDS. Although, the frozen-phonon approach is an accurate way of including TDS in image simulations, it is computationally demanding since for each configuration a full calculation of the wave propagation through the specimen is required. This is especially the case for STEM where the calculation of the exit wave function needs to be repeated for each scanned probe position. A computationally less demanding technique is provided by the so-called absorptive potential method [Pennycook 1991, Ishizuka 2002, Allen 2003, Croitoru 2006, Rosenauer 2008b]. The absorptive potential approach is based on the concept that the intensity produced by the TDS, corresponding to the scattering of electrons away from the Bragg angles, can be explained by an absorption effect in the imaging of the Bragg reflected electrons. Hereby, an important assumption is that the electrons scattered by TDS directly propagate towards the detector without further interaction with the specimen. For relatively thin specimens and for specimens consisting of light atoms, the absorptive potential method is quite accurate, showing good agreement with the frozen-phonon method [Rosenauer 2008a].

Another manner, besides the multislice approach, is to solve the differential Schrödinger

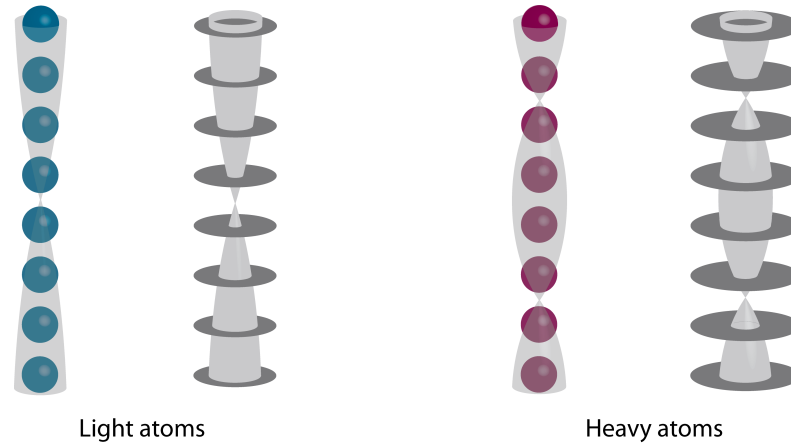


**Figure 2.6:** Illustration of the concept of channelling [van den Bos 2017a]. The electrostatic potential of each atom acts as a lens focussing the incident electrons on the atomic column. The electron wave function is focused at periodic distances.

equation, given by Eq. (2.17), by channelling theory [Broeckx 1995, Op de Beeck 1995, Van Dyck 1996, Van Aert 2007]. Here, the electron-specimen interaction is described for specimens viewed along a major zone-axis orientation, meaning that the atoms in a column are aligned along the propagation direction of the electron beam. When the columns are sufficiently separated, each incoming electron mainly interacts with one specific atomic column which is caused by the interaction between the positive electrostatic potential of the atoms and the incident electrons. As a result, the atomic potentials attract the electrons towards the atoms, keeping the electrons in their close proximity. To some extent, this effect can be described as a lensing effect where each atom acts as a lens focussing the electrons on the column, providing a sort of pathway or channel in which the incident electrons are trapped. When electrons are propagating through the specimen, they pass successive atoms, or equivalently lenses, which focus them at periodic distances. This effect is controlled by the atomic numbers, spacing and vibrations of the atoms in the column [Van Dyck 1999]. In Fig. 2.6, an illustration of the concept of channelling has been depicted. Interestingly, channelling theory suggests that the phase of the electrons leaving the specimen is related to the thickness of the specimen, enabling to count the number of atoms in a column and reconstruct the 3D structure of the object under investigation [Van Dyck 2012].

## 2.6 Image formation

In STEM imaging, after the electron beam passed through the specimen, the scattered electrons propagate further towards the annular detector. Since the detector is placed in the diffraction plane, it is the Fourier transform of the electron exit wave function [Goodman 2005], represented by  $\psi_e(\mathbf{x}, \mathbf{x}_0)$ , that reaches the detector. As such, the final electron wave function that is recorded in STEM is given by:

$$\psi_{final}(\mathbf{k}, \mathbf{x}_0) = FT[\psi_e(\mathbf{x}, \mathbf{x}_0)]. \quad (2.43)$$

For each probe position, the intensity is obtained by integrating the magnitude squared of the final wave function, given by Eq. (2.43). Therefore, the intensity in a pixel located at  $\mathbf{x}_0 = (x_0, y_0)$

follows from:

$$I_{ideal}(\mathbf{x}_0) = \int D(\mathbf{k}) |\psi_{final}(\mathbf{k}, \mathbf{x}_0)|^2 d\mathbf{k}, \quad (2.44)$$

where  $D(\mathbf{k})$  is the detector function:

$$D(\mathbf{k}) = \begin{cases} 1, & \text{for } k_{Dmin} \leq k \leq k_{Dmax} \\ 0, & \text{otherwise} \end{cases} \quad (2.45)$$

with  $k_{Dmin} = \sin(R_{in})/\lambda$  and  $k_{Dmax} = \sin(R_{out})/\lambda$ . These are the minimum and maximum spatial frequency of the recorded electrons by the STEM detector, respectively, and  $R_{in}$  and  $R_{out}$  are the inner and outer angle of the STEM detector in radians. The final STEM image is obtained by calculating the pixel value for each probe position. The detector function  $D(\mathbf{k})$  in Eq. (2.45) assumes a perfect circular annular detector with homogeneous sensitivity. In real experiments, though, this is not completely true since experimental detectors exhibit a non-uniform sensitivity [Rosenauer 2009, Findlay 2013, Martinez 2015a]. In addition, the field-emission sources that are used in the microscope show a minor energy spread of the electrons which decreases with increasing acceleration voltage [Mast 1983]. These fluctuations, though, are usually relatively low as compared to fluctuations due to inelastic scattering [Pennycook 2011]. Therefore, it is justified to neglect fluctuations in the energy of the incident electrons in the image simulations. Furthermore, ideally, the electron probe in STEM is a point source. In practice, though, the electron gun emits radiation from a finite-size source. In order to take this effect into account in image simulations, it is assumed that electrons emitted from one point do not interfere with electrons emitted from any neighbouring point [Pennycook 2011]. As such, the detected image intensities follow from a set of probe positions that are added incoherently, described by a convolution:

$$I(\mathbf{x}_0) = S(\mathbf{x}_0) \otimes I_{ideal}(\mathbf{x}_0), \quad (2.46)$$

where  $S(\mathbf{x}_0)$  is the source size distribution, which can be approximated as a normalised 2D Gaussian distribution [Mory 1985, Nellist 1994, Klenov 2007]:

$$S(\mathbf{x}_0) = \frac{1}{2\pi\sigma_r^2} \exp\left(-\frac{x_0^2}{2\sigma_r^2}\right), \quad (2.47)$$

where  $\sigma_r$  corresponds to the radius containing 39% of the total electron probe intensity. Precise measurements have shown that the shape of the source size distribution corresponds better to a linear combination of a Gaussian and a bivariate Cauchy, or Lorentzian, distribution [Verbeeck 2012]. Although the tails of this distribution are considerably wider as compared to those of a Gaussian shaped source size distribution, the full width at half maximum (FWHM) remains similar.

The full image simulation process for STEM using an ADF detector by the multislice approach as described in section 2.5 has been summarised in Fig. 2.7 for a SrTiO<sub>3</sub> crystal. The imaging process starts with the incident electron wave function interacting with the specimen's potential. Hereby, the specimen potential of SrTiO<sub>3</sub> has been subdivided into several slices, where each slice contains a projected atomic potential. In a first step, the incident wave function transmits through the first slice while interacting with the corresponding projected atomic potentials. Then, the wave propagates to the next slice where the same process is repeated. These succeeding steps of propagation and transmission or interaction continue until the electron wave

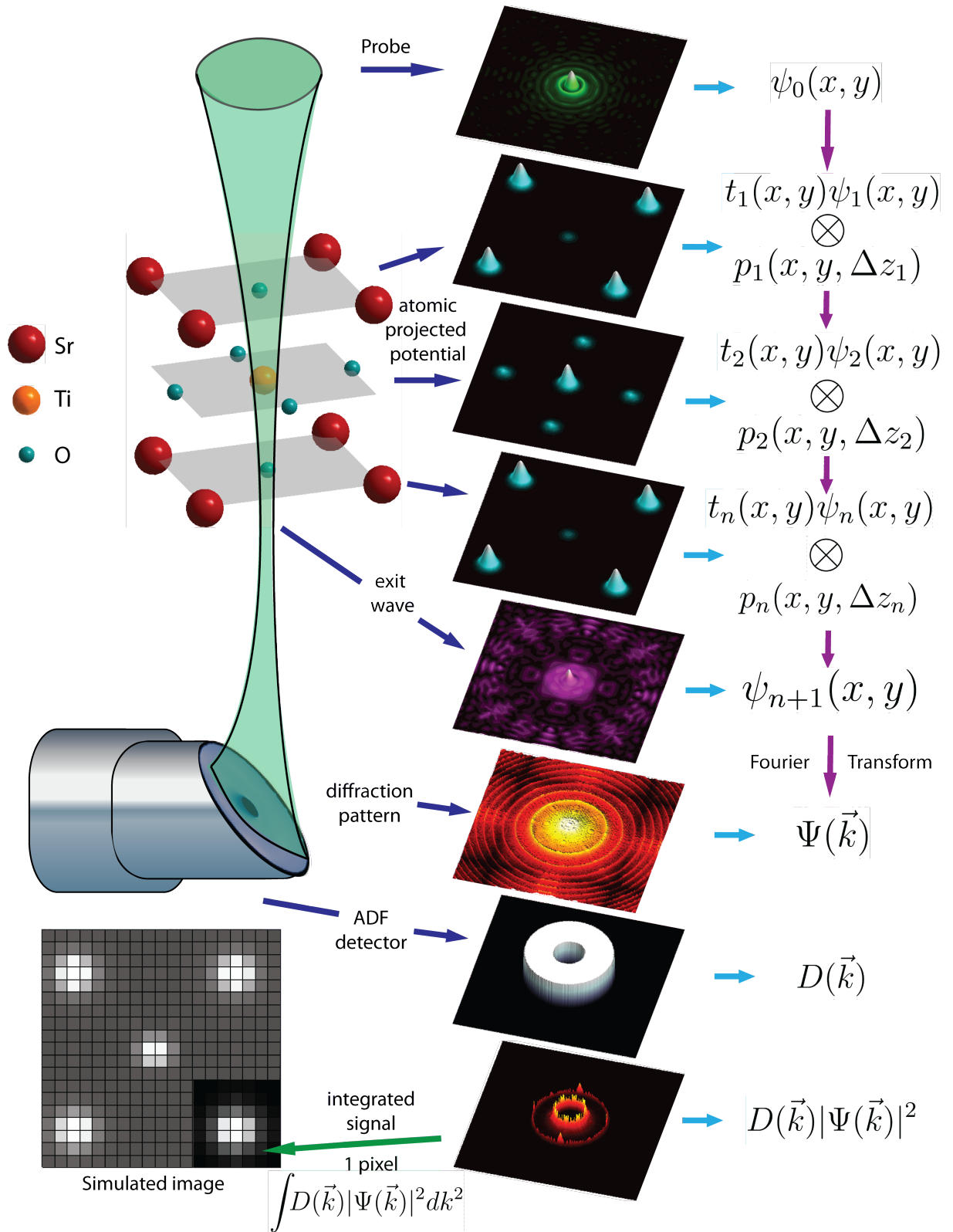


**Figure 2.7:** Schematic overview of the image simulation process for ADF STEM imaging of a  $\text{SrTiO}_3$  unit cell [Martinez 2015a]. The multislice method is used to calculate the electron-specimen interaction.

function reaches the exit plane of the specimen. The resulting exit wave function carries the information of the electron-specimen interaction to the detector, where eventually the intensities for each probe position are recorded, building up a full STEM image of the specimen.

In this thesis, when image simulations are performed, the MULTEM program is used [Lobato 2015, Lobato 2016]. MULTEM is an open source code which provides accurate and fast multislice calculations of the Schrödinger equation. One of the benefits of using MULTEM is the computation time and the availability of performing a variety of other simulations besides CTEM and STEM, including EELS and electron diffraction. An interesting feature of MULTEM is the availability of performing the calculations with graphical processor units (GPUs) instead of central processor units (CPUs), attaining improved time efficiency.

## 2.7 STEM detector

The usual way how electrons are detected in STEM imaging is by means of a scintillator coupled to a photomultiplier tube (PMT) with a mirror or reflective tube [Kirkland 1996]. When electrons scattered from the specimen hit the scintillator, photons are emitted. These photons illuminate the photocathode of the PMT, causing photoelectrons to be produced. This process is followed by a series of multiplying stages that amplify the signal such that the resulting current from the photoelectrons can be measured by a so-called analogue-to-digital converter (ADC) [Grillo 2011]. The output units of recorded STEM images are often displayed in arbitrary counts which should not be confused with electron counts. The hole through the scintillator allows BF electrons to pass to another detector or spectrometer whose signals can be acquired simultaneously with a STEM image. Beside the presence of Poisson noise in STEM images due to the particle nature of electrons hitting the detector, there are some other sources of background counts that might arise [Ishikawa 2014a]. Firstly, the scintillator randomly emits photons and similarly the photocathode randomly emits photoelectrons. In addition to these, also stray electrons and light, and electrical noise, associated with the conversion of photons to an amplified electronic signal, might contribute to the background intensity. As a result, there is some dark level present, even in the absence of electrons hitting the detector, on top of which the experimental signal is added. Nevertheless, because of the rapid progress in detector technology, the dominant noise factor in STEM images is statistical noise [Seki 2018], which is Poisson noise related to the process of electrons hitting the detector and which is unavoidable in finite dose conditions. It is noted that even single electron detection is possible with present-day detection systems with a scintillator coupled to a photomultiplier [Ishikawa 2014a, Sang 2016, Krause 2016] or with state-of-the-art pixelated detectors [Ryll 2016, Tate 2016, Mir 2017, Faruqi 2018].

Quantitative STEM imaging has become one of the standard tools for structural and compositional investigations in electron microscopy. Hereby, in order to extract as much information as possible, it is important that experimental images can be accurately matched with simulated ones, taking into account the experimental microscope settings [Krause 2016]. An important aspect is that the detector linearly amplifies the signal while maintaining a sufficient dynamical range. Furthermore, a correct calibration of the STEM detector is needed [LeBeau 2008, Rosenauer 2009]. The sensitivity of the detector is usually measured by providing a so-called detector scan. In Fig. 2.8, such a detector scan is shown, acquired by K. Müller-Caspary, which is obtained by creating a sharp image of the probe in the detector plane without a specimen present

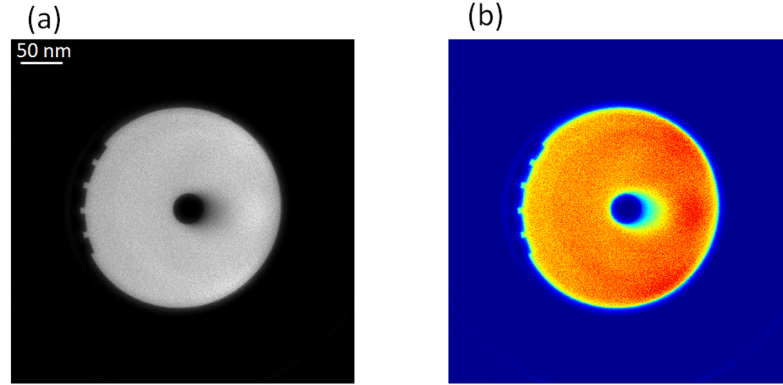


**Figure 2.8:** Example of a detector scan of an ADF detector in STEM in (a) gray scale values and (b) color values.

in the electron path. By scanning the image of the probe over the detector, an image is created whose intensities are proportional to the local sensitivity of the detector, since the intensity of the probe itself remains constant during the scan. From Fig. 2.8, it can be directly seen that an experimental detector exhibits a non-uniform sensitivity. In order to make a comparison with simulated STEM images, experimental images need to be normalised. For this, the detector scan can be used. From this scan, the averaged image intensity in vacuum,  $I_{vac}$ , corresponding to the area next to the detector, and the averaged detector intensity,  $I_{det}$ , can be measured. This is done by segmenting the image of the detector scan by appropriate thresholding, separating the intensities of the detector area from the intensities of the vacuum area. As such, an acquired image of the sample under investigation, or the detector scan itself, can be normalised by [LeBeau 2008, Rosenauer 2009, Krause 2016]:

$$I_{norm} = \frac{I_{raw} - I_{vac}}{I_{det} - I_{vac}}, \quad (2.48)$$

where  $I_{raw}$  is the image before normalisation. Interestingly, given the time during which a single pixel of the image is illuminated, the pixel dwell time, and the beam current, the number of electrons detected in a certain pixel can be determined given the normalised image intensities, providing an image of the sample in absolute electron counts.

Alternatively, there is also another way of calibrating STEM images to absolute dose, or electron counts. This method relies on the determination of the signal of a single electron on the detector [Ishikawa 2014a, Sang 2016, Krause 2016]. This signal can be either obtained by acquiring an image of the specimen using a very low incoming electron dose of less than the order of  $10^2 \text{ e}^-/\text{\AA}^2$  resulting into a very low amount of electrons reaching the detector. As such, individual electron peaks can be distinguished in the histogram of the image. Another way of determining the signal generated by a single electron is by scanning the detector with a very low beam current of around 8 fA with a very fast pixel dwell time of  $0.2 \mu\text{s}$  [Sang 2016]. Alternatively, by acquiring a so-called vacuum image, which is an image recorded under the settings of imaging a specimen, but without the presence of a sample, also single electrons can be detected [Ishikawa 2014a, Krause 2016]. In such a setting, no scattering takes place and one would expect that the complete probe passes the detector undetected. However, it has been

observed that some electrons can still reach the detector due to imperfections in the condenser system [Ishikawa 2014a]. These electrons have been referred to as accidental electrons, whose individual signals can be measured. A vacuum image also offers a way of verifying the Poisson nature of the noise in STEM images since a signal in such an image can be reliably related with a single electron impact. Alternatively, verifying whether the noise is Poisson distributed can also be achieved from a known constant background or from the residuals of the intensities of a known sample. The absolute number of scattered electrons that impinge on the detector during the dwell time of each pixel can be determined by [Krause 2016]:

$$I_{e^- \text{ counts}} = \frac{I_{\text{raw}} - I_{\text{vac}}}{\Delta I_{1e^-}} \frac{t_{\text{raw}}}{t_{\text{vac}}}, \quad (2.49)$$

where the signal generated by a single electron is depicted as  $\Delta I_{1e^-}$ , and the pixel dwell times of the image of a specimen before normalisation and the vacuum image as  $t_{\text{raw}}$  and  $t_{\text{vac}}$ , respectively. Interestingly, this methodology also allows to derive the number of electrons that are in the incident probe when a detector scan, such as the one given in Fig. 2.8, is available. Then, the number  $N_p$  of electrons in the probe during a pixel dwell time of the scan can be determined by [Krause 2016]:

$$N_p = \frac{I_{\text{det}} - I_{\text{vac}}}{\Delta I_{1e^-}} \frac{t_{\text{det}}}{t_{\text{vac}}}, \quad (2.50)$$

where  $t_{\text{det}}$  is the pixel dwell time used for acquiring the detector scan. From Eq. (2.50), the beam current can be derived. It has been shown that this approach is in good agreement with values measured with a Faraday cup and provides a much better estimate for the probe current in terms of both accuracy and precision as compared to the results that follow from the amperemeter connected to the viewing screen of the microscope [Krause 2016].

## 2.8 Conclusions

In this chapter, the most important aspects of the physics of the STEM image formation process have been explained. First, the electron-specimen interaction has been mathematically described by the time-independent Schrödinger equation. Then, the wave function of the incident electron beam and the specimen potential have been introduced. It has been shown that a solution for the Schrödinger equation can be provided by the multislice method, where the specimen's potential is divided into thin slices containing the projected atomic potentials. Hereby, it is important to take into account the effect of atomic vibrations in the specimen in order to reliably describe the image formation process. Finally, when experimental images need to be compared to simulated ones, it is important that the STEM detector is correctly calibrated. In this process, experimental images can also be converted from the arbitrary units, in which they are typically recorded, to absolute electron counts. This conversion is important for accurately describing the statistical fluctuations in the image and for, eventually, accurately detecting atomic columns from STEM images.

# 3

## Quantitative atomic-resolution electron microscopy

### 3.1 Introduction

Nowadays, as materials can be visualised with atomic resolution, also image processing techniques play an important role in order to obtain accurate and precise structural information [Van Aert 2016]. Since the physical properties of nanomaterials are strongly related to their exact atomic arrangement and chemical composition, structural information needs to be extracted down to the atomic level [Voyles 2002, Tedsree 2011, Huang 2012, Fujita 2012]. This is because small changes in the local atomic structure of nanomaterials may already induce significant changes in their properties [Locquet 1998, Muller 1999, Kisielowski 2001, Wang 2003, Urban 2008, Qi 2010, Alem 2011, Van Aert 2012a, Tang 2014, Lee 2016, van der Stam 2017]. Therefore, precisely measuring the atomic arrangement of projected atomic columns or individual atoms, with picometer precision, is important in order to fully understand the structure-properties relation of nanomaterials. For this, a quantitative approach is required which can be provided by statistical parameter estimation theory [den Dekker 2005, Van Aert 2005, van den Bos 2007, Van Aert 2012b, den Dekker 2013, De Backer 2016]. This methodology is becoming recognised as the optimal method for quantitative electron microscopy.

Statistical parameter estimation theory is widely applicable in different fields of science and consists of the estimation of unknown parameters from an available set of experimental observations. Due to the presence of noise, these observations fluctuate around their expectation values, which means that the observations can be modelled as random variables. The starting point of statistical parameter estimation theory is the construction of a parametric (physics-based) model describing the expectations of the experimental observations as a function of the unknown parameters. In TEM, an atomic-resolution image is considered as a data plane where the observations are the pixel values of the image from which unknown structure parameters need to be estimated. Since image intensities are peaked at the atomic column positions, the projected atomic columns

of atomic-resolution TEM images viewed along a major zone axis can be modelled as Gaussian peaks superimposed on a constant background [Van Dyck 2002, Nellist 2007]. Accurate and precise structure information is then obtained by fitting this model to the observed image pixel values with respect to the unknown parameters using a criterion of goodness of fit, quantifying the similarity between the image and the model.

In practice, the unknown structure parameters are often estimated from the available set of observations using an ordinary least squares estimator. If the observations are considered to be independent and normally distributed with equal variance then the maximum likelihood estimator is identical to this uniformly weighted least squares estimator [van den Bos 2001]. Although atomic-resolution TEM images are disturbed by Poisson noise, the assumption of normally distributed observations remains valid for a sufficiently high number of detected electrons since the Poisson distribution tends to be a normal distribution for increasing expectations of the image pixel values [Papoulis 2002]. A direct implementation of the least squares estimator where all the parameters are estimated at the same time is only feasible for images with a limited number of projected atomic columns. For images with a wide field of view such an implementation is computationally very intensive. Since for certain applications it is important to be able to perform a quantitative analysis of a large field of view, a more efficient algorithm has been proposed for obtaining the unknown structure parameters [De Backer 2015a, van den Bos 2017a]. The basic idea of this algorithm consists of segmenting the image into smaller sections containing individual atomic columns [den Dekker 2013]. In this way, only the parameters corresponding to a single atomic column are estimated at the same time, instead of all parameters of the parametric model. The freely available StatSTEM software, developed to facilitate model-based quantitative electron microscopy, is based on this efficient implementation [De Backer 2016].

In addition, statistical parameter estimation theory offers a way of calculating the intrinsic precisions that can be obtained about the parameters present in the expectation model which describes the experimental observations. This follows from the construction of the Fisher information matrix which quantitatively expresses the amount of information that is available about the unknown structure parameters [van den Bos 2001]. From this matrix, lower bounds on the variances of the parameters of the model, representing the attainable precisions, can be calculated. This lower limit is known as the Cramér-Rao lower bound (CRLB). It is noted that when atomic-resolution images are available, which may be interpreted quantitatively, the evaluation of an imaging system by statistical precision is considered to be more optimal than the classical concept of resolution [Van Aert 2006]. Precision should not be mistaken with resolution. Resolution defines the ability to visually distinguish neighbouring components, while precision corresponds to the variance, or standard deviation being the square root of the variance, with which structure parameters can be measured.

Moreover, it is possible to combine parameter estimation with model-order selection. Hereby, besides estimating the unknown parameters of the expectation model, also the number of parameters that most closely represents the underlying process that generated the experimental observations needs to be determined. Typical model-selection methods perform a tradeoff between high goodness of fit and low model complexity, since model fit can be easily improved by increased model complexity without necessarily bearing any interpretable relationship with the underlying data-generating process [Myung 2000, Stoica 2004a, Claeskens 2008, Corsaro 2014]. In TEM, model selection can be used to automatically and objectively determine the number of atomic columns present in the image data [Fatermans 2018, Fatermans 2019]. This is especially

relevant for analysing the structure of beam-sensitive nanomaterials, as such materials need to be imaged in STEM with a limited incoming electron dose of only  $10^3 - 10^5 \text{ e}^-/\text{\AA}^2$ , leading to images exhibiting low SNR and low contrast, and hence low CNR, which makes visual inspection unreliable.

This chapter is organised as follows. In section 3.2, the principles of model-based parameter estimation will be reviewed and commonly used parametric models will be discussed for analysing STEM images. In section 3.3, the maximum likelihood estimator will be introduced, discussing its properties and its connection to the least squares estimator. Relevant quantities such as bias and variance are introduced in section 3.4, followed by a discussion on the attainable precision for the estimation of structure parameters, introducing Fisher information in subsection 3.4.1 and the CRLB in subsection 3.4.2. The working principle of model-order selection is described in detail in section 3.5. Finally, in section 3.6, conclusions will be drawn. It is noted that the derivations in this chapter have been based on [van den Bos 2007].

## 3.2 Model-based parameter estimation

In science, often careful instrumentation and measurements are necessary in order to reduce errors that occur in the observations of a certain phenomenon. However, even if such measures have been taken, unavoidable and unpredictable fluctuations remain present. As a result of these fluctuations, the observations will differ when an experiment is repeated. Of course, this effect manifests itself as well when recording atomic-resolution STEM images. Images recorded under the same conditions will differ from experiment to experiment. The description of observations including errors is covered by parametric model-based statistics. In a parametric model-based statistical method, the observations are modelled as stochastic variables. In a STEM image, the expectation of the observed image pixel value  $w_{kl}$  at position  $(x_k, y_l)$  is supposed to be equal to the value of the parametric model at this position. This can be mathematically stated by the following expression:

$$\mathbb{E}[w_{kl}] = f_{kl}(\boldsymbol{\theta}), \quad (3.1)$$

where  $\mathbb{E}$  denotes the mathematical expectation. The function  $f_{kl}(\boldsymbol{\theta})$  describes the expectation of the observation at position  $(x_k, y_l)$  as a function of the vector of unknown parameters  $\boldsymbol{\theta}$ , represented by an  $M \times 1$  parameter vector:

$$\boldsymbol{\theta} = (\theta_1, \theta_2, \dots, \theta_M)^T. \quad (3.2)$$

In general, the observed pixel values of an image of  $W = K \times L$  pixels are represented by

$$\mathbf{w} = (w_{11}, w_{12}, \dots, w_{1L}, w_{21}, w_{22}, \dots, w_{2L}, \dots, w_{K1}, w_{K2}, \dots, w_{KL})^T. \quad (3.3)$$

In order to extract reliable quantitative structure information from STEM images, the parametric model should describe the image intensities accurately. Ideally, this model describes the image formation process based on a physics-based approach, including dynamical electron diffraction effects, TDS, electron-sample interaction, microscope transfer function and detector efficiency. However, since model parameters are estimated by an iterative optimisation scheme, using this type of complex models becomes very time consuming. In addition, since a large number of unknown parameters, including unknown microscope parameters, need to be taken into

account, the optimisation has an increased chance of ending up in a local minimum if appropriate starting values for the parameters cannot be provided. Furthermore, the precision decreases when more parameters need to be estimated. Therefore, often a simplified empirical model with a reduced number of unknown parameters is used, capturing the most important aspects of the image formation process. For STEM images viewed along a major zone axis, the image intensity is sharply peaked at the atomic column positions [Broeckx 1995, Op de Beeck 1995, Van Dyck 1996, Van Dyck 2002, Nellist 2007, Van Aert 2007] and may, as such, be modelled as a superposition of Gaussian peaks. Although this model does not describe the full physical image formation process, its validity for describing atomic-resolution STEM images has been proven [den Dekker 2005, Van Aert 2005]. The assumption of Gaussian peaks describing the atomic columns in STEM image data is mainly based on the source size distribution being well approximated as a Gaussian distribution [Mory 1985, Nellist 1994, Klenov 2007] and on the fact that the projected potential of an atomic column is well described by considering the 1s-state [Broeckx 1995, Van Dyck 1999, Van Aert 2002], which is also well approximated by a Gaussian function [Geuens 2002]. As such, the atomic columns in atomic-resolution STEM images can be well described by a parametric model of Gaussian peaks. Fig. 3.1 visualises the working principle of model-based parameter estimation in STEM, where the height, width, and position of a Gaussian peak in the model are adjusted in such a way in order to find the best match with an observed Poisson disturbed atomic column.

When a different width is assumed for each estimated Gaussian peak, the expectation  $f_{kl}(\boldsymbol{\theta})$  at position  $(x_k, y_l)$  can then be described as:

$$f_{kl}(\boldsymbol{\theta}) = \zeta + \sum_{n=1}^N \eta_n \exp\left(-\frac{(x_k - \beta_{x_n})^2 + (y_l - \beta_{y_n})^2}{2\rho_n^2}\right) \quad (3.4)$$

where  $\zeta$  is a constant background, and  $\rho_n$ ,  $\eta_n$ ,  $\beta_{x_n}$ , and  $\beta_{y_n}$  are the width, the height and x- and y-coordinates of the  $n$ th atomic column described by a Gaussian peak, respectively, and  $N$  is the total number of atomic columns. The unknown parameters of this expectation model are then represented by the parameter vector:

$$\boldsymbol{\theta} = (\beta_{x_1}, \dots, \beta_{x_N}, \beta_{y_1}, \dots, \beta_{y_N}, \rho_1, \dots, \rho_N, \eta_1, \dots, \eta_N, \zeta)^T \quad (3.5)$$

containing  $M = 4N + 1$  parameters. Parameter estimation theory in atomic-resolution STEM is not restricted to the model given by Eq. (3.4). For example, for a model where the Gaussian peaks describing the atomic columns are assumed to have equal widths, the expectation model  $f_{kl}(\boldsymbol{\theta})$  is given by

$$f_{kl}(\boldsymbol{\theta}) = \zeta + \sum_{n=1}^N \eta_n \exp\left(-\frac{(x_k - \beta_{x_n})^2 + (y_l - \beta_{y_n})^2}{2\rho^2}\right) \quad (3.6)$$

with  $M = 3N + 2$  unknown parameters:

$$\boldsymbol{\theta} = (\beta_{x_1}, \dots, \beta_{x_N}, \beta_{y_1}, \dots, \beta_{y_N}, \eta_1, \dots, \eta_N, \rho, \zeta)^T. \quad (3.7)$$

Even if the material consists of columns of different atom types, the model assuming Gaussian peaks with equal widths, given by Eq. (3.6), is acceptable since the width of an atomic column is mainly determined by the finite source size and to a lesser extent by the atom type [LeBeau 2008].

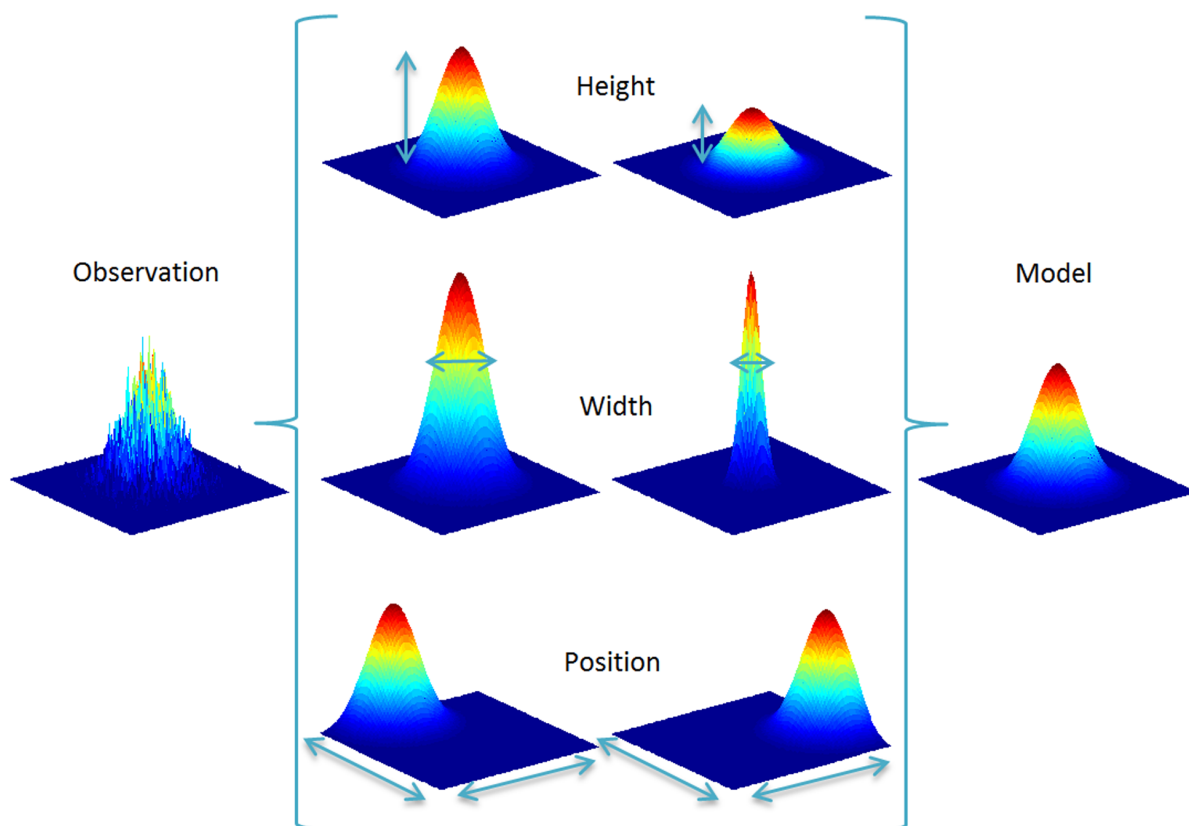


**Figure 3.1:** Visualisation of modelling a Gaussian peak to an observed atomic column by adjusting the height, width and position.

This model contains a lower number of parameters that needs to be estimated as compared to the model in Eq. (3.4) assuming Gaussian peaks with different widths. This reduction of the number of parameters is not only interesting as it enhances the precision with which structure parameters can be measured, it also makes the optimisation more robust, reducing the chance of converging to a local minimum. Nevertheless, the models given by Eqs. (3.4) and (3.6), or a combination of both where atomic columns of the same type are assigned Gaussian peaks with equal widths, are of great use for extracting precise and accurate quantitative structure information from atomic-resolution STEM images. They form the core of the StatSTEM software package [De Backer 2016] developed to facilitate model-based quantitative electron microscopy. This software enables the analysis of images containing a large number of projected atomic columns, i.e. large fields of view. This can be achieved by an efficient model-estimation algorithm [De Backer 2015a, van den Bos 2017a] whose basic idea is the segmentation of the image into smaller sections containing individual columns [den Dekker 2013]. Hereby, overlap between neighbouring Gaussian peaks is taken into account. In this way, only the parameters corresponding to a single atomic column are estimated at the same time, instead of all the parameters of the parametric model. In order to avoid ending up in local minima during the model-estimation procedure, it is important to provide good starting values for the parameters.

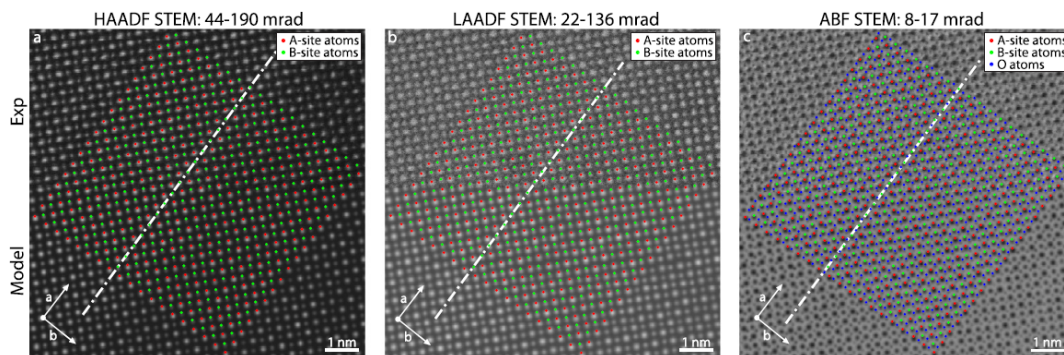


**Figure 3.2:** Experimental images (top part) analysed by parametric modelling describing the atomic columns by Gaussian peaks (bottom part) in a region around a  $\text{La}_{0.67}\text{Sr}_{0.33}\text{MnO}_3\text{-NdGaO}_3$  interface, marked by the white dotted line, in (a) HAADF, (b) LAADF and (c) ABF STEM imaging mode [Gauquelin 2017]. The estimated column positions are shown as an overlay.

For example, starting coordinates of the positions  $\beta_{x_n}$  and  $\beta_{y_n}$  of the projected atomic columns in the image can be provided by visual inspection or by using a peak-finding routine. Both methods, however, require a high-resolution and good-quality image in which the individual columns can be resolved in order to avoid bias. Prior knowledge on the structure of the material under study can also be used to provide starting values, which is helpful when the resolution is only just sufficient to resolve individual columns at the atomic scale.

Statistical parameter estimation has enabled to determine atomic column positions with high precision from CTEM images, reconstructed exit waves, ADF STEM images, and ABF STEM images [Van Aert 2005, Bals 2006, Houben 2006, Jia 2008, Urban 2008, Van Aert 2009b, De Backer 2011, Huijben 2006, Kimoto 2010, Klingstedt 2012, Van Aert 2012b, Kundu 2014, Yankovich 2014, Perez 2016, Liao 2016a, van den Bos 2017a, van den Bos 2017b]. As a result, by using statistical parameter estimation for measuring the atomic column locations, local interatomic distances can be reliably quantified. This information is important for different applications such as strain measurements [Galindo 2007, Llordés 2012, Fujita 2012, Jones 2017], the characterisation of crystalline defects [Van Aert 2012b, Lubk 2012, Polking 2012, Gonnissen 2016a] and the characterisation of interfaces [Jia 2009, Liao 2016a, Liao 2016b, van den Bos 2017b]. An example of the application of statistical parameter estimation is provided in Fig. 3.2. It shows the estimated atomic column positions of a region around a  $\text{La}_{0.67}\text{Sr}_{0.33}\text{MnO}_3\text{-NdGaO}_3$  interface in HAADF, LAADF and ABF STEM mode [Gauquelin 2017]. Characterisation of such an interface at the atomic level is required in order to understand the exotic electronic properties that can arise [Mannhart 2010, Hwang 2012].

Beside measuring atomic column positions, statistical parameter estimation can also be used as a technique to quantify atomic column intensities [Huijben 2006, Van Aert 2009a, Kimoto 2010, Kim 2012, Yankovich 2014]. These intensities can provide information about the thickness of the specimen. As such, the number of atoms in a column may be determined. In CTEM, this can be achieved by acquiring an image by tuning the spherical aberration of the objective lens to a negative value [Jia 2014]. However, CTEM shows contrast oscillations as a function of thickness which limits the applicability of counting atoms in columns to relatively thin structures [Gonnissen 2017]. Exit wave reconstruction offers another way of retrieving thickness information. Here, the phase at the atomic column positions in a reconstructed exit wave

function is measured [Wang 2010, Wang 2012] since each atom shifts the phase of the incident electrons by a certain amount, allowing to obtain the number of atoms in each atomic column. By this procedure, information about surface morphology [Van Dyck 2012] and thickness has been retrieved [Yu 2016]. The atom counting methods in CTEM and exit wave reconstruction are both not straightforward. In CTEM, contrast reversals are present, and in exit wave reconstruction the phase shift also depends on the 3D atom positions.

A more straightforward technique is to perform atom counting using HAADF STEM. In this imaging mode, typically, the so-called scattering cross section of each column is calculated since it monotonically increases with thickness, making it a suitable measure to count the number of atoms in a column [Bals 2011, Bals 2012, E 2013, Van Aert 2013, Martinez 2015b, De Backer 2017]. The scattering cross-section is defined as the total intensity of scattered electrons by a single atomic column [Retsky 1974, Isaacson 1979, Singhal 1997, Van Aert 2009b, Van Aert 2013, E 2013, De Backer 2016]. When atomic columns are described by Gaussian peaks, the scattering cross-section of a column equals the volume under the Gaussian peak describing the column. Then, the scattering cross-section  $\Theta$  for a column with height  $\eta$  and width  $\rho$  is given by

$$\Theta = 2\pi\eta\rho^2. \quad (3.8)$$

The benefit of using the scattering cross-section as compared to using peak intensities is that it is robust to small sample mis-tilts, magnification, defocus, astigmatism and source size broadening [E 2013, Martinez 2014a, MacArthur 2015]. Nowadays, several approaches are available for determining the number of atoms in an atomic column. There is a simulation-based method, where first the intensities in the image should be normalised with respect to the incident electron beam [LeBeau 2008, Rosenauer 2009]. In section 2.7 of chapter 2, a method for normalising image intensities has been described. Then, in order to perform atom counting, experimentally measured image intensities can be directly compared to simulated values [LeBeau 2010, Jones 2014] or, alternatively, measured scattering cross-sections to simulated ones. A drawback of this method is its sensitivity to possible errors in the simulation parameters, caused by inaccuracies in measuring the microscope parameters, such as for example the detector angles. This can lead to biased atom counting results since the simulation-based approach will always find a match between the experimentally measured values and the simulated ones, despite the probability of errors in the image simulations. Another approach is a statistics-based method. Here, the scattering cross-sections are evaluated in a statistical framework, identifying columns with the same thickness [Van Aert 2011, Van Aert 2013, De Backer 2013, De Backer 2015c]. Making use of the property that scattering cross-sections increase monotonically with thickness, the number of atoms in each column can be obtained without the need for image simulations. The statistics-based method does require, though, that a sufficient amount of atomic columns is present, in order to obtain reliable statistical results. This is something that is not required for the simulation-based approach. As compared to the simulated-based method, the statistical method is more robust to inaccuracies in the measured microscope parameters and, in addition, it can measure the precision of the atom-counting results. It has been suggested that the most reliable approach for atom counting is by matching results obtained by both methods [Van Aert 2013, De Backer 2015b]. A combination of both techniques is offered by a hybrid approach where scattering cross-sections, obtained by image simulations, are used as prior knowledge in the statistical framework [De wael 2017].

Interestingly, HAADF STEM image contrast strongly depends on the atomic number  $Z$ , which enables a chemical analysis of the specimen as well. Besides obtaining thickness information,

HAADF STEM may also be used for identifying different column types in a heterogeneous complex structure of constant thickness [Van Aert 2009b, Martinez 2014b, Akamine 2015, Jany 2017]. By directly comparing experimental images that are normalised with respect to the incident electron beam, with simulated images performed under the experimental microscope settings for a range of different sample conditions, including thickness and composition, the material's composition can be quantified [Rosenauer 2009, Rosenauer 2011, Grieb 2012, Kauko 2013a, Mehrtens 2013a, Mehrtens 2013b, Kauko 2013b, Martinez 2014b, van den Bos 2016]. Also other simulation-based approaches are available for determining the locations of dopant atoms in the structure where both the scattering cross-section and peak intensity of an atomic column is measured [Ishikawa 2014b] or STEM images are simultaneously recorded under different imaging conditions [Zhang 2015, Müller-Caspary 2016].

### 3.3 Maximum likelihood estimator

In statistical parametric models, the expectations of the observations are values of the parametric function underlying the observations. The joint probability (density) function describes the fluctuations of the observations around these expectation values. The joint probability (density) function of the observations is given by

$$p(\boldsymbol{\omega}) = p(\omega_{11}, \omega_{12}, \dots, \omega_{1L}, \omega_{21}, \omega_{22}, \dots, \omega_{2L}, \dots, \omega_{K1}, \omega_{K2}, \dots, \omega_{KL}), \quad (3.9)$$

where  $\boldsymbol{\omega}$  denotes independent variables corresponding to the vector of observations  $\boldsymbol{w}$ , given by Eq. (3.3). An explicit expression for the joint probability function can be derived by taking into account knowledge about the statistical properties of the errors in the experimental measurements. Since a high-resolution STEM image is formed by counting electrons scattered to the detector, the pixel values are inevitably subject to Poisson noise causing each observed image pixel value to be Poisson distributed [Haight 1967, Mood 1974, van den Bos 2001]. As briefly discussed in section 2.7 of chapter 2, also other noise sources arise related to the detector system and electronics [Ishikawa 2014a]. Nevertheless, the statistical Poisson noise associated with the particle nature of electrons impinging onto the detector remains the dominant noise source in STEM imaging [Seki 2018]. Hereby, the time between subsequent single electron impacts fits a Poisson random process [Sang 2016], confirming the validity of modelling the observations in STEM as Poisson distributed random variables. This results into the following probability distribution [Herrmann 1997, Papoulis 2002]:

$$p(\omega_{kl}) = \frac{(\lambda_{kl})^{\omega_{kl}}}{\omega_{kl}!} \exp(-\lambda_{kl}), \quad (3.10)$$

where  $\lambda_{kl}$  denotes the expected value of the stochastic variable  $w_{kl}$  at position  $(x_k, y_l)$ . Since for Poisson distributed variables the expected value equals the variance, it follows from Eq. (3.1) that the expected value of  $w_{kl}$  can be written as

$$\mathbb{E}[w_{kl}] = \text{var}(w_{kl}) = \lambda_{kl} = f_{kl}(\boldsymbol{\theta}). \quad (3.11)$$

Under the assumption of statistical independent electron counting results, which holds in STEM because the electron probe is focussed on only one pixel location at the same time, the product

of Eq. (3.10) for all pixels equals the joint probability function for a set of observations being modelled as Poisson distributed random variables:

$$p(\omega) = \prod_{k=1}^K \prod_{l=1}^L p(\omega_{kl}) = \prod_{k=1}^K \prod_{l=1}^L \frac{(\lambda_{kl})^{\omega_{kl}}}{\omega_{kl}!} \exp(-\lambda_{kl}). \quad (3.12)$$

The unknown parameters  $\theta$  are included in this expression through the expectation values  $\lambda_{kl}$ , which are described by a suitable parametric model as noted in Eq. (3.11).

Maximum likelihood estimation is a way of estimating the unknown parameters of an expectation model. The general idea is to find the set of parameters which maximises a likelihood function so that the observations are most probable under the assumed statistical model. The maximum likelihood estimator follows from the parameterised probability (density) function and can be derived following the steps below, which have been based on [van den Bos 2007]. The joint probability (density) function of the observations for Poisson distributed random variables is dependent on the unknown parameter vector  $\theta$ . This follows from Eq. (3.12) since  $\lambda_{kl}$  is equal to  $f_{kl}(\theta)$ , as stated by Eq. (3.11). As such, the joint probability (density) function can be explicitly written as

$$p(\omega; \theta). \quad (3.13)$$

The likelihood function  $L(\mathbf{t})$  of the vector of parameters  $\mathbf{t}$  given the observations  $\mathbf{w}$  is defined as:

$$L(\mathbf{t}) := p(\mathbf{w}; \mathbf{t}). \quad (3.14)$$

This expression follows from Eq. (3.13) by substituting the observations  $\mathbf{w}$  for  $\omega$  and the independent variables  $\mathbf{t}$  for  $\theta$ . Then, the estimate  $\hat{\theta}$  of the parameter vector  $\theta$  is defined by the value of  $\mathbf{t}$  that maximises the likelihood function:

$$\hat{\theta} = \arg \max_{\mathbf{t}} L(\mathbf{t}). \quad (3.15)$$

Equivalently, in Eq. (3.15), one may also make use of the log-likelihood function,  $\log L(\mathbf{t})$ , since the logarithmic function is monotonic. An interesting property of the maximum likelihood estimator is its invariance [van den Bos 2001]. If  $\hat{\theta}$  is the maximum likelihood estimate of the parameter vector  $\theta$ , and  $\gamma(\theta)$  is a vector of functions of  $\theta$ , then the maximum likelihood estimate of  $\gamma(\theta)$  is given by  $\hat{\gamma} = \gamma(\hat{\theta})$ .

For an atomic-resolution STEM image, the observed image pixel values can be considered to be statistically independent electron counting results, and therefore, they are Poisson distributed. This has led to the expression given by Eq. (3.12) for the joint probability function. For an increasing number of electron counts per pixel, i.e. an increasing expectation value  $\lambda_{kl}$ , the Poisson distribution tends to be a normal distribution with both mean and variance equal to  $\lambda_{kl}$  [Papoulis 2002]. This behaviour has been illustrated in Fig. 3.3. If the standard deviations of the Poisson distributed observations are supposed to be equal, it can be written that for each position  $(x_k, y_l)$ ,  $\sqrt{\lambda_{kl}} = \sigma_{kl} \approx cte = \sigma$  [Miedema 1994]. Hereby,  $\sigma$  is considered to be a constant, independent of the parameters to be estimated. Under these assumptions, the joint probability function given by Eq. (3.12) can be approximated as

$$p(\omega) \approx \prod_{k=1}^K \prod_{l=1}^L \frac{1}{\sqrt{2\pi\sigma^2}} \exp\left(-\frac{(\omega_{kl} - \lambda_{kl})^2}{2\sigma^2}\right), \quad (3.16)$$

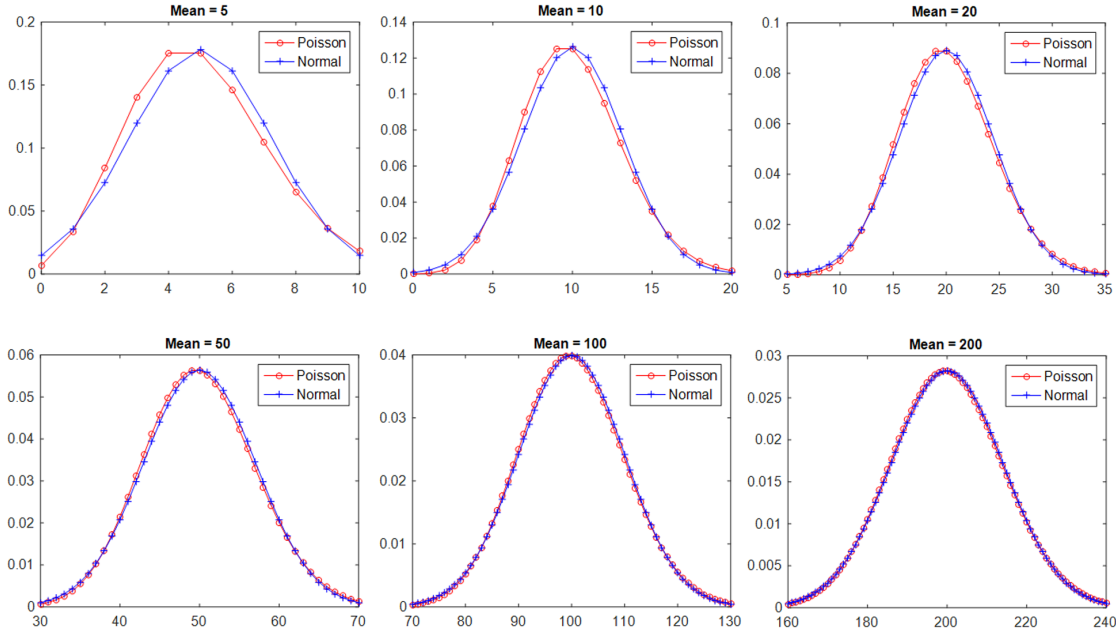


**Figure 3.3:** Comparison of Poisson and normal distribution with equal mean and variance for increasing mean.

describing the probability of a set of statistically independent normally distributed observations with equal variance. The joint probability function can be explicitly written as a function of the parameters  $\theta$  by making use of Eq. (3.11) where  $\lambda_{kl} = f_{kl}(\theta)$ :

$$p(\omega; \theta) \approx \prod_{k=1}^K \prod_{l=1}^L \frac{1}{\sqrt{2\pi\sigma^2}} \exp\left(-\frac{(\omega_{kl} - f_{kl}(\theta))^2}{2\sigma^2}\right). \quad (3.17)$$

As described earlier in this section, the likelihood function follows from  $p(\omega; \theta)$  by replacing the variables  $\omega$  by the observations  $w$ , and the true parameters  $\theta$  by the independent variables  $t$ . As a result, the log-likelihood function, given the joint probability function of Eq. (3.17), can be written as:

$$\log L(t) = -\frac{W}{2} \log(2\pi) - W \log(\sigma) - \frac{1}{2} \sum_{k=1}^K \sum_{l=1}^L \left(\frac{w_{kl} - f_{kl}(t)}{\sigma}\right)^2, \quad (3.18)$$

where  $W = K \times L$ . Then, the maximum likelihood estimator equals

$$\hat{\theta} = \arg \max_t \log L(t) = \arg \min_t \sum_{k=1}^K \sum_{l=1}^L (w_{kl} - f_{kl}(t))^2. \quad (3.19)$$

The right-hand side of Eq. (3.19) depicts the uniformly weighted least squares estimator, which quantifies the similarity between the observations and the expectation model. As such, it has been shown that for statistically independent normally distributed observations with equal variance the maximum likelihood estimator equals the uniformly weighted least squares estimator.

More generally, the condition of normally distributed observations with equal variance can

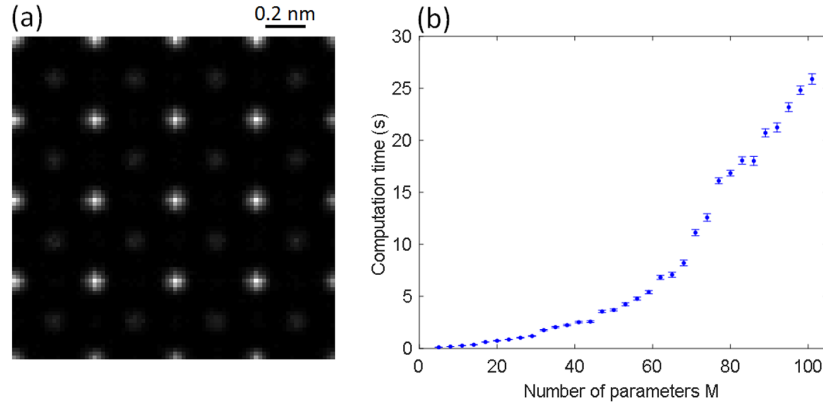


**Figure 3.4:** (a) Simulated STEM image of  $15.60 \text{ \AA}$  by  $15.60 \text{ \AA}$  of  $\text{SrTiO}_3$ . (b) Computation time needed to fit columns from (a) using a parametric model with Gaussian peaks of equal widths as a function of the number of parameters.

be dropped and one can consider the deviations of the observations from their expectations to be normally distributed with a different standard deviation  $\sigma_{kl}$  for each pixel, independent of the parameters to be estimated. As such, the joint probability function of Eq. (3.12) becomes:

$$p(\omega; \theta) \approx \prod_{k=1}^K \prod_{l=1}^L \frac{1}{\sqrt{2\pi\sigma_{kl}^2}} \exp\left(-\frac{(\omega_{kl} - f_{kl}(\theta))^2}{2\sigma_{kl}^2}\right). \quad (3.20)$$

Then, the log-likelihood function and the maximum likelihood estimator equal

$$\log L(\mathbf{t}) = -\frac{W}{2} \log(2\pi) - \sum_{k=1}^K \sum_{l=1}^L \log(\sigma_{kl}) - \frac{1}{2} \sum_{k=1}^K \sum_{l=1}^L \left(\frac{w_{kl} - f_{kl}(\mathbf{t})}{\sigma_{kl}}\right)^2, \quad (3.21)$$

and

$$\hat{\theta} = \arg \max_{\mathbf{t}} \log L(\mathbf{t}) = \arg \min_{\mathbf{t}} \sum_{k=1}^K \sum_{l=1}^L \left(\frac{w_{kl} - f_{kl}(\mathbf{t})}{\sigma_{kl}}\right)^2, \quad (3.22)$$

respectively. The term at the right-hand side of Eq. (3.22) is a weighted least squares estimator, being a generalisation of the aforementioned uniformly weighted least squares estimator.

In this work, the estimate  $\hat{\theta}$  of the parameter vector  $\theta$  is determined by the weighted least squares estimator. This is achieved by solving a nonlinear data-fitting problem where the aim is to numerically deduce the parameter values which minimise the objective function [Levenberg 1944, Marquardt 1963, Coleman 1994, Coleman 1996], as stated by Eq. (3.22). The minimisation procedure is started by providing initial estimates of the parameter vector. These estimates are updated in an iterative manner according to a gradient descent. Convergence is reached when the size of an iteration step or when the change of the value of the objective function becomes smaller than some set lower bound, or tolerance. Here, both the step tolerance and function tolerance have been put to an absolute value of  $10^{-6}$ . In case multiple minima are present, it is important that the initial starting values of the parameters are already close to the

final solution in order for the algorithm to converge to the global minimum. As the location of the global minimum is typically a priori unknown, many different sets of initial parameter vectors are used in order to increase the probability of converging towards the optimal parameter values of a given model related to the global minimum. It is difficult to unambiguously determine how many of these starting configurations are required to reliably reach the global minimum. This will depend on the atomic structure of the material and on the level of noise in the image. In this thesis, the number of sets of initial parameter vectors for fitting a given model to the image data has been based on the dimensions of the image. When an image consists of  $K \times L$  pixels, around  $(K + L)/2$  starting configurations have been used. This number has shown to exhibit good performance in converging towards the global minimum. The computation time needed to optimise the parameters of a given model has been investigated. For this, an ADF STEM image of SrTiO<sub>3</sub>, which is depicted in Fig. 3.4(a), of 15.60 Å by 15.60 Å with a pixel size of 0.195 Å has been simulated using MULTEM [Lobato 2015, Lobato 2016] with an acceleration voltage of 300 kV, a semiconvergence angle of 21.3 mrad, a detector collection range of 58-197 mrad, and an incoming electron dose of  $10^6$  e<sup>-</sup>/Å. The atomic columns in Fig. 3.4(a) have been described using a parametric model assuming the columns to have equal widths, as given in Eq. (3.6). The time required to optimise the parameters of the model has been measured as a function of the number of parameters. Hereby, the optimisation procedure has been initialised from only one set of initial parameter values in order to reduce computation time and has been repeated for 100 random Poisson noise configurations of the simulated SrTiO<sub>3</sub> image data. Fig. 3.4(b) shows the average computation time as a function of the number of parameters  $M$ . The computation time increases for an increasing number of parameters and reaches around 25 s for 100 parameters. Calculations were performed using a single workstation with an Intel Core i7-2600 processor. It is noted that the calculation time may differ based on the capabilities of the computer that is used. In addition, also the size of the image, the noise level, and atomic ordering of the material may influence computation time.

### 3.4 Bias and variance

Relevant quantities associated with a parameter estimator are bias and variance, which are associated with accuracy and precision, respectively. The bias of the estimator  $\hat{\theta}_m$  of one of the parameters  $\theta_m$  of the parameter vector  $\theta$  is given by:

$$\text{bias}(\hat{\theta}_m) = \mathbb{E}[\hat{\theta}_m] - \theta_m \quad (3.23)$$

and describes the difference between the estimator's expected value and the true value of the parameter being estimated. Interestingly, the maximum likelihood estimator is consistent meaning that it converges toward the true value of the parameters for an increasing number of observations [van den Bos 2001]. The variance of  $\hat{\theta}_m$  at the other hand is defined as:

$$\text{var}(\hat{\theta}_m) = \mathbb{E}\left[\left(\hat{\theta}_m - \mathbb{E}[\hat{\theta}_m]\right)^2\right] \quad (3.24)$$

and indicates the spread around the expected value. As an example, the bias and variance of the estimated value of the x-coordinate,  $\hat{\beta}_x$ , of a gold atom have been estimated from a set of simulated 12.5 Å by 12.5 Å ADF STEM images as a function of incoming electron dose varying

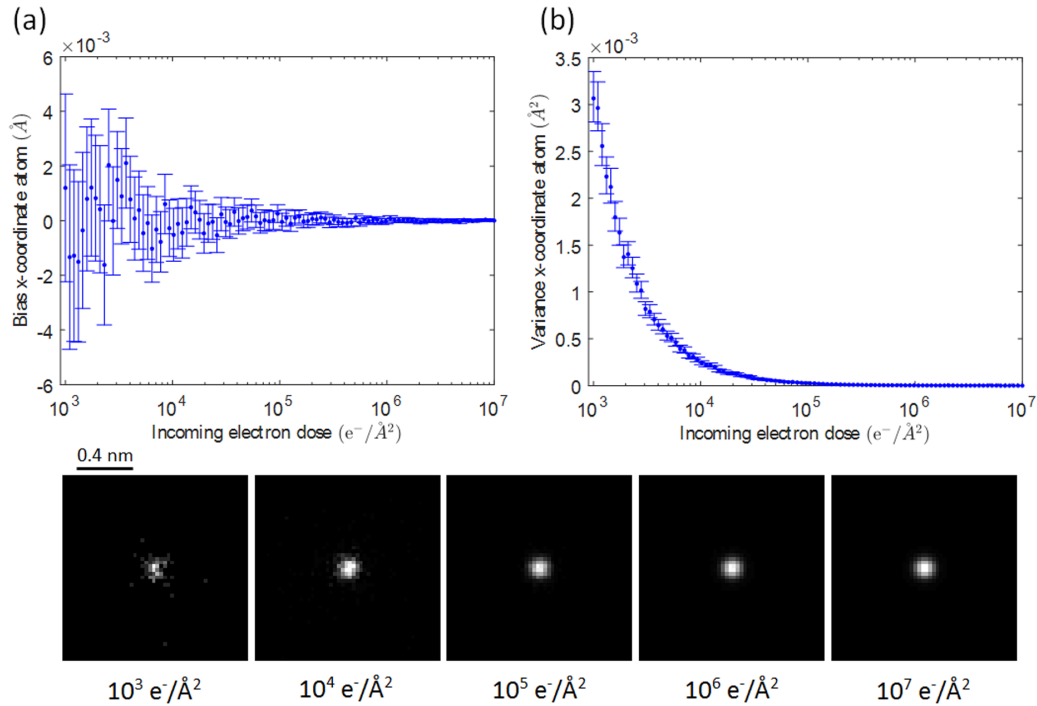


**Figure 3.5:** (a) Bias of the estimated x-coordinate  $\hat{\beta}_x$  of a gold atom from simulated ADF STEM images as a function of electron dose. (b) Variance of  $\hat{\beta}_x$  as a function of dose. The 95 % confidence intervals have been included. The insets below show examples of the simulated images disturbed by Poisson noise for several incoming electron doses.

between  $10^3 e^-/\text{Å}^2$  and  $10^7 e^-/\text{Å}^2$ . The simulation has been performed by using MULTEM [Lobato 2015, Lobato 2016] with an acceleration voltage of 120 kV, a semiconvergence angle of 21.3 mrad, and a detector collection range of 28-172 mrad. For each value of the incoming electron dose, 1000 random Poisson noise configurations have been generated and for each one the parameters of the model have been optimised using Eq. (3.22). The results are shown in Fig. 3.5 where the insets below show examples of the Poisson noise disturbed simulated images of the gold atom for several values of the incoming electron dose. Fig. 3.5(a) shows the bias, along with the 95 % confidence intervals, of the estimated x-coordinate  $\hat{\beta}_x$  of the atom. It can be seen that unbiased estimates for the x-coordinate of the atom are obtained. The confidence intervals, though, become smaller when the incident electron dose is increased. This can also be seen in Fig. 3.5(b) which shows the variance of  $\hat{\beta}_x$  as a function of incoming electron dose. For an increasing dose, the variance decreases which leads to a more precise estimation of the x-coordinate of the gold atom. The dependence of precision on the incident electron dose is an unavoidable effect in parameter estimation. It is noted that in the analysis of Fig. 3.5 only Poisson noise has been taken into account, whereas in real experiments environmental or instrumental disturbances of acoustic, mechanical, or electromagnetic nature can cause additional distortions in images recorded by STEM [von Harrach 1995, Jones 2013]. Scan noise in STEM originates from unwanted lateral movements of the electron probe while scanning the specimen [Recnik 2005, Muller 2006]. It manifests itself as the slicing of atoms or atomic columns in STEM images [Buban 2010]. Scan noise may have a considerable effect on the precision that can be attained of quantities of interest

[Van Aert 2019]. In addition, also the effect of sample or stage drift may contribute to distortions as images can appear warped. Image reconstruction methods have been developed to correct microscopy images, mitigating the occurrence of scan and drift distortions [Anguiano 1999, Salmons 2010, Jones 2013, Sang 2013, Berkels 2014, Jones 2015, Ophus 2016].

### 3.4.1 Fisher information

Theoretically, there exists a lower bound on the variance of unbiased estimators of parameters. The CRLB determines the attainable precision for the estimation of structure parameters from electron microscopy images. More information on the topic can be found in [van den Bos 1982, Frieden 1998, van den Bos 2001, van den Bos 2007].

The concept of the CRLB follows from the Fisher information matrix which is derived from the joint probability (density) function. The joint probability (density) function describes the probability of a set of observations  $\mathbf{w}$ . Hereby, the expectation values of the observations are described by an expectation model containing an  $M \times 1$  unknown parameter vector  $\boldsymbol{\theta}$ , as given by Eq. (3.11). As such, the joint probability (density) function can be explicitly expressed as  $p(\boldsymbol{\omega}; \boldsymbol{\theta})$ . The so-called Fisher information matrix of the observations  $\mathbf{w}$  follows from the joint probability (density) function and is defined by

$$F_{\boldsymbol{\theta}} = -\mathbb{E} \left[ \frac{\partial^2 \log p(\mathbf{w}; \boldsymbol{\theta})}{\partial \boldsymbol{\theta} \partial \boldsymbol{\theta}^T} \right], \quad (3.25)$$

where the vector of independent variables  $\boldsymbol{\omega}$  has been replaced by the corresponding vector of observations  $\mathbf{w}$ . The expression between square brackets at the right-hand side of Eq. (3.25) represents the Hessian matrix of the logarithm of the joint probability (density) function. The Fisher information measures the amount of information that an observable random variable carries about an unknown parameter. For the observed image pixel values in an electron microscopy image,  $p(\mathbf{w}; \boldsymbol{\theta})$  is given by Eq. (3.12). It follows from this expression and Eq. (3.11), where it is explicitly mentioned that  $\mathbb{E}[w_{kl}] = \lambda_{kl}$  and that  $\lambda_{kl}$  is dependent on  $\boldsymbol{\theta}$ , that the  $(r, s)$  element of  $F_{\boldsymbol{\theta}}$  given by Eq. (3.25) can be written as:

$$F_{rs} = \sum_{k=1}^K \sum_{l=1}^L \frac{1}{\lambda_{kl}} \frac{\partial \lambda_{kl}}{\partial \theta_r} \frac{\partial \lambda_{kl}}{\partial \theta_s}. \quad (3.26)$$

### 3.4.2 Cramér-Rao lower bound

From the concept of Fisher information, the highest precision, or equivalently the lowest variance, can be determined with which a parameter can be estimated unbiasedly. The Cramér-Rao inequality, with  $\hat{\boldsymbol{\theta}}$  an unbiased estimator of  $\boldsymbol{\theta}$  meaning that  $\mathbb{E}[\hat{\boldsymbol{\theta}}] = \boldsymbol{\theta}$ , equals

$$\text{cov}(\hat{\boldsymbol{\theta}}, \hat{\boldsymbol{\theta}}) \geq F_{\boldsymbol{\theta}}^{-1}, \quad (3.27)$$

where  $\text{cov}(\hat{\boldsymbol{\theta}}, \hat{\boldsymbol{\theta}})$  is the  $M \times M$  covariance matrix of  $\hat{\boldsymbol{\theta}}$  given by

$$\text{cov}(\hat{\boldsymbol{\theta}}, \hat{\boldsymbol{\theta}}) = \mathbb{E} \left[ (\hat{\boldsymbol{\theta}} - \boldsymbol{\theta})(\hat{\boldsymbol{\theta}} - \boldsymbol{\theta})^T \right]. \quad (3.28)$$

From the inequality expression in Eq. (3.27), it follows that the difference of the covariance matrix and  $F_{\theta}^{-1}$  is a positive semi-definite matrix, meaning that its diagonal elements are non-negative. Since the diagonal elements of  $\text{cov}(\hat{\theta}, \hat{\theta})$  represent the variances of the estimated parameters  $\hat{\theta}_m$ , it follows that these variances are larger than or equal to the corresponding diagonal elements of the  $F_{\theta}^{-1}$  matrix:

$$\text{var}(\hat{\theta}_m) \geq [F_{\theta}^{-1}]_{mm}. \quad (3.29)$$

As such, the diagonal of  $F_{\theta}^{-1}$  forms a lower bound on the variances of unbiased estimators, determining the attainable precision. Interestingly, the maximum likelihood estimator achieves the CRLB asymptotically, i.e. for an increasing number of observations. This property is referred to as asymptotic efficiency [van den Bos 2001]. This means that its covariance matrix is asymptotically equal to the CRLB:

$$\text{cov}(\hat{\theta}, \hat{\theta}) \rightarrow \text{CRLB}. \quad (3.30)$$

In this sense, the maximum likelihood estimator is most precise. Another interesting property of the maximum likelihood estimator is its asymptotic normality [van den Bos 2001] meaning that the probability (density) function of the maximum likelihood estimator tends to be a normal distribution for an increasing number of observations having the true parameter vector  $\theta$  as expectation values and the CRLB matrix as covariance matrix:

$$p(\omega; \hat{\theta}) \approx N(\theta; \text{CRLB}). \quad (3.31)$$

Since the number of observations in electron microscopy images is usually sufficiently high for the asymptotic properties to apply, the maximum likelihood estimator is recommended for quantitative electron microscopy [den Dekker 2005]. In addition, the CRLB can be generalised when one is interested in a new quantity which is a function of the parameters  $\theta$ . When a  $G \times 1$  vector  $\gamma(\theta) = (\gamma_1(\theta), \gamma_2(\theta), \dots, \gamma_G(\theta))^T$  is considered which depends on the  $M \times 1$  parameter vector  $\theta = (\theta_1, \theta_2, \dots, \theta_M)^T$ , the Cramér-Rao inequality, with  $\hat{\gamma}$  an unbiased estimator of  $\gamma$ , can be written as

$$\text{cov}(\hat{\gamma}, \hat{\gamma}) \geq \left( \frac{\partial \gamma(\theta)}{\partial \theta} \right) F_{\theta}^{-1} \left( \frac{\partial \gamma(\theta)}{\partial \theta} \right)^T, \quad (3.32)$$

where  $\text{cov}(\hat{\gamma}, \hat{\gamma})$  is the  $G \times G$  covariance matrix of  $\hat{\gamma}$  and  $\frac{\partial \gamma(\theta)}{\partial \theta}$  is the  $G \times M$  Jacobian matrix of which the elements are given by

$$\begin{pmatrix} \frac{\partial \gamma_1(\theta)}{\partial \theta_1} & \frac{\partial \gamma_1(\theta)}{\partial \theta_2} & \dots & \frac{\partial \gamma_1(\theta)}{\partial \theta_M} \\ \frac{\partial \gamma_2(\theta)}{\partial \theta_1} & \frac{\partial \gamma_2(\theta)}{\partial \theta_2} & \dots & \frac{\partial \gamma_2(\theta)}{\partial \theta_M} \\ \vdots & \vdots & \ddots & \vdots \\ \frac{\partial \gamma_G(\theta)}{\partial \theta_1} & \frac{\partial \gamma_G(\theta)}{\partial \theta_2} & \dots & \frac{\partial \gamma_G(\theta)}{\partial \theta_M} \end{pmatrix}. \quad (3.33)$$

It should be noted that the CRLB can only be computed when the joint probability (density) function  $p(\omega; \theta)$  of the observations is known. This requires knowledge of the true parameter vector  $\theta$ . In general, though, the true parameters are unknown and only estimated parameter values are available. Nevertheless, a lower bound for the variances can be quantified by using the estimated values [Van Aert 2005]. These computed Cramér-Rao variances may be used to compare different experimental designs in order to perform the experiment using the optimal settings, achieving parameter estimates with the highest possible precision [Gonnissen 2014, Gonnissen 2016b].

### 3.5 Model-order selection

In order to extract reliable structure information of nanomaterials from STEM images using parametric models such as in Eqs. (3.4) and (3.6), the number of atomic columns  $N$  present in the image should be known. Usually, this number is provided by visual inspection or by using a peak-finding routine. Both methods, however, require a high-quality image in which the individual columns can be resolved in order to avoid biased structure information. For beam-sensitive and light-element materials, though, acquiring such a high-quality image is, in general, not feasible as these materials are easily damaged by the electron beam. As a result, the incoming electron dose needs to be limited in order to avoid beam damage leading to images exhibiting low SNR and low contrast, and hence low CNR. To overcome this problem, the principles of model-based parameter estimation can be combined with model-order selection. Hereby, besides estimating the parameters of interest, also the number of parameters need to be determined. For STEM images, this approach may be used to detect atomic columns, and even single atoms, which allows for an automatic and objective evaluation of the structure of the material under investigation [Fatermans 2018, Fatermans 2019].

The heart of model selection consists of selecting one model from a set of competing models that represents most closely the underlying process that generated the experimental data. For this purpose, a criterion measuring how well the model fits the data is required. Such a criterion of goodness of fit quantifies the descriptive adequacy of a model, which is possible by, for example, a maximum likelihood evaluation. However, a model-selection criterion based solely on goodness of fit automatically selects the model which fits best to the data. This is undesired, since model fit can be easily improved by increased model complexity, referring to the flexibility of a model to fit the observed data. In this way, a model might be selected without necessarily bearing any interpretable relationship with the underlying data-generating process. For this reason, typical model-selection methods take into account both the goodness of fit and the complexity of the models under investigation [Myung 2000].

There are at least three important factors that contribute to the complexity of a model [Myung 1997]. The first one is the number of parameters. In general, a model with many parameters describes data better than a model with few parameters due to its higher flexibility, and hence complexity. Next, model complexity is also related to functional form, which is described as the way in which the parameters are combined in the model. A model with a more complex functional form is able to describe a wider range of data and can be considered to be more flexible than a model with a less complex functional form. The last dimension of model complexity is covered by the extension of the parameter space. A model of which the parameters can fluctuate over a wide range of values can describe a wider range of data. Therefore, such a model is considered to be more complex than a model of which the parameters can fluctuate over only a small range. All of these three aspects can significantly and independently influence model fit.

Typically, model-selection criteria are written as twice the negative log-likelihood function, accounting for the goodness of fit, plus a penalty term that accounts for model complexity  $C$  [Claeskens 2008]:

$$-2 \log(\hat{L}) + 2C, \quad (3.34)$$

with

$$\hat{L} = L(\hat{\theta}), \quad (3.35)$$

where  $\hat{\theta}$  denotes the maximum likelihood estimator. Different criteria have been proposed in the literature and describe the complexity of the model in a different way, often taking only one dimension of model complexity into account, i.e. the number of parameters [Stoica 2004a]. Some common criteria have been listed below. The Akaike Information Criterion (AIC) [Akaike 1974] can be written as

$$AIC = -2 \log(\hat{L}) + 2M \quad (3.36)$$

with  $M$  the number of parameters in the model. A very similar criterion is the Generalised Information Criterion (GIC) [Broersen 1993], where the contribution of the penalty term can be modified by the parameter  $d$ :

$$GIC = -2 \log(\hat{L}) + dM. \quad (3.37)$$

A clear guideline on how to choose the value of  $d$  is lacking. Different choices of  $d = 3$  [Broersen 1996] and  $d = 4$  [Stoica 2004a] are reported in the literature. These choices cause the GIC to penalise more heavily for the complexity of the model as compared to the AIC. Another common criterion is the Bayesian Information Criterion (BIC) [Schwarz 1978]:

$$BIC = -2 \log(\hat{L}) + M \log(W) \quad (3.38)$$

with  $W$  the sample size, i.e. the number of datapoints. For a STEM image,  $W$  is equal to  $K \times L$  pixels. As opposed to the AIC and GIC, the penalty term is dependent on the sample size. When  $W > 8$ , the BIC accounts more for the complexity of the model than the AIC. An alternative criterion is the Hannan-Quinn Information Criterion (HQC) [Hannan 1979] which replaces the  $\log(W)$  factor in the BIC by the slower diverging quantity  $\log[\log(W)]$ :

$$HQC = -2 \log(\hat{L}) + M \log[\log(W)]. \quad (3.39)$$

It is noted that many other model-selection criteria are available. In chapter 5, the performances to detect atomic column from ADF STEM images of the different model-selection criteria introduced in this section will be investigated.

## 3.6 Conclusions

In this chapter, the principles of statistical parameter estimation theory have been introduced. Due to the presence of noise, image pixel values or observations fluctuate around their expectation values, which means that they can be modelled as random variables. Within the framework of statistical parameter estimation theory, the expectations of the observations are described by a parametric statistical model as a function of unknown parameters. The projected atomic columns of high-resolution STEM images viewed along a major zone-axis are commonly modelled as Gaussian peaks superimposed on a constant background which allows to estimate structure parameters such as column locations and scattering cross-sections accurately and precisely. Moreover, statistical parameter estimation theory provides a theoretical lower bound, i.e. the CRLB, following from the Fisher information matrix, on the variance of any unbiased estimator, allowing for the calculation of the attainable precision. Interestingly, this lower bound can be reached asymptotically by the maximum likelihood estimator, which makes it a recommended estimator for an adequate quantitative analysis. In case of normally distributed observations, it is noted that the maximum likelihood estimator is equal to the well-known least squares estimator,

which is commonly used for evaluating the goodness of fit, quantifying the similarity between the observations and the model. Interestingly, parameter estimation theory can be generalised by combining its principles with model-order selection. Hereby, besides estimating the parameters of the model, also the number of parameters needs to be determined, allowing for an automatic and objective analysis of the experimental observations.

# 4

## Atom column detection from ADF STEM images

### 4.1 Introduction

Reliable detection of atoms is of key importance to solve a wide range of scientific and technological problems. For this, electron microscopy is one of the most promising techniques because of the strong interaction of electrons with matter. In particular, because of several important developments in aberration correction technology [Krivanek 2009, Rose 2009, Hawkes 2015], STEM has become an excellent technique to visualise nanomaterials down to sub-angstrom resolution [Urban 2008, Erni 2009, Sawada 2009, Krivanek 2010, Oltalan 2010], enabling the detection of even single atoms, and hereby solving challenging problems in materials science, such as detecting Au catalysts in a Si nanowire, reconstructing oxygen octahedrons in heterointerfaces, or directly observing dopant atoms [Allen 2008, Jia 2009, Hwang 2013, Ishikawa 2014b].

Detection of an atomic column or single atom, in case the column consists of only one atom, from STEM images is often performed by means of a visual interpretation of the image. Materials that are stable under the electron beam can be imaged with a sufficiently high electron dose, typically of the order of more than  $10^6 - 10^8 \text{ e}^-/\text{\AA}^2$ , resulting into high-quality STEM images exhibiting high SNR and high contrast. This allows one to resolve the individual atomic columns and so, for such beam-stable materials, the atomic columns can be detected in a merely visual manner. However, some materials, especially light-element nanomaterials, are sensitive to the electron beam and, as a result, they cannot withstand a high incoming electron dose. In order to avoid beam damage to occur, such beam-sensitive materials can only be imaged in STEM using a limited electron dose of the order of  $10^3 - 10^5 \text{ e}^-/\text{\AA}^2$ . This leads to recording images exhibiting low SNR and weak contrast, and hence low CNR [Findlay 2014]. Visually inspecting these images, trying to resolve the individual atomic columns, can be unreliable and may lead to biased results, especially when no prior knowledge about the structure of the material is available. To overcome this problem, an objective and quantitative approach is needed.

A possible solution is offered by Bayes' theorem, which enables the calculation of the probability of a certain event in terms of conditions that can be related to that event [Stuart 1994, Jaynes 2003, Sivia 2006]. In principle, this allows one to compare the probability of a certain number of atomic columns present in the image data to the probability of any other number of columns. In this way, the most probable result from the data under investigation can be selected. The idea of using Bayesian probability theory, aiming to obtain relevant information from image data, has been applied in the technique of maximum entropy reconstruction, where use is made of an entropy prior [Jaynes 1957, Gull 1984, Skilling 1984]. The maximum entropy method has been useful for image processing in several physical domains including radio astronomy and X-ray diffraction [Gull 1978]. In electron microscopy, maximum entropy reconstruction has been used as a deconvolution or noise reduction technique on the level of single pixels [Nellist 1998, McGibbon 1999, Watanabe 2002, Nakanishi 2002, Nakanishi 2006, Sang 2009]. The number of unknowns in such a reconstruction, though, can be drastically reduced if some prior knowledge is available about the projected structure. In such a case, a model describing the image pixel values of an electron microscopy image should be constructed as a function of a number of relevant parameters, reducing the number of unknowns. In the previous chapter, it was explained that such parametric models, describing the projected atomic columns of atomic-resolution STEM images as Gaussian peaks superimposed on a constant background [den Dekker 2005, Van Aert 2005], are available due to the fact that image intensities are sharply peaked at the atomic column locations [Van Dyck 2002, Nellist 2007]. It has been explained that by using model-based parameter estimation accurate and precise structure information can be obtained about the material under study. A danger in the approach of model-based parameter estimation, though, is the use of an incorrect model or parameterisation, because it lacks a mechanism to provide information about the most optimal model describing the experimental data. This may lead to biased results as the correct parameterisation may not have been considered in the analysis.

The idea of using Bayesian probability theory can be applied to model-based parameter estimation. The working principle of such a technique is the same as for typical model-selection criteria, of which a few were briefly introduced in the previous chapter in section 3.5. Such an approach allows for selecting the optimal model from a set of competing models by comparing their probabilities of describing the experimental data. Interestingly, Bayesian selection techniques have been used in a wide variety of applications [Knuth 2015] covering fields such as chemistry [Bermejo 2004, Armstrong 2009, Shashilov 2010, Holmes 2014, Vispa 2016, Vispa 2017], nuclear and particle physics [De Cruz 2011, Bergstrom 2012], and astronomy and astrophysics [Pounds 2006, Trotta 2008, Feroz 2011, Debono 2014, Corsaro 2014]. In electron microscopy, the MAP probability rule has been developed as an objective and quantitative method to detect atom columns and even single atoms from high-resolution STEM images [Fatermans 2018, Fatermans 2019], which is also the topic of this thesis. The principles of the MAP probability rule are based on earlier work of [Sivia 1992a, Sivia 1992b, Sivia 1993] in the field of molecular spectroscopy. The method combines statistical parameter estimation theory and model-order selection using a Bayesian framework.

This chapter is organised as follows. In section 4.2, Bayes' theorem will be introduced. In section 4.3, the methodology of the MAP probability rule to determine the most probable number of atomic columns from ADF STEM images is described in detail. Hereby, approximate analytical expressions are derived in subsection 4.3.1. In addition, the algorithm of the MAP

probability rule is explained in subsection 4.3.2. In section 4.4, the MAP probability rule is applied to experimental ADF STEM images of SrTiO<sub>3</sub> in subsection 4.4.1, graphene in subsection 4.4.2, a gold nanorod in subsection 4.4.3, and ultrasmall nanoclusters in 4.4.4. Finally, in section 4.5, conclusions will be drawn.

## 4.2 Bayes' theorem

In principle, probability theory consists of a number of rules quantifying logical and consistent reasoning to express a belief of truth about a certain proposition [Cox 1946]. Hereby, a real number, or probability, is assigned to each of the propositions in such a manner that a larger numerical value associated with a proposition, the more we believe it. In this sense, probability is defined as a degree of belief or plausibility that a given proposition is true [D'Agostini 2003, Jaynes 2003, Gregory 2005, Sivia 2006]. Consistency is preserved if the probabilities describing our beliefs obey the rules of probability theory.

An important property of probabilities is that they are bounded below by 0 and above by 1, such that the probability of a proposition  $X$  to be true given some background information  $I$  can be written as

$$0 \leq p(X|I) \leq 1. \quad (4.1)$$

The symbol " $|$ " depicts a conditional statement, meaning that the probability of anything to the left of " $|$ " is conditional on anything to the right of it. It is noted that Eq. (4.1) is conditional on

proposition will always depend on the available background information as there is no such thing as an absolute probability. Often, though, the term depicting the background information is omitted from equations in Bayesian theory. More properties of probability theory can be derived by the requirement of logical consistency. When the probability of a certain proposition  $X$  to be true is known, this automatically implies that also the probability of  $X$  to be false,  $\bar{X}$ , is known. In combination with Eq. (4.1), this gives rise to the following property:

$$p(X|I) + p(\bar{X}|I) = 1, \quad (4.2)$$

which is referred to as the sum rule. More generally, for a set of  $K$  propositions  $X = (X_1, X_2, \dots, X_K)^T$ , we expect the probabilities to be normalised, such that

$$\sum_{k=1}^K p(X_k|I) = 1. \quad (4.3)$$

Another quantitative statement following from logical consistency is the product rule, defining the joint probability of two or more propositions. Here, when the probability of a proposition  $X$  to be true is known and, in addition, the probability of a proposition  $Y$  to be true, given the truth of  $X$ , is also known, then the probability that both  $X$  and  $Y$  are true can be calculated. This statement can be formulated by the following expression:

$$p(X, Y|I) = p(Y|X, I)p(X|I). \quad (4.4)$$

Since  $X$  and  $Y$  are interchangeable, Eq. (4.4) can also be written as

$$p(X, Y|I) = p(X|Y, I)p(Y|I). \quad (4.5)$$

Furthermore, from Eq. (4.4), it follows that

$$p(X, Y|I) + p(X, \bar{Y}|I) = [p(Y|X, I) + p(\bar{Y}|X, I)]p(X|I). \quad (4.6)$$

Since the expression between square brackets at the right-hand side of Eq. (4.6) is equal to unity, following Eq. (4.2), we can write that

$$p(X|I) = p(X, Y|I) + p(X, \bar{Y}|I). \quad (4.7)$$

For a set of  $L$  propositions  $Y = (Y_1, Y_2, \dots, Y_L)^T$ , Eq. (4.7) can be generalised by making use of the property of Eq. (4.3):

$$p(X|I) = \sum_{l=1}^L p(X, Y_l|I). \quad (4.8)$$

By symmetry, we also have that for a set of  $K$  propositions  $X = (X_1, X_2, \dots, X_K)^T$

$$p(Y|I) = \sum_{k=1}^K p(Y, X_k|I). \quad (4.9)$$

In Eqs. (4.8) and (4.9), a general form of so-called marginalisation of joint probabilities for a discrete set of variables has been defined. In case of continuous variables, the summation is replaced by an integration.

The rules presented above form the basic algebra of probability theory as many other results can be derived from them. An important result following from these fundamental rules is Bayes' theorem, offering a way of calculating the probability of a certain proposition in terms of conditions that can be related to that proposition [Stuart 1994, Jaynes 2003, Sivia 2006]. By equating the expressions given in Eqs. (4.4) and (4.5), Bayes' theorem can be obtained:

$$p(X|Y, I) = \frac{p(Y|X, I)p(X|I)}{p(Y|I)}. \quad (4.10)$$

Typically, the background information  $I$  is explicitly omitted from Eq. (4.10) resulting into a simplified expression:

$$p(X|Y) = \frac{p(Y|X)p(X)}{p(Y)}. \quad (4.11)$$

The relevance of Bayes' theorem for data analysis becomes more apparent when the proposition  $X$  is replaced by a quantity of interest  $Q$  and the proposition  $Y$  by the available data  $D$ :

$$p(Q|D) = \frac{p(D|Q)p(Q)}{p(D)}. \quad (4.12)$$

The power of Eq. (4.12) lies in the fact that the probability of the quantity  $Q$  given the available data  $D$ ,  $p(Q|D)$ , can be calculated from a more accessible term  $p(D|Q)$ , which depicts the probability of observing the data  $D$  given the quantity  $Q$ . The various terms in Bayes' theorem have some formal names. The term on the left-hand side of Eq. (4.12) depicts the posterior probability of  $Q$  conditional on  $D$  and represents the state of knowledge after performing the experiment and obtaining the data. The term  $p(D|Q)$  reflects the evidence that the available data  $D$  was observed given the quantity  $Q$ . Furthermore, the prior information is defined by  $p(Q)$  which asserts the plausibility of  $Q$  before conducting the experiment. Finally, the denominator of Eq. (4.12) is a normalisation constant since it is independent of the quantity of interest  $Q$ .

## 4.3 Maximum a posteriori probability

In this section, the methodology of the maximum a posteriori (MAP) probability rule to detect single atoms from atomic-resolution STEM images is explained in detail<sup>1</sup>. The method is built upon a combination of parameter estimation and model-order selection using the principles of Bayesian probability theory, as discussed in the previous section. The MAP probability rule allows for determining the structure of unknown nanomaterials in an automatic and objective manner and proves to be especially useful for the analysis of the structure of beam-sensitive and light-element nanomaterials [Fatermans 2018]. In subsection 4.3.1, it is shown that approximate analytical expressions can be derived for the probability of the presence of a certain number of atomic columns in ADF STEM image data. The way of how these probabilities can be obtained and compared to each other is discussed in subsection 4.3.2.

### 4.3.1 Bayesian approach

In the previous chapter, commonly used parametric expectation models were discussed to describe STEM images. In Eq. (3.4), such an expectation model  $f_{kl}(\boldsymbol{\theta})$ , describing the expectation of the observed pixel value  $w_{kl}$  at position  $(x_k, y_l)$  with  $\boldsymbol{\theta} = (\theta_1, \dots, \theta_M)^T$  the vector of unknown structure parameters, was given. For this model,  $\boldsymbol{\theta}$  consists of  $M = 4N + 1$  parameters. In order to extract reliable structure information of nanomaterials from ADF STEM images using parametric models, such as the one presented by Eq. (3.4), the number of atomic columns  $N$  present in the image should be known, as each Gaussian peak in the model should correspond to a column in the image. Usually, for beam-stable materials, this number can be determined visually due to the high incoming electron dose that can be used to image these materials, leading to images exhibiting high SNR. For beam-sensitive nanostructures, though, the incoming electron dose is limited in order to avoid beam damage and, as a result, the images exhibit low SNR and weak contrast, and hence low CNR. Visual inspection of such images may lead to biased results. To overcome this problem, the number of atomic columns  $N$  can be reliably quantified by the MAP probability rule. It selects the number of columns  $N$  of which the probability given the observed image pixel values  $\mathbf{w}$ ,  $p(N|\mathbf{w})$ , is maximal. The probability  $p(N|\mathbf{w})$  depicts the posterior probability term in Bayes' theorem, given by Eq. (4.12). As such, for our purpose,  $p(N|\mathbf{w})$  can be written as:

$$p(N|\mathbf{w}) = \frac{p(\mathbf{w}|N)p(N)}{p(\mathbf{w})}. \quad (4.13)$$

The term  $p(\mathbf{w}|N)$  reflects the evidence that the image data  $\mathbf{w}$  is generated by  $N$  atomic columns. The probability  $p(N)$  expresses prior knowledge of the number of atomic columns  $N$  in the image, which, in what follows, has been chosen to be a uniform distribution, reflecting no a priori preference for any number of columns. The denominator in Eq. (4.13) can be explicitly written as

$$p(\mathbf{w}) = \sum_N p(\mathbf{w}|N)p(N) \quad (4.14)$$

<sup>1</sup>The results of this section have been published in J. Fatermans, S. Van Aert, and A.J. den Dekker, *The maximum a posteriori probability rule for atom column detection from HAADF STEM images*, *Ultramicroscopy* **201** (2019), p. 81-91.

and is a normalisation constant, which is independent of the number of columns  $N$  as a summation over  $N$  is performed. Therefore, this term cancels out when comparing posterior probabilities as a function of  $N$ . As a result, Eq. (4.13) reduces to

$$p(N|\mathbf{w}) \propto p(\mathbf{w}|N). \quad (4.15)$$

By making use of the marginalisation property of probability theory, given by Eq. (4.8), the right-hand side of Eq. (4.15) can be written as

$$p(\mathbf{w}|N) = \int p(\mathbf{w}, \boldsymbol{\theta}|N) d^M \boldsymbol{\theta}, \quad (4.16)$$

where the marginalised variables are the parameters  $\boldsymbol{\theta}$  of the expectation model. Then, by following the product rule of Eq. (4.5), this expression becomes

$$p(\mathbf{w}|N) = \int p(\mathbf{w}|\boldsymbol{\theta}, N) p(\boldsymbol{\theta}|N) d^M \boldsymbol{\theta}. \quad (4.17)$$

The first term in the integral,  $p(\mathbf{w}|\boldsymbol{\theta}, N)$ , is the likelihood function which describes the probability of the observed image pixel values  $\mathbf{w}$  for particular values of the parameters  $\boldsymbol{\theta}$  of a model with  $N$  atomic columns. Therefore, it is an explicit function of the parameters  $\boldsymbol{\theta}$ . In essence, the likelihood function is a measure of the goodness of fit of the model with the experimental measurements or image pixel values. The other term in the integral,  $p(\boldsymbol{\theta}|N)$ , is the prior density of the parameters  $\boldsymbol{\theta}$  for a model with  $N$  columns. In practice, calculation of the posterior probability  $p(N|\mathbf{w})$ , given by Eq. (4.15), can be reduced to calculating the marginal likelihood  $p(\mathbf{w}|N)$  described by Eq. (4.17). In order to do so, explicit expressions for the likelihood function  $p(\mathbf{w}|\boldsymbol{\theta}, N)$  and the prior density  $p(\boldsymbol{\theta}|N)$  are required.

An expression for the likelihood function,  $p(\mathbf{w}|\boldsymbol{\theta}, N)$ , can be derived by taking into account knowledge about the statistical properties of the errors in the experimental measurements. In essence, this is covered by the joint probability (density) function, introduced in the previous chapter, describing the probability of a set of given observations. Since a STEM image of  $K \times L$  pixels is formed by counting electrons scattered to the detector, the pixel values are inevitably subject to Poisson noise causing each observed image pixel value  $w_{kl}$  at position  $(x_k, y_l)$  to be Poisson distributed [Haight 1967, Mood 1974, van den Bos 2001]. For an increasing expectation value  $f_{kl}(\boldsymbol{\theta})$  of  $w_{kl}$ , the Poisson distribution tends to be a normal distribution with mean  $\mu_{kl} = f_{kl}(\boldsymbol{\theta})$  and standard deviation  $\sigma_{kl} = \sqrt{f_{kl}(\boldsymbol{\theta})}$  [Papoulis 2002]. Under the assumption that the pixel values are statistically independent, the likelihood function can be expressed as follows:

$$p(\mathbf{w}|\boldsymbol{\theta}, N) = \frac{e^{-\chi^2(\boldsymbol{\theta})/2}}{\prod_{k=1}^K \prod_{l=1}^L \sqrt{2\pi\sigma_{kl}^2}}, \quad (4.18)$$

where

$$\chi^2(\boldsymbol{\theta}) = \sum_{k=1}^K \sum_{l=1}^L \left( \frac{w_{kl} - \mu_{kl}}{\sigma_{kl}} \right)^2. \quad (4.19)$$

For simplicity, it can be assumed that  $\sigma_{kl} \approx \sqrt{w_{kl}}$ , so that  $\sigma_{kl}$  is independent of the parameters  $\boldsymbol{\theta}$ . The likelihood function then becomes

$$p(\mathbf{w}|\boldsymbol{\theta}, N) = \frac{e^{-\chi^2(\boldsymbol{\theta})/2}}{\prod_{k=1}^K \prod_{l=1}^L \sqrt{2\pi w_{kl}}}, \quad (4.20)$$

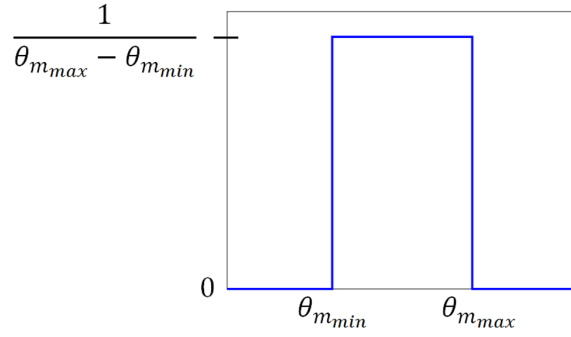


**Figure 4.1:** Plot of uniform prior distribution  $p(\theta|N)$ , given by Eq. (4.22), for a single parameter  $\theta_m$ .

where

$$\chi^2(\boldsymbol{\theta}) = \sum_{k=1}^K \sum_{l=1}^L \frac{(w_{kl} - f_{kl}(\boldsymbol{\theta}))^2}{w_{kl}} \quad (4.21)$$

is a weighted sum-of-squared-residuals misfit between the data and the parametric model.

For the term  $p(\boldsymbol{\theta}|N)$  in Eq. (4.17), different prior density functions can be constructed reflecting different types of prior knowledge. Here,  $p(\boldsymbol{\theta}|N)$  is expressed as a product of uniform distributions over a predefined range for each parameter  $\theta_m$ :

$$p(\boldsymbol{\theta}|N) = \begin{cases} \prod_{m=1}^M \frac{1}{\theta_{m_{max}} - \theta_{m_{min}}} & \text{for } m = 1, \dots, M: \theta_{m_{min}} \leq \theta_m \leq \theta_{m_{max}} \\ 0 & \text{otherwise} \end{cases} \quad (4.22)$$

where the subscripts *max* and *min* refer to a predefined maximum and minimum value, respectively. The expression in Eq. (4.22) has been depicted in Fig. 4.1 for a single parameter  $\theta_m$ . In case of  $\theta_{m_{min}} \leq \theta_m \leq \theta_{m_{max}}$  for  $m = 1, \dots, M$ ,  $p(\boldsymbol{\theta}|N)$  for the parameter vector in Eq. (3.5) of the model given by Eq. (3.4) can be explicitly written as:

$$\frac{1}{[(\beta_{x_{max}} - \beta_{x_{min}})(\beta_{y_{max}} - \beta_{y_{min}})(\rho_{max} - \rho_{min})(\eta_{max} - \eta_{min})]^N (\zeta_{max} - \zeta_{min})}, \quad (4.23)$$

assuming that the predefined maximum and minimum values are the same for  $\beta_{x_n}$ ,  $\beta_{y_n}$ ,  $\rho_n$ , and  $\eta_n$  for each  $n$ . The choice for this type of prior simplifies the subsequent algebra significantly. More importantly, the amount of prior knowledge that is introduced can be kept minimal by using this uniform prior combined with a conservative choice of the predefined parameter ranges, thus avoiding biased results due to the incorporation of possibly invalid prior knowledge. Moreover, this form of prior can also be used in a flexible way since the predefined parameter ranges can easily be adapted depending on the available prior knowledge.

Given the assumption of an a priori equiprobable number of atomic columns  $N$ , the evaluation of the MAP probability rule through Eq. (4.15) comes down to calculating the marginal likelihood  $p(\boldsymbol{w}|N)$  in Eq. (4.17) and determining the number of columns  $N$  with the highest posterior probability  $p(N|\boldsymbol{w})$ . Approximating the likelihood function  $p(\boldsymbol{w}|\boldsymbol{\theta}, N)$  by a normal distribution, given by Eq. (4.20), in combination with the choice of a uniformly distributed prior density

function  $p(\theta|N)$ , given by Eq. (4.22), allows one to derive an approximate analytical expression. Substituting Eq. (4.20) and Eq. (4.22) in Eq. (4.17) results into Eq. (4.15) being written as:

$$p(N|\mathbf{w}) \propto N! \cdot \left( \prod_{m=1}^M \frac{1}{\theta_{m_{\max}} - \theta_{m_{\min}}} \right) \int_{\mathbb{D}} \frac{e^{-\chi^2(\theta)/2}}{\prod_{k=1}^K \prod_{l=1}^L \sqrt{2\pi w_{kl}}} d^M \theta, \quad (4.24)$$

where

$$\mathbb{D} = \{(\theta_1, \dots, \theta_M) \in \mathbb{R}^M \text{ for } m = 1, \dots, M: \theta_{m_{\min}} \leq \theta_m \leq \theta_{m_{\max}}\}. \quad (4.25)$$

The factor  $N!$  arises from the number of combinations the parameters of the Gaussian peaks can be permuted, as labelling of the  $N$  peaks is arbitrary. Therefore, there are  $N!$  equivalent maxima of the likelihood function [Sivia 2006]. The expression in Eq. (4.24) can be calculated by expanding the likelihood function by a second order Taylor series around the parameter vector  $\hat{\theta}$  that maximises the likelihood function, known as the maximum likelihood estimate:

$$e^{-\chi^2(\theta)/2} \approx e^{-\chi^2(\hat{\theta})/2} \times e^{-(\theta-\hat{\theta})^T \left[ \frac{\partial \chi^2(\theta)}{\partial \theta} \Big|_{\theta=\hat{\theta}} \right] / 2} \times e^{-(\theta-\hat{\theta})^T \left[ \frac{\partial^2 \chi^2(\theta)}{\partial \theta \partial \theta^T} \Big|_{\theta=\hat{\theta}} \right] (\theta-\hat{\theta}) / 4}. \quad (4.26)$$

Since  $\frac{\partial \chi^2(\theta)}{\partial \theta} \Big|_{\theta=\hat{\theta}} = 0$ , as  $\hat{\theta}$  minimises  $\chi^2(\theta)$ , the second term in Eq. (4.26) is equal to one. Then, by writing  $\chi^2(\hat{\theta})$  as  $\chi_{\min}^2$  and  $\frac{\partial^2 \chi^2(\theta)}{\partial \theta \partial \theta^T} \Big|_{\theta=\hat{\theta}}$  as  $\nabla \nabla \chi^2$ , which depicts the Hessian matrix of  $\chi(\theta)$  at  $\hat{\theta}$ , Eq. (4.26) becomes:

$$e^{-\chi^2(\theta)/2} \approx e^{-\chi_{\min}^2/2} \times e^{-(\theta-\hat{\theta})^T \nabla \nabla \chi^2 (\theta-\hat{\theta}) / 4}, \quad (4.27)$$

which means that Eq. (4.24) is given by

$$p(N|\mathbf{w}) \propto N! \cdot e^{-\chi_{\min}^2/2} \cdot \left( \prod_{m=1}^M \frac{1}{\theta_{m_{\max}} - \theta_{m_{\min}}} \right) \int_{\mathbb{D}} \frac{e^{-(\theta-\hat{\theta})^T \nabla \nabla \chi^2 (\theta-\hat{\theta}) / 4}}{\prod_{k=1}^K \prod_{l=1}^L \sqrt{2\pi w_{kl}}} d^M \theta. \quad (4.28)$$

This expression contains a Gaussian multiple integral which can be solved analytically under the assumptions that i) the maximum likelihood estimate  $\hat{\theta}$  lies well within the support of the prior density function, described by Eq. (4.22), and ii) the likelihood function has only one significant maximum [Sivia 1992a]. Then, the integral in Eq. (4.28) is well approximated by an integral over  $\mathbb{R}^M$ , resulting in the following expression for the posterior probability of the presence of  $N$  atomic columns in the image, given the observed image pixel values  $\mathbf{w}$ , for the model described by Eq. (3.4) with  $M = 4N + 1$  parameters, including Eq. (4.23):

$$p(N|\mathbf{w}) \propto \frac{N!(4\pi)^{M/2} e^{-\chi_{\min}^2/2} [\det(\nabla \nabla \chi^2)]^{-1/2}}{[(\beta_{x_{\max}} - \beta_{x_{\min}})(\beta_{y_{\max}} - \beta_{y_{\min}})(\rho_{\max} - \rho_{\min})(\eta_{\max} - \eta_{\min})]^N (\zeta_{\max} - \zeta_{\min}) \prod_{k=1}^K \prod_{l=1}^L \sqrt{2\pi w_{kl}}}. \quad (4.29)$$

When the terms which are independent of  $N$  are dropped, the expression for  $p(N|\mathbf{w})$  reduces to

$$p(N|\mathbf{w}) \propto \frac{N!(4\pi)^{2N} e^{-\chi_{\min}^2/2} [\det(\nabla \nabla \chi^2)]^{-1/2}}{[(\beta_{x_{\max}} - \beta_{x_{\min}})(\beta_{y_{\max}} - \beta_{y_{\min}})(\rho_{\max} - \rho_{\min})(\eta_{\max} - \eta_{\min})]^N}. \quad (4.30)$$

The importance of Eq. (4.30) is that it allows one to compute the posterior probability of a certain number of atomic columns present in an ADF STEM image, for a model where the columns are assumed to be Gaussian shaped and to have different widths. It relies, in particular,

on the assumption that  $\sigma_{kl} \approx \sqrt{w_{kl}}$ , as stated below Eq. (4.19). By an iterative procedure, better approximations of  $\sigma_{kl}$  can be obtained, but no significant effect on  $p(N|\mathbf{w})$  could be observed, validating the approximation of  $\sigma_{kl} \approx \sqrt{w_{kl}}$ . The MAP probability rule compares the calculated posterior probabilities and selects the number of columns  $N$  with the highest probability. Similar expressions can be derived for other types of models. For example, for a model where the atomic columns are assumed to be Gaussian shaped and to have equal widths [De Backer 2016], the expectation model  $f_{kl}(\boldsymbol{\theta})$  of pixel (k,l) at position  $(x_k, y_l)$  is given by:

$$f_{kl}(\boldsymbol{\theta}) = \zeta + \sum_{n=1}^N \eta_n \exp\left(-\frac{(x_k - \beta_{x_n})^2 + (y_l - \beta_{y_n})^2}{2\rho^2}\right) \quad (4.31)$$

where the unknown parameter vector can be written as:

$$\boldsymbol{\theta} = (\beta_{x_1}, \dots, \beta_{x_N}, \beta_{y_1}, \dots, \beta_{y_N}, \eta_1, \dots, \eta_N, \rho, \zeta)^T \quad (4.32)$$

containing  $M = 3N + 2$  parameters. For such a model, the posterior probability becomes

$$p(N|\mathbf{w}) \propto \frac{N!(4\pi)^{1.5N} e^{-\chi_{min}^2/2} [\det(\nabla\nabla\chi^2)]^{-1/2}}{[(\beta_{x_{max}} - \beta_{x_{min}})(\beta_{y_{max}} - \beta_{y_{min}})(\eta_{max} - \eta_{min})]^N}. \quad (4.33)$$

As another example, for an expectation model given by

$$f_{kl}(\boldsymbol{\theta}) = \zeta + \sum_{n=1}^N \eta \exp\left(-\frac{(x_k - \beta_{x_n})^2 + (y_l - \beta_{y_n})^2}{2\rho^2}\right), \quad (4.34)$$

where the columns are assumed to be Gaussian shaped with equal widths and equal heights, with unknown parameter vector

$$\boldsymbol{\theta} = (\beta_{x_1}, \dots, \beta_{x_N}, \beta_{y_1}, \dots, \beta_{y_N}, \eta, \rho, \zeta)^T \quad (4.35)$$

containing  $M = 2N + 3$  parameters, the posterior probability becomes

$$p(N|\mathbf{w}) \propto \frac{N!(4\pi)^N e^{-\chi_{min}^2/2} [\det(\nabla\nabla\chi^2)]^{-1/2}}{[(\beta_{x_{max}} - \beta_{x_{min}})(\beta_{y_{max}} - \beta_{y_{min}})]^N}. \quad (4.36)$$

The methodology of the MAP probability rule can be extended to models where other shapes of atomic columns are assumed beside a Gaussian function. In these cases, an expression for the posterior probability as a function of the number of atomic columns can be derived in a similar way. Alternative shapes may be Lorentzian functions or a mixture of Lorentzian and Gaussian distributions, which has been revealed to be a better description of the source size distribution [Verbeeck 2012]. Such a linear combination possesses a similar FWHM as a Gaussian distribution, but considerably longer tails. It should be noted that the analytical expressions for  $p(N|\mathbf{w})$  were derived under the assumption that the Poisson distribution that governs the image pixel values can be approximated by a normal distribution. The accuracy of this approximation, and therefore the accuracy of the expressions given by Eqs. (4.30), (4.33) and (4.36), increases with an increasing amount of detected electrons. The expressions will be most accurate if all image pixel values fully satisfy the normality assumption, but have shown to be robust to small violations of this assumption. Therefore, the MAP probability rule is an adequate method allowing to decide the number of atomic columns present in a STEM image.

### 4.3.2 Algorithm

As stated in the previous subsection, the MAP probability rule selects the most probable number of atomic columns by comparing posterior probabilities as a function of  $N$ , i.e. for different numbers of Gaussian peaks in the model describing the atomic columns in the image. The analysis is performed starting from an initial model containing  $N_0$  peaks up to and including a model containing a value of  $N_{max}$  peaks. The parameters  $\theta$  of the initial model are optimised by minimising the weighted sum-of-squared-residuals misfit  $\chi^2(\theta)$ , given by Eq. (4.21), subject to the constraint that  $\theta$  should belong to the support of the prior density function described by Eq. (4.22). Next, an extra peak is added to the initial configuration, so a model is constructed containing  $N_0 + 1$  peaks. Again, the parameters of this model are optimised by minimising  $\chi^2(\theta)$  subject to the constraint that  $\theta$  belongs to the support of the prior density function. To avoid ending up in a local minimum of  $\chi^2(\theta)$ , many different starting positions for the extra added peak need to be tested. To optimise the parameters associated with the other peaks, the estimated parameter values of the previous optimisation, in this case of a model with  $N_0$  peaks, are used as starting values. Next, another peak is added, in the same way as described above, in order to obtain the optimal parameter values of a model containing  $N_0 + 2$  peaks. This procedure continues until the parameters of a model with  $N_{max}$  peaks are optimised. In order to determine the most probable number of atomic columns present in a STEM image, the posterior probability of  $N = N_0, \dots, N_{max}$  columns is computed relatively to the posterior probability of  $N_{max}$  columns as follows

$$p_{rel}(N|\mathbf{w}) = \frac{p(N|\mathbf{w})/p(N_{max}|\mathbf{w})}{\max_N \left[ p(N|\mathbf{w})/p(N_{max}|\mathbf{w}) \right]}, \quad (4.37)$$

where the denominator is a normalisation constant so that the maximum value of  $p_{rel}(N|\mathbf{w})$  corresponds to one. The most probable number of atomic columns is then given by the value  $N$  that maximises Eq. (4.37). Direct visualisation of the probability of the number of columns in the image is possible by plotting  $p_{rel}(N|\mathbf{w})$  on a logarithmic scale as a function of  $N$  resulting in a relative probability curve. The approach described above has been implemented in the freely available StatSTEM software [De Backer 2016].

The procedure has been illustrated based on a simulated image of graphene, shown in Fig. 4.2(a). The image has been simulated using the MULTEM software [Lobato 2015, Lobato 2016] and the simulation parameters are listed in Table 4.1. The MAP probability rule is applied to

**Table 4.1:** Microscope parameter values for simulation of a STEM image of graphene using MULTEM.

Parameter	Symbol	Value
Acceleration voltage	$V_0$ (kV)	80
Defocus	$\epsilon$ (Å)	-20.0
Spherical aberration	$C_s$ (mm)	0.0037
Spherical aberration of 5th order	$C_5$ (mm)	0
Semiconvergence angle	$\alpha$ (mrad)	24.8
Detector inner radius	$\beta_1$ (mrad)	26
Detector outer radius	$\beta_2$ (mrad)	50
Pixel size	$\Delta x = \Delta y$ (Å)	0.20
Number of scanned pixels	$K \times L$	$40 \times 40$
FWHM of the source image	FWHM (Å)	0.7

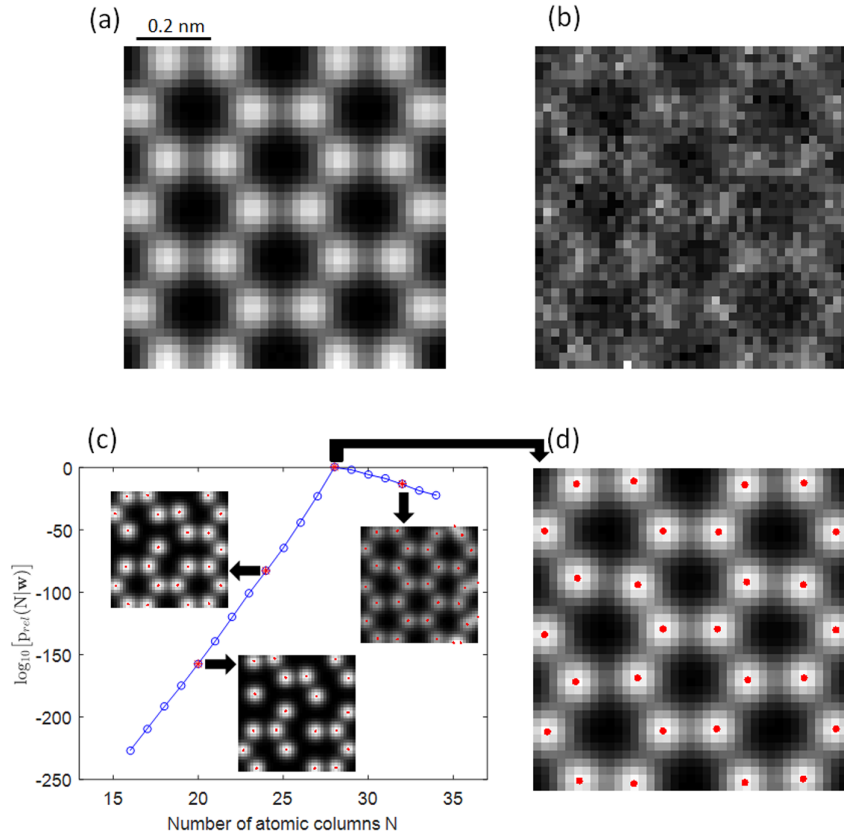


**Figure 4.2:** (a) Simulated ADF STEM image of graphene. (b) Image in (a) disturbed by Poisson noise with an incoming electron dose of  $3 \cdot 10^5 \text{ e}^-/\text{\AA}^2$ . The number of detected electrons equals an average of  $276 \text{ e}^-/\text{\AA}^2$ . (c) MAP probability rule evaluated for the data shown in (b). Refined models with optimised parameters are shown in the inset taking into account 20, 24, and 32 atomic columns. (d) Most probable parametric model of the data in (b) containing 28 atomic columns as indicated by the MAP probability rule in (c).

detect the carbon atoms of graphene from a Poisson disturbed simulated STEM image shown in Fig. 4.2(b), using a parametric model described by a superposition of Gaussian peaks with equal widths and equal heights given by Eq. (4.34). Such a model is acceptable since the simulated graphene consists of a monolayer of only carbon atoms. Fig. 4.2(c) shows the relative probability curve as a function of the number of columns  $N$  calculated by the decimal logarithm of Eq. (4.37). For certain values of  $N$ , the corresponding optimised models are shown. The logarithmic scale is necessary in order to plot the relative probabilities over a wide range of values for the number of columns  $N$ . It is noted that the relative probability curve, as shown in Fig. 4.2(c), is merely a way of visualising the relative probabilities. In order to decide the most probable number of atomic columns in an image one should be aware of the logarithmic scale and should consider the underlying probabilities of the curve. In this manner, the most probable structure found by the MAP probability rule from Fig. 4.2(b) is shown in Fig. 4.2(d), corresponding to the expected hexagonal lattice of graphene, as visually perceived by the noise-free simulated image in Fig. 4.2(a). Interestingly, besides determining the most probable atomic structure from the image data, the MAP probability rule also provides a quantitative statement of how much more

probable a certain number of columns is as compared to another number. This information allows to make an optimal decision of the number of atomic columns that are present in the image and with what confidence. For example, from Fig. 4.2(c) it can be derived that the probability of the presence of 28 atomic columns is around 23 orders of magnitude larger than 27 atomic columns and around 72 times larger than 29 atomic columns. This clearly shows that, for the image data of Fig. 4.2(b), the distinction between 27 and 28 carbon atoms is much clearer than the distinction between 28 and 29 atoms. It is noted that it is not possible to provide such a quantitative statement of the probabilities of the number atomic columns from merely visually interpreting the image.

## 4.4 Experimental examples

The technique of STEM has become a widely used technique to visualise nanomaterials with sub-angstrom resolution due to improvements in aberration correction technology [Krivanek 2009, Rose 2009, Hawkes 2015]. Yet, this does not guarantee visually easily interpretable images as for some materials the incoming electron dose should be limited in order to avoid beam damage. In this section, the validity and usefulness of the MAP probability rule is demonstrated to experimental ADF STEM images of samples of different shape, size, and atom type<sup>2</sup>. The examples include SrTiO<sub>3</sub> in subsection 4.4.1, graphene in subsection 4.4.2, a gold nanorod in subsection 4.4.3, and ultrasmall nanoclusters in subsection 4.4.4.

### 4.4.1 SrTiO<sub>3</sub>

At room temperature, SrTiO<sub>3</sub> adapts the perovskite structure whose general chemical formula is ABX<sub>3</sub>, where "A" and "B" are cations of different sizes. In the perovskite structure, SrTiO<sub>3</sub> is an attractive material for applications in microelectronics because of its high storage capacity, good insulating properties and excellent optical transparency in the visible region [Higuchi 1998, Luo 2004, Kolodiaznyi 2005]. In addition, SrTiO<sub>3</sub> has been used as a substrate for epitaxial growth of high temperature superconducting films [Rehn 1992].

Experimental ADF images of SrTiO<sub>3</sub>, imaged along the [100] direction, have been recorded by K. Müller-Caspary by using a probe corrected FEI Titan, operated at an acceleration voltage of 300 kV. The ADF regime has been selected by using a semiconvergence angle of 21.3 mrad and a detector collection range of 58-197 mrad. Since SrTiO<sub>3</sub> is a beam-stable material, it can be imaged using a high incoming electron dose of around  $10^6 \text{ e}^-/\text{\AA}^2$ . As a result, acquiring an image exhibiting high quality is feasible and may be used as a reference to verify the result obtained from applying the MAP probability rule to an image with low quality. A high CNR image is shown in Fig. 4.3(a) with an incoming electron dose of  $(9.1 \pm 0.4) \cdot 10^5 \text{ e}^-/\text{\AA}^2$ . From this image, the brighter Sr columns and darker Ti-O columns are easily recognisable. The inset indicates the locations of both types of columns. Fig. 4.3(b) shows a noisier counterpart of the inset of Fig. 4.3(a) with an approximately 100 times lower electron dose. Hereby, the dose was varied by defocusing the monochromator. The MAP probability rule has been applied to the image data

<sup>2</sup>The results of this section have been published in J. Fatermans, A.J. den Dekker, K. Müller-Caspary, I. Lobato, C.M. O'Leary, P.D. Nellist, and S. Van Aert, *Single atom detection from low contrast-to-noise ratio electron microscopy images*, Physical Review Letters **121** (2018), 056101.

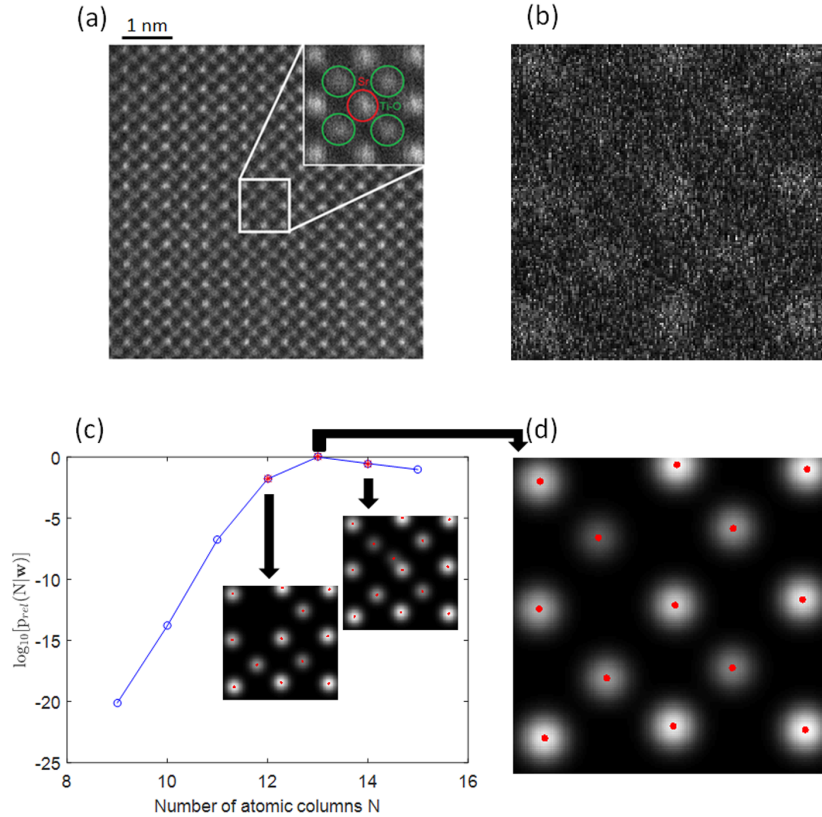


**Figure 4.3:** (a) Experimental ADF STEM image of SrTiO<sub>3</sub> [100] with an incoming electron dose of  $(9.1 \pm 0.4) \cdot 10^5 \text{ e}^-/\text{\AA}^2$ . The region indicated by the square has been magnified in the inset where the Sr columns and Ti-O columns are indicated in red and green, respectively. (b) Noisier counterpart of the inset in (a) with an incoming electron dose of  $(1.08 \pm 0.05) \cdot 10^4 \text{ e}^-/\text{\AA}^2$  and an average number of detected electrons of  $410 \text{ e}^-/\text{\AA}^2$ . (c) MAP probability rule evaluated for the experimental data shown in (b). Refined models with optimised parameters are shown in the inset taking into account 12 and 14 atomic columns. (d) Most probable parametric model of the data in (b) containing 13 atomic columns as indicated by the MAP probability rule in (c).

shown in Fig. 4.3(b) in order to verify whether the expected crystal structure of SrTiO<sub>3</sub> in [100] direction can be retrieved from such low-quality data. The evaluation of the MAP probability rule is shown in Fig. 4.3(c) for an increasing number of atomic columns. Since the width of an atomic column is mainly determined by the finite source size and to a lesser extent by the atom type [LeBeau 2008], a parametric model described by a superposition of Gaussian peaks with equal widths, given by Eq. (4.31), has been used in this analysis. Calculations were performed using a single workstation by using the algorithm described in subsection 4.3.2 resulting in a calculation time of approximately 1 hour in order to obtain Fig. 4.3(c). The most time consuming step is not the optimisation of the parameters of a single model, but the many different starting positions that are required for the optimisation process to avoid ending up in a local minimum when adding a new peak during the execution of the algorithm. It is noted that computation time can be reduced by taking into account knowledge about the expected locations of atomic columns in the material under investigation, which has not been done in this case. Alternatively, in order to speed up calculations one might consider not optimising the entire set of parameters

when searching for a new column, since to some extent the parameters of the peaks that have been detected already do not vary greatly when an extra peak is added to the parametric model. Hereby, one needs to consider a balance between good fit and speed. From Fig. 4.3(c), it follows that the presence of 13 atomic columns in Fig. 4.3(b) is most probable. The refined model with optimised parameters, taking into account 13 atomic columns, is shown in Fig. 4.3(d), corresponding to the expected crystal structure. It has been shown in section 3.4 of chapter 3 that imprecisions of the estimated atomic column positions can be expected due to the limited dose conditions of Fig. 4.3(b). As stated in subsection 4.3.2, the MAP probability provides a quantitative statement of how much more probable a certain number of columns is as compared to another number. Here, from Fig. 4.3(c), it can be derived that the probability of the presence of 13 atomic columns is around 63 times larger than 12 columns and around 3 times larger than 14 columns. The refined models containing 12 and 13 atomic columns are shown in the inset of Fig. 4.3(c). It is noted that in this analysis the MAP probability rule has been applied without introducing any prior knowledge concerning the atomic structure or chemical composition of  $\text{SrTiO}_3$ . In principle, also an ordinary peak finding routine, which searches for local maxima by choosing an arbitrary threshold [De Backer 2016], can be used to determine the number of atomic columns. This technique, though, failed to detect the expected crystal structure of  $\text{SrTiO}_3$  from the image data shown in Fig. 4.3(b). By changing the threshold, one might obtain a better result, but this approach relies heavily on visual inspection which will lead to biased structure information.

## 4.4.2 Graphene

As shown earlier in the simulated image of Fig. 4.2(a), graphene consists of a single layer of carbon atoms arranged in a hexagonal lattice. In essence, it is a single layer of the most common allotrope of carbon, graphite, which can be regarded as a stack of graphene layers. With the isolation of graphene from graphite, the first 2D material was discovered [Novoselov 2004]. This has led to the discovery of a whole family of 2D materials, including hexagonal boron nitride (h-BN) and molybdenum disulphide ( $\text{MoS}_2$ ). As graphene possesses outstanding properties, it plays an important role in developing future applications in a wide variety of domains. Graphene is reported to be many times stronger than steel, yet incredibly lightweight and flexible [Lee 2008]. In addition, it is an efficient conductor of heat and electricity [Balandin 2008] and also optical transparent [Sheehy 2009, Zhu 2014].

Fig. 4.4(a) shows a synthetic ADF image of graphene obtained by C.M. O’Leary of the University of Oxford from an experimental 4D STEM dataset with an acceleration voltage of 80 kV, semiconvergence angle of 24.8 mrad and a detector collection range of 26-50 mrad. A synthetic image is obtained with a pixelated detector where the intensities of the pixels within a certain detector collection range are integrated. It is equivalent to a STEM image obtained with a conventional annular detector with the same collection angles. Graphene, which consists of light elements, carbon, cannot withstand a high incoming electron dose as it can easily be damaged by the electron beam. For this reason, acquiring images of graphene exhibiting high CNR is challenging as the electron dose needs to be limited. The property of beam sensitivity leads to typical rather low-quality ADF STEM images of graphene, such as the one shown in Fig. 4.4(a). Quantitative structure information though, can still be extracted from such images by using the MAP probability rule for determining the most probable atomic arrangement. Fig. 4.4(b)

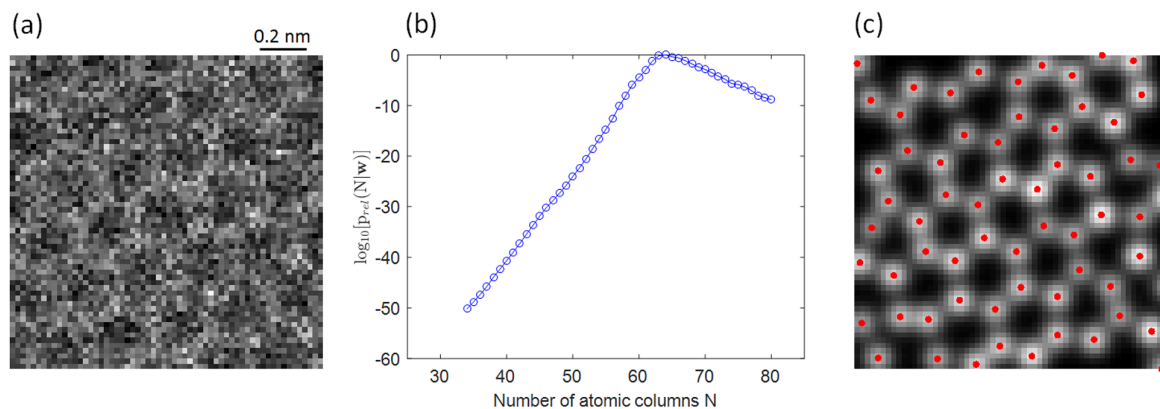


**Figure 4.4:** (a) Synthetic ADF image of graphene obtained from an experimental 4D STEM dataset with an incoming electron dose of around  $3 \cdot 10^5 \text{ e}^-/\text{\AA}^2$  and an average detected electron dose of around  $304 \text{ e}^-/\text{\AA}^2$ . (b) MAP probability rule evaluated for the experimental data shown in (a). (c) Most probable parametric model of the experimental data in (a) as indicated by the MAP probability rule in (b).

shows the evaluation of the MAP probability rule to detect the carbon atoms of graphene from the low contrast data in Fig. 4.4(a), using a parametric model described by a superposition of Gaussian peaks with equal widths, given by Eq. (4.31). Hereby, the fact that graphene consists of a monolayer of carbon atoms has not been taken into account in the analysis, limiting the amount of prior knowledge concerning the atomic structure of graphene. This is opposed to the example of the simulated graphene in Fig. 4.2, where the model given by Eq. (4.34), with equal widths and equal heights, has been used in the analysis. The most probable parametric model that can be obtained by the MAP probability rule from the image data in Fig. 4.4(a) is shown in Fig. 4.4(c), detecting 64 carbon atoms and clearly resolving the hexagonal lattice of graphene. Hereby, imprecisions in the estimated atom positions may arise because of the finite dose conditions of Fig. 4.4(a). Moreover, for the atoms located at the edge of the image, additional imprecisions can be expected. This is related to the fact that these atoms are only partly present in the image data, causing a loss of information. The problem of imprecise estimations for atomic columns located at the edge of an image is often unavoidable since, for example, for large crystallographic structures there might always be atomic columns in the border region of the recorded images. Estimations of atomic columns located close to the border of an image are less precise and can, therefore, be considered to be less reliable. The calculation time needed to obtain the relative probability curve in Fig. 4.4(b) was approximately 11 hours using a single working station following the algorithm as described in subsection 4.3.2. Similar as for the example of  $\text{SrTiO}_3$  in the previous subsection, it is noted that this is mainly due to the many different starting positions that have been used to avoid the optimisation process to end up in a local minimum when adding an extra peak to the model. The considerations to reduce computation time which were discussed in the previous subsection also apply in this example of graphene. In addition, it is noted that, as for the image data of  $\text{SrTiO}_3$  in Fig. 4.3(a), an ordinary peak finding routine failed to obtain the expected atomic arrangement of graphene from the image data shown in Fig. 4.4(a).

### 4.4.3 Gold nanorod

Metal nanorods hold some interesting optical properties which strongly depend on both the particle size and shape and which are not observed in the bulk material [Pérez-Juste 2005]. The possibility to tune their optical response by adjusting size and shape makes these nanorods excellent building blocks for electro-optical devices and contrast agents in biomedical applications [Henglein 2000, Liu 2004, Chen 2005, Becker 2008, Gómez-Graña 2013, Goris 2013a].

An experimental ADF STEM image of a gold nanorod is shown in Fig. 4.5(a) which was obtained by a double-aberration corrected FEI Titan operated at 300 kV with a semiconvergence angle of 21.8 mrad and a detector collection range of 62-190 mrad [Van Aert 2013]. It is noted that, due to the electron beam, especially surface atoms might not stay in the same position during the image acquisition [Williams 2009]. The MAP probability rule has been used to identify the presence of atoms near the edge of the nanorod, which are difficult to detect visually. In this region, the rod is only a few atoms thick which, in combination with the relatively low incoming electron dose of around  $2 \cdot 10^5 \text{ e}^-/\text{\AA}^2$ , leads to a low CNR. The following two-step procedure

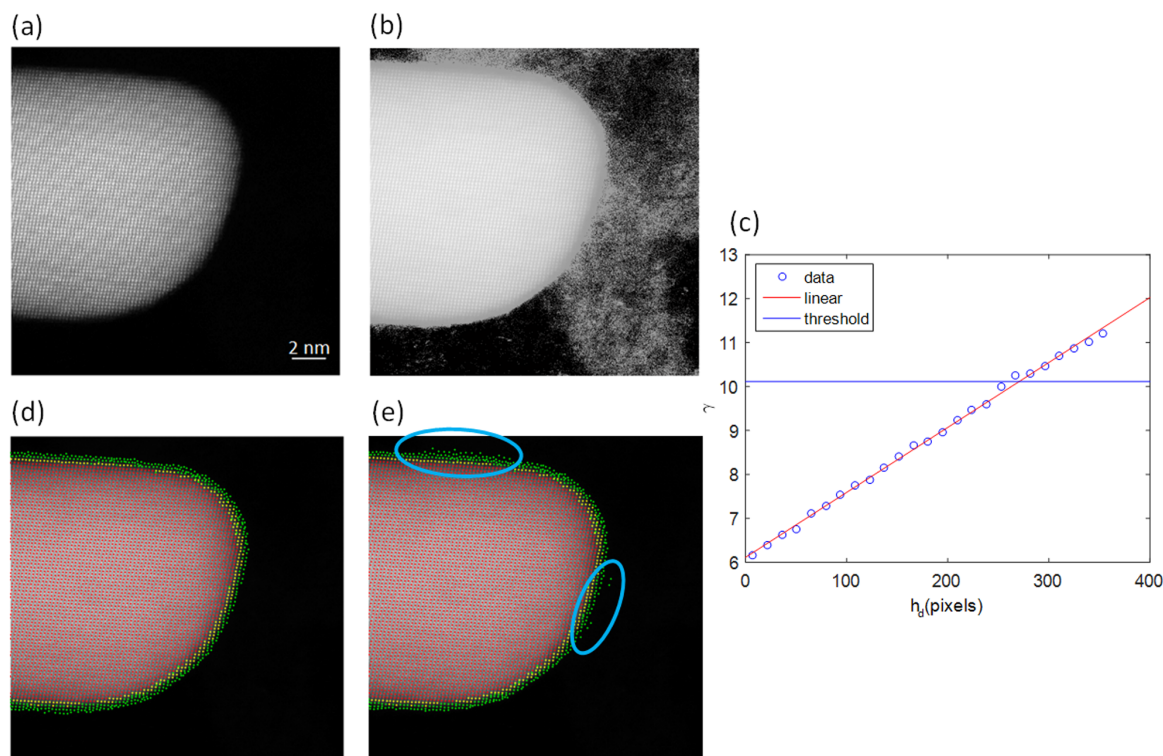


**Figure 4.5:** (a) Experimental ADF STEM image of a gold nanorod with an incoming electron dose of around  $2 \cdot 10^5 \text{ e}^-/\text{\AA}^2$ . (b) Same image as in (a) with adjusted contrast to highlight the variability of the carbon background. (c) Variogram of the background in (a). (d) Most probable atomic columns detected from (a) by a combination of an ordinary peak-finding routine and the MAP probability rule near the edge of the rod, where columns in red have been detected by the ordinary peak-finding routine, columns in yellow by both the ordinary peak-finding routine and the MAP probability rule, and columns in green by the MAP probability rule only. Hereby, the variability of the background has been taken into account. (e) Most probable atomic columns detected from (a) by the same procedure as in (d), but, hereby, neglecting the variability of the background. Regions where extra atoms have been detected as compared to (d).

is suggested to determine the most probable structure of the gold nanorod. First, an ordinary peak-finding routine is applied on the image. This routine is able to quickly detect most of the thicker columns, but has difficulties in correctly detecting atoms near the edge of the particle. Therefore, the MAP probability rule is applied to investigate the presence of atomic columns near the edge. For this, the edge has been divided into different subregions. In each of these subregions, the MAP probability rule has been applied. Dividing the edge into subregions has been done in a manual way taking into account some overlap between neighbouring subregions in order to avoid artefacts and imprecisions arising from atoms that are located right at the border of a subregion, as discussed in the previous subsection. When a column located in an overlap region is detected from different subregions, the average of the estimations is taken. Note that it can be seen from Fig. 4.5(a) that, at the left-hand side, there are columns located right on the border of the image. For these columns, it is unavoidable that the estimations will be less precise. Alternatively, one might consider dividing the region of the edge of the nanorod in a more automated way by using edge detection [Kook 2016, Meng 2018]. During the analysis of the subregions, influence from atomic columns located in the inner part of the nanorod in the neighbourhood of the edge has been taken into account. Hereby, the image data has been modelled by a superposition of Gaussian peaks with equal widths, given by Eq. (4.31), and the total intensity under a Gaussian peak has been chosen to be at least the total intensity scattered by a single gold atom, obtained from simulation with the MULTEM software [Lobato 2015, Lobato 2016]. In order to take thickness fluctuations in the carbon support into account, the background in each of the subregions is allowed to deviate from each other. As such, local fluctuations in the carbon support can be modelled more accurately. From Fig. 4.5(a), it is not directly apparent that the carbon support is fluctuating, but by simply changing the contrast, though, as shown in Fig. 4.5(b), it is clear that the carbon support does not remain constant over the entire image. In order to acquire reliable structure information, the sizes of the defined subregions should be selected in such a way that the background in each subregion can adequately be modelled as a constant. This is the case when the size of a subregion is not larger than a certain maximum distance upon which the variability of the background does not affect atom detection. The so-called variogram, which was originally introduced in geology [Matheron 1963], enables measuring the variability  $\gamma$  of the background as a function of distance  $h_d$  between pixels. This quantity is defined as

$$\gamma(h_d) = \frac{1}{2Z(h_d)} \sum_{z(h_d)=1}^{Z(h_d)} (\Delta s_{z(h_d)})^2, \quad (4.38)$$

where  $Z(h_d)$  denotes the number of paired observations separated by a distance  $h_d$ . The difference between the  $z(h_d)$ th pair of observations is depicted as  $\Delta s_{z(h_d)}$ . The variogram of the carbon background in the image of the gold nanorod is shown in Fig. 4.5(c). It can be seen that the variability of the background  $\gamma$  increases as a function of distance. This indicates that, as the distance between pixels grows, the corresponding pixel values tend to become less similar. In Fig. 4.5(c), it is indicated that the measurements follow a linear trend. In order to determine the maximum size of the defined subregions, ensuring adequate modelling of these regions with a constant background, a threshold value on the variability of the carbon background needs to be chosen. This threshold is indicated by the horizontal line in Fig. 4.5(c) and defines the maximum variability which does not affect atom detection. A mathematical expression for this threshold

can be defined by considering an area consisting of  $K \times L$  pixels, where, besides a background  $\zeta$ , no atomic columns are present. Here, the data is considered to be free of noise. If, due to, for example, surrounding areas with lower backgrounds, a background  $\hat{\zeta}$  is fitted to the area under investigation, for which  $\hat{\zeta} < \zeta$ , there is a possibility of detecting a false atomic column. Detecting such a false column is avoided when adding a peak to the model does not improve the fit to the data. In this case, this means that the uniform sum-of squared-residuals misfit of zero columns,  $\chi_0^2$ , is smaller than or equal to the misfit of one column,  $\chi_1^2$ , including the fitted background  $\hat{\zeta}$ :

$$\chi_0^2 \leq \chi_1^2. \quad (4.39)$$

When an atomic column at position  $(x_k, y_l)$  is described as a Gaussian peak  $g$  with height  $\eta$  and width  $\rho$ :

$$g = \eta \exp\left(-\frac{(x_k - \beta_x)^2 + (y_l - \beta_y)^2}{2\rho^2}\right), \quad (4.40)$$

Eq. (4.39) can be explicitly written as

$$\sum_{k=1}^K \sum_{l=1}^L (\zeta_{kl} - \hat{\zeta}_{kl})^2 \leq \sum_{k=1}^K \sum_{l=1}^L (\zeta_{kl} - (\hat{\zeta}_{kl} + \hat{g}_{kl}))^2 = \sum_{k=1}^K \sum_{l=1}^L (\zeta_{kl} - \hat{\zeta}_{kl} - \hat{g}_{kl})^2. \quad (4.41)$$

When it is defined that  $\zeta_{kl} - \hat{\zeta}_{kl} = \Delta\zeta_{kl} = \Delta\zeta$ , as this difference is the same for all pixel values, since  $\zeta$  and  $\hat{\zeta}$  are both constant for all positions  $(x_k, y_l)$ , Eq. (4.41) becomes

$$KL(\Delta\zeta)^2 \leq \sum_{k=1}^K \sum_{l=1}^L (\Delta\zeta - \hat{g}_{kl})^2. \quad (4.42)$$

From this, it follows that

$$\Delta\zeta \leq \frac{1}{2} \frac{\sum_{k=1}^K \sum_{l=1}^L \hat{g}_{kl}^2}{\sum_{k=1}^K \sum_{l=1}^L \hat{g}_{kl}}. \quad (4.43)$$

In a continuous form, Eq (4.43) can be written as

$$\Delta\zeta \leq \frac{1}{2} \frac{\int \int \hat{g}^2 dx dy}{\int \int \hat{g} dx dy} = \frac{1}{2} \cdot \frac{\pi \hat{\eta}^2 \hat{\rho}^2}{2\pi \hat{\eta} \hat{\rho}^2} = \frac{\hat{\eta}}{4}. \quad (4.44)$$

As the variability  $\gamma$  is calculated by half the average squared difference between pixel values, as given by Eq. (4.38), it can be written, in combination with Eq. (4.44), that

$$\Delta\gamma = \frac{1}{2} (\Delta\zeta)^2 \leq \frac{1}{2} \left(\frac{\hat{\eta}}{4}\right)^2 = \frac{\hat{\eta}^2}{32}. \quad (4.45)$$

Following from Eq. (4.45), as a rule of thumb, the size of each subregion should obey

$$\Delta\gamma \leq \frac{\eta_{min}^2}{32}, \quad (4.46)$$

where  $\eta_{min}$  denotes the minimum height of a Gaussian peak in the model. It is noted that Eq. (4.46) can also be obtained, in an analogous way as described above, by considering an area of

$K \times L$  pixels where an atomic column is present, positioned on top of a background  $\zeta$ . When a background  $\hat{\zeta}$  is fitted, for which  $\hat{\zeta} > \zeta$ , there is a possibility that the atomic column cannot be detected. For such a situation, detecting the column happens when the misfit of one column is smaller than or equal to the misfit of zero columns, given by  $\chi_1^2 \leq \chi_0^2$ . It follows from the threshold in Fig. 4.5(c) given by Eq. (4.46) that the maximum distance  $h_{d_{max}}$  upon which the variability  $\gamma$  of the background does not affect atom detection is given by 271 pixels, which corresponds to around 49 Å. As the size of each subregion has been chosen to be 10 Å by 10 Å, Eq. (4.46) holds and, as a result, the background in each subregion can adequately be modelled as a constant. The result of the analysis is shown in Fig. 4.5(d). Columns in red have been found by the ordinary peak-finding routine. Columns in yellow have been detected by both the ordinary peak-finding routine and the MAP probability rule. Columns in green have been detected by the MAP probability rule only. It is noted that at the edge of the gold nanorod there were no columns found by the ordinary peak-finding procedure which were not detected by the MAP probability rule. To illustrate the importance of adequately modelling the background, the analysis by the MAP probability rule has also been performed by assuming the constant background of all subregions to be equal. As a result, the background is modelled in a less accurate way. Fig. 4.5(e) shows the result of this analysis. As compared to Fig. 4.5(d), extra atoms, which seem to be detached from the rod, have been detected in the indicated regions. These extra detected atoms appear in regions where there is an increased background intensity, as apparent in Fig. 4.5(b). As such, they do not correspond to actual atoms, but are the result of estimating a too low background in these regions.

For radiation-sensitive materials, the incoming electron dose should be kept as low as possible. To illustrate the possibilities of the MAP probability rule when applied to low-dose images, a 10 nm thick gold nanorod has been simulated, which is shown in Fig. 4.6(a), using MULTEM by I. Lobato with an incoming electron dose of merely  $5000 e^-/\text{Å}^2$ . The simulation parameters are listed in Table 4.2. In order to make the simulation more realistic, the structure

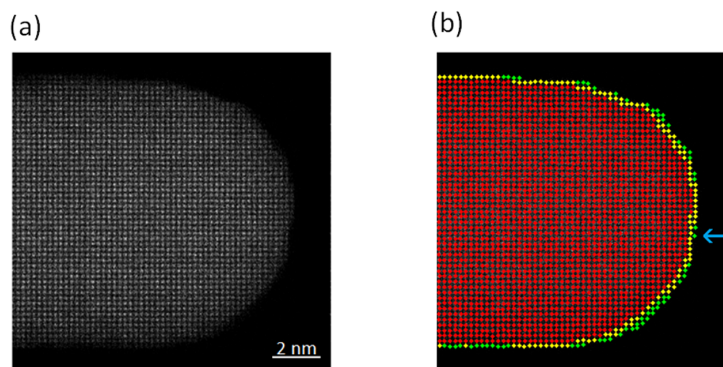


**Figure 4.6:** (a) Simulated ADF STEM image of a gold nanorod with the presence of Poisson noise with an incoming electron dose of  $5000 e^-/\text{Å}^2$ . (b) Most probable atomic columns detected from (a), where the MAP probability rule has been applied to the border region of the nanorod. Columns in red have been detected by the ordinary peak-finding routine, columns in yellow by both the ordinary peak-finding routine and the MAP probability rule, and columns in green by the MAP probability rule only. The arrow indicates an atom detected at a position where no atom was present.

**Table 4.2:** *Microscope parameter values for simulation of a STEM image of a gold nanorod using MULTEM.*

Parameter	Symbol	Value
Acceleration voltage	$V_0$ (kV)	200
Defocus	$\epsilon$ (Å)	15.8
Spherical aberration	$C_s$ (mm)	0.001
Spherical aberration of 5th order	$C_5$ (mm)	0
Semiconvergence angle	$\alpha$ (mrad)	24.0
Detector inner radius	$\beta_1$ (mrad)	60
Detector outer radius	$\beta_2$ (mrad)	165
Pixel size	$\Delta x = \Delta y$ (Å)	0.125
FWHM of the source image	FWHM (Å)	0.7

has been fully relaxed by using molecular dynamics simulations employing the embedded atom method (EAM) potential [Foiles 1986] with the GPU Lammmps package [Brown 2011, Brown 2012, Brown 2013]. For the analysis, the background has been put to zero since no carbon support is present in the simulation and the edge of the rod has been divided into 49 equal subregions to speed up the calculations. Fig. 4.6(b) shows the detected atomic columns from Fig. 4.6(a). From this analysis, it follows that all present atomic columns have been detected and that only one extra atom has been found at a position where the simulation did not include an atom. This atom is indicated by the blue arrow shown in Fig. 4.6(b). This probability for over- or underfitting is an inherent limitation of model-order selection methods and will, in general, increase with decreasing CNR. However, the present example demonstrates the good performance of the MAP probability rule when analysing a low CNR image. Moreover, it can be seen from Fig. 4.6(b) that a substantial amount of atomic columns would not have been detected in the absence of the MAP probability rule. This is an important result since it is well known that the exact surface morphology of nanoparticles can influence their physical properties.

#### 4.4.4 Ultrasmall nanoclusters

The MAP probability rule is also of great importance to detect single atoms in ultrasmall nanoclusters. Such clusters can be thought of as fundamental building blocks leading to metamaterials with physical and chemical properties that are not available in nature [Binns 2001, Claridge 2009]. The growth mechanisms for small nanoclusters are much more exotic than for bulk materials and therefore have a more complex structure.

As a first example, a series of experimental ADF STEM images of a small germanium cluster is shown in Figs. 4.7(a)-(c). The clusters have been imaged using a double aberration-corrected FEI Titan operated at 120 kV and the beam current was set to 40 pA [Bals 2012]. The MAP probability rule, in combination with atom counting [De Backer 2013], can be used to verify whether there is no loss of atoms during the acquisition of the series of the images. In this analysis, one should, however, take into consideration that displacements of individual atoms are possible due to the interaction with the electron beam [Williams 2009]. This may cause atoms to move in or out of the field of view. The MAP probability rule is used to determine the most probable structure of the cluster, using the intensity of a single germanium atom as prior knowledge, obtained from an image simulation with MULTEM. The evaluation of the MAP

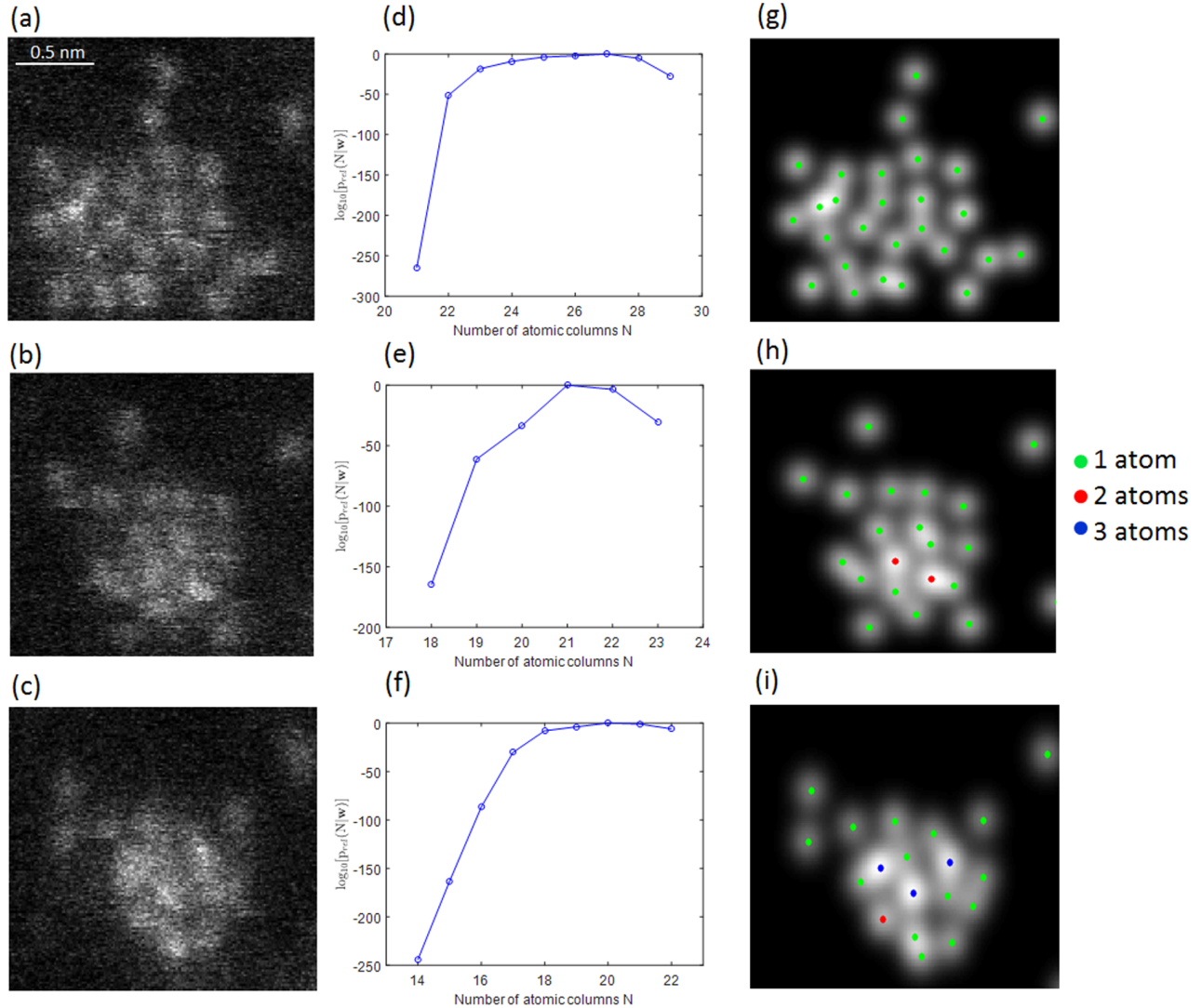


**Figure 4.7:** (a)-(c) Sequence of ADF STEM images of a germanium cluster with an incoming electron dose of around  $6.8 \cdot 10^4 e^- / \text{\AA}^2$ . (d)-(f) MAP probability rule evaluated for the experimental data shown in (a)-(c). (g)-(i) Most probable parametric model of the experimental data in (a)-(c) as indicated by the MAP probability rule in (d)-(f) with atom counting results added in which green, red and blue dots correspond to one, two or three atoms, respectively.

probability rule is shown in Figs. 4.7(d)-(f) for an increasing number of atomic columns. The most probable parametric models are shown in Figs. 4.7(g)-(i), where the dots refer to estimated column positions. The scattering cross sections of the columns, which are equal to the volumes under the estimated Gaussian peaks, have been calculated to count the number of atoms in a column [De Backer 2013]. Hereby, the size of the cluster in Fig. 4.7 has been estimated to be  $26 \pm 2$  atoms. As compared to earlier results obtained by detecting atomic columns by visual inspection of the images [Bals 2012], the MAP probability rule detects more peaks, whereas the total number of atoms in each of the individual frames remains almost constant. The extra peaks correspond to atoms which are not perfectly aligned along the beam direction. This suggests that the MAP probability rule is able to disentangle strongly overlapping peaks resulting into more

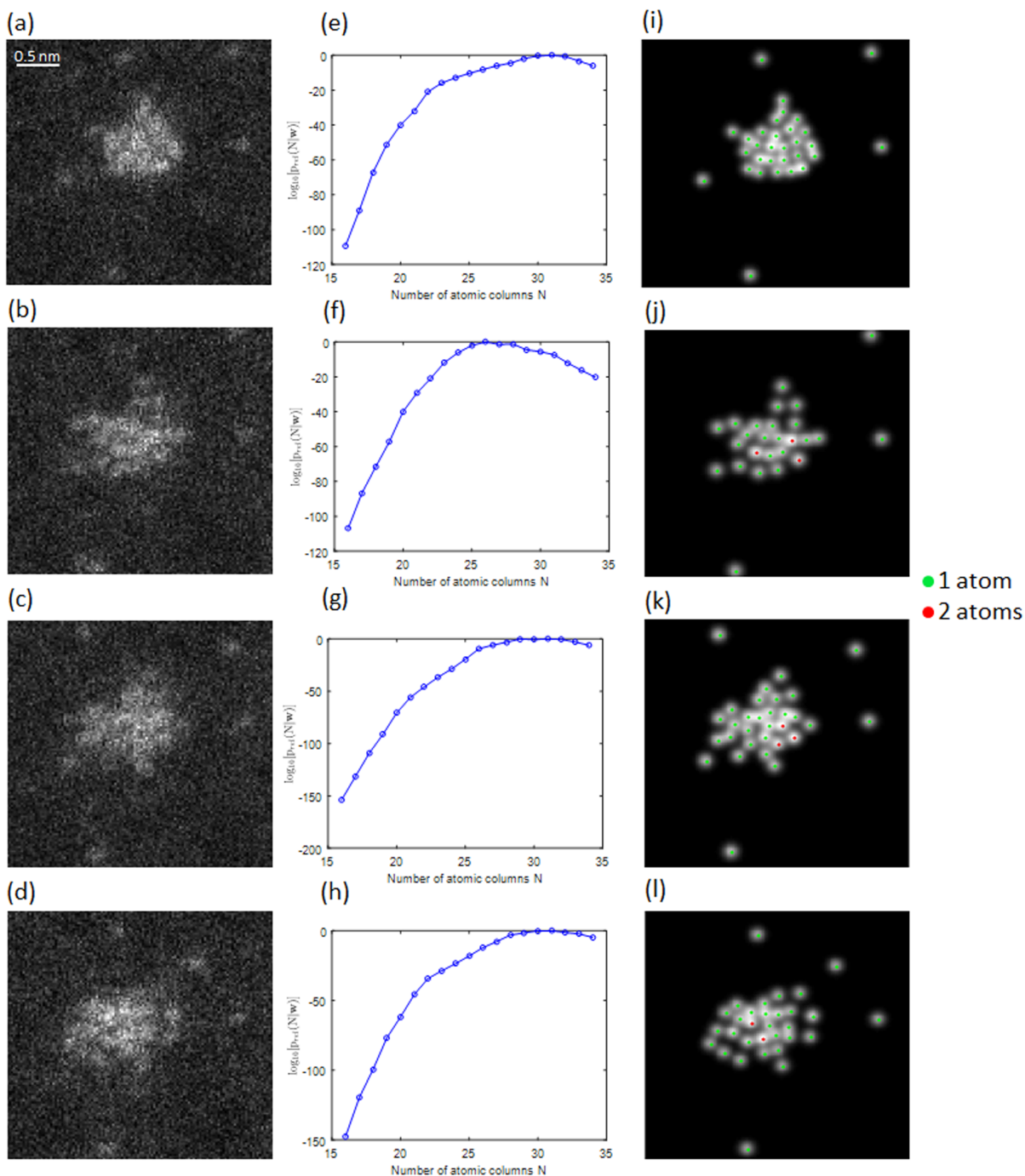


**Figure 4.8:** (a)-(d) Sequence of ADF STEM images of a gold cluster with an incoming electron dose of around  $4500 e^-/\text{\AA}^2$ . (e)-(h) MAP probability rule evaluated for the experimental data shown in (a)-(d). (i)-(l) Most probable parametric model of the experimental data in (a)-(d) as indicated by the MAP probability rule in (e)-(h) with atom counting results added in which green and red dots correspond to one or two atoms, respectively.

accurate structure information as compared to visual inspection. This is of great importance to fully understand the dynamics of such a small nanocluster.

As a second example, a time series of experimental ADF STEM images of a small gold nanocluster is shown in Figs. 4.8(a)-(d), which were obtained by T. Altantzis from a double aberration-corrected FEI Titan operated at 120 kV using a detector range of 28-172 mrad. Gold particles are often investigated because of their tunable properties, such as optical behaviour and catalytic activity [Daniel 2004, Alshammari 2012]. Interestingly, the structure of small gold nanoclusters deviates from the common gold cubic structure. The clusters tend to congregate to stable structures with a specific number of atoms determined by so-called magic numbers [Mackay 1962]. In order to confirm that the size of the nanocluster in Fig. 4.8 is determined by a magic number, the number of atoms needs to be counted. Similar as for the small germanium cluster in Fig. 4.7, the beam sensitivity hinders a visual interpretation since the individual atoms are not clearly distinguishable. In addition, the nanocluster changes shape during the acquisition. In order to obtain a reliable estimation of the structure of the nanocluster, the MAP probability rule has been used, in an analogous way as for the germanium cluster in Fig. 4.7, including the intensity of a single gold atom as prior knowledge obtained from simulation with MULTEM. The evaluation of the MAP probability rule is shown in Figs. 4.8(e)-(h) as a function of the number of columns  $N$ . The most probable parametric models are shown in Figs. 4.8(i)-(l). It follows from this analysis that the size of the cluster in Fig. 4.8 has been estimated to be  $32 \pm 2$  atoms, corresponding to a magic number of 34 atoms.

## 4.5 Conclusions

In this chapter, the methodology of the MAP probability rule to detect single atoms from atomic-resolution ADF STEM images has been explained in detail. The method is built upon model-based parameter estimation, which was the topic of the previous chapter, and Bayesian probability theory, whose basic algebraic calculation rules have been thoroughly elaborated. The combination of statistical parameter estimation and model-order selection allows the MAP probability rule to perform automatic and objective structure quantification of unknown nanomaterials and to detect atomic columns and even single atoms with high reliability. For this purpose, it has been shown that, for a variety of parametric models, approximate analytical expressions can be derived for the probability of the presence of a certain number of atomic columns in ADF STEM image data. The MAP probability rule selects the number of columns that maximises this probability. Furthermore, the MAP probability rule also enables one to quantify how more likely a certain atomic structure is as compared to other structures. Obtaining automatic and objective structure information is especially useful for the analysis of radiation-sensitive and light-element nanostructures. Typically, images of such materials exhibit low CNR due to the use of a limited incoming electron dose in STEM of merely  $10^3 - 10^5 \text{ e}^-/\text{\AA}^2$  in order to avoid beam damage. Visual inspection of such images is unreliable, as it is challenging to distinguish individual atomic columns, and might lead to biased results. The validity and usefulness of applying the MAP probability rule to images exhibiting low CNR have been demonstrated by analysing experimental and simulated ADF STEM images of samples of different shape, size, and atom type. Hereby, it has been shown that important structural information can be obtained by using the MAP probability rule, which would otherwise not have been available.



# 5

## The maximum a posteriori probability rule for atom column detection

### 5.1 Introduction

In the previous chapter, the MAP probability rule has been introduced as a quantitative method to determine the number of atomic columns for which there is most evidence in the ADF STEM image data. The method is based on a combination of statistical parameter estimation [den Dekker 2005, Van Aert 2005, van den Bos 2007, Van Aert 2012b, den Dekker 2013, De Backer 2016] and model-order selection [Myung 2000, Stoica 2004a, Claeskens 2008] from which analytical expressions could be derived using a Bayesian approach [Fatermans 2019]. It was shown that the MAP probability rule is able to automatically and objectively determine the most probable structure of unknown nanomaterials and to detect single atoms with high reliability [Fatermans 2018]. Moreover, the proposed method quantifies how more likely an obtained atomic structure is as compared to other structures.

Since the MAP probability rule can be used to quantify how more likely a certain number of atomic columns is as compared to another number, it offers a way to determine atom detectability, which is defined as the probability to detect an atom from an image. The relation of atom detectability with STEM image quality measures, such as SNR and CNR [Welvaert 2013], can be evaluated. In general, atom detectability is indeed related to image quality, as, for example, one expects the detectability of atomic columns in an image to increase with increasing image quality. In this manner, the probability to detect an atomic column from STEM image data, which can be provided by the MAP probability rule, is correlated with the quality of the image. As such, for STEM images, a new image quality measure, the ICNR, has been proposed that better correlates with atom detectability than conventional image quality measures [Fatermans 2019].

Moreover, the MAP probability rule is related to the concept of model selection, where one aims to select the best model from a set of candidate models given experimental data. Hereby, a tradeoff between both goodness of fit and the complexity of the models under investigation

needs to be performed [Myung 2000]. The working principle of model selection has been briefly described in chapter 3 in section 3.5. The MAP probability rule can be considered as a model-selection criterion, such as the AIC [Akaike 1974] and BIC [Schwarz 1978]. In particular, the MAP probability rule is closely related to the BIC, since both methods are derived from a Bayesian approach. In principle, atom detection from STEM images can be performed with any model-selection criterion, but, interestingly, the MAP probability rule takes into account more dimensions of model complexity as compared to other commonly used model-selection criteria. This allows for a superior performance to detect the correct number of atomic columns from ADF STEM images [Fatermans 2019]. In addition, the MAP probability rule offers a more flexible way to detect atoms from images than other criteria. This is due to the fact that the prior can be tuned, resulting into a different value for the complexity of the model under consideration. Moreover, by using the MAP probability rule, it is clear what prior knowledge has been taken into account during the analysis, which is not always straightforward for other model-selection criteria.

This chapter is organised as follows<sup>3</sup>. In section 5.2, it is explained how the MAP probability rule can be used to evaluate the correlation between measures of image quality and atom detectability. In subsection 5.2.1, the correlation with conventional measures, such as SNR and CNR, is investigated, whereas in subsection 5.2.2 a new image-quality measure which correlates better with atom detectability is introduced. In section 5.3, the relation of the MAP probability rule to model selection is investigated. Hereby, subsection 5.3.1 compares the performance of the MAP probability rule in correctly detecting atoms from STEM images to that of other model-selection criteria. This is followed in subsection 5.3.2 by explicitly showing the connection between the MAP probability rule and the BIC. In subsection 5.3.3, the effect of incorporating a certain amount of prior knowledge in the analysis is explained. Finally, in section 5.4, conclusions will be drawn.

## 5.2 Atom detectability

In general, one expects that the detectability of atomic columns in images will increase with increasing image quality. Fig. 5.1 depicts a set of Poisson noise disturbed simulated ADF STEM images of a single atom with varying background and incoming electron dose. Intuitively, it is clear that detecting the atom will be easiest from high-quality images with a high electron dose and low background, and most difficult from low-quality images with low dose and high background. In this section, the MAP probability rule will be used as a tool to evaluate the relation between image quality and atom detectability. Hereby, it is noted that when only the value of the incoming electron dose is available no information is provided about the detectability of atomic columns in an image. Depending on the sample, the number of electrons that reaches the detector can be very different for the same incoming dose. This is shown by the horizontal lines of Fig. 5.1 where the same incoming electron dose is used, but due to the different backgrounds that are present in the images, the perceived atom detectability may vary significantly. Alternatively, one might consider using detected electron dose instead to evaluate the relation with atom

---

<sup>3</sup>The results in this chapter have been published in J. Fatermans, S. Van Aert, and A.J. den Dekker, *The maximum a posteriori probability rule for atom column detection from HAADF STEM images*, *Ultramicroscopy* **201** (2019), p. 81-91

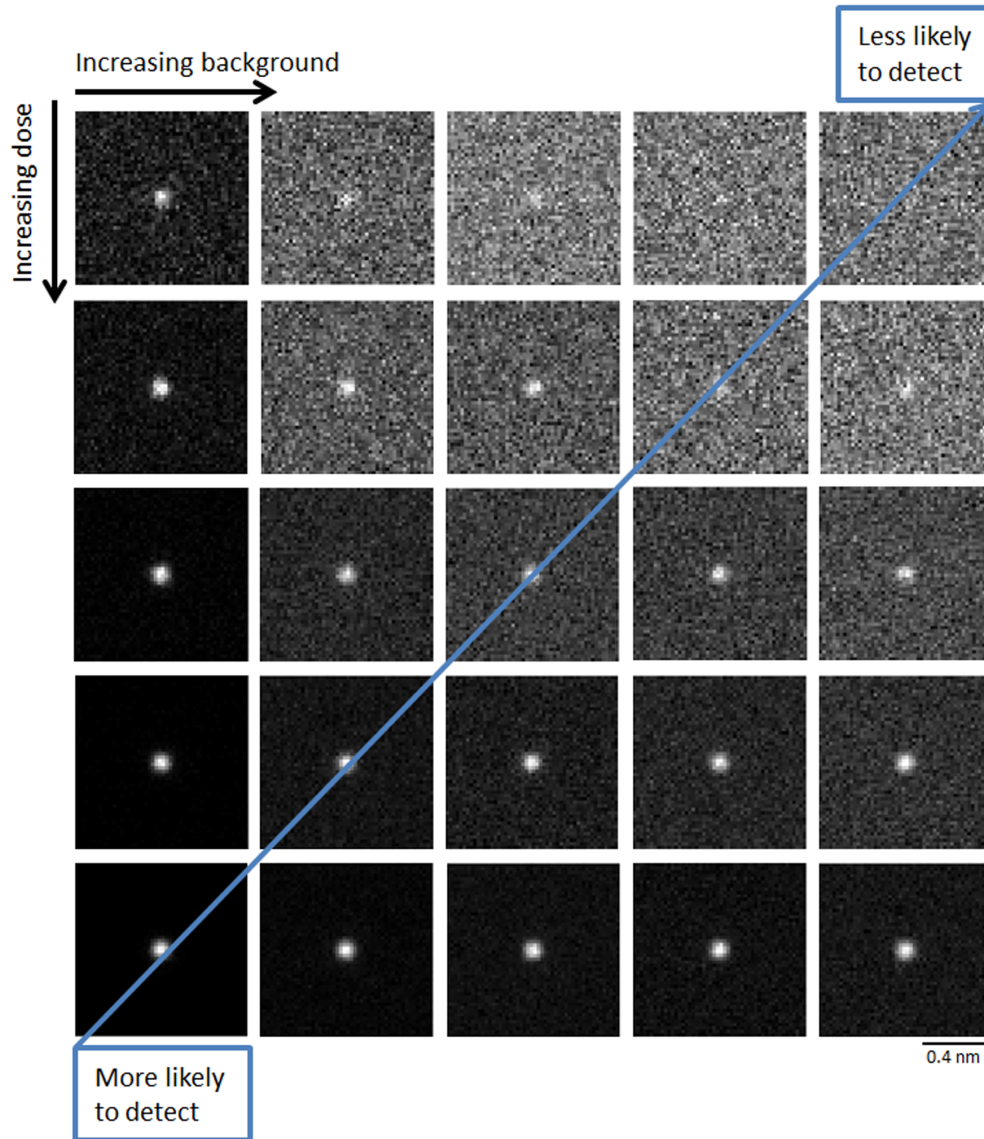


**Figure 5.1:** Set of simulated Poisson noise disturbed ADF STEM images of a single atom with varying incoming electron dose and background.

detectability. Unfortunately, also the detected number of electrons does not provide information about the probability of detecting atomic columns from an image. In Fig. 5.1, the number of detected electrons increases while moving to the right-hand side, but, as visually perceived, this does not guarantee better atom detectability. In addition, a disadvantage of using detected electron dose is that it typically only provides an averaged value, losing information about variations in the detected number of electrons in the image. Therefore, other measures than incoming or detected electron dose are required to evaluate the relation between image quality and atom detectability. In subsection 5.2.1, SNR and CNR are investigated. This is followed by subsection 5.2.2 where a new image-quality measure is proposed that correlates better with atom detectability.

### 5.2.1 SNR and CNR

In this section, the relation of SNR and CNR as image-quality measures to atom detectability is evaluated by using the MAP probability rule. First, SNR is investigated. As local fluctuations of the background or differences in atomic column thicknesses or composition can occur, each column in a STEM image can possess a different SNR value. When the background in the image can be considered to be constant, the SNR of a column at position  $(\beta_x, \beta_y)$  can be written as

$$SNR = \frac{\eta + \zeta}{[\eta + \zeta]^{1/2}}, \quad (5.1)$$

where  $\eta$  and  $\zeta$  denote the height of the atomic column and the background of the image, respectively, for a parametric model based on a superposition of Gaussian peaks, such as the ones discussed in section 3.2 of chapter 3. It is noted that the definition in Eq. (5.1) provides a rather simple description of SNR. There exist several alternative ways of defining SNR [Welvaert 2013]. To investigate the relation of SNR to atom detectability, a set of ADF STEM images of 12.5 Å by 12.5 Å with a pixel size of 0.25 Å has been simulated of an individual Au atom using MULTEM [Lobato 2015, Lobato 2016] to which an arbitrary constant background has been added accounting for the contribution of electrons scattered by an amorphous substrate. The remaining simulation parameters are listed in Table 5.1. Each simulated image has been generated 1000 times containing random Poisson noise. The SNR of the atom in the image has been altered by changing the incoming electron dose ranging from  $10^3 \text{ e}^-/\text{Å}^2$  to  $10^5 \text{ e}^-/\text{Å}^2$  resulting in a higher SNR value for a higher incoming electron dose. For detecting the Au atom from the noise disturbed images by the MAP probability rule, a model assuming the image of the atom to be Gaussian shaped has been used, where a constant background  $\zeta$  and width  $\rho$ , height  $\eta$  and x- and y-coordinate  $\beta_x$  and  $\beta_y$  of the atom need to be estimated. The prior density  $p(\theta|N)$  has been chosen as a product of uniform distributions for each parameter, in correspondence with subsection 4.3.1 of chapter 4, where the parameters  $\zeta$  and  $\eta$  range from 0 up to the maximum pixel intensity in the simulated image, whereas the parameters  $\rho$ ,  $\beta_x$  and  $\beta_y$  range according to the field of view of the image, i.e. from 0 Å up to 12.5 Å. Fig 5.2(a) shows the observed detection rates of the MAP probability rule as a function of SNR. The error bars show the 95 % confidence Wilson score intervals of a binomial distribution [Wilson 1927]. Below the graph, simulated STEM images containing Poisson noise for different SNR values are depicted. Alternatively, the SNR value of the Au atom in the simulated image can be altered by changing the added constant background independently of the incoming electron dose, simulating the

**Table 5.1:** Microscope parameter values for simulation of a set of ADF STEM images of 12.5 Å by 12.5 Å using MULTEM.

Parameter	Symbol	Value
Acceleration voltage	$V_0$ (kV)	120
Defocus	$\epsilon$ (Å)	0
Spherical aberration	$C_s$ (mm)	0.001
Spherical aberration of 5th order	$C_5$ (mm)	0
Semiconvergence angle	$\alpha$ (mrad)	21.3
Detector inner radius	$\beta_1$ (mrad)	28
Detector outer radius	$\beta_2$ (mrad)	172
FWHM of the source image	FWHM (Å)	0.7

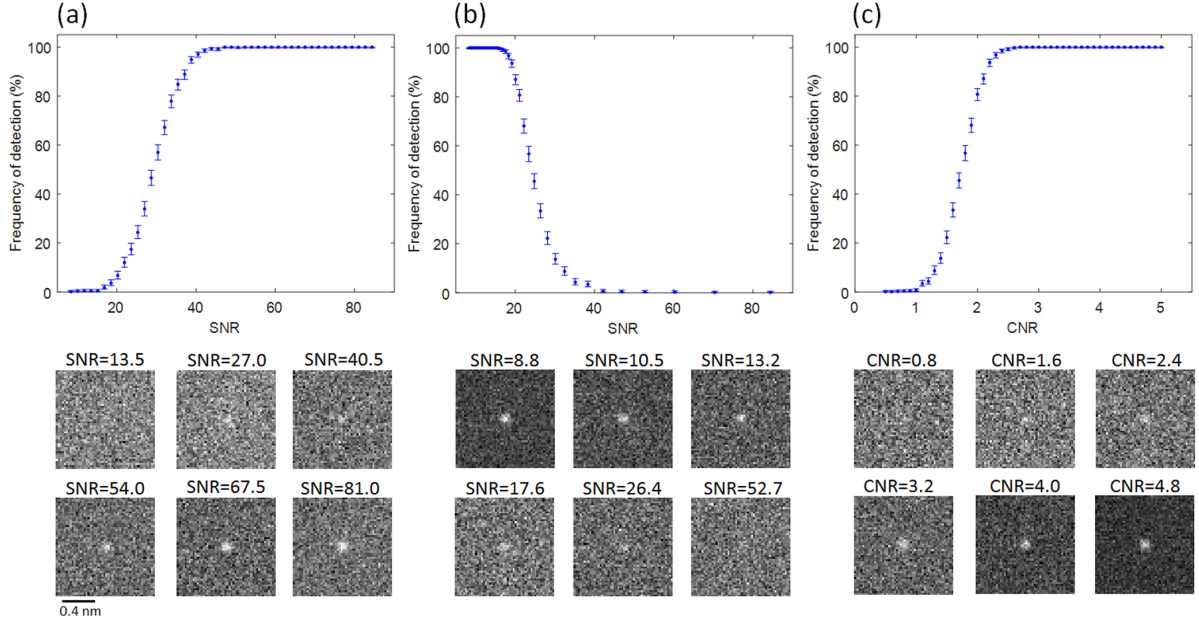


**Figure 5.2:** (a) Observed detection rate of a Au atom by the MAP probability rule from simulated ADF STEM images of  $12.5 \text{ \AA}$  by  $12.5 \text{ \AA}$  with a pixel size of  $0.25 \text{ \AA}$  as a function of SNR using the simulation parameters listed in Table 5.1 where the SNR has been altered by changing the incoming electron dose ranging from  $10^3 e^-/\text{\AA}^2$  to  $10^5 e^-/\text{\AA}^2$  and (b) by changing the constant background for a fixed incoming electron dose of  $10^4 e^-/\text{\AA}^2$ . (c) Detection rate from the same set of images as in (b) as a function of CNR. Below the figures the simulated images disturbed by Poisson noise for different values of SNR and CNR are shown.

effect of the atom to be positioned on a substrate with varying thickness. By altering the SNR by this procedure for a fixed incoming electron dose of  $10^4 e^-/\text{\AA}^2$  and by using the same approach for the MAP probability rule as for Fig. 5.2(a), Fig. 5.2(b) shows that the detection rate decreases with increasing SNR value, as opposed to Fig. 5.2(a). Apparently, a high SNR value does not guarantee high atom detectability. This is also visually perceived by the images below Fig. 5.2(b) showing Poisson disturbed simulated STEM images for different SNR values. The reason for this behaviour lies in the fact that the SNR measure given by Eq. (5.1) only considers the total sum of the height of the atomic column  $\eta$  and the background of the image  $\zeta$ . Therefore, SNR does not take image contrast into account and it is possible that the SNR of an image is high while contrast is low. Contrast, however, also affects the visual perception and detectability of objects in an image, as is apparent from Fig. 5.1. An alternative measure to describe the quality of an image is given by the CNR [Welvaert 2013]. When a parametric model is used to describe the background and atomic columns in an ADF STEM image, the CNR of a column can be defined as

$$CNR = \frac{\eta}{[\eta + \zeta]^{1/2}}. \quad (5.2)$$

Note that the definition of CNR in Eq. (5.2) is closely related to the definition of SNR in Eq. (5.1), but in case of CNR the background  $\zeta$  is subtracted before taking the ratio. As such, the CNR also takes image contrast into account. Therefore, CNR relates better to atom detectability than SNR. This is confirmed by Fig. 5.2(c) where the observed detection rate is shown as a

function of the CNR for the same set of images as for Fig. 5.2(b). From this, it is seen that the detection rate increases with increasing CNR. It is noted that the same behaviour is observed for the set of images of Fig. 5.2(a).

## 5.2.2 Integrated CNR

As followed from the previous section, CNR is a more intuitive image quality measure than SNR when it comes to detecting atoms from ADF STEM images. In this section, the relation between the CNR measure and atom detectability is investigated for variations of atom type, incoming electron dose and image pixel size. First, the detection rate of the MAP probability rule for different types of individual atoms as a function of CNR is shown in Fig. 5.3(a) for simulated ADF STEM images of  $12.5 \text{ \AA}$  by  $12.5 \text{ \AA}$  with a pixel size of  $0.25 \text{ \AA}$ , using MULTEM with an incoming electron dose of  $10^6 \text{ e}^-/\text{\AA}^2$ , where each simulated image has been generated 1000 times containing Poisson noise. The remaining simulation parameters can be found in Table 5.1 in subsection 5.2.1. The CNR of the atom in the image has been altered by adding a constant background. For detecting the atom from the noise disturbed images by the MAP probability rule, the same approach as in Fig. 5.2 has been followed with an equivalent choice for the prior

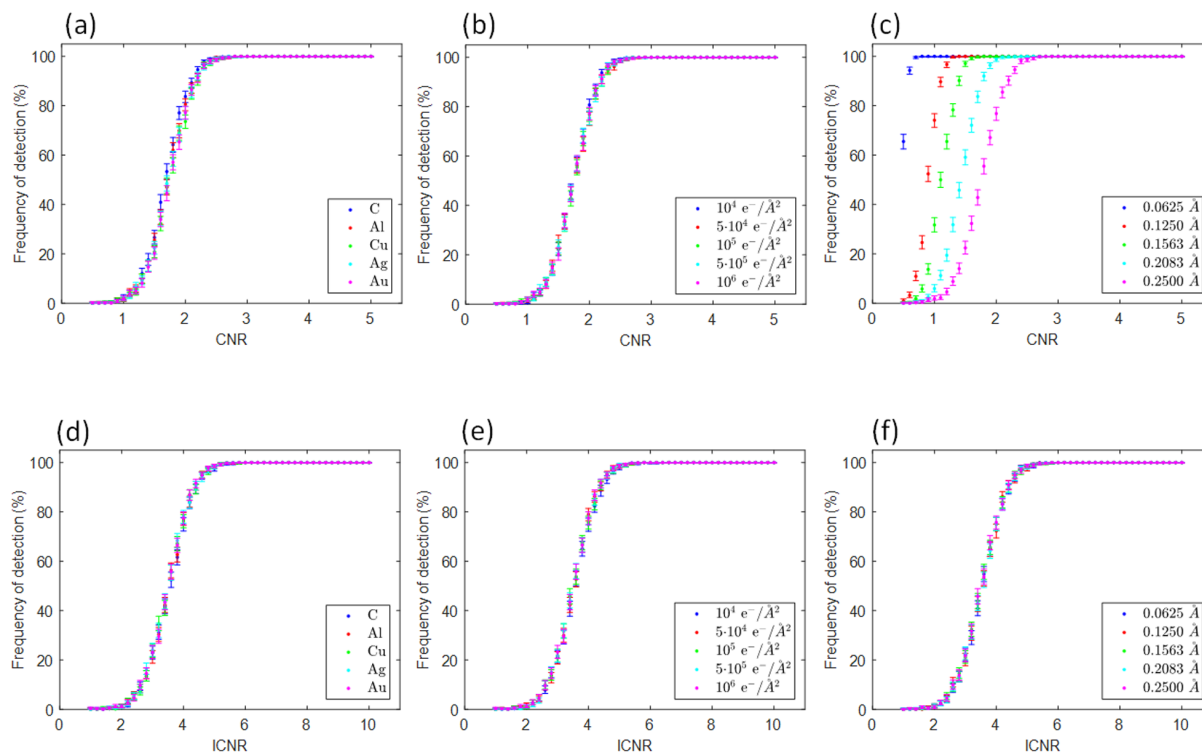


**Figure 5.3:** Observed detection rate of an individual atom by the MAP probability rule from simulated HAADF STEM images of  $12.5 \text{ \AA}$  by  $12.5 \text{ \AA}$  with a pixel size of  $0.25 \text{ \AA}$  for varying atom types with an incoming electron dose of  $10^6 \text{ e}^-/\text{\AA}^2$  as a function of (a) CNR and (d) ICNR. Detection rate of a Au atom from simulated HAADF STEM images of  $12.5 \text{ \AA}$  by  $12.5 \text{ \AA}$  with a pixel size of  $0.25 \text{ \AA}$  for varying incoming electron dose as a function of (b) CNR and (e) ICNR and from images with an incoming electron dose of  $10^5 \text{ e}^-/\text{\AA}^2$  for varying pixel size as a function of (c) CNR and (f) ICNR.

density  $p(\theta|N)$ . It follows from Fig. 5.3(a) that the relation between CNR and detection rate depends hardly, yet slightly, on the atom type. Next, the relation between CNR and detection rate to varying incoming electron dose is investigated. For this, images of 12.5 Å by 12.5 Å with a pixel size of 0.25 Å of an individual Au atom have been simulated with different incoming electron doses. Fig. 5.3(b) shows that the relation between CNR and the atom detection rate is rather robust to incoming electron dose. On the other hand, a different pixel size influences the detection rate as a function of CNR significantly, as shown in Fig. 5.3(c) for images of a Au atom with an incoming electron dose of  $10^5 \text{ e}^-/\text{Å}^2$  and varying pixel size. This is due to the fact that, for a fixed incoming electron dose/ $\text{Å}^2$ , an increased image pixel size leads to an increased electron dose/pixel. The increased value for electron dose/pixel results into a higher value for the background  $\zeta$  and height  $\eta$  of the Au atom, since both  $\zeta$  and  $\eta$  scale with electron dose/pixel, and hence into a higher CNR given by Eq. (5.2) and vice versa. For this reason, the ICNR is proposed whose relationship with atom detectability is independent of atom type, incoming electron dose and, in particular, the pixel size of the image. The ICNR of an atomic column in ADF STEM images is defined as the ratio of the total intensity of electrons scattered by the column, the so-called scattering cross section [Van Aert 2009b, Van Aert 2013, E 2013, De Backer 2016], to the square root of the sum of the scattering cross section and the integrated background under the column. When a parametric model based on a superposition of Gaussian peaks is used to describe the background and atomic columns, the ICNR of a column can be calculated as

$$ICNR = \frac{2\pi\eta\rho^2}{[2\pi\eta\rho^2 + \pi(3\rho)^2\zeta]^{1/2}}, \quad (5.3)$$

where  $\rho$  denotes the estimated width of the atomic column. In this work, ICNR values are calculated by expressing  $\rho$  in units of pixels. In order to estimate the integrated background under the column, the area under the column has been considered to be a circle with a radius of  $3\rho$ , since 99.46 % of the volume under the Gaussian peak describing the column is contained within this distance. It should be noted that Eq. (5.3) is only valid for individual atomic columns that are well separated in the image. For denser crystallographic structures, the contrast of a column depends, not only on the height of the column  $\eta$  and on the background in the image  $\zeta$ , but also on the heights of and the distances from the surrounding columns. For the investigation of the relation between ICNR and atom detectability to varying atom type, incoming electron dose and pixel size, the same procedure for the simulated images has been followed as for the investigation of CNR. It is shown in Figs. 5.3(d) and (e) that the detection rate does not change with atom type or incoming electron dose, respectively, as long as the ICNR value remains unchanged. The functional relationship between detection rate and ICNR is also independent of pixel size, as shown in Fig. 5.3(f), as opposed to the relationship between detection rate and CNR, as shown in Fig. 5.3(c). The results indicate that ICNR is a more robust measure for atom detectability from high-resolution HAADF STEM images than CNR.

## 5.3 Relation to model selection

Model selection methods consider a tradeoff between high goodness of fit and low model complexity in order to select the model which most closely describes the underlying process that generated the experimental data. In essence, the MAP probability rule is also a model-selection

method where the posterior probability of the presence of  $N$  atomic columns in a STEM image of  $W = K \times L$  pixels can be written in general terms as

$$p(N|\mathbf{w}) \propto \frac{\text{goodness of fit}}{\text{model complexity}}. \quad (5.4)$$

The numerator, goodness of fit, is the likelihood function evaluated at the maximum likelihood estimate  $\hat{\theta}$ , as explained in subsection 4.3.1 of chapter 4:

$$p(\mathbf{w}|\hat{\theta}, N) = \frac{e^{-\chi^2(\hat{\theta})/2}}{\prod_{k=1}^K \prod_{l=1}^L \sqrt{2\pi w_{kl}}}, \quad (5.5)$$

with

$$\chi^2(\hat{\theta}) = \sum_{k=1}^K \sum_{l=1}^L \frac{(w_{kl} - f_{kl}(\hat{\theta}))^2}{w_{kl}}. \quad (5.6)$$

The full expression for the posterior probability  $p(N|\mathbf{w})$  for a model with  $M$  parameters describing the atomic columns in a STEM image by Gaussian peaks with different widths is given in subsection 4.3.1 of chapter 4 as

$$p(N|\mathbf{w}) \propto \frac{N!(4\pi)^{M/2} e^{-\chi_{min}^2/2} [\det(\nabla\nabla\chi^2)]^{-1/2}}{[(\beta_{x_{max}} - \beta_{x_{min}})(\beta_{y_{max}} - \beta_{y_{min}})(\rho_{max} - \rho_{min})(\eta_{max} - \eta_{min})]^N (\zeta_{max} - \zeta_{min}) \prod_{k=1}^K \prod_{l=1}^L \sqrt{2\pi w_{kl}}}. \quad (5.7)$$

The prior density  $p(\theta|N)$  for such a model is given in subsection 4.3.1 as

$$p(\theta|N) = \frac{1}{[(\beta_{x_{max}} - \beta_{x_{min}})(\beta_{y_{max}} - \beta_{y_{min}})(\rho_{max} - \rho_{min})(\eta_{max} - \eta_{min})]^N (\zeta_{max} - \zeta_{min})}, \quad (5.8)$$

By considering Eq. (5.7), a mathematical expression for the model complexity in Eq. (5.4) can be provided. From Eq. (5.5), where  $\chi^2(\hat{\theta}) = \chi_{min}^2$ , and from the expression for the prior density in Eq. (5.8), it follows that the posterior probability in Eq. (5.7) can be written as

$$p(N|\mathbf{w}) \propto \frac{p(\mathbf{w}|\hat{\theta}, N)}{[\det(\nabla\nabla\chi^2)]^{1/2} / [N!(4\pi)^{M/2} p(\theta|N)]}. \quad (5.9)$$

Since the goodness of fit is given by  $p(\mathbf{w}|\hat{\theta}, N)$ , the model complexity in Eq. (5.4) for the MAP probability rule is given by

$$\text{model complexity} = \frac{[\det(\nabla\nabla\chi^2)]^{1/2}}{N!(4\pi)^{M/2} p(\theta|N)}. \quad (5.10)$$

The term  $\nabla\nabla\chi^2$  in Eq. (5.10) is related to the observed Fisher information matrix  $\hat{J}$  [Dodge 2003], as described in subsection 3.4.1 of chapter 3, which holds the information that is contained by the observed data about the unknown parameters  $\theta$ . It is described by the Hessian matrix of minus the logarithm of the likelihood function  $p(\mathbf{w}|\theta, N)$ , given by Eq. (5.5), evaluated at the maximum likelihood estimate  $\hat{\theta}$ . As such,

$$\hat{J} = - \frac{\partial^2 \log[p(\mathbf{w}|\theta, N)]}{\partial\theta\partial\theta^T} \Big|_{\theta=\hat{\theta}} = \frac{\partial^2 [\chi^2(\theta)/2]}{\partial\theta\partial\theta^T} \Big|_{\theta=\hat{\theta}} \quad (5.11)$$

where  $\frac{\partial^2 \chi^2(\theta)}{\partial \theta \partial \theta^T} \Big|_{\theta=\hat{\theta}}$  can be written in short as  $\nabla \nabla \chi^2$ . The term  $\nabla \nabla \chi^2$  is an  $M \times M$  dimensional matrix and, therefore, it depends on the number of parameters. In addition, it explicitly contains the expectation model  $f_{kl}$ , describing the intensity of pixel  $(k, l)$  at position  $(x_k, y_l)$ , as follows from Eq. (5.6). Therefore, the term  $\nabla \nabla \chi^2$  in Eq. (5.10) takes into account two dimensions of model complexity, which are the number of parameters on the one hand and the functional form of the model on the other hand. The third dimension of model complexity, which is the extension of the parameter space, is described by the prior density  $p(\theta|N)$ . By choosing  $p(\theta|N)$  as a product of uniform distributions for each parameter individually, large ranges for the possible values of the parameters correspond with a small value for  $p(\theta|N)$ . Since the model complexity in Eq. (5.10) is inversely proportional to  $p(\theta|N)$ , model complexity increases as the extension of the parameter space increases. As a result, the complexity term of the MAP probability rule depends on three dimensions of model complexity as opposed to other more common criteria, such as the AIC [Akaike 1974], the GIC [Broersen 1993], which is an extension of AIC by introducing a general parameter  $d$ , the BIC [Schwarz 1978] and the HQC [Hannan 1979], whose mathematical forms are given by:

$$\begin{aligned} AIC &= -2\log(\hat{L}) + 2M \\ GIC &= -2\log(\hat{L}) + dM. \\ BIC &= -2\log(\hat{L}) + M\log(W) \\ HQC &= -2\log(\hat{L}) + M\log[\log(W)], \end{aligned} \tag{5.12}$$

where the first term denotes the goodness of fit and the second term accounts for model complexity [Stoica 2004a, Claeskens 2008]. It is clear from Eq. (5.12) that the complexity terms of these criteria only depend on the number of parameters  $M$ . By taking the logarithm of Eq. (5.9) multiplied by -2, the posterior probability  $p(N|\mathbf{w})$  can be written in the same form as the model-selection criteria in Eq. (5.12):

$$\begin{aligned} -2\log[p(N|\mathbf{w})] &= -2\log(\hat{L}) + \log[\det(\nabla \nabla \chi^2)] - 2\log(N!) \\ &\quad - M\log(4\pi) - 2\log[p(\theta|N)] + cst, \end{aligned} \tag{5.13}$$

where  $p(\mathbf{w}|\hat{\theta}, N)$  has been written as  $\hat{L}$ . The term *cst* in Eq. (5.13) refers to a constant coming from the proportionality of Eq. (5.9). From this expression, it can be directly seen that the MAP probability rule holds a more complex penalty term than the criteria given in Eq. (5.12).

The remainder of this section is organised as follows. In subsection 5.3.1, the performance of the MAP probability rule in detecting atoms from STEM images is compared to that of other selection criteria. This is followed by subsection 5.3.2 where the relation between the MAP probability rule and the BIC is explicitly shown. In subsection 5.3.3, the effect of the prior density on atom detection is discussed.

### 5.3.1 Performance in detecting atoms

In this section, the performance of the MAP probability rule in detecting atoms from ADF STEM images is compared to the AIC, GIC, BIC and HQC, which were introduced in Eq. (5.12). For the GIC,  $d = 3$  [Broersen 1996] and  $d = 4$  [Stoica 2004a] are considered, which are referred to, in what follows, as GIC3 and GIC4, respectively. A set of 1000 images of Au atoms has

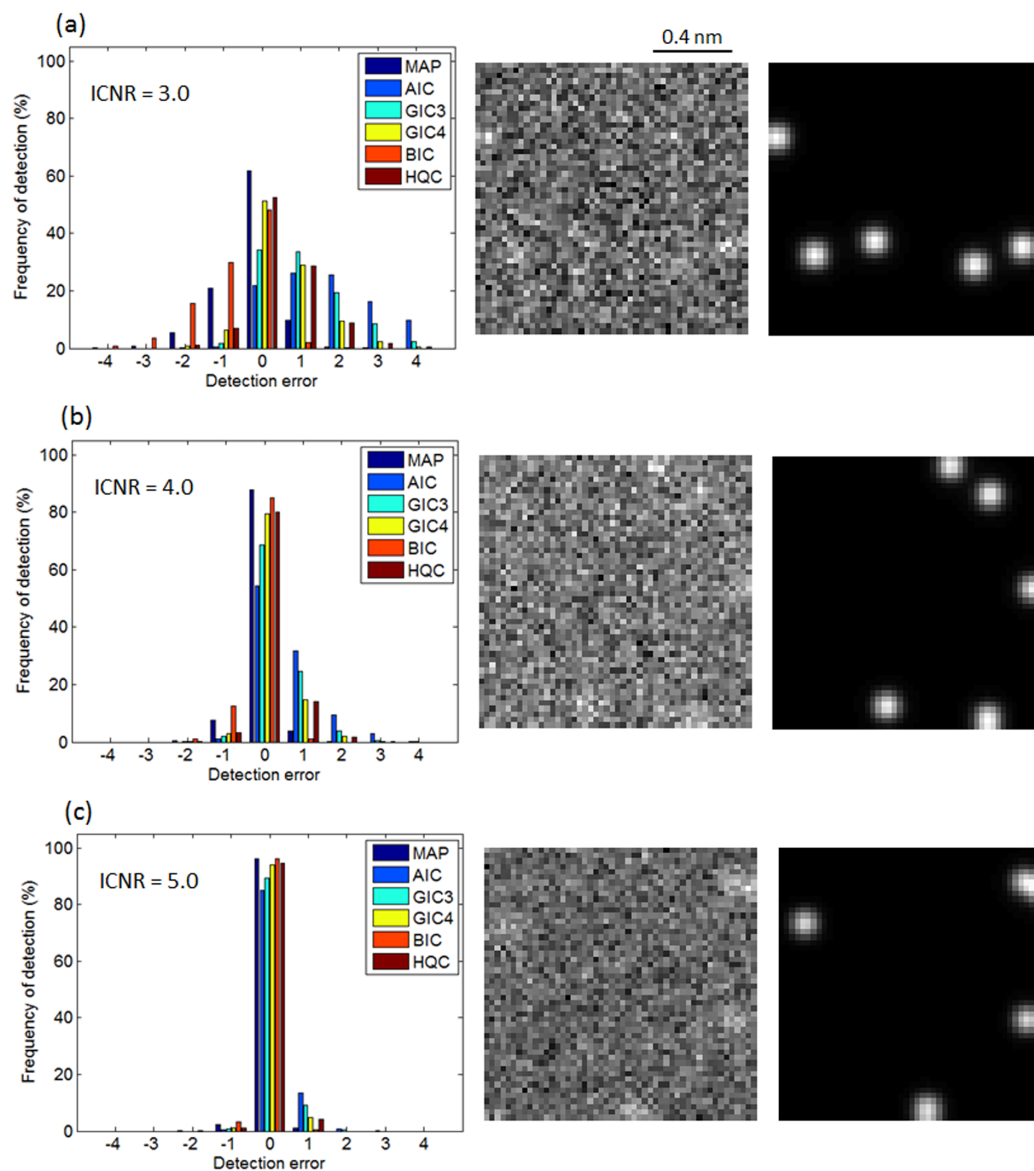


**Figure 5.4:** Average frequency of various selected orders for different model selection-criteria for detecting the number of Au atoms from a set of simulated HAADF STEM images of  $12.5 \text{ \AA}$  by  $12.5 \text{ \AA}$  with a pixel size of  $0.25 \text{ \AA}$  and with (a) an ICNR value of 3.0, (b) an ICNR value of 4.0, and (c) an ICNR value of 5.0. At the right-hand side, randomly generated simulated images of 5 atoms disturbed by Poisson noise with the noise-free images as references are shown for each ICNR value.

been simulated by MULTTEM with dimensions of  $12.5 \text{ \AA}$  by  $12.5 \text{ \AA}$  and a pixel size of  $0.25 \text{ \AA}$ . The remaining simulation parameters are listed in Table 5.1 in subsection 5.2.1. Hereby, the number of Au atoms in an individual image is uniformly distributed between 1 and 5 atoms. The atoms are randomly positioned within the field of view of the image according to a uniform distribution and the incoming electron dose of the image can uniformly fluctuate between  $5 \cdot 10^3 \text{ e}^-/\text{\AA}^2$  and  $10^5 \text{ e}^-/\text{\AA}^2$ , affecting the peak intensities of the atoms. Depending on the incoming electron dose, a constant background has been added to an individual image such that all 1000

simulated images have the same ICNR value. Hereby, each simulated image has been disturbed by Poisson noise. The performances of the model-selection criteria are evaluated by comparing the detected number of atoms in the image with the true number of atoms by calculating the average frequency of various selected orders [Stoica 2004b]. For the analysis, a superposition of Gaussian peaks with equal widths and equal intensities has been used to model the Au atoms in the image. Since the width  $\rho$  has been considered to be a fixed value, the parameters to be estimated are the background  $\zeta$ , height  $\eta$  and x- and y-coordinates  $\beta_{x_n}$  and  $\beta_{y_n}$ . For the MAP probability rule, the prior density  $p(\theta|N)$  was chosen as a product of uniform distributions where the background  $\zeta$  ranges from 0 up to the maximum pixel intensity in the simulated image and where the distributions for the height  $\eta$  and x- and y-coordinates  $\beta_{x_n}$  and  $\beta_{y_n}$  exactly correspond with the uniform distributions that were used to generate these parameters. The performances of the model-selection criteria are shown in Fig. 5.4 for three different ICNR values, defined by Eq. (5.3). A positive value of the detection error refers to the detection of too many atoms, whereas a negative value refers to the detection of too few atoms. Next to the graphs, randomly generated simulated images of 5 atoms disturbed by Poisson noise with the noise-free images as references are shown for each ICNR value. From Fig. 5.4(a), it can be seen that the MAP probability rule outperforms the other criteria for an ICNR value of 3.0. The AIC, GIC3, GIC4 and HQC have a tendency to detect too many atoms, whereas the BIC often detects too few atoms. This behaviour is related to the different ways the model-selection criteria penalize the complexity of the model. From subsection 5.2.2, showing that the detection rate increases when the ICNR of an image increases, it is expected that the frequency of detecting the correct number of atoms increases for increasing ICNR. This is confirmed in Fig. 5.4(b) and (c) for an ICNR value of 4.0 and 5.0, respectively. Moreover, in these cases, the performances of the different criteria tend to become more equal.

### 5.3.2 Relation between MAP and BIC

Previously, it has been explained that the MAP probability rule is related to the concept of model selection. In particular, it can be expected that the MAP probability rule has a close correspondence with the BIC as they both follow from Bayesian probability theory. The relation between the MAP probability rule and the BIC can be indicated starting from Eq. (5.13). The second term at the right-hand side of this expression can be written as

$$\begin{aligned} \log[\det(\nabla\nabla\chi^2)] &= \log[\det(W \cdot \frac{1}{W} \nabla\nabla\chi^2)] \\ &= M\log(W) + \log[\det(\frac{1}{W} \nabla\nabla\chi^2)], \end{aligned} \quad (5.14)$$

where use is made of the fact that  $\det(sA_M) = s^M \det(A_M)$  for a scalar  $s$  and  $M \times M$  matrix  $A_M$ . As such, Eq. (5.13) can be rewritten as

$$\begin{aligned} -2\log[p(N|\mathbf{w})] &= -2\log(\hat{L}) + M\log(W) + \log[\det(\frac{1}{W} \nabla\nabla\chi^2)] \\ &\quad - 2\log(N!) - M\log(4\pi) - 2\log[p(\theta|N)] + cst. \end{aligned} \quad (5.15)$$

Interestingly, the first two terms of Eq. (5.15) correspond to the BIC given in Eq. (5.12). This indicates a relation between the MAP probability rule and the BIC, which is not surprising as both

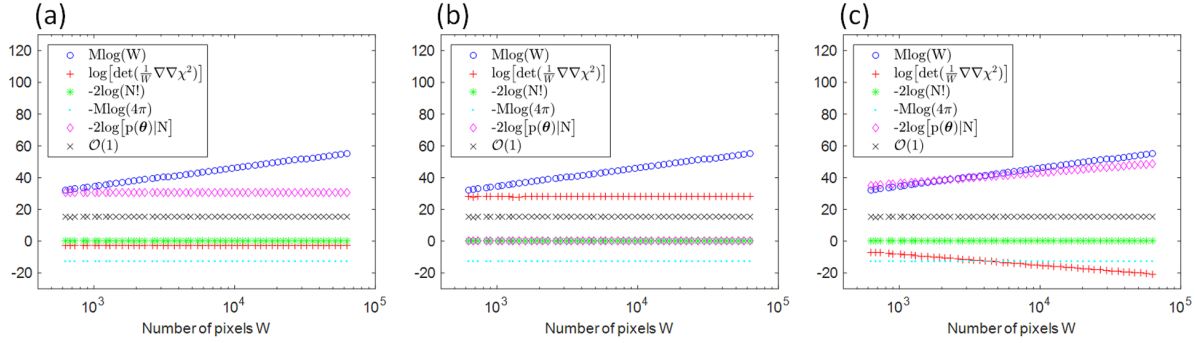


**Figure 5.5:** Behaviour of the individual terms of the MAP probability rule in function of the number of pixels  $W$  for a set of simulated ADF STEM images of  $12.5 \text{ \AA}$  by  $12.5 \text{ \AA}$  of a single Au atom with a pixel size ranging from  $0.5 \text{ \AA}$  until  $0.05 \text{ \AA}$  and an incoming electron dose of  $625 e^-/\text{pixel}$ . For clarity, the term  $-2\log(\hat{L})$  has not been visualised. Three different parameterisations of the model describing the STEM images have been used. In (a), the background  $\zeta$  and height  $\eta$  have been fitted in electron counts and the width  $\rho$  and  $x$ - and  $y$ -coordinate  $\beta_x$  and  $\beta_y$  in  $\text{\AA}$ , in (b), the parameters have been normalised between 0 and 1, and in (c),  $\zeta$  and  $\eta$  have been fitted in electron counts and  $\rho$ ,  $\beta_x$  and  $\beta_y$  in pixels.

techniques are based on a Bayesian approach. In order to understand this relation, the behaviour of the terms in Eq. (5.15) has been investigated as a function of the sample size by simulating a set of ADF STEM images of  $12.5 \text{ \AA}$  by  $12.5 \text{ \AA}$  of a single Au atom. The STEM simulations have been obtained from MULTEM and the simulation parameters are listed in Table 5.1 in subsection 5.2.1. In order to acquire a set of simulated images containing an increasing number of pixels  $W$ , the pixel size has been decreased starting from  $0.5 \text{ \AA}$  up to and including  $0.05 \text{ \AA}$ . As such, 50 images have been simulated where for each image 20 random Poisson noise configurations have been applied. Hereby, the incoming electron dose has been set to  $625 e^-/\text{pixel}$  to keep the amount of detected electrons per pixel constant, irrespective of the pixel size, so that the behaviour of the terms of the MAP probability rule is only dependent on the number of pixels  $W$ . Note that since the number of  $e^-/\text{pixel}$  is kept constant throughout the analysis this means that the electron dose/ $\text{\AA}^2$  increases when the image pixel size decreases. For the analysis of the MAP probability rule, a model where the atom is assumed to be Gaussian shaped has been used consisting of  $M = 5$  parameters: a constant background  $\zeta$ , width  $\rho$ , height  $\eta$  and  $x$ - and  $y$ -coordinate  $\beta_x$  and  $\beta_y$ . The prior density  $p(\theta|N)$  has been chosen to be a product of uniform distributions where the parameters  $\zeta$  and  $\eta$  range from 0 up to the maximum pixel intensity in the simulated image, whereas the parameters  $\rho$ ,  $\beta_x$  and  $\beta_y$  range according to the field of view of the image, i.e. from  $0 \text{ \AA}$  up to  $12.5 \text{ \AA}$ . The different terms contributing to the MAP probability rule given by Eq. (5.15) are shown in Fig. 5.5. The term  $-2\log(\hat{L})$  depends on  $W$  and increases with an increasing number of pixels, but, for clarity, it has not been visualised since it would dominate the graphs as it has values up to three orders of magnitude larger than the other terms. It can be seen from Fig. 5.5(a) that the term  $M\log(W)$  increases as the number of pixels  $W$  increases, as expected. The terms  $\log[\det(\frac{1}{W}\nabla\nabla\chi^2)]$ ,  $-2\log(N!)$ ,  $-M\log(4\pi)$  and  $-2\log[p(\theta|N)]$  remain constant as  $W$  increases. As such, also the sum of these terms remains constant for more pixels. This sum has been depicted as  $O(1)$  in Fig. 5.5, denoting a term that tends to a constant as  $W \rightarrow \infty$ . In this

way, Eq. (5.15) can be written for  $W \rightarrow \infty$  as

$$\begin{aligned} -2\log[p(N|\mathbf{w})] &= -2\log(\hat{L}) + M\log(W) + O(1) \\ &\approx -2\log(\hat{L}) + M\log(W) \end{aligned} \quad (5.16)$$

implying that the MAP probability rule is asymptotically equivalent with the BIC since  $-2\log(\hat{L})$  and  $M\log(W)$  are the dominant terms when  $W \rightarrow \infty$ . Interestingly, the behaviour of the Hessian matrix of  $\chi^2(\boldsymbol{\theta})$  evaluated at  $\hat{\boldsymbol{\theta}}$ ,  $\nabla\nabla\chi^2$ , and of the prior density,  $p(\boldsymbol{\theta}|N)$ , chosen as a product of uniform distributions for each parameter, is dependent on the parameterisation of the model. Fig. 5.5(a) results from fitting the parameters  $\zeta$  and  $\eta$  in pixel intensities, depicted in electron counts, and  $\rho, \beta_x$  and  $\beta_y$  in  $\text{\AA}$ . A different parameterisation of  $\boldsymbol{\theta}$  might be to use a normalised model where the parameters can fluctuate between 0 and 1. Fig. 5.5(b) shows the behaviour of the various terms of Eq. (5.15) of such a model. Here, the terms  $\log[\det(\frac{1}{W}\nabla\nabla\chi^2)]$  and  $-2\log[p(\boldsymbol{\theta}|N)]$  have been shifted as compared to Fig. 5.5(a). Yet, they show the same constant behaviour as a function of the number of pixels  $W$ . The behaviour of these terms does not necessarily remain constant as a function of  $W$  under all parameterisations of  $\boldsymbol{\theta}$  as shown in Fig. 5.5(c). Here, the parameters  $\zeta$  and  $\eta$  have been fitted in electron counts and  $\rho, \beta_x$  and  $\beta_y$  in pixels. From Fig. 5.5(c), it is apparent that both  $\log[\det(\frac{1}{W}\nabla\nabla\chi^2)]$  and  $-2\log[p(\boldsymbol{\theta}|N)]$  depend on the number of pixels  $W$ . Although  $\nabla\nabla\chi^2$  and  $p(\boldsymbol{\theta}|N)$  are not invariant under reparameterisation of  $\boldsymbol{\theta}$ , yet the term  $O(1)$ , which is the sum of  $\log[\det(\frac{1}{W}\nabla\nabla\chi^2)]$ ,  $-2\log(N!)$ ,  $-M\log(4\pi)$  and  $-2\log[p(\boldsymbol{\theta}|N)]$ , remains invariant under all presented parameterisations, as shown in Fig. 5.5. Therefore, the model complexity of Eq. (5.10) as described by the MAP probability rule remains unchanged under different parameterisations of the model. Moreover, as the goodness of fit is also independent of the model description, the MAP probability rule, given by the evaluation of the posterior probability  $p(N|\mathbf{w})$ , remains invariant under reparameterisation of  $\boldsymbol{\theta}$ . It is noted that in general the MAP estimate following from  $p(N|\mathbf{w})$  is not invariant.

### 5.3.3 Influence of prior density

Since the prior density  $p(\boldsymbol{\theta}|N)$  is part of how the MAP probability rule determines model complexity, as shown in Eq. (5.10), atom detection in ADF STEM images depends on the predefined parameter ranges when  $p(\boldsymbol{\theta}|N)$  is defined as a product of uniform distributions for each parameter individually, as given by Eq. (5.8). Ideally, the result of a robust detection method should not depend strongly on the prior. In this section, the influence of different a priori chosen parameter ranges to atom detection is investigated as a function of ICNR. For this, ADF STEM images of  $12.5 \text{ \AA}$  by  $12.5 \text{ \AA}$  with a pixel size of  $0.25 \text{ \AA}$  with different ICNR values have been simulated of an individual Au atom using MULTEM, where the atom is located in the middle of each simulated image, i.e.  $\beta_x = \beta_y = 6.25 \text{ \AA}$ . The remaining simulation parameters can be found in Table 5.1 in subsection 5.2.1. Each image has been generated 1000 times containing random Poisson noise and the ICNR of the atom in the image has been altered by adding a constant background while keeping the incoming electron dose fixed to  $10^4 \text{ e}^-/\text{\AA}^2$ . For detecting the Au atom from the noise disturbed images by the MAP probability rule, a model assuming the atom to be Gaussian shaped has been used, where a constant background  $\zeta$  and width  $\rho$ , height  $\eta$  and x- and y-coordinate  $\beta_x$  and  $\beta_y$ , of the atom need to be estimated. First, the parameters  $\zeta$  and  $\eta$  have been chosen to range from 0 up to the maximum pixel intensity in the simulated images, whereas

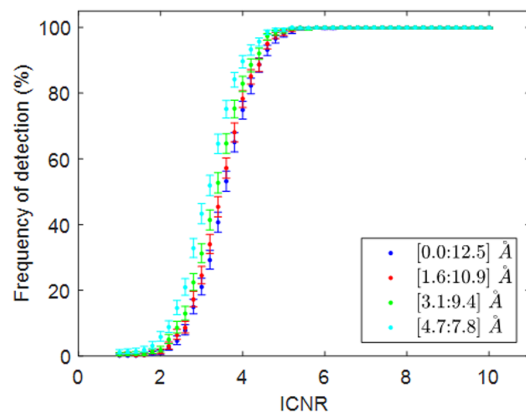


**Figure 5.6:** Detection rate of a Au atom from simulated ADF STEM images of  $12.5 \text{ \AA}$  by  $12.5 \text{ \AA}$  with a pixel size of  $0.25 \text{ \AA}$  and an incoming electron dose of  $10^4 \text{ e}^-/\text{\AA}^2$  as a function of ICNR for different predefined ranges of  $\beta_x$  and  $\beta_y$ .

the parameters  $\rho$ ,  $\beta_x$  and  $\beta_y$  range according to the field of view of the image, i.e. from  $0 \text{ \AA}$  up to  $12.5 \text{ \AA}$ . In order to investigate the effect of a different choice of the predefined parameter ranges, the ranges of  $\beta_x$  and  $\beta_y$  have been reduced, corresponding to taking into account more and more informative prior knowledge about the location of the Au atom. Fig. 5.6 shows that the detection rate as a function of ICNR is not influenced by different predefined ranges on  $\beta_x$  and  $\beta_y$  when the ICNR is high. For lower ICNR values, though, the detection rate of the Au atom increases for smaller predefined ranges on  $\beta_x$  and  $\beta_y$ . This shows that when more correct prior knowledge can be taken into account, it is beneficial to do so since it increases the chance of detecting atoms from low ICNR STEM images. As compared to the other model-selection criteria considered in this chapter, the MAP probability rule offers a more flexible way to detect atoms from ADF STEM images due to the fact that the prior can be tuned, resulting into a different value for the complexity of the model under consideration. Moreover, by using the MAP probability rule, it is clear what prior knowledge has been taken into account during the analysis, which is not always straightforward for other model-selection criteria.

## 5.4 Conclusions

In this chapter, it has been shown that the MAP probability rule can be effectively used as a tool to evaluate the relation between STEM image-quality measures and atom detectability. This has resulted into the introduction of the ICNR as a new image-quality measure that better correlates with atom detectability than conventional measures such as SNR and CNR. Atomic columns resulting from images with ICNR values of less than around 5.0 become challenging to accurately detect since typically the detection rate of 100 % drops rapidly starting from this value. In addition, the relation of the MAP probability rule with model selection has been thoroughly investigated. Hereby, it has been explicitly shown that the MAP probability is asymptotically equivalent with the BIC. Interestingly, the complexity term of the MAP probability rule depends on three dimensions of model complexity, namely the number of parameters, the functional form

of the model and the extension of the parameter space, as opposed to other model-selection criteria which typically depend on the number of parameters only. This extended complexity term allows the MAP probability rule to perform more accurately in detecting atoms from STEM images, especially from images exhibiting low ICNR values. Furthermore, the MAP probability rule allows for a clear and flexible incorporation of prior knowledge, which is often not the case for other model-selection methods.



# 6

## Atom column detection from ABF-ADF STEM images

### 6.1 Introduction

In STEM, a well-established imaging mode is that of ADF imaging, in which the collection range of the annular detector lies outside of the illumination cone of the focussed electron beam [Crewe 1970, Pennycook 1988]. The ADF STEM mode allows to obtain images with high resolution and easily interpretable image contrast, which is strongly dependent on the atomic number [Jesson 1995, Nellist 2000]. The visualisation of light-element atomic columns from ADF STEM images is challenging, though, since light elements only scatter electrons weakly to high detector angles leading to low intensities in ADF images. As a result, in combination with the strong dependence on atomic number, light elements are barely visible and especially difficult to detect in the presence of heavy elements [Varela 2005, Mkhoyan 2006, Fatermans 2018]. For certain materials, it is important to be able to directly visualise the light-element atomic columns, as their exact locations might influence the physical properties of the material. Direct visualisation of light elements has been enabled by the ABF mode in STEM where an annular detector spanning a range within the illumination cone of the electron beam is used [Okunishi 2009, Findlay 2009]. Due to the fact that ABF image contrast is less dependent on atomic number than ADF contrast [Findlay 2010, Brydson 2011], light elements can be visualised better in the presence of heavy elements. This reduced dependence on atomic number, though, makes differentiating between atomic columns with close atomic numbers more difficult. In addition, due to coherent scattering, there is a non-monotonic intensity relationship with atomic number at all thicknesses. As a result, identifying the atom types of columns in an ABF image is not straightforward. Therefore, a simultaneous acquisition of both ABF and ADF STEM images, by using ABF and ADF detectors operating at the same time, is an interesting option to visualise atoms of a large range of atomic numbers for studying and interpreting materials at the atomic scale consisting of both light and heavy atoms.

Merely visually interpreting acquired high-resolution STEM images is insufficient to obtain precise structure information, which is crucial to fully understand the structure-properties relation of nanomaterials since their physical and chemical properties are strongly dependent on their exact structural and chemical composition. As such, a quantitative approach is required which is provided by statistical parameter estimation theory [den Dekker 2005, Van Aert 2005, van den Bos 2007, Van Aert 2012b, den Dekker 2013, De Backer 2016], which has been described in chapter 3. Extracting reliable structure information requires knowledge about the number of atomic columns in the image. For beam-sensitive nanostructures, though, the incoming electron dose needs to be limited in order to avoid beam damage. Therefore, images of such materials typically exhibit low SNR and low contrast, and hence low CNR. As a result, a visual determination of the number of columns in such images is unreliable and may lead to biased structure information. To overcome this problem, statistical parameter estimation has been combined with model-order selection, leading to the MAP probability rule [Fatermans 2018, Fatermans 2019], in order to determine the structure of unknown nanomaterials in an automatic and objective manner and to detect atomic columns and even single atoms from high-resolution STEM images with high reliability. This technique has been introduced and described in chapter 4 for analysing ADF STEM images.

Although, the ABF imaging mode allows for better visualisation of light elements as compared to ADF imaging, it is, in general, not straightforward to visually detect light-element atomic columns. Light-element nanomaterials are typically sensitive to the electron beam, limiting the incoming electron dose and leading to images exhibiting low CNR [Findlay 2014]. The MAP probability rule, introduced for ADF STEM images, can be extended to determine the number of atomic columns for which there is most evidence in the simultaneously acquired ABF and ADF image data. In atomic-resolution STEM images, the projected atomic columns are typically modelled as Gaussian peaks superimposed on a constant background [Van Dyck 2002, Nellist 2007, De Backer 2016]. This methodology has been applied predominantly in the analysis of ADF STEM images [Van Aert 2009b, Van Aert 2011, Bals 2011, Bals 2012, Van Aert 2013, Martinez 2014b, Kundu 2014, Akamine 2015, van den Bos 2016, Gonnissen 2016a, De Backer 2017], but has also been used for obtaining quantitative information from ABF STEM images [Gauquelin 2017]. In order to quantify simultaneously acquired ABF and ADF STEM images, an extension of the commonly used parametric models in STEM is required. Hereby, it is important to take the effect of specimen tilt into account, since small tilts from the crystal zone axis affect especially ABF STEM intensities [Zhou 2016, Brown 2017, Gao 2018]. The proposed methodology not only improves the probability of detecting an atom by the MAP probability rule from simulated ABF and ADF image data, it also improves the accuracy and precision of locating this atom as compared to analysing the ABF and ADF images separately.

This chapter is organised as follows<sup>4</sup>. In section 6.2, the current commonly used parametric models to describe STEM images are extended in order to quantitatively analyse ABF and ADF STEM images simultaneously. Using these models, analytical expressions for the MAP probability rule are derived in section 6.3. In section 6.4, the advantages of analysing ABF and ADF STEM images simultaneously as compared to a separate analysis are highlighted. This

---

<sup>4</sup>The results in this chapter are being prepared for publication in J. Fatermans, A.J. den Dekker, N. Gauquelin, K. Müller-Caspary, and S. Van Aert, *Atom column detection from simultaneously acquired ABF and ADF STEM images*, Ultramicroscopy.

includes the effect on atom detectability in section 6.4.1 and atom position accuracy and precision in section 6.4.2. Then, in section 6.5, the proposed methodology is applied to simultaneously acquired experimental ABF and ADF STEM images of SrTiO<sub>3</sub> in section 6.5.1 and LiMn<sub>2</sub>O<sub>4</sub> in section 6.5.2. Finally, in section 6.6, conclusions are drawn.

## 6.2 Model-based parameter estimation

In statistical parameter estimation theory, which has been thoroughly discussed in chapter 3, STEM images are considered as data planes from which unknown structure parameters need to be estimated. The starting point of this procedure is the construction of a parametric model that describes the expectations of the image pixel values or observations as a function of unknown parameters. Then, quantitative structure information is obtained by fitting the model to the observed experimental data with respect to the unknown parameters using a criterion of goodness of fit. For atomic-resolution STEM images, the projected atomic columns can be described as a superposition of Gaussian peaks [De Backer 2016], as discussed in chapter 3. Examples of expectation models  $f_{kl}(\theta)$  describing the expectation of the observed pixel value  $w_{kl}$  at position  $(x_k, y_l)$  have been stated in Eq. (3.4) for a model where a different width is assumed for each estimated Gaussian peak, and in Eq. (3.6) assuming equal widths, respectively.

For analysing materials containing both light and heavy atoms, an interesting option is to acquire ABF and ADF STEM images simultaneously. Hereby, two annular detectors are used. One collects the electrons scattered toward high scattering angles, whereas the other is placed within the illumination cone of the electron probe. This technique combines the improved light-element visualisation of ABF STEM with the easily interpretable image contrast of ADF STEM. In addition, due to the simultaneous acquisition, a pixel at location  $(x_k, y_l)$  possesses both an ABF and ADF intensity. In order to obtain quantitative measurements from the ABF and ADF image data, statistical parameter estimation theory may be applied using a parametric model such as, for example, the one given in Eq. (3.4), as well as other similar models [De Backer 2016]. Although this methodology has been predominantly applied to quantify ADF STEM images, it can be used to describe both ABF and ADF image data. For ADF STEM images, the atomic columns are fitted by Gaussian peaks with a positive height  $\eta$  as columns in ADF STEM are depicted as bright spots on a dark background. Atomic columns in ABF STEM, though, are depicted as dark spots on a bright background. As a result, they are fitted by Gaussian peaks with a negative height  $\eta$ . Nevertheless, models such as the one given by Eq. (3.4) are not optimal for quantifying simultaneously acquired ABF and ADF STEM images since the correlation between the images is neglected. To overcome this problem, the currently used models for quantifying STEM images need to be extended to fit both the ABF and ADF images simultaneously. This can be done by assuming that the Gaussian peaks describing a particular atomic column, one with negative height for the ABF image and one with positive height for the ADF image, are located at the same position, corresponding to the actual position of the projected atomic column. When the observed STEM pixel values of the ABF and ADF image are depicted as  $w^{ABF}$  and  $w^{ADF}$ , respectively, and under the assumption that each estimated Gaussian peak has a different width, the expectation model  $f_{kl}(\theta)$ , describing simultaneously acquired ABF and ADF STEM images, gives the expectation of the observed pixel values  $w_{kl} = (w_{kl}^{ABF}, w_{kl}^{ADF})$  at position  $(x_k, y_l)$ :

$$\begin{aligned}
f_{kl}(\boldsymbol{\theta}) &= (f_{kl}^{ABF}, f_{kl}^{ADF}) \\
&= \left( \zeta^{ABF} + \sum_{n=1}^N \eta_n^{ABF} \exp\left(-\frac{(x_k - \beta_{x_n})^2 + (y_l - \beta_{y_n})^2}{2(\rho_n^{ABF})^2}\right), \right. \\
&\quad \left. \zeta^{ADF} + \sum_{n=1}^N \eta_n^{ADF} \exp\left(-\frac{(x_k - \beta_{x_n})^2 + (y_l - \beta_{y_n})^2}{2(\rho_n^{ADF})^2}\right) \right)
\end{aligned} \tag{6.1}$$

where  $f_{kl}^{ABF}$  and  $f_{kl}^{ADF}$  denote the expectation models describing the ABF and ADF image, respectively. The parameters  $\zeta^{ABF}$  and  $\zeta^{ADF}$  describe the constant background and  $\rho_n^{ABF}$ ,  $\rho_n^{ADF}$ ,  $\eta_n^{ABF}$ ,  $\eta_n^{ADF}$  depict the widths and heights of the  $n$ th atomic column described by two Gaussian peaks, respectively, in both the ABF and ADF images. For the model given by Eq. (6.1), the unknown parameters are represented by the parameter vector:

$$\begin{aligned}
\boldsymbol{\theta} &= (\beta_{x_1}, \dots, \beta_{x_N}, \beta_{y_1}, \dots, \beta_{y_N}, \rho_1^{ABF}, \dots, \rho_N^{ABF}, \rho_1^{ADF}, \dots, \rho_N^{ADF}, \\
&\quad \eta_1^{ABF}, \dots, \eta_N^{ABF}, \eta_1^{ADF}, \dots, \eta_N^{ADF}, \zeta^{ABF}, \zeta^{ADF})^T.
\end{aligned} \tag{6.2}$$

However, it is well known that the observed atomic column positions in ABF STEM images are sensitive to specimen tilt [Zhou 2016, Brown 2017, Gao 2018]. This causes a deviation of the observed positions from the actual positions of the projected atomic columns. The observed locations of the atomic columns in ADF STEM images, though, are less sensitive to specimen tilt and can be considered to be reliable indicators of the true column positions even in the presence of some tilt [Maccagnano-Zacher 2008, Findlay 2010, So 2012]. Thus, due to the effect of specimen tilt, the observed column positions in ABF STEM can be shifted as compared to the observed positions in ADF STEM. Since small tilts of the electron beam with respect to the crystal zone axis can easily be present in STEM experiments, it is important to take into account the effect of the shifted observed column positions in ABF images in statistical parameter estimation theory in order to obtain accurate quantitative measurements. For this purpose, the expectation model proposed in Eq. (6.1) can be altered by allowing the ABF peak locations to

Parameter	Symbol	Value
Acceleration voltage	$V_0$ (kV)	300
Defocus	$\epsilon$ (Å)	0
Spherical aberration	$C_s$ (mm)	0.001
Spherical aberration of 5th order	$C_5$ (mm)	0
Semiconvergence angle	$\alpha$ (mrad)	22.9
ABF detector inner radius	$\beta_1^{ABF}$ (mrad)	12
ABF detector outer radius	$\beta_2^{ABF}$ (mrad)	22
ADF detector inner radius	$\beta_1^{ADF}$ (mrad)	88
ADF detector outer radius	$\beta_2^{ADF}$ (mrad)	98
Pixel size	$\Delta x = \Delta y$ (Å)	0.23
Number of scanned pixels	$K \times L$	$27 \times 27$
FWHM of the source image	FWHM (Å)	0.7

**Table 6.1:** Microscope parameter values for simulation of an ABF and ADF STEM image of a 10 nm thick SrTiO<sub>3</sub> unit cell using MULTEM including 5 mrad specimen tilt.

deviate from the ADF peak locations along the tilting direction:

$$\begin{aligned} f_{kl}(\boldsymbol{\theta}) &= (f_{kl}^{ABF}, f_{kl}^{ADF}) \\ &= \left( \zeta^{ABF} + \sum_{n=1}^N \eta_n^{ABF} \exp\left(-\frac{(x_k - \gamma_{x_n})^2 + (y_l - \gamma_{y_n})^2}{2(\rho_n^{ABF})^2}\right), \right. \\ &\quad \left. \zeta^{ADF} + \sum_{n=1}^N \eta_n^{ADF} \exp\left(-\frac{(x_k - \beta_{x_n})^2 + (y_l - \beta_{y_n})^2}{2(\rho_n^{ADF})^2}\right) \right) \end{aligned} \quad (6.3)$$

with

$$(\gamma_{x_n}, \gamma_{y_n}) = (\beta_{x_n} + \alpha_n \cos\phi, \beta_{y_n} + \alpha_n \sin\phi) \quad (6.4)$$

where  $\phi$  and  $\alpha_n$  indicate the direction and amplitude of the shift of the  $n$ th Gaussian peak in the ABF image with respect to the corresponding peak in the ADF image, respectively. The amplitude of the shift is not necessarily equal for all atomic columns in the image, but depends on atom type and orientation [Zhou 2016, Brown 2017, Gao 2018]. This is due to the coherent image formation process in ABF STEM. In Eqs. (6.3) and (6.4), a general approach has been followed where no prior knowledge about the atom types and orientations are considered. Note that the shift of the ABF peaks only occurs along the tilting direction, as no atom position shift is observed in a direction perpendicular to this direction [Zhou 2016]. For the model given by Eq. (6.3) the parameter vector containing the unknown parameters is given by

$$\boldsymbol{\theta} = (\beta_{x_1}, \dots, \beta_{x_N}, \beta_{y_1}, \dots, \beta_{y_N}, \rho_1^{ABF}, \dots, \rho_N^{ABF}, \rho_1^{ADF}, \dots, \rho_N^{ADF}, \eta_1^{ABF}, \dots, \eta_N^{ABF}, \eta_1^{ADF}, \dots, \eta_N^{ADF}, \alpha_1, \dots, \alpha_N, \phi, \zeta^{ABF}, \zeta^{ADF})^T. \quad (6.5)$$

In order to verify whether the proposed parametric model in Eq. (6.3) is a valid model to describe images in the presence of tilt, a simulation of a SrTiO<sub>3</sub> unit cell with a thickness of 10 nm has been performed using MULTTEM [Lobato 2015, Lobato 2016] with a specimen tilt of 5 mrad. The parameters of this simulation are included in Table 6.1. The simulated ADF and ABF STEM images are shown in Figs. 6.1(a) and (b), respectively. First, these images

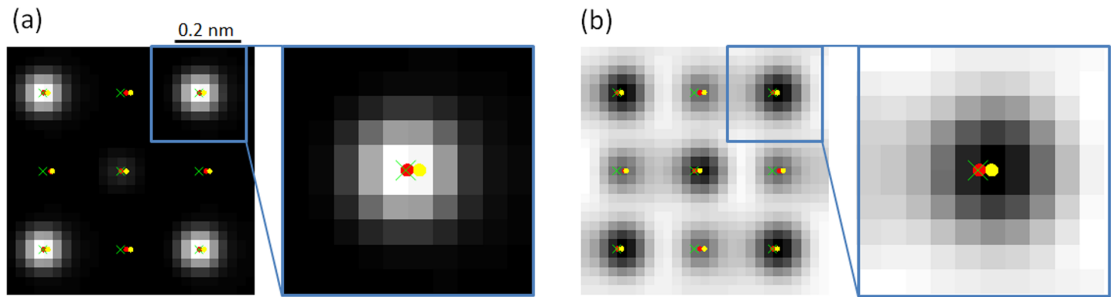


**Figure 6.1:** (a) Simulated ADF and (b) ABF STEM image of a 10 nm thick SrTiO<sub>3</sub> unit cell with a tilt angle of 5 mrad where the highlighted areas have been enlarged in the insets. The green crosses depict the true atomic column positions. The estimated atomic column positions obtained by performing model fitting including specimen tilt are shown by red dots, whereas for neglecting specimen tilt the estimated column positions are depicted by yellow dots.

have been analysed using the parametric model including the effect of specimen tilt given by Eq. (6.3), where equal widths for the Gaussian peaks in the ABF image,  $\rho^{ABF}$ , and ADF image,  $\rho^{ADF}$ , have been used. The estimated column positions that follow from this approach are shown in Figs. 6.1(a) and (b) by red dots. From Figs. 6.1(a) and (b), it can be seen that there is a close correspondence between the estimated column positions and the true column positions, shown by green crosses, which have been determined by the atom positions of the top plane of the tilted specimen. In case the analysis is, instead, performed using a parametric model neglecting the effect of specimen tilt, such as the one given by Eq. (6.1), the estimated column positions deviate further from the true positions. This is shown in Figs. 6.1(a) and (b) where the estimated column positions using a model without taking specimen tilt into account are shown by yellow dots. Quantitatively, the average deviation of the 9 estimated atomic column positions in the simulated image from their true column positions including the effect of specimen tilt is  $8 \pm 3$  pm, whereas for neglecting tilt this is  $18 \pm 3$  pm. This indicates that the estimated atomic column locations, obtained from analysing simultaneously acquired ABF and ADF STEM image data by the parametric model proposed in Eq. (6.3) including the effect of specimen tilt, correspond better with the true atomic column locations than for analysing the image data by a model neglecting the effect of specimen tilt.

### 6.3 Maximum a posteriori probability

In order to extract reliable structure information from simultaneously acquired ABF and ADF STEM images using a model neglecting specimen tilt, such as in Eq. (6.1), or including tilt, such as in Eq. (6.3), knowledge about the number of atomic columns  $N$  present in the images is required. For beam-stable materials this number can be determined visually due to the high incoming electron dose, typically of the order of more than  $10^6 - 10^8 \text{ e}^-/\text{\AA}^2$ , that can be used to image these materials. Beam-sensitive nanostructures, such as specimens containing light elements, though, do not withstand a high incoming electron dose and, consequently, the dose should be limited in order to avoid beam damage resulting into images exhibiting low CNR. Since a simultaneous acquisition of ABF and ADF STEM images is, in particular, interesting for characterising materials containing light elements, which are typically beam sensitive, a visual inspection of such images may lead to biased results. To overcome this problem, the number of atomic columns  $N$  can be reliably quantified by the MAP probability rule, introduced in chapter 4 for detecting atomic columns from ADF STEM images, which is a combination of statistical parameter estimation and model-order selection [Fatermans 2018, Fatermans 2019], derived from Bayes' theorem [Sivia 2006]:

$$p(N|\mathbf{w}) = \frac{p(\mathbf{w}|N)p(N)}{p(\mathbf{w})} \quad (6.6)$$

where  $p(N|\mathbf{w})$  denotes the posterior probability of the presence of  $N$  atomic columns given the observed image pixel values  $\mathbf{w}$ . For a simultaneous acquisition of ABF and ADF images,  $\mathbf{w}$  can be considered as the ensemble of the observed image pixel values of both images,  $\{\mathbf{w}^{ABF}, \mathbf{w}^{ADF}\}$ . The MAP probability rule aims to select the number of columns  $N$  that maximizes  $p(N|\mathbf{w})$ . The term  $p(\mathbf{w}|N)$  reflects the evidence that the image data  $\mathbf{w}$  is generated by  $N$  atomic columns. The probability  $p(N)$  expresses prior knowledge of the number of atomic columns present in the

image data. Assuming that there is no a priori preference for any number of columns,  $p(N)$  can be described as a uniform distribution. The term in the denominator of Eq. (6.6) is merely a normalisation constant, which is independent of the number of columns  $N$ , and, therefore, cancels out when comparing posterior probabilities as a function of  $N$ .

In chapter 4, it has been shown that Eq. (6.6) can be reduced to

$$p(N|\mathbf{w}) \propto \int p(\mathbf{w}|\boldsymbol{\theta}, N) p(\boldsymbol{\theta}|N) d^M \boldsymbol{\theta}, \quad (6.7)$$

where the first term in the integral,  $p(\mathbf{w}|\boldsymbol{\theta}, N)$ , is the likelihood function which describes the probability of the observed image pixel values  $\mathbf{w}$  for particular values of the parameters  $\boldsymbol{\theta}$  of a model with  $N$  atomic columns. In essence, the likelihood function is a measure of the goodness of fit of the model with the experimental measurements or image pixel values. For simultaneously acquired ABF and ADF STEM image data, the likelihood function can be expressed in a similar way as described in chapter 4:

$$p(\mathbf{w}|\boldsymbol{\theta}, N) = \frac{e^{-\chi^2(\boldsymbol{\theta})/2}}{\prod_{k=1}^K \prod_{l=1}^L 2\pi \sqrt{w_{kl}^{ABF} w_{kl}^{ADF}}}, \quad (6.8)$$

where

$$\chi^2(\boldsymbol{\theta}) = \sum_{k=1}^K \sum_{l=1}^L \left[ \frac{[w_{kl}^{ABF} - f_{kl}^{ABF}]^2}{w_{kl}^{ABF}} + \frac{[w_{kl}^{ADF} - f_{kl}^{ADF}]^2}{w_{kl}^{ADF}} \right] \quad (6.9)$$

is a weighted sum-of-squared residuals misfit between the data and the parametric model. This expression follows from the fact that the noise can be considered to be uncorrelated in simultaneously acquired STEM images with different detector geometries [Rose 1974, Hammel 1995, Brown 2016]. The other term in the integral in Eq. (6.7),  $p(\boldsymbol{\theta}|N)$ , is the prior density of the parameters  $\boldsymbol{\theta}$  for a model with  $N$  columns. Different expressions for the prior density function can be constructed reflecting different types of prior knowledge. Here, similarly as in chapter 4,  $p(\boldsymbol{\theta}|N)$  is expressed as a product of uniform distributions over a predefined range for each parameter  $\theta_m$ :

$$p(\boldsymbol{\theta}|N) = \begin{cases} \prod_{m=1}^M \frac{1}{\theta_{m_{max}} - \theta_{m_{min}}} & \text{for } m = 1, \dots, M: \theta_{m_{min}} \leq \theta_m \leq \theta_{m_{max}} \\ 0 & \text{otherwise} \end{cases} \quad (6.10)$$

where the subscripts *max* and *min* refer to a predefined maximum and minimum value for each parameter, respectively. As described in chapter 4, approximate analytical expressions for  $p(N|\mathbf{w})$  can be derived for several parametric models to determine the number of atomic columns for which there is most evidence in ADF image data [Fatermans 2019]. From Eqs. (6.7), (6.8) and (6.10), following the same methodology,  $p(N|\mathbf{w})$  for simultaneously acquired ABF and ADF STEM images using the model given by Eq. (6.1), neglecting the effect of specimen tilt, results into

$$p(N|\mathbf{w}) \propto \frac{N!}{[(\beta_{x_{max}} - \beta_{x_{min}})(\beta_{y_{max}} - \beta_{y_{min}})(\rho_{max}^{ABF} - \rho_{min}^{ABF})]^N} \times \frac{e^{-\chi_{min}^2/2} (4\pi)^{3N} [\det(\nabla \nabla \chi^2)]^{-1/2}}{[(\rho_{max}^{ADF} - \rho_{min}^{ADF})(\eta_{max}^{ABF} - \eta_{min}^{ABF})(\eta_{max}^{ADF} - \eta_{min}^{ADF})]^N}, \quad (6.11)$$

where  $\chi_{min}^2 = \chi^2(\hat{\theta})$ , with  $\hat{\theta}$  the parameter vector that minimizes  $\chi^2(\theta)$  given by Eq. (6.9) and where the term  $\det(\nabla\nabla\chi^2) = \det\left(\frac{\partial^2\chi^2(\theta)}{\partial\theta\partial\theta^T}\bigg|_{\theta=\hat{\theta}}\right)$  represents the determinant of the Hessian matrix of  $\chi^2(\theta)$  evaluated at  $\hat{\theta}$ . For the model given by Eq. (6.3), including the effect of tilt, the posterior probability becomes

$$p(N|\mathbf{w}) \propto \frac{N!(\alpha_{max} - \alpha_{min})^{-N}}{[(\beta_{x_{max}} - \beta_{x_{min}})(\beta_{y_{max}} - \beta_{y_{min}})(\rho_{max}^{ABF} - \rho_{min}^{ABF})]^N} \quad (6.12)$$

$$\times \frac{e^{-\chi_{min}^2/2}(4\pi)^{3.5N}[\det(\nabla\nabla\chi^2)]^{-1/2}}{[(\rho_{max}^{ADF} - \rho_{min}^{ADF})(\eta_{max}^{ABF} - \eta_{min}^{ABF})(\eta_{max}^{ADF} - \eta_{min}^{ADF})]^N}.$$

By using Eqs. (6.11) or (6.12), depending on the underlying parametric model, the MAP probability rule allows to select the most probable number of atomic columns present in simultaneously acquired ABF and ADF STEM images, and hence the most probable atomic structure, by evaluating  $p(N|\mathbf{w})$  as a function of  $N$ . It should be noted that the MAP probability rule is not limited to the models given by Eqs. (6.1) and (6.3). Similar expressions as Eqs. (6.11) and (6.12) can be derived for other types of models as well.

## 6.4 Advantages of simultaneous model fitting

In this section, the quantitative information that can be obtained by simultaneously fitting the ABF and ADF STEM image data, as introduced in the previous section, is compared with the quantitative information that is attainable by combining the measurements of the parameters from two separate models describing the ABF and ADF images independently of each other. More specifically, the probability of detecting an atom as well as the accuracy and precision of locating this atom from Poisson noise disturbed simulated ABF and ADF STEM images is investigated in section 6.4.1 and section 6.4.2, respectively.

### 6.4.1 Atom detectability

In chapter 5, an alternative ADF STEM image quality measure, ICNR, has been introduced correlating better with atom detectability than conventional measures such as SNR and CNR [Fatermans 2019]. This measure is defined for an individual atomic column as follows

$$ICNR = \frac{2\pi\eta^{ADF}(\rho^{ADF})^2}{[2\pi\eta^{ADF}(\rho^{ADF})^2 + \pi(3\rho^{ADF})^2\zeta^{ADF}]^{1/2}}, \quad (6.13)$$

where  $\eta^{ADF}$ ,  $\rho^{ADF}$ , and  $\zeta^{ADF}$  denote the estimated height and width of the column, and the background in the ADF image, respectively. A similar expression for ICNR can also be defined for ABF STEM images:

$$ICNR = \frac{2\pi|\eta^{ABF}|(\rho^{ABF})^2}{[2\pi|\eta^{ABF}|(\rho^{ABF})^2 + \pi(3\rho^{ABF})^2(\zeta^{ABF} + \eta^{ABF})]^{1/2}}, \quad (6.14)$$

where, similarly as for Eq. (6.13),  $\eta^{ABF}$ ,  $\rho^{ABF}$ , and  $\zeta^{ABF}$  denote the estimated height and width of the column, and the background in the ABF image, respectively. Note that  $\eta^{ABF}$  in Eq. (6.14)

has a negative value, because columns in ABF images are displayed as dark spots on a bright background. Although, at first sight, Eqs. (6.13) and (6.14) calculate the ICNR in a different way, they, in fact, represent the same formula. This can be better understood by considering the maximum pixel values,  $w_{max}^{ADF}$  and  $w_{max}^{ABF}$ , and minimum pixel values,  $w_{min}^{ADF}$  and  $w_{min}^{ABF}$ , of an ADF and ABF image, respectively, in the area around the column. As such, the following expressions hold:

$$\begin{aligned} w_{max}^{ADF} - w_{min}^{ADF} &\approx \eta^{ADF} \\ w_{max}^{ABF} - w_{min}^{ABF} &\approx |\eta^{ABF}| \\ w_{min}^{ADF} &\approx \zeta^{ADF} \\ w_{min}^{ABF} &\approx \zeta^{ABF} + \eta^{ABF}. \end{aligned} \quad (6.15)$$

From Eq. (6.15), Eqs. (6.13) and (6.14) can be rewritten in one expression as

$$ICNR \approx \frac{2\pi(w_{max} - w_{min})\rho^2}{[2\pi(w_{max} - w_{min})\rho^2 + \pi(3\rho)^2 w_{min}]^{1/2}}, \quad (6.16)$$

where  $w_{max}$  represents either  $w_{max}^{ADF}$  or  $w_{max}^{ABF}$ ,  $w_{min}$  either  $w_{min}^{ADF}$  or  $w_{min}^{ABF}$ , and  $\rho$  either  $\rho^{ADF}$  or  $\rho^{ABF}$  depending on what type of image is being analysed.

For investigating atom detectability, an ABF and ADF image of an individual Si atom, deposited on a 5 nm thick amorphous C support, have been simulated using MULTEM. The amorphous C support has been obtained by placing C atoms on random positions within the volume of the layer, reaching a density of  $2.2 \text{ g} \times \text{cm}^{-3}$  [Ricolleau 2013]. During this procedure a new C atom is only included if its distance with the other atoms is above a chosen minimal distance of 0.14 nm, which is slightly lower than the C-C bond length in graphene. The parameters of this simulation are listed in Table 6.2. A varying incoming electron dose has been applied to the simulated images in order to obtain a set of images containing different ICNR values, where a higher electron dose results into a higher ICNR value and a lower dose into a lower ICNR value. It is noted that in this procedure the simulated ABF and ADF STEM data are not necessarily subject to the same incoming electron dose. In this way, a great variety of ICNR values for the ABF and ADF images can be obtained. The ICNR of the ADF STEM images has

Parameter	Symbol	Value
Acceleration voltage	$V_0$ (kV)	120
Defocus	$\epsilon$ (Å)	0
Spherical aberration	$C_s$ (mm)	0.001
Spherical aberration of 5th order	$C_5$ (mm)	0
Semiconvergence angle	$\alpha$ (mrad)	21.0
ABF detector inner radius	$\beta_1^{ABF}$ (mrad)	10
ABF detector outer radius	$\beta_2^{ABF}$ (mrad)	20
ADF detector inner radius	$\beta_1^{ADF}$ (mrad)	25
ADF detector outer radius	$\beta_2^{ADF}$ (mrad)	100
Pixel size	$\Delta x = \Delta y$ (Å)	0.25
Number of scanned pixels	$K \times L$	$50 \times 50$
FWHM of the source image	FWHM (Å)	0.7

**Table 6.2:** Microscope parameter values for simulation of an ABF and ADF STEM image of an individual Si atom on a 5 nm thick C support using MULTEM.

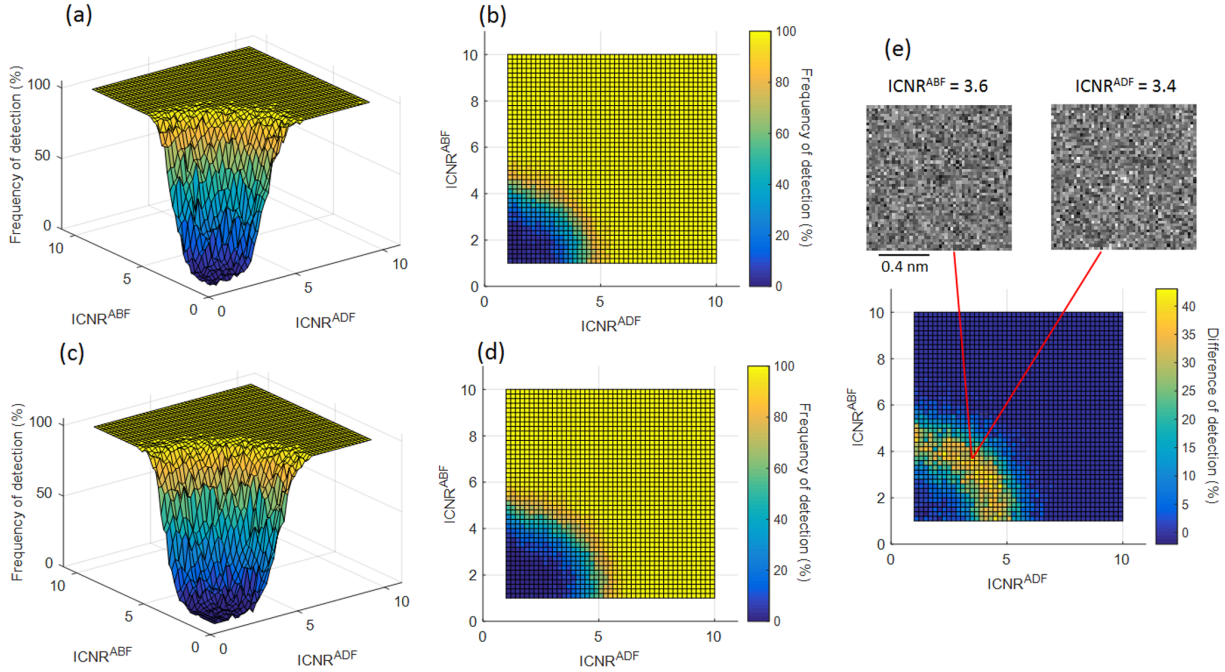


**Figure 6.2:** (a) Observed detection rate of a Si atom by the MAP probability rule from Poisson noise disturbed simulated ADF and ABF STEM images as a function of  $ICNR^{ADF}$  and  $ICNR^{ABF}$  by simultaneous model fitting. (b) Top view of (a). (c) Observed detection rate by separate model fitting. (d) Top view of (c). (e) Difference of detection between (b) and (d), where the inset shows the Poisson noise disturbed ABF and ADF images for which the largest difference between (b) and (d) is attained.

been calculated using Eq. (6.13), whereas Eq. (6.14) has been used for the ABF STEM images. Each image obtained in this manner has been generated 100 times containing random Poisson noise. Figs. 6.2(a) and (b) show the observed detection rate of the Si atom, i.e. the number of times the atom can be successfully detected from the noise disturbed simulated images by simultaneously analysing the ABF and ADF STEM image data. The detection rate is displayed as a function of the ICNR of the ADF and ABF images, depicted as  $ICNR^{ADF}$  and  $ICNR^{ABF}$ , respectively, and is calculated by the MAP probability rule given by Eq. (6.11) evaluated for  $N = 0$  and  $N = 1$  atomic columns using a parametric model assuming the images of the atom to be Gaussian shaped, where the backgrounds  $\zeta^{ADF}$  and  $\zeta^{ABF}$ , and widths  $\rho^{ADF}$  and  $\rho^{ABF}$ , heights  $\eta^{ADF}$  and  $\eta^{ABF}$  and x- and y-coordinate  $\beta_x$  and  $\beta_y$  of the atom need to be estimated. It is clear from Figs. 6.2(a) and (b) that the detection rate decreases with decreasing ICNR values. Moreover, the circular symmetry indicates that atom detectability is independent of the exact  $ICNR^{ADF}$  and  $ICNR^{ABF}$  values as long as the square root of their quadratic sum remains unchanged. As a result, an alternative ICNR expression, directly correlating with atom detectability, can be proposed for determining the combined quality of atomic columns in ABF and ADF STEM images:

$$ICNR = \sqrt{(ICNR^{ADF})^2 + (ICNR^{ABF})^2}. \quad (6.17)$$

Figs. 6.2(c) and (d) show the observed detection rate of the Si atom from the noise disturbed images by analysing the ABF and ADF image data without taking into account that both images depict the same atom. Hereby, a model is used, such as the one given by Eq. (6.1), where  $\zeta^{ADF}$ ,

$\zeta^{ABF}$ ,  $\rho^{ADF}$ ,  $\rho^{ABF}$ ,  $\eta^{ADF}$ ,  $\eta^{ABF}$ ,  $\beta_x^{ADF}$ ,  $\beta_y^{ADF}$ ,  $\beta_x^{ABF}$  and  $\beta_y^{ABF}$  need to be estimated, where  $\beta_x^{ADF}$  and  $\beta_y^{ADF}$ , and  $\beta_x^{ABF}$  and  $\beta_y^{ABF}$  denote the x- and y-coordinate of the fitted Gaussian in the ADF and ABF images, respectively. Note that this model contains two extra parameters as compared to the model used to obtain Figs. 6.2(a) and (b). Qualitatively, Figs. 6.2(c) and (d) show the same behavior as Figs. 6.2(a) and (b), but the overall detection rate of the Si atom is lower. This has been explicitly shown in Fig. 6.2(e) depicting the difference between Figs. 6.2(b) and (d). The positive values for the difference of detection indicate that the detection rate can be up to 40 % higher for simultaneous model fitting. The inset of Fig. 6.2(e) shows the Poisson noise disturbed ABF and ADF STEM images for which there is the largest difference between the simultaneous and separate analysis. From this investigation, it follows that simultaneously analysing ABF and ADF STEM images is advantageous, as compared to a separate analysis, since it positively affects atom detectability.

## 6.4.2 Spatial deviation and precision

Beside comparing the atom detectability for a simultaneous and separate analysis of ABF and ADF STEM images, also the deviation from the true atom position and precision can be evaluated. For this, the set of images of the Si atom on a 5 nm amorphous C support is used and analysed in the same way as described in section 6.4.1. Hereby, a model containing one atomic column has been considered. The deviation  $d_i$  of the estimated position of the Si atom ( $\hat{\beta}_x, \hat{\beta}_y$ ) from the true atom position ( $\beta_x, \beta_y$ ) for the  $i$ th pair of noise disturbed simulated ABF and ADF STEM images for a certain  $\text{ICNR}^{ADF}$  and  $\text{ICNR}^{ABF}$  value from simultaneously fitting the ABF and ADF image data is investigated. The expression for  $d_i$  is given by

$$d_i = \sqrt{(\hat{\beta}_x - \beta_x)^2 + (\hat{\beta}_y - \beta_y)^2}. \quad (6.18)$$

Fig. 6.3(a) shows a top view image of the average deviation  $\bar{d}$  as a function of  $\text{ICNR}^{ADF}$  and  $\text{ICNR}^{ABF}$ . As such,

$$\bar{d} = \frac{1}{I} \sum_{i=1}^I d_i, \quad (6.19)$$

with  $I = 100$  for each combination of  $\text{ICNR}^{ADF}$  and  $\text{ICNR}^{ABF}$ . The standard deviation of  $\bar{d}$ ,  $\sigma_{\bar{d}}$ , is given by

$$\sigma_{\bar{d}} = \frac{\sigma}{\sqrt{I}}, \quad (6.20)$$

with

$$\sigma = \sqrt{\frac{\sum_{i=1}^I (d_i - \bar{d})^2}{I - 1}}, \quad (6.21)$$

denoting the standard deviation of  $d_i$ . It can be concluded from Fig. 6.3(a) that for high ICNR values the deviation of the estimated location from the true position of the Si atom is small. For decreasing ICNR values, the deviation increases. Fig 6.3(b) shows the results obtained from a separate analysis of the ABF and ADF image data. Here,  $\bar{d}$  has been calculated using a weighted

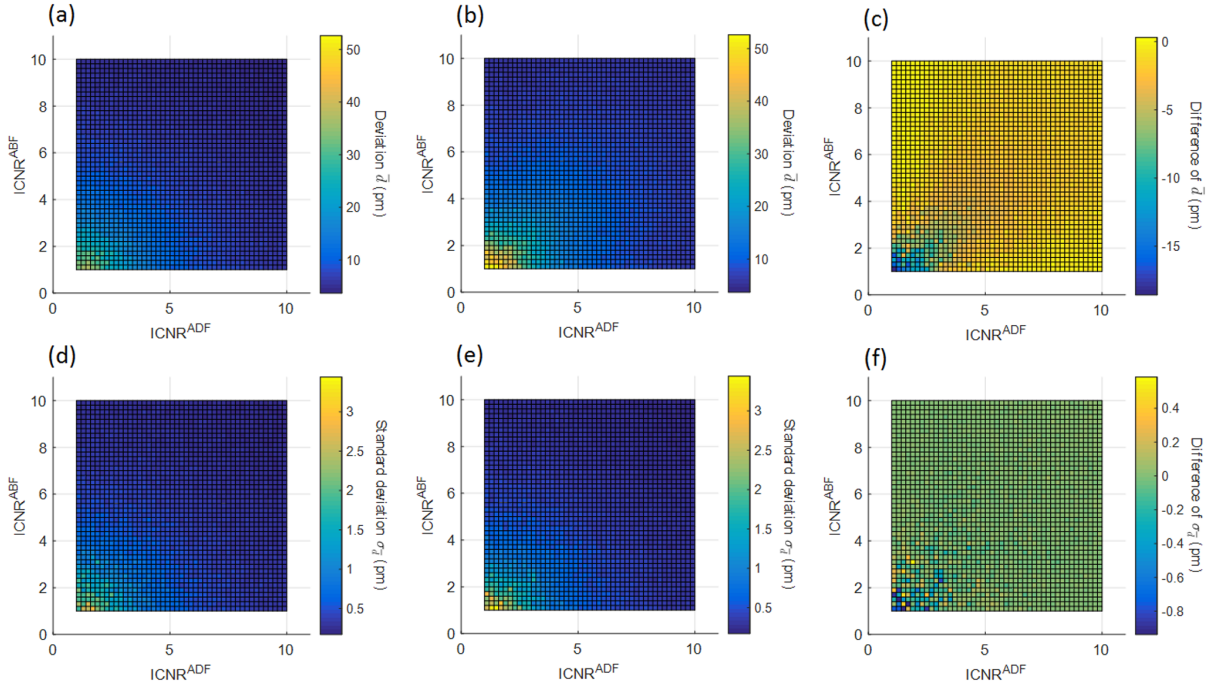


**Figure 6.3:** (a) Deviation of locating a simulated Si atom from its true position from Poisson noise disturbed simulated ADF and ABF STEM images as a function of  $\text{ICNR}^{\text{ADF}}$  and  $\text{ICNR}^{\text{ABF}}$  by simultaneous model fitting. (b) Deviation by separate model fitting. (c) Difference of deviation between (a) and (b). (d) Standard deviation of locating the Si atom by simultaneous model fitting. (e) Standard deviation by separate model fitting. (f) Difference of standard deviation between (d) and (e).

average where the weights have been chosen to be equal to the reciprocal of the variances,

$$\bar{d} = \frac{\frac{\overline{d^{\text{ABF}}}}{(\sigma_{\overline{d^{\text{ABF}}}})^2} + \frac{\overline{d^{\text{ADF}}}}{(\sigma_{\overline{d^{\text{ADF}}}})^2}}{\frac{1}{(\sigma_{\overline{d^{\text{ABF}}}})^2} + \frac{1}{(\sigma_{\overline{d^{\text{ADF}}}})^2}}. \quad (6.22)$$

The expression in Eq. (6.19) has been used to compute  $\overline{d^{\text{ABF}}}$  and  $\overline{d^{\text{ADF}}}$ , where  $d_i$ , given by Eq. (6.18), represents either  $d_i^{\text{ABF}}$  or  $d_i^{\text{ADF}}$ , corresponding to the deviation from the true atom position  $(\beta_x, \beta_y)$  of the estimated position of the Si atom obtained from the ABF image,  $(\hat{\beta}_x^{\text{ABF}}, \hat{\beta}_y^{\text{ABF}})$ , or ADF image,  $(\hat{\beta}_x^{\text{ADF}}, \hat{\beta}_y^{\text{ADF}})$ , respectively. The standard deviations  $\sigma_{\overline{d^{\text{ABF}}}}$  and  $\sigma_{\overline{d^{\text{ADF}}}}$  are calculated from Eq. (6.20). Fig. 6.3(b) shows the same qualitative behavior as Fig. 6.3(a), but the overall deviation from the true atom position is smaller for Fig. 6.3(a). This is illustrated in Fig. 6.3(c) showing the difference of deviation between Figs. 6.3(a) and (b). The negative differences indicate that the deviation from the true atom position is smaller for simultaneously analysing the ABF and ADF STEM images as compared to analysing these images in a separate manner. For investigating the precision of locating the Si atom from ABF and ADF image data, the standard deviations of  $\bar{d}$  have been displayed in Fig. 6.3(d) and (e) for simultaneously and separately modelling the ABF and ADF images, respectively. For Fig. 6.3(d), the standard deviation  $\sigma_{\bar{d}}$  is

given by Eq. (6.20). The standard deviation for Fig. 6.3(e) is calculated using

$$\sigma_{\bar{d}} = \sqrt{\frac{1}{\frac{1}{(\sigma_{d^{ABF}})^2} + \frac{1}{(\sigma_{d^{ADF}})^2}}}}, \quad (6.23)$$

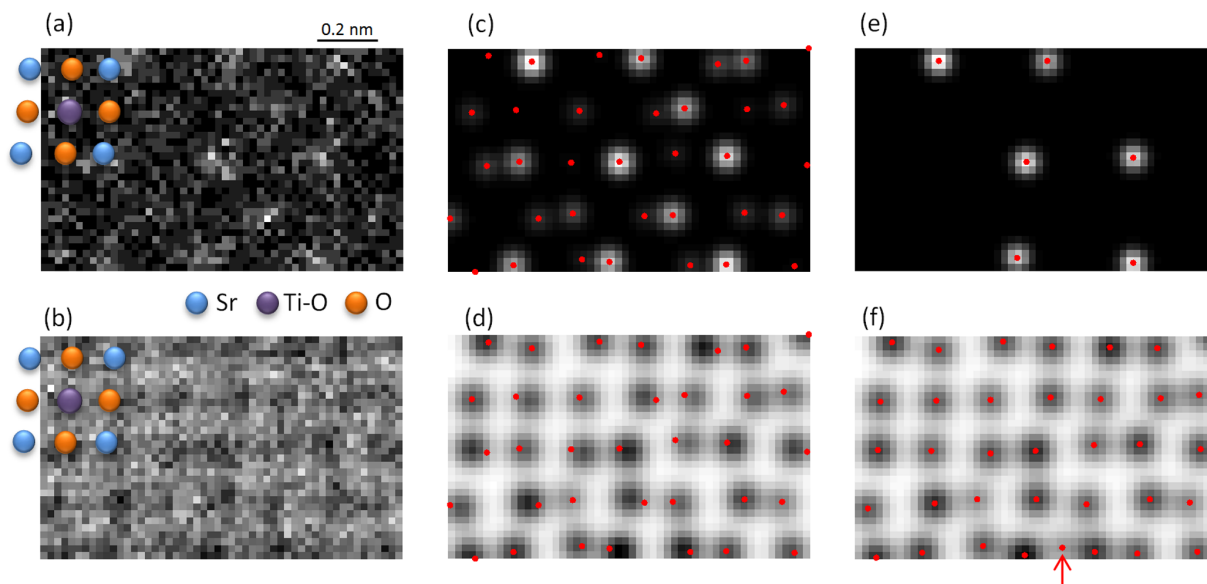
corresponding to the standard error of a weighted mean. It can be seen from Figs. 6.3(d) and (e) that  $\sigma_{\bar{d}}$  increases, or, in other words, the precision decreases, for decreasing ICNR values and vice versa. The difference between Figs. 6.3(d) and (e) is shown in Fig. 6.3(f), where the negative values indicate that the standard deviation of locating the atom is, in general, smaller, or that the precision is higher, for a simultaneous analysis as compared to a separate analysis of ABF and ADF images. This shows that, beside a smaller spatial deviation, also the precision improves by simultaneously analysing ABF and ADF STEM images.

## 6.5 Experimental examples

In this section, the proposed methodology to detect atomic columns by the MAP probability rule from simultaneously acquired ABF and ADF STEM images is applied to two experimental examples exhibiting low CNR. In section 6.5.1, SrTiO<sub>3</sub> is analysed, whereas, in section 6.5.2, LiMn<sub>2</sub>O<sub>4</sub> is investigated. Hereby, the effect of specimen tilt has been taken into account as small tilts might be present causing a possible shift of the measured atomic column locations in the ABF image as compared to the locations in the ADF image.

### 6.5.1 SrTiO<sub>3</sub>

Figs. 6.4(a) and (b) show a synthetic ADF and ABF STEM image of SrTiO<sub>3</sub>, respectively, obtained by K. Müller-Caspary from an experimental 4D STEM dataset using a Medipix3 Merlin camera attached to a probe-corrected FEI Titan, where the Sr, Ti-O and O columns have been indicated. The detector collection range for the ADF image has been chosen to be equal to 88-98 mrad, whereas the collection range for the ABF image is 12-22 mrad. The MAP probability rule for simultaneously acquired ABF and ADF STEM data has been applied to these images in order to obtain the number of atomic columns for which there is most evidence in the image data, and, as a result, the most probable atomic structure. For this, the parametric model including the effect of specimen tilt given by Eq. (6.3) has been used, since tilt might be present, where equal widths for the Gaussian peaks in the ABF image,  $\rho^{ABF}$ , and ADF image,  $\rho^{ADF}$ , have been used. Hereby, it has been assumed that the shift of the ABF peaks from the ADF peak locations cannot exceed 50 pm, which is already a high value for typical shifts due to specimen tilt [Zhou 2016, Gao 2018]. Figs. 6.4(c) and (d) show the most probable parametric models indicated by the MAP probability rule by simultaneously analysing the ADF and ABF STEM image data of Figs. 6.4(a) and (b), respectively, consisting of 35 atomic columns corresponding to the expected number of columns of SrTiO<sub>3</sub> in [100] direction. As compared to the detection of the atomic columns of SrTiO<sub>3</sub> from only an ADF STEM image in subsection 4.4.1, the O columns can, in this case, also be detected due to the simultaneous acquisition of an ABF STEM image. It is noted that in the analysis no prior knowledge about the expected locations of the atomic columns in SrTiO<sub>3</sub> have been taken into account. The MAP probability rule is able to retrieve the atomic columns present in the



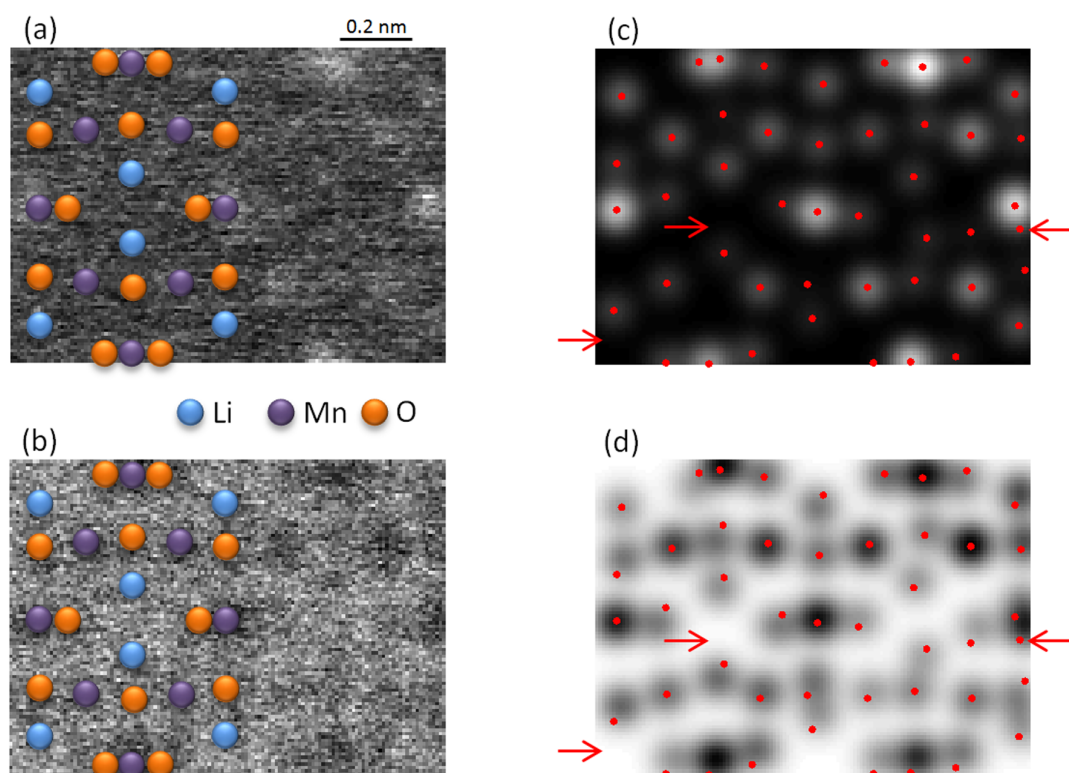
**Figure 6.4:** (a) Synthetic ADF and (b) ABF STEM image of  $\text{SrTiO}_3$  obtained from an experimental 4D STEM dataset. (c) and (d) Most probable refined models of the experimental ADF data in (a) and the ABF data in (b), respectively, obtained from the MAP probability rule by analysing the data in (a) and (b) simultaneously taking into account specimen tilt. The red dots indicate the estimated column locations corresponding to the fitted ADF peak positions. (e) and (f) Most probable refined models by separately analysing (a) and (b), where the red dots correspond to the fitted peak positions in the image data. The arrow in (f) indicates the detection of an extra column at a position where no column is expected.

image data because the ICNR values of the columns are sufficiently high. The average ICNR values of each column type have been calculated, using Eq. (6.17), to be around 8.7, 6.0, and 7.4 for the Sr, Ti-O, and O columns, respectively. From the analysis given in Fig. 6.2, it followed that for such ICNR values the MAP probability rule can reliably detect atomic columns from ABF and ADF STEM data. The estimated column positions which are shown in Figs. 6.4(c) and (d) by red dots correspond to the fitted ADF peak positions since measured atomic column locations in ADF STEM are considered to be reliable indicators of the true column positions because of the insensitivity to specimen tilt [Maccagnano-Zacher 2008, So 2012]. In Figs. 6.4(e) and (f), the most probable refined models of the image data in Figs. 6.4(a) and (b), respectively, are shown, obtained by the MAP probability rule by separately analysing the ADF and ABF image data. For this, a parametric model such as given by Eq. (3.10) has been used, where equal widths for the estimated Gaussian peaks have been assumed. From Fig. 6.4(e), it can be seen that from only analysing the ADF STEM image only some of the Sr columns can be detected. This is due to the fact that the average ICNR value of the Sr columns in the ADF image, calculated from Eq. (6.13), is around 4.0, which typically restricts a 100 % detection rate. The average ICNR values in the ADF image of the other types of columns in  $\text{SrTiO}_3$  are even lower, around 1.9 for the Ti-O and 0.6 for the O columns, restricting detection of these columns even further. The average ICNR values of the atomic columns in the ABF image, though, calculated from Eq. (6.14), are higher, around 7.7, 5.7, and 7.4 for the Sr, Ti-O, and O columns, respectively, improving their detectability. It can be seen from Fig. 6.4(f) that the expected atomic columns in  $\text{SrTiO}_3$  are found. In this process, though, one atomic column, which has been indicated by the

red arrow in Fig. 6.4(f), has been detected at a position where no column is expected. Although from analysing the ABF image data independently of the ADF image data the atomic columns can be detected quite reliably, it followed from the analysis, performed in section 6.4.2 and shown in Fig. 6.3, that simultaneously analysing the ADF and ABF image data improves atom position accuracy and precision. Furthermore, the ABF peak locations are sensitive to specimen tilt, which causes them to shift from their true column positions. When only analysing an ABF STEM image, the estimated column positions are prone to this effect, which may lead to biased structure information.

### 6.5.2 $\text{LiMn}_2\text{O}_4$

As another example, simultaneous ADF and ABF STEM images of  $\text{LiMn}_2\text{O}_4$  have been acquired which are shown in Figs. 6.5(a) and (b), respectively, together with the spinel structure of  $\text{LiMn}_2\text{O}_4$ . The images have been obtained by N. Gauquelin from a probe-corrected FEI Titan operated at 300 kV with a semiconvergence angle of 19.8 mrad. The detector collection ranges for the ABF and ADF images are 8-17 mrad and 44-190 mrad, respectively. The average ICNR



**Figure 6.5:** (a) Experimental ADF and (b) ABF STEM image of  $\text{LiMn}_2\text{O}_4$  overlain with the spinel atomic arrangement. (c) Most probable refined model of the experimental ADF data in (a) and (d) most probable model of the ABF data in (b) obtained from the MAP probability rule by analysing the data in (a) and (b) simultaneously taking into account specimen tilt. The red dots indicate the estimated column locations corresponding to the fitted ADF peak positions. The arrows in (c) and (d) indicate the expected locations of two columns that were not detected and the detection of an extra column at a position where no column is expected.

values of the Li, Mn, and O columns have been estimated by Eq. (6.17) to be around 7.7, 15.0, and 7.8, respectively. Analysing Li-containing materials is of relevance since they have great technological interest because of their importance in battery devices [Li 2009a, Nitta 2015]. Therefore, the direct visualisation of the Li atoms has been an important research topic in STEM and has been achieved by imaging in the ABF mode [Oshima 2010, Huang 2011, Gu 2011, He 2011, Lee 2011]. Nevertheless, materials containing light elements, such as Li, are sensitive to the electron beam. For such materials, beam damage is limited by imaging the specimen with a low incoming electron dose, typically varying between around  $10^3$  to around  $10^5$   $e^-/\text{\AA}^2$  in atomic-resolution STEM leading to images exhibiting low CNR. This is also the case for the images shown in Figs. 6.5(a) and (b) where the determination of the number of atomic columns and their positions is not straightforward by merely visually interpreting the image data. In order to overcome this problem, the MAP probability rule for simultaneously acquired ABF and ADF STEM images is applied to Figs. 6.5(a) and (b) by using the parametric model given by Eq. (6.3) including the effect of specimen tilt, since some tilt might have been present during the acquisition of the images. Similarly as for the example of  $\text{SrTiO}_3$  in Fig. 6.4, equal widths for the Gaussian peaks in the ABF and ADF image have been used and the shift of the ABF peaks from the ADF peak locations has been chosen not to be larger than 50 pm. Figs. 6.5(c) and (d) show the most probable parametric models indicated by the MAP probability rule for the ADF and ABF STEM image data of Figs. 6.5(a) and (b), respectively, consisting of 46 atomic columns. The estimated column locations, shown by red dots, correspond to the fitted ADF peak positions. The detected number of atomic columns is slightly less than the expected 47 columns considering the spinel structure of  $\text{LiMn}_2\text{O}_4$  since two columns were not detected and one extra column position was found in the experimental data. These columns have been indicated in Figs. 6.5(c) and (d) by red arrows. The reason why two atomic columns were not detected by the MAP probability rule, although expected by the spinel structure of  $\text{LiMn}_2\text{O}_4$ , is related to their ICNR values. It has been estimated by Eq. (6.17) that these columns exhibit ICNR values of around 5.4. From the analysis performed in section 6.4.1, shown in Fig. 6.2, it followed that for such ICNR values typically a 100 % detection rate cannot be attained. The probability for over- or underfitting is an inherent limitation of model-order selection methods, like the MAP probability rule, and will generally increase with decreasing CNR. Despite this, the MAP probability rule has been able to retrieve a reliable representation of the atomic column locations in  $\text{LiMn}_2\text{O}_4$  without including any prior information about the expected spinel atomic arrangement.

## 6.6 Conclusions

In this chapter, a new method for analysing simultaneously acquired ABF and ADF STEM images using statistical parameter estimation has been introduced. For this, the existing parametric models have been extended enabling the possibility to simultaneously analyse ABF and ADF image data. Hereby, the effect of specimen tilt, which shifts the ABF peak locations from the true atomic column locations, has been taken into account since small tilts of the electron beam with respect to the crystal zone axis can easily be present in STEM experiments. The advantages of simultaneous model fitting, as compared to combining quantitative measurements from analysing the ABF and ADF STEM images separately, has been thoroughly discussed as a function of ICNR. It has been demonstrated that a simultaneous analysis improves atom detectability, as

---

well as atom position accuracy and precision especially for ICNR values of less than around 5.0. In addition, it has been shown that the MAP probability rule [Fatermans 2018, Fatermans 2019], which aims to determine the most probable atomic structure from images of beam-sensitive materials, can also be applied to the proposed framework of simultaneously fitting the ABF and ADF image data. This has been illustrated by using the MAP probability rule to investigate experimental STEM data, allowing to obtain a reliable estimation of atomic column locations without including prior information about the expected positions of these columns.



# 7

## General conclusions and future perspectives

In this thesis, quantitative atomic-resolution STEM is pushed forward by the introduction of a new method which enables to obtain structure information of unknown nanomaterials in an automatic and objective manner and to detect atomic columns and even single atoms with high reliability. The foundation of this technique is a model-based analysis using statistical parameter estimation theory which consists of the estimation of unknown parameters from an available set of experimental observations. Due to the presence of noise, these observations fluctuate around their expectation values. The starting point of statistical parameter estimation theory is the construction of a parametric (physics-based) model describing the expectations of the experimental observations as a function of the unknown parameters. Here, atomic-resolution electron microscopy images are considered as data planes where the observations are the pixel values of the image from which unknown structure parameters need to be estimated. Since image intensities are sharply peaked at the atomic column positions, the projected atomic columns of atomic-resolution STEM images viewed along a major zone axis can be modelled as Gaussian peaks superimposed on a constant background. Accurate and precise structure information is then obtained by fitting this model to the observed image pixel values with respect to the unknown parameters using a criterion of goodness of fit quantifying the similarity between the image and the model.

In order to extract reliable structure information of nanomaterials from atomic-resolution STEM images using model-based parameter estimation, the number of atomic columns in the image should be known. The detection of an atomic column or single atom, in case the column consists of only one atom, from STEM images often depends on a visual interpretation of the image. Materials that are stable under the electron beam can be imaged with a sufficiently high electron dose, typically of the order of more than  $10^6 - 10^8 \text{ e}^-/\text{\AA}^2$ , resulting into high-quality images exhibiting high SNR and high contrast. This allows one to resolve the individual atomic columns and, therefore, for such beam-stable materials, the atomic columns can be detected in

a merely visual manner. However, some materials, especially light-element nanomaterials, are sensitive to the electron beam and, as a result, they cannot withstand a high incoming electron dose, since the high-energy electrons in the beam cause damage to the material. In order to avoid this beam damage to occur, such beam-sensitive materials can only be imaged in STEM using a limited electron dose of around  $10^3 - 10^5 \text{ e}^-/\text{\AA}^2$ . This leads to recording images exhibiting low SNR and weak contrast, and hence low CNR. Visually inspecting these images, trying to resolve the individual atomic columns, can be unreliable and may lead to biased results, especially when no prior knowledge about the structure of the material is available. To overcome this problem, an objective and quantitative approach is needed for detecting atomic columns from STEM images.

Interestingly, parameter estimation theory can be generalised by combining its principles with model-order selection. Hereby, besides estimating the unknown parameters of the expectation model, also the number of parameters that most closely represents the underlying process that generated the experimental observations needs to be determined. Typical model-selection methods perform a tradeoff between high goodness of fit and low model complexity, since model fit can be easily improved by increased model complexity without necessarily bearing any interpretable relationship with the underlying data-generating process. In STEM, model selection can be used to automatically and objectively determine the number of atomic columns which are present in the image data.

In the first part of this thesis, the MAP probability rule has been proposed as a quantitative method to detect atomic columns from atomic-resolution ADF STEM images. The method is built upon model-based parameter estimation and Bayesian probability theory. This combination of statistical parameter estimation and model-order selection allows the MAP probability rule to perform automatic and objective structure quantification of unknown nanomaterials and to detect atomic columns and even single atoms with high reliability. For this purpose, it has been shown that, for a variety of parametric models, approximate analytical expressions can be derived for the probability of the presence of a certain number of atomic columns in ADF STEM image data. The MAP probability rule selects the number of columns that maximises this probability. Furthermore, the MAP probability rule also enables one to quantify how more likely a certain atomic structure is as compared to other structures. The validity and usefulness of applying the MAP probability rule to low-quality image data have been demonstrated by analysing experimental and simulated ADF STEM images of samples of different shape, size, and atom type. Hereby, it has been shown that important structural information can be obtained by using the MAP probability rule, which would otherwise have been lost.

Furthermore, besides detecting atomic columns from ADF STEM images, it has been shown in this thesis that the MAP probability rule can be effectively used as a way to evaluate the relation between STEM image quality measures, such as SNR and CNR, and atom detectability, which is defined as the probability to detect an atom from an image. In general, atom detectability is indeed related to image quality, since, for example, one expects the detectability of atomic columns in an image to increase with increasing image quality. In this way, the probability to detect an atomic column from STEM image data, which can be provided by the MAP probability rule, is correlated with the quality of the image. As such, for ADF STEM images, a new image-quality measure, the ICNR, has been proposed that better correlates with atom detectability than conventional image-quality measures. Atomic columns resulting from images with ICNR values of less than around 5.0 become challenging to accurately detect since, typically, the detection rate of 100 % drops rapidly starting from this value.

Moreover, the relation of the MAP probability rule with model selection has been thoroughly investigated. In particular, the MAP probability rule is closely related to the BIC, since both methods are derived using a Bayesian approach. In principle, atom detection from STEM images can be performed with any model-selection criterion, but, interestingly, the MAP probability rule takes into account more dimensions of model complexity as compared to other commonly used model-selection criteria. More specifically, the complexity term of the MAP probability rule depends on three dimensions of model complexity, namely the number of parameters, the functional form of the model, and the extension of the parameter space, as opposed to other model-selection criteria which typically depend on the number of parameters only. This extended complexity term allows the MAP probability rule to more accurately detect atoms from STEM images, especially from images exhibiting low ICNR values. Furthermore, the MAP probability rule allows for a clear and flexible incorporation of prior knowledge, which is often not the case for other model-selection methods.

In the last part of this thesis, the methodology of the MAP probability rule has been extended for detecting atomic columns from simultaneously acquired ABF and ADF STEM images. A simultaneous acquisition of ABF and ADF STEM image data combines the improved light-element visualisation of ABF STEM with the easily interpretable image contrast of ADF STEM, allowing to visualise atoms of a large range of atomic numbers for studying and interpreting materials at the atomic scale consisting of both light and heavy atoms. Although, the ABF imaging mode allows for better visualisation of light elements as compared to ADF imaging, it is, in general, not straightforward to visually detect light-element atomic columns since light-element nanomaterials are typically sensitive to the electron beam, limiting the incoming electron dose and leading to images exhibiting low CNR. In order to use the MAP probability rule for detecting atomic columns by simultaneously analysing ABF and ADF STEM image data, the existing parametric models for describing STEM images need to be extended. Hereby, it is important to take into account the effect of specimen tilt, which shifts the ABF peak locations from the true atomic column locations, since small tilts of the electron beam with respect to the crystal zone axis can easily be present in STEM experiments. The advantages of simultaneous model fitting, as compared to combining quantitative measurements from analysing the ABF and ADF STEM images separately, has been thoroughly investigated as a function of ICNR. It has been demonstrated that a simultaneous analysis improves atom detectability, as well as atom position accuracy and precision especially for ICNR values of less than around 5.0. In addition, it has been illustrated that by using the MAP probability rule to analyse simultaneously acquired experimental ABF and ADF STEM data, a reliable estimation of atomic column locations can be obtained without including prior information about the expected positions of these columns.

Overall, in this thesis, the MAP probability rule has been presented as a new quantitative method which enables to determine the structure of unknown nanomaterials in an automatic and objective manner and to detect atomic columns and even single atoms from atomic-resolution STEM images with high reliability. This technique allows to obtain accurate and precise measurements of the atomic arrangement of the projected atomic columns or individual atoms which plays an important role for fully understanding the structure-properties relation of nanomaterials. Nowadays, a software package, called StatSTEM, is freely available which aims to facilitate quantitative electron microscopy. Currently, the MAP probability rule is available in this software for analysing images with a small field of view containing a limited number of projected atomic

columns. Furthermore, although in this thesis the proposed technique has only been applied to STEM, it is not limited to this imaging mode as the foundations of the MAP probability rule are very general and applicable to different domains. Therefore, it may be possible to apply the MAP probability rule also to other signals that can be collected in the electron microscope such as EELS and EDX signals. In this way, more optimal quantitative information can be obtained about the specimen under investigation.

The development of a new quantitative method in this thesis, which generalises the characterisation of nanomaterials at the atomic scale in STEM, has pushed quantitative electron microscopy towards a more objective interpretation. Future developments of novel quantification methods will continue to appear step by step for further unravelling the link between the structure and the properties at the atomic level of nanomaterials.

# Bibliography

- [Adrian 1984] M. Adrian, J. Dubochet, J. Lepault, and A. W. McDowell. *Cryo-electron microscopy of viruses*. Nature, vol. 308, 32–36, 1984.
- [Akaike 1974] H. Akaike. *A new look at the statistical model identification*. IEEE Trans. Autom. Control, vol. 19, 716–723, 1974.
- [Akamine 2015] H. Akamine, K. H. W. van den Bos, N. Gauquelin, S. Farjami, S. Van Aert, D. Schryvers, and M. Nishida. *Determination of the atomic width of an APB in ordered CoPt using quantified HAADF-STEM*. Journal of Alloys and Compounds, vol. 644, 570–574, 2015.
- [Akashi 2015] T. Akashi, Y. Takahashi, T. Tanigaki, T. Shimakura, T. Kawasaki, T. Furutsu, H. Shinada, H. Müller, M. Haider, N. Osakabe, and A. Tonomura. *Aberration corrected 1.2-MV cold field-emission transmission electron microscope with a sub-50-pm resolution*. Applied Physics Letters, vol. 106, 074101, 2015.
- [Alania 2017a] M. Alania. *Quantification of 3D atomic positions for nanoparticles using scanning transmission electron microscopy: statistical parameter estimation, dose-limited precision and optimal experimental design*. PhD thesis, University of Antwerp, 2017.
- [Alania 2017b] M. Alania, T. Altantzis, A. De Backer, I. Lobato, S. Bals, and S. Van Aert. *Depth sectioning combined with atom-counting in HAADF STEM to retrieve the 3D atomic structure*. Ultramicroscopy, vol. 177, 36–42, 2017.
- [Alem 2011] N. Alem, O. V. Yazyev, C. Kisielowski, P. Denes, U. Dahmen, P. Hartel, M. Haider, M. Bischoff, B. Jiang, S. G. Louie, and A. Zettl. *Probing the Out-of-Plane Distortion of Single Point Defects in Atomic Thin Hexagonal Boron Nitride at the Picometer Scale*. Physical Review Letters, vol. 106, 126102, 2011.
- [Allen 2003] L. J. Allen, S. D. Findlay, M. P. Oxley, and C. J. Rossouw. *Lattice-resolution contrast from a focused coherent electron probe. Part I*. Ultramicroscopy, vol. 96, no. 1, 47–63, 2003.
- [Allen 2004] L. J. Allen, W. McBride, N. L. O’Leary, and M. P. Oxley. *Exit wave reconstruction at atomic resolution*. Ultramicroscopy, vol. 100, 91–104, 2004.
- [Allen 2008] J. E. Allen, D. E. Hemesath, D. E. Perea, J. L. Lensch-Falk, Z. Y. Li, F. Yin, M. H. Gass, P. Wang, A. L. Bleloch, R. E. Palmer, and L. J. Lauhon. *High-resolution detection of Au catalyst atoms in Si nanowires*. Nature Nanotechnology, vol. 3, 168–173, 2008.
- [Allen 2012] L. J. Allen, A. J. D’Alfonso, B. Freitag, and D. O. Klenov. *Chemical mapping at atomic resolution using energy-dispersive x-ray spectroscopy*. MRS Bulletin, vol. 37, 47–52, 2012.
- [Allpress 1972] J. G. Allpress, E. A. Hewat, A. F. Moodie, and J. V. Sanders. *n-beam lattice images. I. Experimental and computed images from  $W_4Nb_{26}O_{77}$* . Acta Crystallographica Section A: Crystal Physics, Diffraction, Theoretical and General Crystallography, vol. 28, no. 6, 528–536, 1972.
- [Allpress 1973] J. G. Allpress, and J. V. Sanders. *The direct observation of the structure of real crystals by lattice imaging*. Journal of Applied Crystallography, vol. 6, no. 3, 165–190, 1973.

- [Alshammari 2012] A. Alshammari, A. Köckritz, V. N. Kalevaru, A. Bagabas, and A. Martin. *Influence of Single Use and Combination of Reductants on the Size, Morphology and Growth Steps of Gold Nanoparticles in Colloidal Mixture*. Open Journal of Physical Chemistry, vol. 2, no. 4, 252–261, 2012.
- [Altantzis 2016] T. Altantzis, E. Coutino-Gonzalez, W. Baekelant, G. T. Martinez, A. M. Abakumov, G. Van Tendeloo, M. B. J. Roeffaers, S. Bals, and J. Hofkens. *Direct observation of luminescent silver clusters confined in faujasite zeolites*. ACS Nano, vol. 10, 7604, 2016.
- [Anguiano 1999] E. Anguiano, and M. Aguilar. *A cross-measurement procedure (cmp) for near noise-free imaging in scanning microscopes*. Ultramicroscopy, vol. 76, 39–47, 1999.
- [Armstrong 2009] N. Armstrong, and D. B. Hibbert. *An introduction to Bayesian methods for analyzing chemistry data Part 1: An introduction to Bayesian theory and methods*. Chemometrics and Intelligent Laboratory Systems, vol. 97, 194–210, 2009.
- [Balandin 2008] A. A. Balandin, S. Ghosh, W. Bao, I. Calizo, D. Teweldebrhan, F. Miao, and C. N. Lau. *Superior thermal conductivity of single-layer graphene*. Nano Letters, vol. 8, 902–907, 2008.
- [Bals 2006] S. Bals, S. Van Aert, G. Van Tendeloo, and D. Ávila-Brandé. *Statistical Estimation of Atomic Positions from Exit Wave Reconstruction with a Precision in the Picometer Range*. Physical Review Letters, vol. 96, 096106, 2006.
- [Bals 2007] S. Bals, K. J. Batenburg, J. Verbeeck, J. Sijbers, and G. Van Tendeloo. *Quantitative three-dimensional reconstruction of catalyst particles of bamboo-like carbon nanotubes*. NanoLetters, vol. 7, 3669–3674, 2007.
- [Bals 2011] S. Bals, M. Casavola, M. A. van Huis, S. Van Aert, K. J. Batenburg, G. Van Tendeloo, and D. Vanmaekelbergh. *Three-Dimensional Atomic Imaging of Colloidal Core-Shell Nanocrystals*. Nano Letters, vol. 11, no. 8, 3420–3424, 2011.
- [Bals 2012] S. Bals, S. Van Aert, C. P. Romero, K. Lauwaet, M. J. Van Bael, B. Schoeters, B. Partoens, E. Yücelen, P. Lievens, and G. Van Tendeloo. *Atomic scale dynamics of ultrasmall germanium clusters*. Nature Communications, vol. 3, 897, 2012.
- [Bals 2013] S. Bals, S. Van Aert, and G. Van Tendeloo. *High resolution electron tomography*. Current Opinion in Solid State and Materials Science, vol. 17, 107–114, 2013.
- [Bals 2014] S. Bals, B. Goris, L. M. Liz-Marzán, and G. Van Tendeloo. *Three-Dimensional Characterization of Noble-Metal Nanoparticles and their Assemblies by Electron Tomography*. Angewandte Chemie International Edition, vol. 53, no. 40, 10600–10610, 2014.
- [Bartesaghi 2015] A. Bartesaghi, A. Merk, S. Banerjee, D. Matthies, X. Wu, J. L. Milne, and S. Subramaniam. *2.2 Å resolution cryo-EM structure of  $\beta$ -galactosidase in complex with a cell-permeant inhibitor*. Science, vol. 348, 1147–1151, 2015.
- [Batson 2002] P. E. Batson, N. Dellby, and O. L. Krivanek. *Sub-ångstrom resolution using aberration corrected electron optics*. Nature, vol. 418, 617–620, 2002.
- [Béché 2016] A. Béché, B. Goris, B. Freitag, and J. Verbeeck. *Development of a fast electromagnetic beam blanker for compressed sensing in scanning transmission electron microscopy*. Applied Physics Letters, vol. 108, no. 9, 093103, 2016.
- [Becker 2008] J. Becker, I. Zins, A. Jakab, Y. Khalavka, O. Schubert, and C. Sönnichsen. *Plasmonic Focusing Reduces Ensemble Linewidth of Silver-Coated Gold Nanorods*. Nano Letters, vol. 8, no. 6, 1719–1723, 2008.
- [Bergstrom 2012] J. Bergstrom. *Bayesian evidence for non-zero  $\theta_{13}$  and CP-violation in neutrino oscillations*. J High Energy Phy., vol. 8, 1–20, 2012.

- [Berkels 2014] B. Berkels, P. Binev, D. A. Blom, W. Dahmen, R. C. Sharpley, and T. Vogt. *Optimized imaging using non-rigid registration*. Ultramicroscopy, vol. 138, 46–56, 2014.
- [Bermejo 2004] F. J. Bermejo, W. S. Howells, M. Jimenez-Ruiz, M. A. Gonzalez, D. L. Price, M. L. Saboungi, and C. Cabrillo. *liquid of the complex dielectric relaxation spectra of molecular glass formers*. Physical Review B, vol. 69, 174201, 2004.
- [Biermans 2010] E. Biermans, L. Molina, K. J. Batenburg, S. Bals, and G. Van Tendeloo. *Measuring porosity at the nanoscale by quantitative electron tomography*. Nano Letters, vol. 7, 5014–5019, 2010.
- [Binev 2012] P. Binev, W. Dahmen, R. DeVore, P. Lamby, D. Savu, and R. Sharpley. *Compressed sensing and electron microscopy*. In Modeling Nanoscale Imaging in Electron Microscopy, 73–126. Springer, 2012.
- [Binns 2001] C. Binns. *Nanoclusters deposited on surfaces*. Surf. Sci. Rep., vol. 44, 1–49, 2001.
- [Borisevich 2006] A. Y. Borisevich, A. R. Lupini, and S. J. Pennycook. *Depth sectioning with the aberration-corrected scanning transmission electron microscope*. PNAS, vol. 103, no. 9, 3044–3048, 2006.
- [Boyes 2013] E. D. Boyes, M. R. Ward, L. Lari, and P. L. Gai. *ESTEM imaging of single atoms under controlled temperature and gas environment conditions in catalyst reaction studies*. Annalen der Physik, vol. 525, 423–429, 2013.
- [Broeckx 1995] J. Broeckx, M. Op de Beeck, and D. Van Dyck. *A useful approximation of the exit wave function in coherent STEM*. Ultramicroscopy, vol. 60, 71–80, 1995.
- [Broersen 1993] P.M.T. Broersen, and H.E. Wensink. *On finite sample theory for autoregressive model order selection*. IEEE Trans. Signal Process., vol. 41, 194–204, 1993.
- [Broersen 1996] P.M.T. Broersen, and H. E. Wensink. *On the penalty factor for autoregressive order selection in finite samples*. IEEE Trans. Signal Process., vol. 44, 748–752, 1996.
- [Brown 2011] M. W. Brown, P. Wang, S. J. Plimpton, and A. N. Tharrington. *Implementing Molecular Dynamics on Hybrid High Performance Computers - Short Range Forces*. Comput. Phys. Commun., vol. 182, 898–911, 2011.
- [Brown 2012] M. W. Brown, A. Kohlmeyer, S. J. Plimpton, and A. N. Tharrington. *Implementing Molecular Dynamics on Hybrid High Performance Computers - Particle-Particle Particle-Mesh*. Comput. Phys. Commun., vol. 183, 449–459, 2012.
- [Brown 2013] M. W. Brown, and M. Yamada. *Implementing molecular dynamics on hybrid high performance computers - Three-body potentials*. Comput. Phys. Commun., vol. 184, 2785–2793, 2013.
- [Brown 2016] H. G. Brown, A. J. D’Alfonso, Z. Chen, A. J. Morgan, M. Weyland, C. Zheng, M. S. Fuhrer, S. D. Findlay, and L. J. Allen. *Structure retrieval with fast electrons using segmented detectors*. Phys. Rev. B, vol. 93, 134116, 2016.
- [Brown 2017] H. G. Brown, R. Ishikawa, G. Sanchez-Santolino, N. R. Lugg, Y. Ikuhara, L. J. Allen, and N. Shibata. *A new method to detect and correct sample-tilt in scanning transmission electron microscopy bright-field imaging*. Ultramicroscopy, vol. 173, 76–83, 2017.
- [Brunelli 2009] R. Brunelli. *Template Matching Techniques in Computer Vision: Theory and Practice*. Wiley Press, 2009.
- [Brydson 2011] R. Brydson. *Aberration-corrected analytical transmission electron microscopy*. RMS-Wiley, 2011.
- [Buban 2010] J. P. Buban, Q. Ramasse, B. Gipson, N. D. Browning, and H. Stahlberg. *High-resolution low-dose scanning transmission electron microscopy*. Journal of Electron Microscopy, vol. 59, 103–112, 2010.

- [Burnham 2002] K. P. Burnham, and D. R. Anderson. *Model Selection and Multimodal Inference*. Springer-Verlag, 2002.
- [Callaway 2015] E. Callaway. *The revolution will not be crystallized: a new method sweeps through structural biology*. *Nature*, vol. 525, 172–176, 2015.
- [Callister 2007] W. D. Callister. *Materials Science and Engineering: An Introduction*. John Wiley & Sons, Inc., 7th edition edition, 2007.
- [Campbell 2015] M. G. Campbell, D. Veessler, A. Cheng, C. S. Potter, and B. Carragher. *2.8 Å resolution reconstruction of the Thermoplasma acidophilum 20S proteasome using cryo-electron microscopy*. *eLife*, vol. 4, e06380, 2015.
- [Chen 2005] J. Chen, B. Wiley, Z.-Y. Li, D. Campbell, F. Saeki, H. Cang, L. Au, J. Lee, X. Li, and Y. Xia. *Gold Nanocages: Engineering Their Structure for Biomedical Applications*. *Advanced Materials*, vol. 17, no. 18, 2255–2261, 2005.
- [Chen 2015] Z. Chen, A. J. D’Alfonso, M. Weyland, D. J. Taplin, L. J. Allen, and S. D. Findlay. *Energy dispersive X-ray analysis on an absolute scale in scanning transmission electron microscopy*. *Ultramicroscopy*, vol. 157, 21–26, 2015.
- [Cheng 2018] Y. Cheng. *Single-particle cryo-EM: How did it get here and where will it go*. *Science*, vol. 361, 876–880, 2018.
- [Chiu 1987] W. Chiu, K. H. Downing, J. Dubochet, R. M. Glaeser, H. G. Heide, E. Knapek, D. A. Kopf, M. K. Lamvik, J. Lepault, J. D. Robertson, J. D. Zeitler, and F. Zemlin. *Cryoprotection in electron microscopy*. *Journal of Microscopy*, vol. 141, 385–391, 1987.
- [Claeskens 2003] G. Claeskens, and N. L. Hjort. *The focused information criterion*. *Journal of the American Statistical Association*, vol. 98, 879–899, 2003.
- [Claeskens 2008] G. Claeskens, and N. L. Hjort. *Model selection and model averaging*. Cambridge University Press, 2008.
- [Claeskens 2016] G. Claeskens. *Statistical model choice*. *Annu. Rev. Stat. Appl.*, vol. 3, 10.1–10.24, 2016.
- [Claridge 2009] S. A. Claridge, A. W. Castleman, S. N. Khanna, C. B. Murray, A. Sen, and P. S. Weiss. *Cluster-assembled materials*. *ACS Nano*, vol. 3, 244–255, 2009.
- [Cliff 1975] G. Cliff, and G. W. Lorimer. *The quantitative analysis of thin specimens*. *Journal of Microscopy*, vol. 103, no. 2, 203–207, 1975.
- [Coleman 1994] T. F. Coleman, and Y. Li. *On the convergence of reflective Newton methods for large-scale nonlinear minimization subject to bounds*. *Mathematical Programming*, vol. 67, 189–224, 1994.
- [Coleman 1996] T. F. Coleman, and Y. Li. *An interior, trust region approach for nonlinear minimization subject to bounds*. *SIAM Journal on Optimization*, vol. 6, 418–445, 1996.
- [Corsaro 2014] E. Corsaro, and De Ridder J. *DIAMONDS: A new Bayesian nested sampling tool - Application to peak bagging of solar-like oscillations*. *Astronomy and Astrophysics*, vol. 571, A71, 2014.
- [Cosgriff 2007] E. C. Cosgriff, and P. D. Nellist. *A Bloch wave analysis of optical sectioning in aberration-corrected STEM*. *Ultramicroscopy*, vol. 107, no. 8, 626–634, 2007.
- [Coulthard 1967] M. A. Coulthard. *A relativistic Hartree-Fock atomic field calculation*. *Proceedings of the Physical Society*, vol. 91, no. 1, 44, 1967.
- [Cowley 1957] J. M. Cowley, and A. F. Moodie. *The Scattering of Electrons by Atoms and Crystals. I. A New Theoretical Approach*. *Acta Crystallographica*, vol. 10, no. 10, 609–619, 1957.

- [Cowley 1969] J. M. Cowley. *Image contrast in a transmission scanning electron microscope*. Applied Physics Letters, vol. 15, no. 2, 58–59, 1969.
- [Cowley 1972] J. M. Cowley, and S. Iijima. *Electron Microscope Image Contrast for Thin Crystal*. Zeitschrift für Naturforschung A, vol. 27, no. 3, 445–451, 1972.
- [Cowley 1995] J. M. Cowley. *Diffraction Physics*. Elsevier Science B.V, 3rd edition, 1995.
- [Cox 1946] R. T. Cox. *Probability, frequency and reasonable expectation*. Am. J. Phys., vol. 14, no. 1, 1–13, 1946.
- [Crewe 1966] A. V. Crewe. *Scanning Electron Microscopes: Is High Resolution Possible?* Science, vol. 154, no. 3750, 729–738, 1966.
- [Crewe 1968] A. V. Crewe, J. Wall, and L. M. Welter. *A High-Resolution Scanning Transmission Electron Microscope*. Journal of Applied Physics, vol. 39, no. 13, 5861–5868, 1968.
- [Crewe 1970] A. V. Crewe, J. Wall, and J. Langmore. *Visibility of Single Atoms*. Science, vol. 168, no. 3937, 1338–1340, 1970.
- [Croitoru 2006] M. Croitoru, D. Van Dyck, S. Van Aert, S. Bals, and J. Verbeeck. *An efficient way of including thermal diffuse scattering in simulation of scanning transmission electron microscopy images*. Ultramicroscopy, vol. 106, 933–940, 2006.
- [Crozier 2014] P. A. Crozier, and T. W. Hansen. *In situ and operando transmission electron microscopy of catalytic materials*. MRS Bulletin, vol. 40, 38–45, 2014.
- [Csencsits 1987] R. Csencsits, and R. Gronsky. *Damage of zeolite Y in the TEM and its effects on TEM images*. Ultramicroscopy, vol. 23, 421–431, 1987.
- [Cukier 2013] K. Cukier, and V. Mayer-Schoenberger. *The rise of big data*. Foreign Affairs, 28–40, 2013.
- [D’Agostini 2003] G. D’Agostini. *Bayesian inference in processing experimental data: principles and basic applications*. Rep. Prog. Phys., vol. 66, 1383–1419, 2003.
- [d’Alfonso 2010] A. J. d’Alfonso, B. Freitag, D. Klenov, and L. J. Allen. *Atomic-resolution chemical mapping using energy-dispersive x-ray spectroscopy*. Physical Review B, vol. 81, no. 10, 100101, 2010.
- [Daniel 2004] M.-C. Daniel, and D. Astruc. *Gold nanoparticles: assembly, supramolecular chemistry, quantum-size-related properties, and applications toward biology, catalysis, and nanotechnology*. Chemical reviews, vol. 104, no. 1, 293–346, 2004.
- [De Backer 2011] A. De Backer, S. Van Aert, and D. Van Dyck. *High precision measurements of atom column positions using model-based exit wave reconstruction*. Ultramicroscopy, vol. 111, 1475–1482, 2011.
- [De Backer 2013] A. De Backer, G. T. Martinez, A. Rosenauer, and S. Van Aert. *Atom counting in HAADF STEM using a statistical model-based approach: methodology, possibilities, and inherent limitations*. Ultramicroscopy, vol. 134, 23–33, 2013.
- [De Backer 2015a] A. De Backer. *Quantitative atomic resolution electron microscopy using advanced statistical techniques*. PhD thesis, University of Antwerp, 2015.
- [De Backer 2015b] A. De Backer, A. De wael, J. Gonnissen, and S. Van Aert. *Optimal experimental design for nano-particle atom-counting from high-resolution STEM images*. Ultramicroscopy, vol. 151, 46–55, 2015.
- [De Backer 2015c] A. De Backer, G. T. Martinez, K. E. MacArthur, L. Jones, A. Béché, P. D. Nellist, and S. Van Aert. *Dose limited reliability of quantitative annular dark field scanning transmission electron microscopy for nano-particle atom-counting*. Ultramicroscopy, vol. 151, 56–61, 2015.

- [De Backer 2016] A. De Backer, K. H. W. van den Bos, W. Van den Broek, J. Sijbers, and S. Van Aert. *StatSTEM: An efficient approach for accurate and precise model-based quantification of atomic resolution electron microscopy images*. *Ultramicroscopy*, vol. 171, 104–116, 2016.
- [De Backer 2017] A. De Backer, L. Jones, I. Lobato, T. Altantzis, B. Goris, P. D. Nellist, S. Bals, and S. Van Aert. *Three-dimensional atomic models from a single projection using Z-contrast imaging: verification by electron tomography and opportunities*. *Nanoscale*, 2017.
- [De Cruz 2011] L. De Cruz, D. G. Ireland, P. Vancraeyveld, and J. Ryckebusch. *Bayesian model selection for electromagnetic kaon production on the nucleon*. *Int. J. Mod. Phys. A*, vol. 26, no. 03n04, 642–644, 2011.
- [De Graef 2003] M. De Graef. *Introduction to Conventional Transmission Electron Microscopy*. Cambridge University Press, 2003.
- [de Jonge 2011] N. de Jonge, and F. M. Ross. *Electron microscopy of specimens in liquid*. *Nature Nanotechnology*, vol. 6, 695–704, 2011.
- [De wael 2017] A. De wael, A. De Backer, L. Jones, P. D. Nellist, and S. Van Aert. *Hybrid statistics-simulations based method for atom-counting from ADF STEM images*. *Ultramicroscopy*, vol. 177, 69, 2017.
- [Debono 2014] I. Debono. *Bayesian model selection for dark energy using weak lensing forecasts*. *Mon. Not R. Astron. Soc. Lett.*, vol. 437, no. 1, 887–897, 2014.
- [Dellisanti 2015] C. Dellisanti. *A barrier-breaking resolution*. *Nature Structural & Molecular Biology*, vol. 22, 361, 2015.
- [Demetzos 2004] C. Demetzos. *Pharmaceutical Nanotechnology*, volume 8. Springer, 2004.
- [den Dekker 2005] A. J. den Dekker, S. Van Aert, A. van den Bos, and D. Van Dyck. *Maximum likelihood estimation of structure parameters from high resolution electron microscopy images. Part I: A theoretical framework*. *Ultramicroscopy*, vol. 104, 83–106, 2005.
- [den Dekker 2013] A. J. den Dekker, J. Gonnissen, A. De Backer, J. Sijbers, and S. Van Aert. *Estimation of unknown structure parameters from high-resolution (S)TEM images: What are the limits?* *Ultramicroscopy*, vol. 134, 34–43, 2013.
- [Dhar 2013] V. Dhar. *Data science and prediction*. *Communications of the ACM*, vol. 56, 64–73, 2013.
- [Dodge 2003] Y. Dodge. *The Oxford dictionary of statistical terms*. Oxford University Press, 2003.
- [Downing 2001] K. H. Downing, and H. Li. *Accurate recording and measurement of electron diffraction data in structural and difference Fourier studies of proteins*. *Microscopy and Microanalysis*, vol. 7, 407–417, 2001.
- [Du Pasquier 2003] A. Du Pasquier, I. Plitz, S. Menocal, and G. Amatucci. *A comparative study of Li-ion battery, supercapacitor and nonaqueous asymmetric hybrid devices for automotive applications*. *Journal of Power Sources*, vol. 115, 171–178, 2003.
- [Dwyer 2005] C. Dwyer. *Multislice theory of fast electron scattering incorporating atomic inner-shell ionization*. *Ultramicroscopy*, vol. 104, no. 2, 141–151, 2005.
- [E 2013] H. E. K. E. MacArthur, T. J. Pennycook, E. Okunishi, A. J. D’Alfonso, N. R. Lugg, L. J. Allen, and P. D. Nellist. *Probe integrated scattering cross sections in the analysis of atomic resolution HAADF STEM images*. *Ultramicroscopy*, vol. 133, 109–119, 2013.
- [Egerton 1996] R. F. Egerton. *Electron Energy Loss Spectroscopy in the Electron Microscope*. Plenum Press New York, 1996.

- [Egerton 2004] R. F. Egerton, P. Li, and M. Malac. *Radiation damage in the TEM and SEM*. *Micron*, vol. 35, 399–409, 2004.
- [Egerton 2008] R. F. Egerton. *Electron energy-loss spectroscopy in the TEM*. *Reports on Progress in Physics*, vol. 72, no. 1, 016502, 2008.
- [Egerton 2014] R. F. Egerton. *Choice of operating voltage for a transmission electron microscope*. *Ultramicroscopy*, vol. 145, 85–93, 2014.
- [Einspahr 2006] J. J. Einspahr, and P. M. Voyles. *Prospects for 3D, nanometer-resolution imaging by confocal STEM*. *Ultramicroscopy*, vol. 106, no. 11, 1041–1052, 2006.
- [Erni 2009] R. Erni, M. D. Rossell, C. Kisielowski, and U. Dahmen. *Atomic-Resolution Imaging with a Sub-50-pm Electron Probe*. *Physical Review Letters*, vol. 102, 096101, 2009.
- [Everitt 2010] B. S. Everitt, and A. Skrondal. *Cambridge Dictionary of Statistics*. Cambridge Univ Press, 2010.
- [Faruqi 2018] A. R. Faruqi, and G. McMullan. *Direct imaging detector for electron microscopy*. *Nucl. Inst. Methods Phys. Rev. A*, vol. 878, 180–190, 2018.
- [Fatermans 2018] J. Fatermans, A. J. den Dekker, K. Muller-Caspary, I. Lobato, C. M. O’Leary, P. D. Nellist, and S Van Aert. *Single atom detection from low contrast-to-noise ratio electron microscopy images*. *Physical Review Letters*, vol. 121, 056101, 2018.
- [Fatermans 2019] J. Fatermans, S. Van Aert, and A. J. den Dekker. *The maximum a posteriori probability rule for atom column detection from HAADF STEM images*. *Ultramicroscopy*, vol. 201, 81–91, 2019.
- [Feroz 2011] F. Feroz, S. T. Balan, and M. P. Hobson. *Bayesian evidence for two companions orbiting HIP 5158*. *Mon*, vol. 416, no. 1, L104–L108, 2011.
- [Ferrando 2008] R. Ferrando, J. Jellinek, and R. L. Johnston. *Nanoalloys: from theory to applications of alloy clusters and nanoparticles*. *Chemical Reviews*, vol. 108, 845–910, 2008.
- [Ferwerda 1986a] H. A. Ferwerda, B. J. Hoendersa, and C. H. Slumpa. *The Fully Relativistic Foundation of Linear Transfer Theory in Electron Optics Based on the Dirac Equation*. *Optica Acta*, vol. 33, 159–183, 1986.
- [Ferwerda 1986b] H. A. Ferwerda, B. J. Hoendersa, and C. H. Slumpa. *Fully relativistic treatment of electron-optical image formation based on the Dirac equation*. *Optica Acta*, vol. 33, 145–157, 1986.
- [Findlay 2009] S. D. Findlay, N. Shibata, H. Sawada, E. Okunishi, Y. Kondo, T. Yamamoto, and Y. Ikuhara. *Robust atomic resolution imaging of light elements using scanning transmission electron microscopy*. *Applied Physics Letters*, vol. 95, no. 19, 191913, 2009.
- [Findlay 2010] S. D. Findlay, N. Shibata, H. Sawada, E. Okunishi, Y. Kondo, and Y. Ikuhara. *Dynamics of annular bright field imaging in scanning transmission electron microscopy*. *Ultramicroscopy*, vol. 110, no. 7, 903–923, 2010.
- [Findlay 2013] S. Findlay, and J. LeBeau. *Detector non-uniformity in scanning transmission electron microscopy*. *Ultramicroscopy*, vol. 124, 52–60, 2013.
- [Findlay 2014] S. D. Findlay, Y. Kohno, L. A. Cardamone, Y. Ikuhara, and N. Shibata. *Enhanced light element imaging in atomic resolution scanning transmission electron microscopy*. *Ultramicroscopy*, vol. 136, 31–41, 2014.
- [Fischer 1977] C. F. Fischer. *Hartree–Fock method for atoms. A numerical approach*. John Wiley and Sons, Inc., New York, 1977.
- [Foiles 1986] S. M. Foiles, M. I. Baskes, and M. S. Daw. *Embedded-atom-method function for the fcc metals Cu, Ag, Au, Ni, Pd, Pt, and their alloys*. *Phys. Rev. B*, vol. 33, 7983–7991, 1986.

- [Frieden 1998] B.R. Frieden. *Physics from Fisher Information - A Unification*. Cambridge Univ Press, 1998.
- [Fujita 2012] T. Fujita, P. Guan, K. McKenna, X. Lang, A. Hirata, L. Zhang, T. Tokunaga, S. Arai, Y. Yamamoto, N. Tanaka, Y. Ishikawa, N. Asao, Y. Yamamoto, J. Erlebacher, and M. Chen. *Atomic origins of the high catalytic activity of nanoporous gold*. *Nature materials*, vol. 11, no. 9, 775–780, 2012.
- [Fujiwara 1961] K. Fujiwara. *Relativistic dynamical theory of electron diffraction*. *Journal of the Physical Society of Japan*, vol. 16, 2226–2238, 1961.
- [Galindo 2007] P. L. Galindo, S. Kret, A. M. Sanchez, J.-Y. Laval, Yáñez, J. Pizarro, E. Guerrero, T. Ben, and S. I. Molina. *The Peak Pairs algorithm for strain mapping from HRTEM images*. *Ultramicroscopy*, vol. 107, 1186–1193, 2007.
- [Gao 2018] P. Gao, A. Kumamoto, N. Lugg, N. Shibata, and Y. Ikuhara. *Picometer-scale atom position analysis in annular bright-field STEM imaging*. *Ultramicroscopy*, vol. 184, 177–187, 2018.
- [García 2013] R. A. García. *Stellar Pulsations: Impact of New Instrumentation and New Insights*. In *Advances in Solid State Physics*, J. C. Suárez, R. Garrido, L. A. Balona, and J. Christensen-Dalsgaard (eds.), volume 31. Springer, 2013.
- [Gauch 2003] H. G. Gauch. *Scientific Method in Practice*. Cambridge Univ Press, 2003.
- [Gauquelin 2017] N. Gauquelin, K. H. W. van den Bos, A. Beche, F. F. Krause, I. Lobato, S. Lazar, A. Rosenauer, S. Van Aert, and J. Verbeeck. *Determining oxygen relaxations at an interface: A comparative study between transmission electron microscopy techniques*. *Ultramicroscopy*, vol. 181, 178–190, 2017.
- [Geman 1992] S. Geman, E. Bienenstock, and R. Doursat. *Neural networks and the bias/variance dilemma*. *Neural Computation*, vol. 4, 1–58, 1992.
- [Geuens 2002] P. Geuens, and D. Van Dyck. *The S-state model: a work horse for HRTEM*. *Ultramicroscopy*, vol. 93, 179–198, 2002.
- [Girit 2009] C. O. Girit, J. C. Meyer, R. Erni, M. D. Rosell, C. Kisielowski, L. Yang, C.-H. Park, M. F. Crommie, M. L. Cohen, S. G. Louie, and A. Zettl. *Graphene at the edge: stability and dynamics*. *Science*, vol. 323, 1705–1708, 2009.
- [Gómez-Graña 2013] S. Gómez-Graña, J. Pérez-Juste, R. A. Alvarez-Puebla, A. Guerrero-Martínez, and L. M. Liz-Marzán. *Self-Assembly of Au@Ag Nanorods Mediated by Gemini Surfactants for Highly Efficient SERS-Active Supercrystals*. *Advanced Optical Materials*, vol. 1, no. 7, 477–481, 2013.
- [Gonnissen 2014] J. Gonnissen, A. De Backer, A. J. den Dekker, G. T. Martinez, A. Rosenauer, J. Sijbers, and S. Van Aert. *Optimal experimental design for the detection of light atoms from high-resolution scanning transmission electron microscopy images*. *Applied Physics Letters*, vol. 105, no. 063116, 2014.
- [Gonnissen 2016a] J. Gonnissen, D. Batuk, G. F. Nataf, L. Jones, A. M. Abakumov, S. Van Aert, D. Schryvers, and E. K. H. Salje. *Direct Observation of Ferroelectric Domain Walls in LiNbO<sub>3</sub>: Wall-Meanders, Kinks, and Local Electric Charges*. *Advanced Functional Materials*, vol. 26, no. 42, 7599–7604, 2016.
- [Gonnissen 2016b] J. Gonnissen, A. De Backer, A. J. den Dekker, J. Sijbers, and S. Van Aert. *Detecting and locating light atoms from high-resolution STEM images: The quest for a single optimal design*. *Ultramicroscopy*, vol. 170, 128–138, 2016.
- [Gonnissen 2017] J. Gonnissen, A. De Backer, A. J. den Dekker, J. Sijbers, and S. Van Aert. *Atom-counting in High Resolution Electron Microscopy: TEM or STEM—That’s the question*. *Ultramicroscopy*, vol. 174, 112–120, 2017.

- [Goodman 1974] P. Goodman, and A. F. Moodie. *Numerical evaluations of N-beam wave functions in electron scattering by the multi-slice method*. Acta Crystallographica Section A, vol. 30, no. 2, 280–290, 1974.
- [Goodman 2005] J. W. Goodman. *Introduction to Fourier optics*. Roberts and Company Publishers, 3rd edition, 2005.
- [Goris 2012a] B. Goris, S. Bals, W. Van den Broek, E. Carbó-Argibay, S. Gómez-Graña, L. M. Liz-Marzán, and G. Van Tendeloo. *Atomic-scale determination of surface facets in gold nanorods*. Nature Materials, vol. 11, 930–935, 2012.
- [Goris 2012b] B. Goris, W. Van den Broek, K. J. Batenburg, H. Heidari, and S. Bals. *Electron tomography based on a total variation minimization reconstruction technique*. Ultramicroscopy, vol. 113, 120–130, 2012.
- [Goris 2013a] B. Goris, A. De Backer, S. Van Aert, S. Gómez-Graña, L. M. Liz-Marzán, G. Van Tendeloo, and S. Bals. *Three-Dimensional Elemental Mapping at the Atomic Scale in Bimetallic Nanocrystals*. Nano Letters, vol. 13, 4236–4241, 2013.
- [Goris 2013b] B. Goris, T. Roelandts, K. J. Batenburg, H. Heidari Mezerji, and S. Bals. *Advanced reconstruction algorithms for electron tomography: From comparison to combination*. Ultramicroscopy, vol. 127, 40–47, 2013.
- [Goris 2014a] B. Goris, L. Polavarapu, S. Bals, G. Van Tendeloo, and L. M. Liz-Marzán. *Monitoring galvanic replacement through three-dimensional morphological and chemical mapping*. Nano letters, vol. 14, no. 6, 3220–3226, 2014.
- [Goris 2014b] B. Goris, S. Turner, S. Bals, and G. Van Tendeloo. *Three-dimensional valency mapping in ceria nanocrystals*. ACS nano, vol. 8, no. 10, 10878–10884, 2014.
- [Goris 2015] B. Goris, J. De Beenhouwer, A. De Backer, D. Zanaga, K. J. Batenburg, A. Sánchez-Iglesias, L. M. Liz-Marzán, S. Van Aert, S. Bals, J. Sijbers, and G. Van Tendeloo. *Measuring Lattice Strain in Three Dimensions through Electron Microscopy*. Nano Letters, vol. 15, no. 10, 6996–7001, 2015.
- [Goshtasby 2005] A. A. Goshtasby. *2-D and 3-D Image Registration: for Medical, Remote Sensing, and Industrial Applications*. Wiley Press, 2005.
- [Gregory 2005] P. C. Gregory. *Bayesian Logical Data Analysis for the Physical Sciences*. Cambridge Univ Press, 2005.
- [Grieb 2012] T. Grieb, K. Müller, R. Fritz, M. Schowalter, N. Neugebohrn, N. Knaub, K. Volz, and A. Rosenauer. *Determination of the chemical composition of GaNAs using STEM HAADF imaging and STEM strain state analysis*. Ultramicroscopy, vol. 117, 15–23, 2012.
- [Grillo 2011] V. Grillo. *An advanced study of the response of ADF detector*. J. Phys. Conf. Ser., vol. 326, 012036, 2011.
- [Gu 2011] L. Gu, C. Zhu, H. Li, Y. Yu, C. Li, S. Tsukimoto, J. Maier, and Y. Ikuhara. *Direct observation of lithium staging in partially delithiated LiFePO<sub>4</sub> at atomic resolution*. J. Am. Chem. Soc., vol. 133, 4661–4663, 2011.
- [Gull 1978] S.F. Gull, and G. J. Daniell. *Image reconstruction from incomplete and noisy data*. Nature, vol. 272, 686–690, 1978.
- [Gull 1984] S. F. Gull, and Skil. *Maximum entropy method in image processing*. IEE Proc., vol. 131F, 646–659, 1984.
- [Habeck 2011] M. Habeck. *Statistical mechanics analysis of sparse data*. J. Struct. Biol., vol. 173, 541–548, 2011.

- [Hadermann 2011] J. Hadermann, A. M. Abakumov, S. Turner, S. Hafideddine, N. R. Khasanova, E. V. Antipov, and G. Van Tendeloo. *Solving the structure of Li ion battery materials with precession electron diffraction: application to  $\text{Li}_2\text{CoPo}_4\text{F}$* . Chem. Mater., vol. 23, 3540, 2011.
- [Hadermann 2012] J. Hadermann, A. Abakumov, S. Van Rompaey, T. Perkisas, Y. Filinchuk, and G. Van Tendeloo. *Crystal structure of a lightweight borohydride from submicrometer crystallites by precession electron diffraction*. Chem. Mater., vol. 24, 3401, 2012.
- [Haider 1995] M. Haider, G. Braunshausen, and E. Schwan. *Correction of the spherical aberration of a 200 kV TEM by means of a hexapole-corrector*. Optik, vol. 99, no. 4, 167–179, 1995.
- [Haider 1998a] M. Haider, H. Rose, S. Uhlemann, B. Kabius, and K. Urban. *Towards 0.1 nm resolution with the first spherical corrected transmission electron microscope*. Journal of Electron Microscopy, vol. 47, no. 5, 395–405, 1998.
- [Haider 1998b] M. Haider, S. Uhlemann, E. Schwan, H. Rose, B. Kabius, and K. Urban. *Electron microscopy image enhanced*. Nature, vol. 392, 768–769, 1998.
- [Haider 2010] M. Haider, P. Hartel, H. Müller, S. Uhlemann, and J. Zach. *Information Transfer in a TEM Corrected for Spherical and Chromatic Aberration*. Microsc. Microanal., vol. 16, 393–408, 2010.
- [Haight 1967] F.A. Haight. *Handbook of the Poisson Distribution*. Wiley, 1967.
- [Hammel 1995] M. Hammel, and H. Rose. *Optimum rotationally symmetric detector configurations for phase-contrast imaging in scanning transmission electron microscopy*. Ultramicroscopy, vol. 58, 403–415, 1995.
- [Hannan 1979] E. J. Hannan, and B. G. Quinn. *The determination of the order of an autoregression*. J. R. Stat. Soc., vol. 41, 190–195, 1979.
- [Hartel 1996] P. Hartel, H. Rose, and C. Dinges. *Conditions and reasons for incoherent imaging in STEM*. Ultramicroscopy, vol. 63, 63–114, 1996.
- [Hawkes 2015] P. W. Hawkes. *The correction of electron lens aberrations*. Ultramicroscopy, vol. 156, A1–A64, 2015.
- [Hayashi 1998] C. Hayashi. *Data Science, Classification, and Related Methods. Studies in Classification, Data Analysis, and Knowledge Organization*, Chapter What is Data Science? Fundamental Concepts and a Heuristic Example, 40–51. Springer, 1998.
- [He 2011] X. He, L. Gu, C. Zhu, Y. Yu, C. Li, Y.-S. Hu, S. Tsukimoto, J. Maier, Y. Ikuhara, and X. Duan. *Direct imaging of lithium ions using aberration corrected annular-bright-field scanning transmission electron microscopy and associated contrast mechanisms*. Mater. Express, vol. 1, 43–50, 2011.
- [Henderson 1995] R. Henderson. *The potential and limitations of neutrons, electrons and X-rays for atomic resolution microscopy of unstained biological molecules*. Quarterly Reviews of Biophysics, vol. 28, 171–193, 1995.
- [Henglein 2000] A. Henglein. *Preparation and Optical Absorption Spectra of  $\text{Au}_{\text{core}}\text{Pt}_{\text{shell}}$  and  $\text{Pt}_{\text{core}}\text{Au}_{\text{shell}}$  Colloidal Nanoparticles in Aqueous Solution*. The Journal of Physical Chemistry B, vol. 104, no. 10, 2201–2203, 2000.
- [Herman 2007] G. T. Herman, and A. Kuba. *Advances in Discrete Tomography and Its Applications*. Birkhauser Boston, 2007.
- [Herrmann 1997] K.-H. Herrmann. *Image recording in microscopy*. In Handbook of microscopy - Applications in materials science, solid-state physics, and chemistry, Methods II, 885–921. Weinheim VCH, 1997.

- [Higuchi 1998] T. Higuchi, Tsukamoto T., N. Sata, Ishigame M., Y. Tezuka, and Shin S. *Electronic structure of p-type SrTiO<sub>3</sub> by photoemission spectroscopy*. Phys. Rev. B, vol. 57, 6978, 1998.
- [Hirsch 2013] P. B. Hirsch, J. G. Lozano, S. Rhode, M. K. Horton, M. A. Moram, S. Zhang, M. J. Kappers, C. J. Humphreys, A. Yasuhara, E. Okunishi, and P. D. Nellist. *The dissociation of the [a+ c] dislocation in GaN*. Philosophical Magazine, vol. 93, no. 28-30, 3925–3938, 2013.
- [Hjort 2006] N. L. Hjort, and G. Claeskens. *Focused information criterion and model averaging for the Cox hazard regression model*. Journal of the American Statistical Association, vol. 98, 900–916, 2006.
- [Hofer 2003] W. A. Hofer. *Challenges and errors: interpreting high resolution images in scanning tunneling microscopy*. Progress in surface science, vol. 71, no. 5, 147–183, 2003.
- [Hoffman 1997] R. Hoffman, V. I. Minkin, and B. K. Carpenter. *Ockham's razor and chemistry*. International Journal for Philosophy of Chemistry, vol. 3, 3–28, 1997.
- [Holmes 2014] A. T. Holmes. *Simple Bayesian method for improved analysis of quasi-two-dimensional scattering data*. Physical Review B, vol. 90, 024514, 2014.
- [Houben 2006] L. Houben, A. Thust, and K. Urban. *Atomic-precision determination of the reconstruction of a 90° tilt boundary in YBa<sub>2</sub>Cu<sub>3</sub>O<sub>7-δ</sub> by aberration corrected HRTEM*. Ultramicroscopy, vol. 106, 200–214, 2006.
- [Houben 2011] L. Houben, and M. B. Sadan. *Refinement procedure for the image alignment in high-resolution electron tomography*. Ultramicroscopy, vol. 111, no. 9, 1512–1520, 2011.
- [Hovden 2012] R. Hovden, and D. A. Muller. *Efficient elastic imaging of single atoms on ultrathin supports in a scanning transmission electron microscope*. Ultramicroscopy, vol. 109, 59–65, 2012.
- [Hsieh 2004] W.-K. Hsieh, F.-R. Chen, J.-J. Kai, and A. I. Kirkland. *Resolution extension and exit wave reconstruction in complex HREM*. Ultramicroscopy, vol. 98, 99–114, 2004.
- [Huang 2010] T. Huang, and X.-H. N. Xu. *Synthesis and characterization of tunable rainbow colored colloidal silver nanoparticles using single-nanoparticle plasmonic microscopy and spectroscopy*. Journal of Materials Chemistry, vol. 20, 9867–9876, 2010.
- [Huang 2011] R. Huang, T. Hitosugi, S. D. Findlay, C. A. J. Fisher, Y. H. Ikuhara, H. Moriwake, H. Oki, and Y. Ikuhara. *Real-time direct observation of Li in LiCoO<sub>2</sub> cathode material*. Appl. Phys. Lett., vol. 98, 051913, 2011.
- [Huang 2012] R. Huang, Y.-H. Wen, Z.-Z. Zhu, and S.-G. Sun. *Pt–Pd bimetallic catalysts: structural and thermal stabilities of core–shell and alloyed nanoparticles*. The Journal of Physical Chemistry C, vol. 116, no. 15, 8664–8671, 2012.
- [Huijben 2006] M. Huijben, Rijnders G., D. H. A. Blank, S. Bals, S. Van Aert, J. Verbeeck, G. Van Tendeloo, A. Brinkman, and H. Hilgenschamp. *Electronically coupled complementary interfaces between perovskite band insulators*. Nature Materials, vol. 5, 556–560, 2006.
- [Husain 2016] M. Husain, and Z. H. Khan. *Advances in nanomaterials*. Springer, 2016.
- [Hwang 2012] H. Y. Hwang, Y. Iwasa, M. Kawasaki, B. Keimer, N. Nagaosa, and Y. Tokura. *Emergent phenomena at oxide interfaces*. Nature Materials, vol. 11, 103–113, 2012.
- [Hwang 2013] J. Hwang, J. Y. Zhang, A. J. D'Alfonso, L. J. Allen, and S. Stemmer. *Three-dimensional imaging of individual dopant atoms in SrTiO<sub>3</sub>*. Physical Review Letters, vol. 111, 266101, 2013.

- [Ievlev 2015] A. V. Ievlev, S. Jesse, T. J. Cochell, R. R. Unocic, V. A. Protopopescu, and S. V. and Kalinin. *Quantitative description of crystal nucleation and growth from in situ liquid scanning transmission electron microscopy*. ACS Nano, vol. 9, 11784–11791, 2015.
- [Isaacson 1979] M. Isaacson, D. Kopf, M. Ohtsuki, and M. Utlaut. *Atomic imaging using the dark-field annular detector in the STEM*. Ultramicroscopy, vol. 4, 1979.
- [Ishikawa 2014a] R. Ishikawa, A. R. Lupini, S. D. Findlay, and S. J. Pennycook. *Quantitative annular dark field electron microscopy using single electron singles*. Microsc. Microanal., vol. 20, 99, 2014.
- [Ishikawa 2014b] R. Ishikawa, R. Mishra, A. R. Lupini, S. D. Findlay, T. Taniguchi, S. T. Pantelides, and S. J. Pennycook. *Direct observation of dopant atom diffusion in a bulk semiconductor crystal enhanced by a large size mismatch*. Physical Review Letters, vol. 113, 155501, 2014.
- [Ishizuka 2002] K. Ishizuka. *A practical approach for STEM image simulation based on the FFT multislice method*. Ultramicroscopy, vol. 90, no. 2, 71–83, 2002.
- [Jagannathan 1989] R. Jagannathan, R. Simon, and E. C. G. Sudarshan. *Quantum theory of magnetic electron lenses based on the Dirac equation*. Physics Letters A, vol. 134, 457–464, 1989.
- [Jagannathan 1990] R. Jagannathan. *Quantum theory of electron lenses based on the Dirac equation*. Physical Review A, vol. 42, 6674–6689, 1990.
- [Jany 2017] B. R. Jany, N. Gauquelin, T. Willhammar, M. Nikiel, K. H. W. van den Bos, A. Janas, K. Szajna, J. Verbeeck, S. Van Aert, G. Van Tendeloo, and F. Krok. *Controlled growth of hexagonal gold nanostructures during thermally induced self-assembling on Ge (001) surface*. Scientific Reports, vol. 7, 42420, 2017.
- [Jaynes 1957] E. Jaynes. *Information Theory and Statistical mechanics*. Physical Rev, vol. 106, 620–630, 1957.
- [Jaynes 2003] E. T. Jaynes. *Probability Theory: The logic of Science*. Cambridge University Press, 2003.
- [Jesson 1995] D. E. Jesson, and S. J. Pennycook. *Incoherent imaging of crystals using thermally scattered electrons*. Proc. Roy. Soc. A, vol. 449, 273–293, 1995.
- [Jia 2004] C. L. Jia, M. Lentzen, and K. Urban. *High-Resolution Transmission Electron Microscopy Using Negative Spherical Aberration*. Microsc. Microanal., vol. 10, 174–184, 2004.
- [Jia 2008] C.-L. Jia, S.-B. Mi, K. Urban, I. Vrejoiu, M. Alexe, and D. Hesse. *Atomic-scale study of electric dipoles near charged and uncharged domain walls in ferroelectric films*. Nature Materials, vol. 7, 57–61, January 2008.
- [Jia 2009] C. L. Jia, S. B. Mi, M. Faley, U. Poppe, J. Schubert, and K. Urban. *Oxygen octahedron reconstruction in the SrTiO<sub>3</sub>/LaAlO<sub>3</sub> heterointerfaces investigated using aberration-corrected ultrahigh-resolution transmission electron microscopy*. Physical Review B, vol. 79, no. 8, 081405, 2009.
- [Jia 2014] C. L. Jia, S. B. Mi, J. Barthel, D. W. Wang, R. E. Dunin-Borkowski, K. W. Urban, and A. Thust. *Determination of the 3D shape of a nanoscale crystal with atomic resolution from a single image*. Nature Materials, vol. 13, 1044–1049, 2014.
- [Jones 2013] L. Jones, and P. D. Nellist. *Identifying and correcting scan noise and drift in the scanning transmission electron microscope*. Microscopy and Microanalysis, vol. 19, 1050–1060, 2013.

- [Jones 2014] L. Jones, K. E. MacArthur, V. T. Fauske, A. T. J. van Helvoort, and P. D. Nellist. *Rapid Estimation of Catalyst Nanoparticle Morphology and Atomic-Coordination by High-Resolution Z-Contrast Electron Microscopy*. *Nano Letters*, vol. 14, no. 11, 6336–6341, 2014.
- [Jones 2015] L. Jones, H. Yang, T. J. Pennycook, M. S. J. Marshall, S. Van Aert, N. D. Browning, M. R. Castell, and P. D. Nellist. *Smart align - a new tool for robust non-rigid registration of scanning microscope data*. *Advanced Structural and Chemical Imaging*, vol. 1, :8, 2015.
- [Jones 2017] L. Jones, Sigurd Wenner, M. Nord, P. H. Ninive, O. M. Løvvik, R. Holmestad, and P. D. Nellist. *Optimising multi-frame ADF-STEM for high-precision atomic-resolution strain mapping*. *Ultramicroscopy*, vol. 179, 57–62, 2017.
- [Karakulina 2018] O. M. Karakulina, A. Demortiere, W. Dachraoui, A. M. Abakumov, and J. Hadermann. *In situ electron diffraction tomography using a liquid electrochemical transmission electron microscopy cell for crystal structure determination of cathode materials for Li-ion batteries*. *Nano Letters*, vol. 18, 6286, 2018.
- [Kauko 2013a] H. Kauko, T. Grieb, R. Bjørge, M. Schowalter, A. M. Munshi, H. Weman, A. Rosenauer, and A. T. J. van Helvoort. *Compositional characterization of GaAs/GaAsSb nanowires by quantitative HAADF-STEM*. *Micron*, vol. 44, 254–260, 2013.
- [Kauko 2013b] H. Kauko, C. L. Zheng, Y. Zhu, S. Glanvill, C. Dwyer, A. M. Munshi, B. O. Fimland, A. T. J. van Helvoort, and J. Etheridge. *Compositional analysis of GaAs/AlGaAs heterostructures using quantitative scanning transmission electron microscopy*. *Applied Physics Letters*, vol. 103, no. 23, 232111, 2013.
- [Ke 2010] X. Ke, S. Bals, D. Cott, T. Hantschel, H. Bender, and G. Van Tendeloo. *Three-dimensional analysis of carbon nanotube networks in interconnects by electron tomography without missing wedge artefacts*. *Microscopy and Microanalysis*, vol. 16, 210–217, 2010.
- [Khoshouei 2017] M. Khoshouei, M. Radjainia, W. Baumeister, and R. Danev. *Cryo-EM structure of haemoglobin at 3.2 Å determined with the Volta phase plate*. *Nature Communications*, vol. 8, 16099, 2017.
- [Kim 2012] Y.-M. Kim, J. He, M. D. Biegalski, H. Ambaye, V. Lauter, H. M. Christen, S. T. Pantelides, S. J. Pennycook, S. V. Kalinin, and A. Y. Borisevich. *Probing oxygen vacancy concentration and homogeneity in solid-oxide fuel-cell cathode materials on the subunit-cell level*. *Nature Materials*, vol. 11, 888–894, 2012.
- [Kimoto 2010] K. Kimoto, T. Asaka, X. Yu, T. Nagai, Y. Matsui, and K. Ishizuka. *Local crystal structure analysis with several picometer precision using scanning transmission electron microscopy*. *Ultramicroscopy*, vol. 110, 778–782, 2010.
- [Kirkland 1996] E. J. Kirkland, and M. G. Thomas. *A high efficient annular dark field detector for STEM*. *Ultramicroscopy*, vol. 62, 79–88, 1996.
- [Kirkland 2010] E. J. Kirkland. *Advanced Computing in Electron Microscopy*. Springer, 2nd edition, 2010.
- [Kirkland 2011] E. J. Kirkland. *On the optimum probe in aberration corrected ADF-STEM*. *Ultramicroscopy*, vol. 111, 1523–1530, 2011.
- [Kirkland 2016] E. J. Kirkland. *Computation in electron microscopy*. *Acta Crystallographica Section A: Foundations and Advances*, vol. 72, 1–27, 2016.
- [Kisielowski 2001] C. Kisielowski, C. J. D. Hetherington, Y. C. Wang, R. Kilaas, M. A. O’Keefe, and A. Thust. *Imaging columns of light elements carbon, nitrogen and oxygen with sub Ångstrom resolution*. *Ultramicroscopy*, vol. 89, 243–263, 2001.

- [Kisielowski 2008] C. Kisielowski, B. Freitag, M. Bischoff, H. van Lin, S. Lazar, G. Knippels, P. Tiemeijer, M. van der Stam, S. von Harrach, M. Stekelenburg, M. Haider, S. Uhlemann, H. Müller, P. Hartel, B. Kabius, D. Miller, I. Petrov, E. A. Olson, T. Donchev, E. A. Kenik, A. R. Lupini, J. Bentley, S. J. Pennycook, I. M. Anderson, A. M. Minor, A. K. Schmid, T. Duden, V. Radmilovic, Q. M. Ramasse, M. Watanabe, R. Erni, E. A. Stach, P. Denes, and U. Dahmen. *Detection of Single Atoms and Buried Defects in Three Dimension by Aberration-Corrected Electron Microscope with 0.5-Å Information Limit*. *Microsc. Microanal.*, vol. 14, 469–477, 2008.
- [Kittel 2004] C. Kittel, and A. Zetl. *Introduction to Solid State Physics*. John Wiley And Sons Ltd, 8th edition, 2004.
- [Klabunde 2002] K. J. Klabunde (ed.). *Nanoscale Materials in Chemistry*. John Wiley and Sons, Inc., 2002.
- [Klenov 2007] D. O. Klenov, S. D. Findlay, L. J. Allen, and S. Stemmer. *Influence of orientation on the contrast of high-angle annular dark-field images of silicon*. *Physical Review B*, vol. 76, no. 1, 014111, 2007.
- [Klingstedt 2012] M. Klingstedt, M. Sundberg, L. Eriksson, S. Haigh, A. Kirkland, Grüner D., A. De Backer, S. Van Aert, and O. Terasaki. *Exit wave reconstruction from focal series of HRTEM images, single crystal XRD and total energy studies on  $Sb_xWO_{3+y}$  ( $x < 0.11$ )*. *Z. Kristallogr.*, vol. 227, 341–349, 2012.
- [Knapek 1980] E. Knapek, and J. Dubochet. *Beam damage to organic material is considerably reduced in cryo-electron microscopy*. *Journal of Molecular Biology*, vol. 141, 147–161, 1980.
- [Knoll 1932] M. Knoll, and E. Ruska. *Das elektronenmikroskop*. *Zeitschrift für Physik*, vol. 78, no. 5, 318–339, 1932.
- [Knoll 1935] M. Knoll. *Aufladepotential und sekundäremission elektronenbestrahlter körper*. *Zeitschrift für Technische Physik*, vol. 16, 467–475, 1935.
- [Knuth 2012] K. H. Knuth, B. Placek, and Z. Richards. *Detection and characterization of non-transiting extra-solar planets in Kepler data using reflected light variations*. In *Proceedings of the Conference on Intelligent Data Understanding 2012*, 31–38, 2012.
- [Knuth 2015] K. H. Knuth, M. Habeck, N. K. Malakar, A. M. Mubeen, and B. Placek. *Bayesian evidence and model selection*. *Digital Signal Processing*, vol. 47, 50–67, 2015.
- [Kolodiaznyi 2005] T. Kolodiaznyi, and A. Petric. *The applicability of Sr-deficient n-type  $SrTiO_3$  for SOFC anodes*. *Jof Electroceramics*, vol. 15, 5–11, 2005.
- [Koneti 2019] S. Koneti, L. Roiban, F. Dalmas, C. Langlois, A.-S. Gay, A. Cabiac, T. Grenier, H. Banjak, V. Maxim, and T. Epicier. *Fast electron tomography: Applications to beam sensitive samples and in situ TEM or operando environmental TEM studies*. *Materials Characterization*, vol. 151, 480–495, 2019.
- [Konishi 2008] S. Konishi, and G. Kitagawa. *Information Criteria and Statistical Modeling*. Springer, 2008.
- [Kook 2016] S. Kook, R. Zhang, Q. N. Chan, T. Aizawa, K. Kondo, L. M. Pickett, E. Cenker, G. Bruneaux, O. Andersson, J. Pagels, and E. Z. Nordin. *Automated detection of primary particles from transmission electron microscope (TEM) images of soot aggregates in diesel engine environments*. *SAE International Journal of Engines*, vol. 9, 279–296, 2016.
- [Korneychuk 2018] S. Korneychuk. *Local study of the band gap and structure of diamond-based nano-materials by analytical transmission electron microscopy*. PhD thesis, University of Antwerp, 2018.

- [Kosasih 2018] F. U. Kosasih, and C. Ducati. *Characterising degradation of perovskite solar cells through in situ and operando electron microscopy*. *Nano Energy*, vol. 47, 243–256, 2018.
- [Kothleitner 2014] G. Kothleitner, M. J. Neish, N. R. Lugg, S. D. Findlay, W. Grogger, F. Hofer, and L. J. Allen. *Quantitative elemental mapping at atomic resolution using X-ray spectroscopy*. *Physical Review Letters*, vol. 112, no. 8, 085501, 2014.
- [Kramberger 2016] C. Kramberger, and J. C. Meyer. *Progress in structure recovery from low dose exposures: Mixed molecular adsorption, exploitation of symmetry and reconstruction from the minimum signal level*. *Ultramicroscopy*, vol. 170, 60–68, 2016.
- [Kramberger 2017] C. Kramberger, A. Mittelberger, C. Hofer, and J. C. Meyer. *Analysis of point defects in graphene using low dose scanning transmission electron microscopy imaging and maximum likelihood reconstruction*. *Phys. Status Solidi B*, vol. 254, 1700176, 2017.
- [Krause 2016] F. F. Krause, M Schowalter, T. Grieb, K. Müller-Casparly, T. Mehrrens, and A Rosenauer. *Effects of instrument imperfections on quantitative scanning transmission electron microscopy*. *Ultramicroscopy*, vol. 161, 146–160, 2016.
- [Krivanek 2009] O. L. Krivanek, N. Dellby, and M. F. Murfitt. In *Handbook of Charged Particle Optics*, 601–641. CRC Press, 2009.
- [Krivanek 2010] O. L. Krivanek, M. F. Chisholm, V. Nicolosi, T. J. Pennycook, G. J. Corbin, N. Dellby, M. F. Murfitt, C. S. Own, Z. S. Szilagy, M. P. Oxley, S. T. Pantelides, and S. J. Pennycook. *Atom-by-atom structural and chemical analysis by annular dark-field electron microscopy*. *Nature*, vol. 464, 571–574, 2010.
- [Krivanek 2015] O. L. Krivanek, T. C. Lovejoy, and N. Dellby. *Aberration-corrected STEM for atomic-resolution imaging and analysis*. *Journal of Microscopy*, vol. 259, 165–172, 2015.
- [Kundu 2014] P. Kundu, S. Turner, S. Van Aert, N. Ravishankar, and G. Van Tendeloo. *Atomic Structure of Quantum Gold Nanowires: Quantification of the Lattice Strain*. *ACS Nano*, vol. 8, 599–606, 2014.
- [Leary 2013] R. Leary, Z. Saghi, P. A. Midgley, and D. J. Holland. *Compressed sensing electron tomography*. *Ultramicroscopy*, vol. 131, 70–91, 2013.
- [LeBeau 2008] J. M. LeBeau, and S. Stemmer. *Experimental quantification of annular dark-field images in scanning transmission electron microscopy*. *Ultramicroscopy*, vol. 108, 1653–1658, 2008.
- [LeBeau 2010] J. M. LeBeau, S. D. Findlay, L. J. Allen, and S. Stemmer. *Standardless Atom Counting in Scanning Transmission Electron Microscopy*. *Nanoletters*, vol. 10, 4405–4408, 2010.
- [Lee 2008] C. Lee, X. Wei, J. W. Kysar, and J. Hone. *Measurement of the elastic properties and intrinsic strength of monolayer graphene*. *Science*, vol. 321, 385–388, 2008.
- [Lee 2011] S. Lee, Y. Oshima, H. Sawada, F. Hosokawa, E. Okunishi, T. Kaneyama, Y. Kondo, S. Nikita, H. Takagi, Y. Tanishiro, and K. Takayanagi. *Counting lithium ions in the diffusion channel of a  $\text{LiV}_2\text{O}_4$* . *Journal of Applied Physics*, vol. 109, 113530, 2011.
- [Lee 2016] P. W. Lee, V. N. Singh, G. Y. Guo, H.-J. Liu, J.-C. Lin, Y.-H. Chu, C. H. Chen, and M.-W. Chu. *Hidden lattice instabilities as origin of the conductive interface between insulating  $\text{LaAlO}_3$  and  $\text{SrTiO}_3$* . *Nature communications*, vol. 7, 12773, 2016.
- [Levenberg 1944] K. Levenberg. *A method for the solution of certain nonlinear problems in least-squares*. *Quarterly Applied Mathematics*, vol. 2, 164–168, 1944.
- [Lever 2016] J. Lever, M. Krzywinski, and N. Altman. *Model selection and overfitting*. *Nature Methods*, vol. 13, no. 9, 2016.

- [Levi 1999] M. D. Levi, G. Salitra, B. Markovsky, H. Teller, D. Aurbach, U. Heider, and L. Heider. *Solid-state electrochemical kinetics of Li-ion intercalation into  $\text{Li}_{1-x}\text{CoO}_2$ : simultaneous application of electroanalytical techniques SSCV, PITT, and EIS*. Journal of the Electrochemical Society, 1999.
- [Levin 2017] B. D. Levin, M. J. Zachmann, J. G. Werner, R. Sahore, K. X. Nguyen, Y. Han, B. Xie, L. Ma, L. A. Archer, E. P. Giannelis, U. Wiesner, L. F. Kourkoutis, and D. A. Muller. *Characterization of sulfur and nanostructured sulfur battery cathodes in electron microscopy without sublimation artefacts*. Microscopy and Microanalysis, vol. 23, 155–162, 2017.
- [Li 2009a] H. Li, Z. Wang, and L. Chen. *Research on advanced materials for Li-ion batteries*. Advanced Materials, vol. 21, 4593–4607, 2009.
- [Li 2009b] Z. Li, M. L. Baker, W. Jiang, M. K. Estes, and B. V. Prasad. *Rotavirus architecture at subnanometer resolution*. Journal of Virology, 2009.
- [Li 2015] Y. Li, D. Zakharov, S. Zhao, R. Tappero, U. Jung, A. Elsen, P. Baumann, R. G. Nuzzo, E. A. Stach, and A. I. Frenkel. *Complex structural dynamics of nanocatalysts revealed in operando conditions by correlated imaging and spectroscopy probes*. Nature Communications, vol. 6, 7583, 2015.
- [Liao 2016a] Z. Liao, M. Huijben, Z. Zhong, N. Gauquelin, S. Macke, R. J. Green, S. Van Aert, J. Verbeeck, G. Van Tendeloo, K. Held, G. A. Sawatzky, G. Koster, and G. Rijnders. *Controlled lateral anisotropy in correlated manganite heterostructures by interface-engineered oxygen octahedral coupling*. Nature Materials, vol. 15, 425–431, 2016.
- [Liao 2016b] Z. Liao, M. Huijben, Z. Zhong, N. Gauquelin, S. Macke, R. J. Green, S. Van Aert, J. Verbeeck, G. Van Tendeloo, K. Held, G. A. Sawatzky, G. Koster, and G. Rijnders. *Controlled lateral anisotropy in correlated manganite heterostructures by interface-engineered oxygen octahedral coupling*. Nature Materials, vol. 15, 425–431, 2016.
- [Liu 2004] M. Z. Liu, and P. Guyot-Sionnest. *Synthesis and optical characterization of Au/Ag core/shell nanorods*. Journal of Physical Chemistry B, vol. 108, 5882–5888, 2004.
- [Liz-Marzán 2003] L. Liz-Marzán, and P. V. Kamat. *Nanoscale Materials*. Springer, US, 2003.
- [Llordés 2012] A. Llordés, A. Palau, J. Gázquez, M. Coll, R. Vlad, A. Pomar, J. Arbiol, R. Guzman, S. Ye, V. Rouco, F. Sandiumenge, S. Ricart, T. Puig, M. Varela, D. Chateigner, J. Vanacken, J. Gutiérrez, V. Moshchalkov, G. Deutscher, C. Magen, and X. Obradors. *Nanoscale strain-induced pair suppression as a vortex-pinning mechanism in high-temperature superconductors*. Nature materials, vol. 11, no. 4, 329–336, 2012.
- [Loane 1991] R. F. Loane, P. Xu, and J. Silcox. *Thermal vibrations in convergent-beam electron diffraction*. Acta Crystallographica Section A, vol. 47, no. 3, 267–278, 1991.
- [Lobato 2014] I. Lobato. *Accurate modelling of high angle electron scattering*. PhD thesis, University of Antwerp, 2014.
- [Lobato 2015] I. Lobato, and D. Van Dyck. *MULTEM: A new multislice program to perform accurate and fast electron diffraction and imaging simulation using Graphics Processing Units with CUDA*. Ultramicroscopy, vol. 156, 9–17, 2015.
- [Lobato 2016] I. Lobato, S. Van Aert, and J. Verbeeck. *Progress and new advances in simulating electron microscopy datasets using {MULTEM}*. Ultramicroscopy, vol. 168, 17 – 27, 2016.
- [Locquet 1998] J.-P. Locquet, J. Perret, J. Fompeyrine, E. Mächler, J. W. Seo, and G. Van Tendeloo. *Doubling the critical temperature of  $\text{La}_{1.9}\text{Sr}_{0.1}\text{CuO}_4$  using epitaxial strain*. Nature, vol. 394, no. 6692, 453–456, 1998.

- [Lubk 2012] A. Lubk, M. D. Rossell, J. Seidel, Q. He, S. Y. Yang, Y. H. Chu, R. Ramesh, M. J. Hytch, and E. Snoeck. *Evidence of sharp and diffuse domain walls in BiFeO<sub>3</sub> by means of unit-cell-wise strain and polarization maps obtained with high resolution scanning transmission electron microscopy*. Physical review letters, vol. 109, no. 4, 047601, 2012.
- [Luo 2004] W. Luo, W. Duan, S. G. Louie, and M. L. Cohen. *Structural and electronic properties of n-doped and p-doped SrTiO<sub>3</sub>*. Phys. Rev. B, vol. 70, 214109, 2004.
- [Lynch 1972] D. F. Lynch, and M.A. O’Keefe. *n-Beam lattice images. II. Methods of calculation*. Acta Crystallographica Section A: Crystal Physics, Diffraction, Theoretical and General Crystallography, vol. 28, no. 6, 536–548, 1972.
- [MacArthur 2015] K. E. MacArthur, A. J. D’Alfonso, D. Ozkaya, L. J. Allen, and P. D. Nellist. *Optimal ADF STEM imaging parameters for tilt-robust image quantification*. Ultramicroscopy, vol. 156, 1–8, 2015.
- [MacArthur 2016a] K. E. MacArthur, T. J. A. Slater, S. J. Haigh, D. Ozkaya, P. D. Nellist, and S. Lozano-Perez. *Compositional quantification of PtCo acid-leached fuel cell catalysts using EDX partial cross sections*. Materials Science and Technology, vol. 32, no. 3, 248–253, 2016.
- [MacArthur 2016b] K. E. MacArthur, T. J. A. Slater, S. J. Haigh, D. Ozkaya, P. D. Nellist, and S. Lozano-Perez. *Quantitative Energy-Dispersive X-Ray Analysis of Catalyst Nanoparticles Using a Partial Cross Section Approach*. Microscopy and Microanalysis, vol. 22, no. 01, 71–81, 2016.
- [Maccagnano-Zacher 2008] S. E. Maccagnano-Zacher, K. A. Mkhoyan, E. J. Kirkland, and J. Silcox. *Effects of tilt on high-resolution ADF STEM imaging*. Ultramicroscopy, vol. 108, 718–726, 2008.
- [Mackay 1962] A. L. Mackay. *A dense non-crystallographic packing of equal spheres*. Acta Crystallographica, vol. 15, 916, 1962.
- [MacLaren 2014] I. MacLaren, and Q. Ramasse. *Aberration-corrected scanning transmission electron microscopy for atomic-resolution studies of functional oxides*. International Materials Review, vol. 59, 115–131, 2014.
- [Madsen 2018] J. Madsen, P. Liu, J. Kling, J. Birkedal Wagner, T. W. Hansen, O. Winther, and J. Schiotz. *A deep learning approach to identify local structures in atomic-resolution transmission electron microscopy images*. Adv. Theory Simul., vol. 1, 1800037, 2018.
- [Maheshwari 2015] A. K. Maheshwari. *Business Intelligence and Data Mining*. Business Expert Press, 2015.
- [Malakar 2013] N. K. Malakar, D. Gladkov, and K. H. Knuth. *Modeling a sensor to improve its efficacy*. J. Sens., vol. 2013, 481054, 2013.
- [Mana 2014] G. Mana, P. A. Giuliano Alba, and S. Lago. *Bayesian estimate of the degree of a polynomial given a noisy data sample*. Measurement, vol. 55, 564–570, 2014.
- [Mannhart 2010] J. Mannhart, and D. G. Schlom. *Oxide interfaces: an opportunity for electronics*. Science, vol. 327, 1607–1611, 2010.
- [Marquardt 1963] D. Marquardt. *An algorithm for least-squares estimation of nonlinear parameters*. SIAM Journal on Applied Mathematics, vol. 11, 431–441, 1963.
- [Martin 2010] L. W. Martin, Y.-H. Chu, and R. Ramesh. *Advances in the growth and characterization of magnetic, ferroelectric, and multiferroic oxide thin films*. Materials Science and Engineering: R: Reports, vol. 68, 89–133, 2010.
- [Martinez 2014a] G. T. Martinez, A. De Backer, A. Rosenauer, J. Verbeeck, and S. Van Aert. *The effect of probe inaccuracies on the quantitative model-based analysis of high angle annular dark field scanning transmission electron microscopy images*. Micron, vol. 63, 57–63, 2014.

- [Martinez 2014b] G. T. Martinez, A. Rosenauer, A. De Backer, J. Verbeeck, and S. Van Aert. *Quantitative composition determination at the atomic level using model-based high-angle annular dark field scanning transmission electron microscopy*. *Ultramicroscopy*, vol. 137, 12–19, 2014.
- [Martinez 2015a] G. T. Martinez. *Quantitative model-based high angle annular dark field scanning transmission electron microscopy*. PhD thesis, University of Antwerp, 2015.
- [Martinez 2015b] G. T. Martinez, L. Jones, A. De Backer, A. Béch , J. Verbeeck, S. Van Aert, and P. D. Nellist. *Quantitative STEM normalisation: The importance of the electron flux*. *Ultramicroscopy*, vol. 159, 46–58, 2015.
- [Mast 1983] K. D. Mast. *Field emission, developments and possibilities*. *Journal of Microscopy*, vol. 130, no. 3, 309–324, 1983.
- [Matheron 1963] G. Matheron. *Principles of geostatistics*. *Econ. Geol.*, vol. 58, 1246–1266, 1963.
- [Mazzucco 2012] S. Mazzucco, N. Geuquet, J. Ye, O. St phan, W. Van Roy, P. Van Dorpe, L. Henrard, and M. Kociak. *Ultralocal modification of surface plasmons properties in silver nanocubes*. *Nano letters*, vol. 12, no. 3, 1288–1294, 2012.
- [McGibbon 1999] A. J. McGibbon, S. J. Pennycook, and D. E. Jesson. *Crystal structure retrieval by maximum entropy analysis of atomic resolution incoherent images*. *Journal of Microscopy*, vol. 195, no. 1, 44–57, 1999.
- [McQuarrie 1998] A. D. McQuarrie, and C.-L. Tsai. *Regression and Time Series Model Selection*. World Scientific, 1998.
- [Mehrtens 2013a] T. Mehrtens, K. M ller, M. Schowalter, D. Hu, D. M. Schaadt, and A. Rosenauer. *Measurement of indium concentration profiles and segregation efficiencies from high-angle annular dark field-scanning transmission electron microscopy images*. *Ultramicroscopy*, vol. 131, 1–9, 2013.
- [Mehrtens 2013b] T. Mehrtens, M. Schowalter, D. Tytko, P. Choi, D. Raabe, L. Hoffmann, H. Jonen, U. Rossow, A. Hangleiter, and A. Rosenauer. *Measurement of the indium concentration in high indium content InGaN layers by scanning transmission electron microscopy and atom probe tomography*. *Applied Physics Letters*, vol. 102, 132112, 2013.
- [Meng 2018] Y. Meng, Z. Zhang, H. Yin, and T. Ma. *Automatic detection of particle size distribution by image analysis based on local adaptive canny edge detection and modified circular Hough transform*. *Micron*, vol. 106, 34–41, 2018.
- [Merk 2016] A. Merk, A. Bartesaghi, S. Banerjee, V. Falconieri, P. Rao, M. I. Davis, R. Pragani, M. B. Boxer, L. A. Earl, J. L. Milne, and S. Subramaniam. *Breaking Cryo-EM resolution barriers to facilitate drug discovery*. *Cell*, vol. 165, 1698–1707, 2016.
- [Meyer 2014] J. C. Meyer, J. Kotakoski, and C. Mangler. *Atomic structure from large-area, low-dose exposures of materials: A new route to circumvent radiation damage*. *Ultramicroscopy*, vol. 145, 13–21, 2014.
- [Midgley 2003] P. A. Midgley, and M. Weyland. *3D electron microscopy in the physical sciences: the development of Z-contrast and EFTEM tomography*. *Ultramicroscopy*, vol. 96, 413–431, 2003.
- [Midgley 2009] P. A. Midgley, and R. E. Dunin-Borkowski. *Electron tomography and holography in materials science*. *Nature Materials*, vol. 8, 271–280, 2009.
- [Miedema 1994] M. A. O. Miedema, A. van den Bos, and A. H. Buist. *Experimental design of exit wave reconstruction from a transmission electron microscope defocus series*. *IEEE Transactions on Instrumentation and Measurement*, vol. 43, 181–186, 1994.

- [Migunov 2015] V. Migunov, H. Ryll, X. Zhuge, M. Simson, L. Struder, K. J. Batenburg, L. Houben, and R. E. Dunin-Borkowski. *Rapid low dose electron tomography using a direct electron detection camera*. Scientific Reports, vol. 5, 14516, 2015.
- [Mir 2017] J. A. Mir, R. Plackett, I. Shipsey, and J. M. F. dos Santos. *Using the Medipix3 detector for direct electron imaging in the range 60keV-200keV in electron microscopy*. J. Instrum., vol. 12, C11015, 2017.
- [Mkhoyan 2006] K. A. Mkhoyan, P. E. Batson, J. Cha, W. J. Schaff, and J. Silcox. *Direct determination of local lattice polarity in crystals*. Science, vol. 312, 1354, 2006.
- [Möbus 2003] G. Möbus, R. C. Doole, and B. J. Inkson. *Spectroscopic electron tomography*. Ultramicroscopy, vol. 96, no. 3, 433–451, 2003.
- [Monserrat 2015] D. Monserrat, L. C. Vispa A.and PVis, R. Tolchenov, S. Mukhopadhyay, and F. Fernandez-Alonso. *FABADA goes MANTID to answer an old question: how many lines are there?* Journal of Physics: Conference Series, vol. 663, 012009, 2015.
- [Mood 1974] A. M. Mood, F. A. Graybill, and D. C. Boes. *Introduction to the Theory of Statistics*. McGraw-Hill Book Company, 3 edition, 1974.
- [Morcrette 2003] M. Morcrette, P. Rozier, L. Dupont, E. Mugnier, L. Sannier, J. Galy, and J.-M. Tarascon. *A reversible copper extrusion-insertion electrode for rechargeable Li batteries*. Nature Materials, vol. 2, 755–761, 2003.
- [Mory 1985] C. Mory, M. Tence, and C. Colliex. *Theoretical-Study Of The Characteristics Of The Probe For A Stem With A Field-Emission Gun*. Journal De Microscopie Et De Spectroscopie Electroniques, vol. 10, no. 5, 381–387, 1985.
- [Mubeen 2013] A. M. Mubeen, and K. H. Knuth. *Bayesian odds-ratio filters: a template-based method for online detection of P300 evoked responses*. arXiv: 1304.1565 [q-bio.NC], 2013.
- [Müller-Caspary 2016] K. Müller-Caspary, O. Oppermann, T. Grieb, F. F. Krause, A. Rosenauer, M. Schowalter, T. Mehrrens, A. Beyer, K. Volz, and P. Potapov. *Materials characterisation by angle-resolved scanning transmission electron microscopy*. Scientific reports, vol. 6, 37146, 2016.
- [Muller 1999] D. A. Muller. *Why changes in bond lengths and cohesion lead to core-level shifts in metals, and consequences for the spatial difference method*. Ultramicroscopy, vol. 78, 163–174, 1999.
- [Muller 2001] D. A. Muller, B. Edwards, E. J. Kirkland, and J. Silcox. *Simulation of thermal diffuse scattering including a detailed phonon dispersion curve*. Ultramicroscopy, vol. 86, 371–380, 2001.
- [Muller 2006] D. A. Muller, E. J. Kirkland, M. G. Thomas, J. L. Grazul, L. Fitting, and M. Weyland. *Room design for high-performance electron microscopy*. Ultramicroscopy, vol. 106, 1033–1040, 2006.
- [Myung 1997] I. J. Myung, and M. A. Pitt. *Applying Occam's razor in model cognition: a Bayesian approach*. Psychon. Bull. Rev., vol. 4, 79–95, 1997.
- [Myung 2000] I. J. Myung. *The importance of complexity in model selection*. J. Math. Psychol., vol. 44, 190–204, 2000.
- [Nakanishi 2002] N. Nakanishi, T. Yamazaki, A. Recnik, M. Ceh, M. Kawasaki, K. Watanabe, and M. Shiojiri. *Retrieval process of high-resolution HAADF-STEM images*. Journal of Electron, vol. 51, no. 6, 383–390, 2002.
- [Nakanishi 2006] N. Nakanishi, Y. Kotaka, and T. Yamazaki. *An expanded approach to noise reduction from high-resolution STEM images based on the maximum entropy method*. Ultramicroscopy, vol. 106, 233–239, 2006.

- [Nebel 2003] C. E. Nebel. *Semiconductor materials: From gemstone to semiconductor*. Nature Materials, vol. 2, 431–432, 2003.
- [Nellist 1994] P. D. Nellist, and J. M. Rodenburg. *Beyond the conventional information limit: the relevant coherence function*. Ultramicroscopy, vol. 54, no. 1, 61–74, 1994.
- [Nellist 1998] P. D. Nellist, and Penny. *Accurate structure determination from image reconstruction in ADF STEM*. Journal of Microsc, vol. 190, no. 1/2, 159–170, 1998.
- [Nellist 2000] P. D. Nellist, and S. J. Pennycook. *The Principles and Interpretation of Annular Dark-Field Z-Contrast Imaging*. Advances in Imaging and Electron Physics, vol. 113, 147–203, 2000.
- [Nellist 2004] P. D. Nellist, M. F. Chisholm, N. Dellby, O. L. Krivanek, M. F. Murfitt, Z. S. Szilagy, A. R. Lupini, A. Y. Borisevich, W. H. Sides Jr., and S. J. Pennycook. *Direct sub-angstrom imaging of a crystal lattice*. Science, vol. 305, 1741, 2004.
- [Nellist 2007] P. D. Nellist. *Scanning Transmission Electron Microscopy*. In Science of Microscopy, P. W. Hawkes, and J. H. C. Spence (eds.), volume 1, Chapter 2, 65–132. Springer New York, 2007.
- [Newmark 1982] P. Newmark. *Cryo-transmission microscopy: Fading hopes*. Nature, vol. 299, 386–387, 1982.
- [Nishimura 2008] S. Nishimura, G. Kobayashi, K. Ohoyama, R. Kanno, M. Yashima, and A. Yamada. *Experimental Visualization of lithium diffusion in  $Li_xFePO_4$* . Nature Materials, vol. 7, 707–711, 2008.
- [Nitta 2015] N. Nitta, F. Wu, and J. T. Lee. *Lio-ion battery materials: present and future*. Materials Today, vol. 18, 252–264, 2015.
- [Nørskov 2009] J. K. Nørskov, T. Bligaard, J. Rossmeisl, and C. H. Christensen. *Towards the computational design of solid catalysts*. Nature Chemistry, vol. 1, no. 1, 37–46, 2009.
- [Novoselov 2004] K. S. Novoselov, A. K. Geim, S. V. Morozov, D. Jiang, Y. Zhang, Dubonos S. V., I. V. Grigorieva, and A. A. Firsov. *Electric field effect in atomatomic thin carbon films*. Science, vol. 306, 666–669, 2004.
- [Ohtomo 2002] A. Ohtomo, D. A. Muller, J. L. Grazul, and H. Y. Hwang. *Artificial charge-modulation in atomic-scale perovskite titanate superlattices*. Nature, vol. 419, 378–380, 2002.
- [Ohtomo 2004] A. Ohtomo, and H. Y. Hwang. *A high-mobility electron gas at the  $LaAlO_3/SrTiO_3$  heterointerface*. Nature, vol. 427, 423–426, 2004.
- [Okunishi 2009] E. Okunishi, I. Ishikawa, H. Sawada, F. Hosokawa, M. Hori, and Y. Kondo. *Visualization of light elements at ultrahigh resolution by STEM annular bright field microscopy*. Microscopy and Microanalysis, vol. 15, no. S2, 164–165, 2009.
- [Oltalan 2010] V. Oltalan, A. Uzun, B. C. Gates, and N. D. Browning. *Towards full-structure determination of bi metallic nanoparticles with an aberration-corrected electron microscope*. Nature Nanotechnology, vol. 5, 843–847, 2010.
- [O’Neil 2013] C. O’Neil, and R. Schutt. *Doing Data Science*. O’Reilly Media, 2013.
- [Op de Beeck 1995] M. Op de Beeck, and D. Van Dyck. *An Analytical Approach for the Fast Calculation of Dynamical Scattering in HRTEM*. Physica Status Solidi A., vol. 150, 587–602, 1995.
- [Ophus 2016] C. Ophus, J. Ciston, and C. T. Nelson. *Correcting nonlinear drift distortion of scanning probe and scanning transmission electron microscopes from image pairs with orthogonal scan directions*. Ultramicroscopy, vol. 162, 1–9, 2016.

- [Oshima 2010] Y. Oshima, H. Sawada, F. Hosokawa, E. Okunishi, T. Kaneyama, Y. Kondo, S. Niitaka, H. Takagi, Y. Tanishiro, and K. Takayanagi. *Direct imaging of lithium atoms in  $\text{LiV}_2\text{O}_4$  by spherical aberration-corrected electron microscopy*. *Journal of Electron Microscopy*, vol. 59, 457–461, 2010.
- [Papoulis 2002] A. Papoulis, and S.U. Pillai. *Probability, random variable, and stochastic processes*. McGraw-Hill, 2002.
- [Pennycook 1988] S. J. Pennycook, and L. A. Boatner. *Chemically sensitive structure-imaging with a scanning transmission electron microscope*. *Nature*, vol. 336, 565–567, 1988.
- [Pennycook 1991] S. J. Pennycook, and D. E. Jesson. *High-resolution Z-contrast imaging of crystals*. *Ultramicroscopy*, vol. 37, 14–38, 1991.
- [Pennycook 2011] S. J. Pennycook, and P. D. Nellist. *Scanning Transmission Electron Microscopy*. Springer, 2011.
- [Pérez-Juste 2005] J. Pérez-Juste, I. Pastoriza-Santos, L. Liz-Marzán, and P. Mulvaney. *Gold nanorods: Synthesis, characterization and applications*. *Coordination Chemistry Reviews*, vol. 249, 1870–1901, 2005.
- [Perez 2016] A. J. Perez, D. Batuk, M. Saubanère, G. Rousse, D. Foix, E. McCalla, E. J. Berg, R. Dugas, K. H. W. van den Bos, M.-L. Doublet, D. Gonbeau, A. M. Abakumov, G. Van Tendeloo, and J.-M. Tarascon. *Strong oxygen participation in the redox governing the structural and electrochemical properties of Na-rich layered oxide  $\text{Na}_2\text{IrO}_3$* . *Chemistry of Materials*, vol. 28, no. 22, 8278–8288, 2016.
- [Placek 2014] B. Placek, K. H. Knuth, and D. Angerhausen. *EXONEST: Bayesian model selection applied to the detection and characterization of exoplanets via photometric variations*. *Astrophys. J.*, vol. 795, 112, 2014.
- [Polking 2012] M. J. Polking, M.-G. Han, A. Yourdkhani, V. Petkov, C. F. Kisielowski, V. V. Volkov, Y. Zhu, G. Caruntu, A. P. Alivisatos, and R. Ramesh. *Ferroelectric order in individual nanometre-scale crystals*. *Nature materials*, vol. 11, no. 8, 700–709, 2012.
- [Pounds 2006] K. Pounds, and S. Vaughan. *X-ray reflection in the nearby Seyfert 2 galaxy NGC 1068*. *Mon. J.*, vol. 368, no. 2, 707–714, 2006.
- [Qi 2010] T. Qi, I. Grinberg, and A.M. Rappe. *Correlations between tetragonality, polarization, and ionic displacement in  $\text{PbTiO}_3$ -derived ferroelectric perovskite solid solutions*. *Physical Review B*, vol. 82, 134113, 2010.
- [Rayleigh 1896] Lord Rayleigh. *On the theory of optical images, with special reference to the microscope*. *Philosophical Magazine*, vol. 42, no. 255, 167–195, 1896.
- [Recnik 2005] A. Recnik, G. Möbus, and S. Sturm. *IMAGE-WARP: A real-space restoration method for high-resolution STEM images using quantitative HRTEM analysis*. *Ultramicroscopy*, vol. 103, 285–301, 2005.
- [Rehn 1992] L.E. Rehn. *Ion-beams in high-temperature superconductivity research*. *Nucl. Instrum. and Methods*, vol. 64, 161–168, 1992.
- [Retsky 1974] M. Retsky. *Observed single atom elastic cross sections in a scanning electron microscope*. *Optik*, vol. 41, 127, 1974.
- [Ricolleau 2012] C. Ricolleau, J. Nelayah, T. Oikawa, Y. Kohno, N. Braidy, G. Wang, F. Hue, and D. Alloyeau. *High Resolution Imaging and Spectroscopy Using Cs-corrected TEM with cold FEG JEM-ARM200F*. *JEOL news*, vol. 47, no. 1, 2–8, 2012.
- [Ricolleau 2013] C. Ricolleau, Y. Le Bouar, H. Amara, O. Landon-Cardinal, and D. Alloyeau. *Random vs realistic amorphous carbon models for high resolution microscopy and electron diffraction*. *J. Appl. Phys.*, vol. 114, 213504, 2013.

- [Roduner 2006] E. Roduner. *Size matters: why nanomaterials are different*. Chemical Society Reviews, vol. 35, no. 7, 583–592, 2006.
- [Rose 1974] H. Rose. *Phase contrast in scanning transmission electron microscopy*. Optik, vol. 39, 416–436, 1974.
- [Rose 2009] H. H. Rose. *Historical aspects of aberration correction*. Journal of electron microscopy, dfp012, 2009.
- [Rosenauer 2008a] A. Rosenauer, and M. Schowalter. *STEMSIM - a New Software Tool for Simulation of STEM HAADF Z-Contrast Imaging*. In Microscopy of Semiconducting Materials 2007, A.G. Cullis, and P.A. Midgley (eds.), volume 120 of *Springer Proceedings in Physics*, 170–172. Springer Netherlands, 2008.
- [Rosenauer 2008b] A. Rosenauer, M. Schowalter, J. Titantah, and D. Lamoen. *An emission-potential multislice approximation to simulate thermal diffuse scattering in high-resolution transmission electron microscopy*. Ultramicroscopy, vol. 108, 1504–1513, 2008.
- [Rosenauer 2009] A. Rosenauer, K. Gries, K. Müller, A. Pretorius, M. Schowalter, A. Avramescu, K. Engl, and S. Lutgen. *Measurement of specimen thickness and composition in  $Al_xGa_{1-x}N/GaN$  using high-angle annular dark field images*. Ultramicroscopy, vol. 109, 1171–1182, 2009.
- [Rosenauer 2011] A. Rosenauer, T. Mehrtens, K. Müller, K. Gries, M. Schowalter, P. V. Satyam, S. Bley, C. Tessarek, D. Hommel, K. Sebald, M. Seyfried, J. Gutowski, A. Avramescu, K. Engl, and S. Lutgen. *Composition mapping in InGaN by scanning transmission electron microscopy*. Ultramicroscopy, vol. 111, 1316–1327, 2011.
- [Ross 2015] F. M. Ross. *Opportunities and challenges in liquid cell electron microscopy*. Science, vol. 350, 1490–1501, 2015.
- [Ryll 2016] H. Ryll, M. Simson, P. Holl, M. Huth, S. Ihle, Y. Kondo, P. Kotula, A. Liebel, K. Müller-Caspary, A. Rosenauer, R. Sagawa, J. Schmidt, H. Soltau, and L. Strüder. *A pnCCD-based, fast direct single electron imaging camera for TEM and STEM*. J. Instrum., vol. 11, P04006, 2016.
- [Saghi 2015] Z. Saghi, M. Benning, R. Leary, M. Macias-Montero, A. Borrás, and P. A. Midgley. *Reduced-dose and high-speed acquisition strategies for multi-dimensional electron microscopy*. Advanced Structural and Chemical Imaging, vol. 1, no. 1, 1–10, 2015.
- [Salmons 2010] B. S. Salmons, D. R. Katz, and M. L. Trawick. *Correction of distortion due to thermal drift in scanning probe microscopy*. Ultramicroscopy, vol. 110, 339–349, 2010.
- [Sammur 2011] C. Sammut, and G. I. Webb. *Encyclopedia of Machine Learning*, Chapter Bias-Variance Decomposition, 100–101. Springer, 2011.
- [Sang 2009] X. Sang, K. Du, M. Zhuo, and H. Ye. *On the accuracy of maximum entropy reconstruction of high-resolution Z-contrast STEM images*. Micron, vol. 40, 247–254, 2009.
- [Sang 2013] X. Sang, and J. M. LeBeau. *Revolving scanning transmission electron microscopy: correcting sample drift distortion without prior knowledge*. Ultramicroscopy, vol. 138, 28–35, 2013.
- [Sang 2016] X. Sang, and J. M. LeBeau. *Characterizing the response of a scintillator-based detector to single electrons*. Ultramicroscopy, vol. 161, 3–9, 2016.
- [Sawada 2009] H. Sawada, Y. Tanishori, N. Ohashi, T. Tomita, F. Hosokawa, T. Kaneyama, Y. Kondo, and K. Takayanagi. *STEM imaging of 47-pm-separated atomic columns by a spherical aberration-corrected electron microscope with a 300-kV cold field emission gun*. Journal of Electron Microscopy, vol. 58, no. 6, 357–361, 2009.

- [Schaffer 2015] J. Schaffer. *What not to multiply without necessity*. Australasian Journal of Philosophy, vol. 93, 644–664, 2015.
- [Schlapbach 2001] L. Schlapbach, and A. Züttel. *Hydrogen-storage materials for mobile applications*. Nature, vol. 414, 353–358, 2001.
- [Schlossmacher 2010] P. Schlossmacher, D. O. Klenov, B. Freitag, S. von Harrach, and A. Steinbach. *Nanoscale chemical compositional analysis with an innovative S/TEM-EDX system*. Microscopy and analysis, no. 142, S5, 2010.
- [Schwarz 1978] G. Schwarz. *Estimating the dimension of a model*. Ann. Stat., vol. 6, 461–464, 1978.
- [Scott 2012] M. C. Scott, C.-C. Chen, M. Mecklenburg, C. Zhu, R. Xu, P. Ercius, U. Dahmen, B. C. Regan, and J. Miao. *Electron tomography at 2.4-ångström resolution*. Nature, vol. 483, 444–448, 2012.
- [Seidel 2009] J. Seidel, L. W. Martin, Q. He, Q. Zhan, H.-Y. Chu, A. Rother, M. E. Hawkrigde, P. Maksymovych, P. Yu, M. Gajek, N. Balke, S. V. Kalinin, S. Gemming, F. Wang, G. Catalan, J. F. Scott, N. A. Spaldin, J. Orenstein, and R. Ramesh. *Conduction at domain walls in oxide multiferroics*. Nature materials, vol. 8, 229–234, 2009.
- [Seki 2018] T. Seki, Y. Ikuhara, and N. Shibata. *Theoretical framework of statistical noise in scanning transmission electron microscopy*. Ultramicroscopy, vol. 193, 118–125, 2018.
- [Shah 2010] A. B. Shah, Q. M. Ramasse, S. J. May, J. Kavich, J. G. Wen, X. Zhai, J. N. Eckstein, J. Freeland, A. Bhattacharya, and J. M. Zuo. *Presence and spatial distribution of interfacial electronic states in LaMnO<sub>3</sub>-SrMnO<sub>3</sub> superlattices*. Physical Review B, vol. 82, 115112, 2010.
- [Shashilov 2010] V. A. Shashilov, V. Sikirzhytski, L. A. Popova, and I. K. Lednev. *Quantitative methods for structural characterization of proteins based on deep UV resonance Raman spectroscopy*. Methods, vol. 52, no. 1, 23–37, 2010.
- [Sheehy 2009] D. E. Sheehy, and J. Schmalian. *Optical transparency of graphene as determined by the fine-structure constant*. Phys. Rev. B, vol. 80, 193411, 2009.
- [Shibata 2010] N. Shibata, Y. Kohno, S. D. Findlay, H. Sawada, Y. Kondo, and Y. Ikuhara. *New area detector for atomic resolution scanning transmission electron microscopy*. Journal of Electron Microscopy, vol. 59, no. 6, 473–479, 2010.
- [Silver 2012] N. Silver. *The Signal and the Noise*. The Penguin Press, 2012.
- [Singhal 1997] A. Singhal, J. C. Yang, and J. M. Gibson. *STEM-based mass spectroscopy of supported Re clusters*. Ultramicroscopy, vol. 67, 191–206, 1997.
- [Sirohi 2016] D. Sirohi, Z. Chen, L. Sun, T. Klose, T. C. Pierson, M. G. Rossmann, and R. J. Kuhn. *The 3.8 Å resolution cryo-EM structure of Zika virus*. Science, vol. 352, 467–470, 2016.
- [Sivia 1992a] D. S. Sivia, and C. J. Carlile. *Molecular spectroscopy and Bayesian spectral analysis - how many lines are there*. J. Chem. Phys., vol. 96, no. 1, 1992.
- [Sivia 1992b] D. S. Sivia, C. J. Carlile, and W. S. Howells. *Bayesian analysis of quasielastic neutron scattering data*. Physica, vol. 182, 341–348, 1992.
- [Sivia 1993] D. S. Sivia, W. I. F. David, and K. S. Knight. *An introduction to Bayesian model selection*. Physica D, vol. 66, 234–242, 1993.
- [Sivia 2006] D. S. Sivia, and J. Skilling. *A Bayesian Tutorial*. Oxford University Press, 2006.
- [Skilling 1984] J. Skilling, and R. K. Bryan. *Maximum entropy reconstruction: general algorithm*. Mon. Not. R. astr. Soc., vol. 211, 111–124, 1984.

- [Slater 2016] T. J. A. Slater, A. Janssen, P. H. C. Camargo, M. G. Burke, N. J. Zaluzec, and S. J. Haigh. *STEM-EDX tomography of bimetallic nanoparticles: A methodological investigation*. *Ultramicroscopy*, vol. 162, 61–73, 2016.
- [So 2012] Y.-G. So, and K. Kimoto. *Effect of specimen misalignment on local structure analysis using annular dark-field imaging*. *J. Electron Microsc.*, vol. 61, 207–215, 2012.
- [Stoica 2004a] P. Stoica, and Selen Y. *Model-order selection: a review of information criterion rules*. *IEEE Signal Process. Mag.*, vol. 21, 36–47, 2004.
- [Stoica 2004b] P. Stoica, Selen Y., and J. Li. *Multi-modal approach to model-selection*. *Digital Signal Processing*, vol. 14, 399–412, 2004.
- [Stuart 1994] A. Stuart, and K. Ord. *Kendall's Advanced Theory of Statistics: Volume I - Distribution Theory*. Edward Arnold, 1994.
- [Tach 1971] R. E. Tach, and S. S. Tach. *Damage to biological samples caused by the electron beam during electron microscopy*. *Biophysical Journal*, vol. 11, 204–210, 1971.
- [Tan 2017] C. Tan, X. Cao, X.-J. Wu, Q. He, J. Yang, X. Zhang, J. Chen, W. Zhao, S. Han, G.-H. Nam, M. Sindoro, and H. Zhang. *Recent Advances in Ultrathin Two-Dimensional Nanomaterials*. *Chemical reviews*, vol. 117, no. 9, 6225–6331, 2017.
- [Tang 2014] Y. L. Tang, Y.L. Zhu, Y.J. Wang, W.Y. Wang, Y.B. Xu, W.J. Ren, Z.D. Zhang, and X.L. Ma. *Atomic-scale mapping of dipole frustration at 90° charged domain walls in ferroelectric PbTiO<sub>3</sub> films*. *Scientific Reports*, vol. 4, 4115, 2014.
- [Tarascon 2001] J.-M. Tarascon, and M. Armand. *Issues and challenges facing rechargeable lithium batteries*. *Nature*, vol. 414, 359–367, 2001.
- [Tate 2016] M. W. Tate, P. Purohit, D. Chamberlain, K. X. Nguyen, R. Hovden, C. S. Chang, P. Deb, E. Turgut, J. T. Heron, D. G. Schlom, D. C. Ralph, G. D. Fuchs, K. S. Shanks, H. T. Philipp, D. A. Muller, and S. M. Gruner. *High dynamic range pixel array detector for scanning transmission electron microscopy*. *Microscopy and Microanalysis*, vol. 22, 237–249, 2016.
- [Tedsree 2011] K. Tedsree, T. Li, S. Jones, C. W. A. Chan, K. M. K. Yu, P. A. J. Bagot, E. A. Marquis, G. D. W. Smith, and S. C. E. Tsang. *Hydrogen production from formic acid decomposition at room temperature using a Ag-Pd core-shell nanocatalyst*. *Nature Nanotechnology*, vol. 6, no. 5, 302–307, 2011.
- [Thust 1996] A. Thust, W. M. J. Coene, M. Op de Beeck, and D. Van Dyck. *Focal-series reconstruction in HRTEM: simulation studies on non-periodic objects*. *Ultramicroscopy*, vol. 64, 211–230, 1996.
- [Trotta 2008] R. Trotta. *Bayes in the sky: Bayesian inference and model selection in cosmology*. *Contemp. Phys.*, vol. 49, no. 2, 71–104, 2008.
- [Tseng 2011] A. A. Tseng. *Advancements and challenges in development of atomic force microscopy for nanofabrication*. *Nano Today*, vol. 6, no. 5, 493–509, 2011.
- [Ugurlu 2011] O. Ugurlu, J. Haus, A. A. Gunawan, M. G. Thomas, S. Maheshwari, M. Tsapatsis, and K. A. Mkhoyan. *Radiolysis to knock-on damage transition in zeolites under electron beam irradiation*. *Physical Review B*, vol. 83, 113408, 2011.
- [Unocic 2016] R. R. Unocic, A. R. Lupini, A. Y. Borisevich, D. A. Cullen, S. V. Kalinin, and S. Jesse. *Direct-write liquid phase transformations with a scanning transmission electron microscope*. *Nanoscale*, vol. 8, 15581–15588, 2016.
- [Unwin 1975] P. N. Unwin, and R. Henderson. *Molecular structure determination by electron microscopy of unstained crystalline specimens*. *Journal of Molecular Biology*, vol. 94, 425–440, 1975.

- [Urban 2008] K. W. Urban. *Studying Atomic Structures by Aberration-Corrected Transmission Electron Microscopy*. Science, vol. 321, 506–510, 2008.
- [Van Aert 2002] S. Van Aert, A. J. den Dekker, D. Van Dyck, and A. van den Bos. *Optimal experimental design of STEM measurement of atom column positions*. Ultramicroscopy, vol. 90, 273–289, 2002.
- [Van Aert 2005] S. Van Aert, A. J. den Dekker, A. van den Bos, D. Van Dyck, and J. H. Chen. *Maximum likelihood estimation of structure parameters from high resolution electron microscopy images: Part II: A practical example*. Ultramicroscopy, vol. 104, 107–125, 2005.
- [Van Aert 2006] S. Van Aert, D. Van Dyck, and A. J. den Dekker. *Resolution of coherent and incoherent imaging systems reconsidered - Classical criteria and a statistical alternative*. Optics Express, vol. 9, no. 14, 3830–3839, 2006.
- [Van Aert 2007] S. Van Aert, P. Geuens, D. Van Dyck, C. Kisielowski, and J. R. Jinscheck. *Electron channelling based crystallography*. Ultramicroscopy, vol. 107, 551–558, 2007.
- [Van Aert 2009a] S. Van Aert, L. Y. Chang, S. Bals, A. I. Kirkland, and G. Van Tendeloo. *Effect of amorphous layers on the interpretation of restored exit waves*. Ultramicroscopy, vol. 109, 237–246, 2009.
- [Van Aert 2009b] S. Van Aert, J. Verbeeck, R. Erni, S. Bals, M. Luysberg, D. Van Dyck, and G. Van Tendeloo. *Quantitative atomic resolution mapping using high-angle annular dark field scanning transmission electron microscopy*. Ultramicroscopy, vol. 109, 1236–1244, 2009.
- [Van Aert 2011] S. Van Aert, K. J. Batenburg, M. D. Rossell, R. Erni, and G. Van Tendeloo. *Three-dimensional atomic imaging of crystalline nanoparticles*. Nature, vol. 470, 374–377, 2011.
- [Van Aert 2012a] S. Van Aert, S. Turner, R. Delville, D. Schryvers, G. Van Tendeloo, and E. K. H. Salje. *Direct observation of ferroelectricity at ferroelastic domain boundaries in CaTiO<sub>3</sub> by electron microscopy*. Advanced Materials, vol. 24, 523–527, 2012.
- [Van Aert 2012b] S. Van Aert, W. Van den Broek, P. Goos, and D. Van Dyck. *Model-based electron microscopy: From images toward precise numbers for unknown structure parameters*. Micron, vol. 43, no. 4, 509 – 515, 2012.
- [Van Aert 2013] S. Van Aert, A. De Backer, G. T. Martinez, B. Goris, S. Bals, and G. Van Tendeloo. *Procedure to count atoms with trustworthy single-atom sensitivity*. Physical Review B, vol. 87, no. 064107, 2013.
- [Van Aert 2016] S. Van Aert, A. De Backer, G. T. Martinez, A. J. den Dekker, D. Van Dyck, S. Bals, and G. Van Tendeloo. *Advanced electron crystallography through model-based imaging*. IUCrJ, vol. 3, 71–83, 2016.
- [Van Aert 2019] S. Van Aert, A. De backer, L. Jones, G. T. Martinez, A. Bèchè, and P. D. Nellist. *Control of knock-on damage for 3D atomic scale quantification of nanostructures: Making every electron count in scanning transmission electron microscopy*. Physical Review Letters, vol. 122, 066101, 2019.
- [van Benthem 2005] K. van Benthem, A. R. Lupini, M. Kim, H. S. Baik, S. Doh, J.-H. Lee, M. P. Oxley, S. D. Findlay, L. J. Allen, J. T. Luck, and S. J. Pennycook. *Three-dimensional imaging of individual hafnium atoms inside a semiconductor device*. Applied Physics Letters, vol. 87, no. 034104, 2005.
- [van Benthem 2006] K. van Benthem, A. R. Lupini, M. P. Oxley, S. D. Findlay, L. J. Allen, and S. J. Pennycook. *Three-dimensional ADF imaging of individual atoms by through-focal series scanning transmission electron microscopy*. Ultramicroscopy, vol. 106, 1062–1068, 2006.

- [van den Bos 1982] A. van den Bos. *Parameter estimation*. In Handbook of Measurement Science, volume 1, 331–377. 1982.
- [van den Bos 2001] A. van den Bos, and A.J. den Dekker. *Resolution reconsidered - Conventional approaches and an alternative*. In Advances in Imaging and Electron Physics, P. W. Hawkes (ed.), volume 117, 241–360. Academic press, 2001.
- [van den Bos 2007] A. van den Bos. *Parameter estimation for scientists and engineers*. Wiley, 2007.
- [van den Bos 2016] K. H. W. van den Bos, A. De Backer, G. T. Martinez, N. Winckelmans, S. Bals, P. D. Nellist, and S. Van Aert. *Unscrambling Mixed Elements using High Angle Annular Dark Field Scanning Transmission Electron Microscopy*. Physical Review Letters, vol. 116, no. 24, 246101, 2016.
- [van den Bos 2017a] K. H. W. van den Bos. *Quantitative atomic resolution transmission electron microscopy for heterogeneous nanomaterials*. PhD thesis, University of Antwerp, 2017.
- [van den Bos 2017b] K. H. W. van den Bos, F.F. Krause, A. Béch e, J. Verbeeck, A. Rosenauer, and S. Van Aert. *Locating light and heavy atomic column positions with picometer precision using ISTEM*. Ultramicroscopy, vol. 172, 75–81, 2017.
- [Van den Broek 2010] W. Van den Broek, S. Van Aert, and D. Van Dyck. *A model based reconstruction technique for depth sectioning with scanning transmission electron microscopy*. Ultramicroscopy, vol. 110, 548–554, 2010.
- [van der Stam 2017] W. van der Stam, J. J. Geuchies, T. Altantzis, K. H. W. van den Bos, J. D. Meeldijk, S. Van Aert, S. Bals, D. Vanmaekelbergh, and C. de Mello Donega. *Highly Emissive Divalent-Ion-Doped Colloidal CsPb<sub>1-x</sub>M<sub>x</sub>Br<sub>3</sub> Perovskite Nanocrystals through Cation Exchange*. Journal of the American Chemical Society, vol. 139, no. 11, 4087–4097, 2017.
- [Van Dyck 1975] D. Van Dyck. *The path integral formalism as a new description for the diffraction of high-energy electrons in crystals*. Physica Status Solidi B: Basic Solid State Physics, vol. 72, 321–336, 1975.
- [Van Dyck 1985] D. Van Dyck. *Image Calculations in High-Resolution Electron Microscopy: Problems, Progress, and Prospects*. Advances in Electronics and Electron Physics, vol. 65, 295–355, 1985.
- [Van Dyck 1989] D. Van Dyck, J. Danckaert, W. Coene, E. Selderslaghs, D. Broddin, J. Van Landuyt, S. Amelinckx, W. Krakow, and M. O’Keefe. *Computer Simulation of Electron Microscopy Diffraction and Images*, 107–134. TMS Publications, 1989.
- [Van Dyck 1993] D. Van Dyck, M. Op de Beeck, and W. Coene. *A new approach to object wave function reconstruction in electron microscopy*. Optik, vol. 93, no. 3, 103–107, 1993.
- [Van Dyck 1996] D. Van Dyck, and M. Op de Beeck. *A simple intuitive theory for electron diffraction*. Ultramicroscopy, vol. 64, 99–107, 1996.
- [Van Dyck 1999] D. Van Dyck, and J. H. Chen. *A simple theory for dynamical electron diffraction in crystals*. Solid State Communications, vol. 109, no. 8, 501–505, 1999.
- [Van Dyck 2002] D. Van Dyck. *High-Resolution Electron Microscopy*. Advances in Imaging and Electron Physics, vol. 123, 105–171, 2002.
- [Van Dyck 2009] D. Van Dyck. *Is the frozen phonon model adequate to describe inelastic phonon scattering?* Ultramicroscopy, vol. 109, 677–682, 2009.
- [Van Dyck 2012] D. Van Dyck, J. R. Jinscheck, and F.-R. Chen. *’Big Bang’ tomography as a new route to atomic-resolution electron tomography*. Nature, vol. 486, 243–246, 2012.

- [Varela 2005] M. Varela, A. R. Lupini, K. van Benthem, A. Y. Borisevich, M. F. Chisholm, N. Shibata, E. Abe, and S. J. Pennycook. *Materials characterization in the aberration-corrected scanning transmission electron microscope*. Annual Review of Materials Research, vol. 35, 539–569, 2005.
- [Verbeeck 2004] J. Verbeeck, and S. Van Aert. *Model based quantification of EELS spectra*. Ultramicroscopy, vol. 101, 207–224, 2004.
- [Verbeeck 2006] J. Verbeeck, S. Van Aert, and G. Bertonni. *Model-based quantification of EELS spectra: Including the fine structure*. Ultramicroscopy, vol. 106, 976–980, 2006.
- [Verbeeck 2012] J. Verbeeck, A. Béch e, and W. Van den Broek. *A holographic method to measure source size broadening in STEM*. Ultramicroscopy, vol. 120, 35–40, 2012.
- [Vieira 2013] M. A. C. Vieira, P. R. Bakic, and A. D. A. Maidment. *Effect of denoising on the quality of reconstructed images in digital breast tomosynthesis*. Proc. of SPIE, vol. 8668, 86680C–1, 2013.
- [Vispa 2016] A. Vispa, S. Busch, Tamarit J. Ll., T. Unruh, F. Fernandez-Alonso, and L. C. Pardo. *A robust comparison of dynamical scenarios in a glass forming liquid*. Physical Chemistry, vol. 18, 3975, 2016.
- [Vispa 2017] A. Vispa, D. Monserrat, G. J. Cuello, F. Fernandez-Alonso, S. Mukhopadhyay, F. Demmel, Tamarit J. Ll., and L. C. Pardo. *On the microscopic mechanism behind the pupure orientation disorder-disorder transition in the plastic phase of 1-chloroadamantane*. Physical Chemistry Chemical Physics, vol. 30, 2017.
- [Von Ardenne 1938] M. Von Ardenne. *Das elektronen-rastermikroskop*. Zeitschrift für Physik A Hadrons and Nuclei, vol. 109, no. 9, 553–572, 1938.
- [von Colbe 2019] J. B. von Colbe, J. R. Ares, J. Barale, M. Baricco, C. Buckley, G. Capurso, N. Gallandat, D. M. Grant, M. N. Guzik, and I. Jacob. *Applications of hydrides in hydrogen storage and compression: achievements, outlook and perspectives*. International Journal of Hydrogen Energy, vol. 44, no. 7780-7808, 2019.
- [von Harrach 1995] H. von Harrach. *Instrumental factors in high-resolution FEG STEM*. Ultramicroscopy, vol. 58, 1–5, 1995.
- [Vonck 2017] J. Vonck, and D. J. Mills. *Advances in high-resolution cryo-EM of oligomeric enzymes*. Current Opinion in Structural Biology, vol. 46, 48–54, 2017.
- [Voyles 2002] P. M. Voyles, D. A. Muller, J. L. Grazul, P. H. Citrin, and H.-J. L. Gossmann. *Atomic-scale imaging of individual dopant atoms and clusters in highly n-type bulk Si*. Nature, vol. 416, 826–829, 2002.
- [Walther 2013] T. Walther, and I. M. Ross. *Aberration corrected high-resolution transmission and scanning transmission electron microscopy of thin perovskite layers*. Physics Procedia, vol. 40, 49–55, 2013.
- [Wang 2003] J. Wang, J. B. Neaton, H. Zheng, V. Nagarajan, S. B. Ogale, B. Liu, D. Viehland, V. Vaithyanathan, D. G. Schlom, U. V. Waghmare, N. A. Spaldin, K. M. Rabe, and R. Ramesh. *Epitaxial BiFeO<sub>3</sub> multiferroic thin film heterostructures*. Science, vol. 299, no. 5613, 1719–1722, 2003.
- [Wang 2010] A. Wang, F. R. Chen, S. Van Aert, and D. Van Dyck. *Direct structure inversion from exit waves Part I: Theory and simulations*. Ultramicroscopy, vol. 110, 527–534, 2010.
- [Wang 2012] A. Wang, F. R. Chen, S. Van Aert, and D. Van Dyck. *Direct structure inversion from exit waves. Part II: A practical example*. Ultramicroscopy, vol. 116, 77–85, 2012.
- [Wang 2015] W. Wang, S. Liao, Y. Zhu, M. Liu, Q. Zhao, and Y. Fu. *Recent applications of nanomaterials in prosthodontics*. Journal of nanomaterials, vol. 2015, 3, 2015.

- [Watanabe 2002] K. Watanabe, Y. Kotaka, N. Nakanishi, T. Yamazaki, I. Hashimoto, and M. Shiojiri. *Deconvolution processing of HAADF STEM images*. *Ultramicroscopy*, vol. 92, 191–199, 2002.
- [Watanabe 2006] M. Watanabe, and D. B. Williams. *The quantitative analysis of thin specimens: a review of progress from the Cliff-Lorimer to the new  $\zeta$ -factor methods*. *Journal of Microscopy*, vol. 221, no. 2, 89–109, 2006.
- [Welvaert 2013] M. Welvaert, and Y. Rosseel. *On the definition of signal-to-noise ratio and contrast-to-noise ratio for fMRI data*. *PloS ONE*, vol. 8, e77089, 2013.
- [Westin 2000] C.-F. Westin, H. Knutsson, and R. Kikinis. *Handbook of Medical Imaging*, Chapter Adaptive Image Filtering. Academic Press, 2000.
- [Weyland 2004] M. Weyland, and P. A. Midgley. *Electron tomography*. *Materials Today*, vol. 7, no. 12, 32–40, 2004.
- [Wiesendanger 1994] R. Wiesendanger. *Scanning Probe Microscopy and Spectroscopy - Methods and Applications*. Cambridge University Press, 1994.
- [Williams 2009] D. B. Williams, and C. B. Carter. *Transmission electron microscopy*. Springer US, 2nd edition, 2009.
- [Wilson 1927] E. B. Wilson. *Probable inference, the law of succession, and statistical inference*. *J. Stat. Am. Assoc.*, vol. 22, 209–212, 1927.
- [Winckelmans 2018a] N. Winckelmans. *Advanced electron tomography to investigate the growth of homogeneous and heterogeneous nanoparticles*. PhD thesis, University of Antwerp, 2018.
- [Winckelmans 2018b] N. Winckelmans, T. Altantzis, M. Grzelczak, A. Sanchez-Iglesias, L. Liz-Marzán, and S. Bals. *Multimode electron tomography as a tool to characterize the internal structure and morphology of gold nanoparticles*. *J. Phys. Chem. C. Nanomater. Interfaces*, vol. 122, 13522–13528, 2018.
- [Wolf 2014] S. G. Wolf, L. Houben, and M. Elbaum. *Cryo-scanning transmission electron tomography of vitrified cells*. *Nature Methods*, vol. 11, 423–428, 2014.
- [Wu 2015] R. Wu, K. Zhou, C. Y. Yue, J. Wei, and Y. Pan. *Recent progress in synthesis, properties and potential applications of SiC nanomaterials*. *Progress in Materials Science*, vol. 72, 1–60, 2015.
- [Xu 2015] R. Xu, C.-C. Chen, L. Wu, M. C. Scott, W. Theis, C. Ophus, M. Bartels, Y. Yang, H. Ramezani-Dakhel, M. R. Sawaya, H. Heinz, L. D. Marks, P. Ercius, and J. Miao. *Three-dimensional coordinates of individual atoms in materials revealed by electron tomography*. *Nature Materials*, vol. 14, 1099–1103, 2015.
- [Xu 2016] W. Xu, J. H. Dycus, X. Sang, and J. M. LeBeau. *A numerical model for multiple detector energy dispersive X-ray spectroscopy in the transmission electron microscope*. *Ultramicroscopy*, vol. 164, 51–61, 2016.
- [Yang 2012] P. Yang, and J.-M. Tarascon. *Towards systems materials engineering*. *Nature materials*, vol. 11, no. 7, 560–563, 2012.
- [Yang 2015a] H. Yang, J. G. Lozano, T. J. Pennycook, L. Jones, P. B. Hirsch, and P. D. Nellist. *Imaging screw dislocations at atomic resolution by aberration-corrected electron optical sectioning*. *Nature Communications*, vol. 6, 7266, 2015.
- [Yang 2015b] H. Yang, T. J. Pennycook, and P. D. Nellist. *Efficient phase contrast imaging in STEM using a pixelated detector. Part II: Optimisation of imaging conditions*. *Ultramicroscopy*, vol. 151, 232–239, 2015.

- [Yang 2017] Y. Yang, C.-C. Chen, M. C. Scott, C. Ophus, R. Xu, A. Pryor, L. Wu, F. Sun, W. Theis, J. Zhou, M. Eisenbach, P. R. C. Kent, R. F. Sabirianov, H. Zeng, P. Ercius, and J. Miao. *Deciphering chemical order/disorder and material properties at the single-atom level*. *Nature*, vol. 542, no. 7639, 75–79, 2017.
- [Yankovich 2014] A. B. Yankovich, B. Berkels, W. Dahmen, P. Binev, S. I. Sanchez, S. A. Bradley, A. Li, I. Szlufarska, and Voy. *Picometre-precision analysis of scanning transmission electron microscopy images of platinum nanocatalysts*. *Nature Communications*, vol. 5, 4155, 2014.
- [Yedra 2014] L. Yedra, A. Eljarrat, J. M. Rebled, L. Lopez-Conesa, N. Dix, F. Sánchez, S. Estrade, and F. Peiro. *EELS tomography in multiferroic nanocomposites: from spectrum images to the spectrum volume*. *Nanoscale*, vol. 6, no. 12, 6646–6650, 2014.
- [Yoshioka 1957] H. Yoshioka. *Effect of inelastic waves on electron diffraction*. *Journal of the Physical Society of Japan*, vol. 12, no. 6, 618–628, 1957.
- [Yu 2010] P. Yu, J.-S. Lee, S. Okamoto, M. D. Rossell, M. Huijben, C.-H. Yang, Q. He, J. X. Zhang, S. Y. Yang, M. J. Lee, Q. M. Ramasse, R. Erni, H.-Y. Chu, D. Arena, C. C. Kao, L. W. Martin, and R. Ramesh. *Interface ferromagnetism and orbital reconstruction in  $\text{BiFeO}_3\text{-La}_{0.7}\text{Sr}_{0.3}\text{MnO}_3$  heterointerfaces*. *Physical Review Letters*, vol. 105, 027201, 2010.
- [Yu 2016] Y. Yu, D. Zhang, C. Kisielowski, L. Dou, N. Kornienko, Y. Bekenstein, A. B. Wong, A. P. Alivisatos, and P. Yang. *Atomic Resolution Imaging of Halide Perovskites*. *Nano Letters*, vol. 16, no. 12, 7530–7535, 2016.
- [Zambelli 1996] T. Zambelli, J. Wintterlin, J. Trost, and G. Ertl. *Identification of the "active sites" of a surface-catalyzed reaction*. *Science*, vol. 273, no. 5282, 1688–1690, 1996.
- [Zanaga 2016] D. Zanaga, T. Altantzis, P. Lakshminarayana, L. Liz-Marzán, B. Freitag, and S. Bals. *A new method for quantitative XEDS tomography of complex heteronanostructures*. *Particle & Particle Systems Characterization*, vol. 33, 396–403, 2016.
- [Zanchet 2001] D. Zanchet, B. D. Hall, and D. Ugarte. *Characterization of Nanophase Materials*, Chapter X-ray characterization of nanoparticles, 13–36. Wiley-VCH, 2001.
- [Zandbergen 2000] H. W. Zandbergen, and D. Van Dyck. *Exit wave reconstructions using through focus series of HREM images*. *Microscopy Research and Technique*, vol. 49, no. 3, 301–323, 2000.
- [Zhang 2015] J. Y. Zhang, J. Hwang, B. J. Isaac, and S. Stemmer. *Variable-angle high-angle annular dark-field imaging: application to three-dimensional dopant atom profiling*. *Scientific reports*, vol. 5, 12419, 2015.
- [Zhou 2016] D. Zhou, K. Muller-Caspary, W. Sigle, F. F. Krause, A. Rosenauer, and P. A. van Aken. *Sample tilt effects on atom column position determination in ABF-STEM imaging*. *Ultramicroscopy*, vol. 160, 110–117, 2016.
- [Zhu 2014] S.-E. Zhu, S. Yuan, and G. C. A. M. Janssen. *Optical transmittance of multilayer graphene*. *EPL*, vol. 108, 17007, 2014.
- [Zucchini 2000] W. Zucchini. *An introduction to model selection*. *Journal of Mathematical Psychology*, vol. 44, 41–61, 2000.



# List of Symbols and Abbreviations

## Roman characters

Character	Page	Explanation
$A$	64	arbitrary cation
$A(\mathbf{k})$	22	aperture function
$A_0$	22	normalisation constant
$A_M$	87	arbitrary $M \times M$ matrix
$B$	64	arbitrary cation
$bias(\hat{\theta}_m)$	46	bias of estimator of $m$ th element of parameter vector
$C$	50	model complexity
$C_1$	24	1st order spherical aberration
$C_3$	24	3rd order spherical aberration
$C_5$	24	5th order spherical aberration
$C_n$	24	$n$ th order spherical aberration
$C_s$	24	3th order spherical aberration
$c$	19	speed of light in vacuum
$cov(\hat{\theta}, \hat{\theta})$	48	covariance matrix of parameter estimator
$cov(\hat{\gamma}, \hat{\gamma})$	49	covariance matrix of function of parameter estimator
$cst$	85	arbitrary constant
$D$	56	experimental data
$D(\mathbf{k})$	30	detector function
$\mathbb{D}$	60	domain of integration
$d$	51	modifying parameter in GIC
$det(\nabla\nabla\chi^2)$	60	determinant of Hessian matrix
$d_i$	103	$i$ th deviation between estimated and true column position
$d_i^{ABF}$	104	$i$ th deviation between estimated and true ABF column position
$d_i^{ADF}$	104	$i$ th deviation between estimated and true ADF column position
$dz$	25	thickness of slice through specimen
$\bar{d}$	103	average deviation between estimated and true column position
$\overline{d^{ABF}}$	104	average deviation between estimated and true ABF column position
$\overline{d^{ADF}}$	104	average deviation between estimated and true ADF column position
$E$	20	total kinetic energy of an electron
$E_0$	19	kinetic energy of an electron accelerated by a potential
$\mathbb{E}$	37	mathematical expectation

$e$	19	elementary charge
$F_{rs}$	48	$(r, s)$ th element of Fisher information matrix
$F_{\theta}$	48	Fisher information matrix
$f(\mathbf{r})$	27	arbitrary function in real space
$f_{kl}(\boldsymbol{\theta})$	37	expectation model at position $(x_k, y_l)$
$f_{kl}(\hat{\boldsymbol{\theta}})$	84	optimal expectation model at position $(x_k, y_l)$
$f_{kl}^{ABF}$	96	ABF expectation model at position $(x_k, y_l)$
$f_{kl}^{ADF}$	96	ADF expectation model at position $(x_k, y_l)$
$f_{kl}(\boldsymbol{\theta})$	95	simultaneous ABF and ADF expectation model at position $(x_k, y_l)$
$G$	49	number of elements in vector $\boldsymbol{\gamma}(\boldsymbol{\theta})$
$g$	70	arbitrary Gaussian peak
$g(\mathbf{r})$	27	arbitrary function in real space
$g(\mathbf{k})$	22	arbitrary two-dimensional function in reciprocal space
$g(\mathbf{x})$	22	arbitrary two-dimensional function in real space
$g_{kl}$	70	intensity of gaussian peak at position $(x_k, y_l)$
$\hat{g}$	70	estimated arbitrary Gaussian peak
$\hat{g}_{kl}$	70	intensity of estimated gaussian peak at position $(x_k, y_l)$
$H_0(\mathbf{k})$	23	transfer function of objective lens
$h$	19	Planck's constant
$h_d$	69	distance in pixels
$h_{d_{max}}$	71	maximum distance in pixels
$\hbar$	20	Planck's constant divided by $2\pi$
$I$	55	background information
$I(\mathbf{x}_0)$	30	recorded image intensity
$I_{det}$	33	averaged detector intensity
$I_{e^- \text{ counts}}$	34	image intensity in electron counts
$I_{ideal}(\mathbf{x}_0)$	30	recorded image intensity with ideal detector
$I_{norm}$	33	normalised image intensity
$I_{raw}$	33	image intensity before normalisation
$I_{vac}$	33	image intensity in vacuum
$i$	103	index
$\hat{J}$	84	observed Fisher information matrix
$K$	37	number of pixels in x-direction
$k$	37	index
$k_{Dmax}$	30	maximum spatial frequency of recorded electrons
$k_{Dmin}$	30	minimum spatial frequency of recorded electrons
$k_x$	20	component of wave vector perpendicular to optical axis
$k_y$	20	component of wave vector perpendicular to optical axis
$k_z$	20	component of wave vector parallel to optical axis
$\mathbf{k}$	20	electron wave vector
$\mathbf{k}_{MAX}$	22	maximum spatial frequency of recorded electrons
$L$	37	number of pixels in y-direction
$L(\mathbf{t})$	43	likelihood function
$\hat{L}$	50	maximum likelihood estimate
$l$	37	index

$M$	37	number of parameters in expectation model
$m$	19	relativistic mass of the electron
$m_o$	19	mass of the electron
$N$	38	number of atomic columns
$N(\boldsymbol{\theta}; \text{CRLB})$	49	normal distribution with $\boldsymbol{\theta}$ as expectation values and CRLB matrix as covariance matrix
$N_0$	62	initial number of Gaussian peaks
$N_{max}$	62	maximum number of Gaussian peaks
$N_p$	34	number of electrons in probe
$n$	25	index
$\mathcal{O}(1)$	88	constant for increasing number of pixels
$\mathcal{O}(dz^2)$	26	error term
$P(k_x, k_y, dz)$	27	propagator function for a distance $dz$ in reciprocal space
$p$	19	momentum of accelerated electron
$p(D Q)$	56	probability of observing data $D$ given quantity $Q$
$p(N)$	57	prior probability of number of columns $N$
$p(N \boldsymbol{w})$	57	posterior probability of number of columns $N$ in observed image pixel values $\boldsymbol{w}$
$p(Q)$	56	prior information about quantity $Q$
$p(Q D)$	56	probability of quantity $Q$ given data $D$
$p(x, y, dz)$	27	propagator function for a distance $dz$ in real space
$p(\boldsymbol{w})$	57	normalization constant
$p(\boldsymbol{w}; \boldsymbol{t})$	43	joint probability (density) function as a function of the observations $\boldsymbol{w}$ and independent variables $\boldsymbol{t}$
$p(\boldsymbol{w} N)$	57	evidence that the image data $\boldsymbol{w}$ is generated by $N$ columns
$p(\boldsymbol{w} \boldsymbol{\theta}, N)$	58	likelihood function describing probability of observed image data $\boldsymbol{w}$ for parameter vector $\boldsymbol{\theta}$ of a model with $N$ columns
$p(\boldsymbol{w} \hat{\boldsymbol{\theta}}, N)$	84	likelihood function describing probability of observed image data $\boldsymbol{w}$ for parameter vector $\hat{\boldsymbol{\theta}}$ of a model with $N$ columns
$p(\boldsymbol{\theta} N)$	58	prior density of the parameters vector $\boldsymbol{\theta}$ for a model with $N$ columns
$p(\omega_{kl})$	42	probability distribution for observation at position $(x_k, y_l)$
$p(\boldsymbol{\omega})$	42	joint probability (density) function
$p(\boldsymbol{\omega}; \boldsymbol{\theta})$	48	joint probability (density) function explicitly written as a function of parameter vector $\boldsymbol{\theta}$
$p_n(x, y, dz)$	27	propagator function for a distance $dz$ in real space for $n$ th slice
$p_{rel}(N \boldsymbol{w})$	62	relative posterior probability
$Q$	56	arbitrary quantity of interest
$R_{in}$	30	inner angle of STEM detector in radians
$R_{out}$	30	outer angle of STEM detector in radians
$S(\mathbf{x}_0)$	30	source size distribution of electron probe function
$s$	87	arbitrary scalar
$t(x, y, z)$	26	transmission function between $z$ and $z + dz$
$t_{det}$	34	pixel dwell time of detector scan
$t_n(x, y, z)$	27	transmission function between $z$ and $z + dz$ for $n$ th slice
$t_{raw}$	34	pixel dwell time of raw image

$t_{vac}$	34	pixel dwell time of vacuum image
$\mathbf{t}$	43	vector of independent variables
$V(x, y, z)$	20	electrostatic specimen potential
$V_0$	19	acceleration voltage
$v$	19	velocity of accelerated electron
$var(\hat{\theta}_m)$	46	variance of estimate of $m$ th element of parameter vector
$v_{dz}(x, y, z)$	26	projected electrostatic specimen potential in slice through specimen
$v_z(\mathbf{x})$	25	projected electrostatic specimen potential along optical axis
$v_{z,n}(\mathbf{x} - \mathbf{x}_n)$	25	projected potential of the $n$ th atom at position $\mathbf{x}_n$
$W$	37	number of pixels in image
$w_{max}$	101	maximum observed pixel value
$w_{max}^{ABF}$	101	maximum observed ABF pixel value
$w_{max}^{ADF}$	101	maximum observed ADF pixel value
$w_{min}$	101	minimum observed pixel value
$w_{min}^{ABF}$	101	minimum observed ABF pixel value
$w_{min}^{ADF}$	101	minimum observed ADF pixel value
$w_{kl}$	37	image pixel value observed at position $(x_k, y_l)$
$w_{kl}^{ABF}$	95	ABF image pixel value observed at position $(x_k, y_l)$
$w_{kl}^{ADF}$	95	ADF image pixel value observed at position $(x_k, y_l)$
$\mathbf{w}$	37	observed image pixel values
$\mathbf{w}^{ABF}$	95	observed ABF image pixel values
$\mathbf{w}^{ADF}$	95	observed ADF image pixel values
$\mathbf{w}_{kl}$	95	observed ABF and ADF image pixel values at position $(x_k, y_l)$
$X$	55	arbitrary proposition
$\bar{X}$	55	probability of proposition $X$
$x$	20	spatial coordinate
$x_k$	37	$x$ -coordinate at the pixel value $(k, l)$
$\mathbf{x}$	22	two-dimensional coordinate vector
$\mathbf{x}_0$	22	two-dimensional coordinate vector of electron probe function
$\mathbf{x}_n$	25	two-dimensional coordinate vector of $n$ th atom
$Y$	55	arbitrary proposition
$y$	20	spatial coordinate
$y_l$	37	$y$ -coordinate at the pixel value $(k, l)$
$Z$	15	atomic number
$Z(h_d)$	69	number of paired observations separated by distance $h_d$
$z$	20	spatial coordinate
$z_n$	27	depth of $n$ th slice through specimen
$\{\mathbf{w}^{ABF}, \mathbf{w}^{ADF}\}$	98	ensemble of observed ABF and ADF pixel values

## Greek characters

Character	Page	Explanation
$\alpha$	14	convergence semi angle of STEM electron probe

$\alpha_{max}$	100	maximum predefined value of magnitude of deviation between ABF and ADF column position
$\alpha_{min}$	100	minimum predefined value of magnitude of deviation between ABF and ADF column position
$\alpha_{MAX}$	22	maximum angle in STEM objective aperture
$\alpha_n$	97	magnitude of deviation between $n$ th ABF and ADF column position
$\beta_1$	14	inner STEM detector collection angle
$\beta_1^{ABF}$	96	inner ABF STEM detector collection angle
$\beta_1^{ADF}$	96	inner ADF STEM detector collection angle
$\beta_2$	14	outer STEM detector collection angle
$\beta_2^{ABF}$	96	outer ABF STEM detector collection angle
$\beta_2^{ADF}$	96	outer ADF STEM detector collection angle
$\beta_x$	80	x-coordinate of atomic column
$\beta_x^{ABF}$	103	x-coordinate of ABF atomic column
$\beta_x^{ADF}$	103	x-coordinate of ADF atomic column
$\beta_{x_{max}}$	59	maximum predefined value of x-coordinate of atomic column
$\beta_{x_{min}}$	59	minimum predefined value of x-coordinate of atomic column
$\beta_{x_n}$	38	x-coordinate of $n$ th atomic column
$\beta_y$	80	y-coordinate of atomic column
$\beta_y^{ABF}$	103	y-coordinate of ABF atomic column
$\beta_y^{ADF}$	103	y-coordinate of ADF atomic column
$\beta_{y_{max}}$	59	maximum predefined value of y-coordinate of atomic column
$\beta_{y_{min}}$	59	minimum predefined value of y-coordinate of atomic column
$\beta_{y_n}$	38	y-coordinate of $n$ th atomic column
$\hat{\beta}_x$	46	estimated x-coordinate of atomic column
$\hat{\beta}_x^{ABF}$	104	estimated x-coordinate of ABF atomic column
$\hat{\beta}_x^{ADF}$	104	estimated x-coordinate of ADF atomic column
$\hat{\beta}_y$	103	estimated y-coordinate of atomic column
$\hat{\beta}_y^{ABF}$	104	estimated y-coordinate of ABF atomic column
$\hat{\beta}_y^{ADF}$	104	estimated y-coordinate of ADF atomic column
$\gamma(h_d)$	69	variability of background as a function of distance
$\gamma_{x_n}$	97	x-coordinate of $n$ th ABF atomic column depending on x-coordinate of $n$ th ADF atomic column
$\gamma_{y_n}$	97	y-coordinate of $n$ th ABF atomic column depending on y-coordinate of $n$ th ADF atomic column
$\gamma(\theta)$	43	arbitrary function of parameter vector
$\hat{\gamma}$	43	unbiased estimator of $\gamma$
$\Delta$	20	three-dimensional Laplace operator
$\Delta I_{1e^-}$	34	intensity generated by single electron
$\Delta S_{z(h_d)}$	69	difference between $z(h_d)$ th pair of observations
$\Delta x$	62	pixel size in x-direction
$\Delta_{x,y}$	21	two-dimensional Laplace operator in $x$ and $y$
$\Delta y$	62	pixel size in y-direction
$\Delta \gamma$	70	difference of variability
$\Delta \zeta$	70	difference between true and estimated background

$\Delta\zeta_{kl}$	70	difference between true and estimated background at position $(x_k, y_l)$
$\epsilon$	24	defocus
$\zeta$	38	constant background
$\zeta^{ABF}$	96	constant ABF background
$\zeta^{ADF}$	96	constant ADF background
$\zeta_{kl}$	70	constant background at position $(x_k, y_l)$
$\zeta_{max}$	59	maximum predefined value of constant background
$\zeta_{min}$	59	minimum predefined value of constant background
$\hat{\zeta}$	70	estimated constant background
$\hat{\zeta}_{kl}$	70	estimated constant background at position $(x_k, y_l)$
$\eta$	41	intensity of atomic column
$\eta^{ABF}$	100	intensity of ABF atomic column
$\eta^{ADF}$	100	intensity of ADF atomic column
$\eta_{max}$	59	maximum predefined value of intensity of atomic column
$\eta_{max}^{ABF}$	99	maximum predefined value of intensity of ABF atomic column
$\eta_{max}^{ADF}$	99	maximum predefined value of intensity of ADF atomic column
$\eta_{min}$	59	minimum predefined value of intensity of atomic column
$\eta_{min}^{ABF}$	99	minimum predefined value of intensity of ABF atomic column
$\eta_{min}^{ADF}$	99	minimum predefined value of intensity of ADF atomic column
$\eta_n$	38	intensity of $n$ th atomic column
$\eta_n^{ABF}$	96	intensity of $n$ th ABF atomic column
$\eta_n^{ADF}$	96	intensity of $n$ th ADF atomic column
$\hat{\eta}$	70	estimated intensity of atomic column
$\Theta$	41	scattering cross section of atomic column
$\theta_m$	46	$m$ th element of parameter vector
$\theta_{mmax}$	59	maximum predefined value of $m$ th element of parameter vector
$\theta_{min}$	59	minimum predefined value of $m$ th element of parameter vector
$\theta_r$	48	$r$ th element of parameter vector
$\theta_s$	48	$s$ th element of parameter vector
$\hat{\theta}_m$	46	estimate of $m$ th element of parameter vector
$\theta$	37	parameter vector
$\hat{\theta}$	43	estimate of $\theta$
$\lambda$	19	electron wavelength
$\lambda_{kl}$	42	expected value of stochastic variable at position $(x_k, y_l)$
$\mu_{kl}$	58	expectation value at position $(x_k, y_l)$
$\rho$	38	width of atomic column
$\rho^{ABF}$	98	width of ABF atomic column
$\rho^{ADF}$	98	width of ADF atomic column
$\rho_{max}$	59	maximum predefined value of width of atomic column
$\rho_{max}^{ABF}$	99	maximum predefined value of width of ABF atomic column
$\rho_{max}^{ADF}$	99	maximum predefined value of width of ADF atomic column
$\rho_{min}$	59	minimum predefined value of width of atomic column
$\rho_{min}^{ABF}$	99	minimum predefined value of width of ABF atomic column
$\rho_{min}^{ADF}$	99	minimum predefined value of width of ADF atomic column
$\rho_n$	38	width of $n$ th atomic column

$\rho_n^{ABF}$	96	width of $n$ th ABF atomic column
$\rho_n^{ADF}$	96	width of $n$ th ADF atomic column
$\hat{\rho}$	70	estimated width of atomic column
$\sigma$	43	standard deviation of expected pixel values
$\sigma_{\bar{d}}$	103	standard deviation of $\bar{d}$
$\sigma_{\overline{d^{ABF}}}$	104	standard deviation of $\overline{d^{ABF}}$
$\sigma_{\overline{d^{ADF}}}$	104	standard deviation of $\overline{d^{ADF}}$
$\sigma_i$	21	interaction parameter
$\sigma_{kl}$	43	standard deviation of expected pixel value at position $(x_k, y_l)$
$\sigma_r$	30	radius containing 39% of total STEM electron probe intensity
$\phi$	97	direction of deviation between ABF and ADF column position
$\chi(\mathbf{k})$	24	lens aberration function
$\chi^2(\boldsymbol{\theta})$	59	weighted sum-of-squared-residuals misfit between data and parametric model
$\chi^2(\hat{\boldsymbol{\theta}})$	60	$\chi^2(\boldsymbol{\theta})$ evaluated at $\hat{\boldsymbol{\theta}}$
$\chi_0^2$	70	uniform sum-of squared-residuals misfit of zero columns
$\chi_1^2$	70	uniform sum-of squared-residuals misfit of one column
$\chi_{min}^2$	60	$\chi^2(\boldsymbol{\theta})$ evaluated at $\hat{\boldsymbol{\theta}}$
$\psi(x, y, z)$	20	electron wave function
$\psi_0(\mathbf{x})$	22	initial electron wave function
$\psi_e(\mathbf{x})$	29	exit electron wave function
$\psi_f(x, y, z)$	20	full electron wave function
$\psi_{final}(\mathbf{k}, \mathbf{x}_0)$	29	final electron wave function
$\psi_n(x, y)$	27	electron wave function through $n$ th slice
$\psi_{n+1}(x, y)$	27	electron wave function through $(n + 1)$ th slice
$\psi_t(\mathbf{x})$	25	transmission electron wave function
$\omega_{kl}$	42	independent variable of observation at position $(x_k, y_l)$
$\omega$	37	independent variables corresponding to observations

## Abbreviations

Character	Page	Explanation
2D	6	two-dimensional
3D	16	three-dimensional
4D	16	four-dimensional
ABF	11	annular bright-field
ADC	32	analogue-to-digital converter
ADF	10	annular dark-field
AFM	6	atomic force microscopy
AIC	51	Akaike Information Criterion
BF	15	bright-field
BIC	51	Bayesian Information Criterion
CBED	15	convergent beam electron diffraction

CCD	14	charge-coupled device
CNR	10	contrast-to-noise ratio
CPU	32	central processor unit
CRLB	36	Cramér-Rao lower bound
CryoTEM	7	transmission electron cryomicroscopy
CTEM	6	conventional transmission electron microscopy
EAM	72	embedded atom method
EDX	16	energy dispersive X-ray spectroscopy
EELS	16	electron energy loss spectroscopy
FWHM	30	full width at half maximum
GIC	51	Generalised Information Criterion
GPU	32	graphical processor unit
HAADF	15	high-angle annular dark-field
HQC	51	Hannan-Quinn Information Criterion
ICNR	11	integrated contrast-to-noise ratio
ICNR <sup>ABF</sup>	102	integrated annular bright-field contrast-to-noise ratio
ICNR <sup>ADF</sup>	102	integrated annular dark-field contrast-to-noise ratio
LAADF	15	low-angle annular dark-field
MAADF	15	medium-angle annular dark-field
MAP	10	maximum a posteriori
NMR	3	nuclear magnetic resonance
PMT	32	photomultiplier tube
PSD	4	power spectral density
SNR	7	signal-to-noise ratio
STEM	6	scanning transmission electron microscopy
STM	6	scanning tunneling microscopy
TDS	28	thermal diffuse scattering
TEM	6	transmission electron microscopy
XPS	3	X-ray photoelectron spectroscopy

# List of publications

## Contributions to scientific journals

- J. Fatermans, A.J. den Dekker, K. Müller-Caspary, I. Lobato, C.M. O’Leary, P.D. Nellist, and S. Van Aert, *Single atom detection from low contrast-to-noise ratio electron microscopy images*, Physical Review Letters **121** (2018), 056101.
- J. Fatermans, S. Van Aert, and A.J. den Dekker, *The maximum a posteriori probability rule for atom column detection from HAADF STEM images*, Ultramicroscopy **201** (2019), p. 81-91.
- J. Fatermans, A.J. den Dekker, N. Gauquelin, K. Müller-Caspary, and S. Van Aert, *Atom column detection from simultaneously acquired ABF and ADF STEM images*, Ultramicroscopy (2019), in preparation.

## Contributions to scientific meetings

- J. Fatermans, S. Van Aert, and A.J. den Dekker, *Bayesian model-order selection in electron microscopy to detect atomic columns in noisy images*, Golden Jubilee Meeting of the Royal Belgian Society for Microscopy, Brussels, Belgium, September 2016, *Poster presentation*.
- J. Fatermans, K. Müller-Caspary, A.J. den Dekker, and S. Van Aert, *Detection of atomic columns from noisy STEM images*, Microscopy Conference, Lausanne, Switzerland, August 2017, *Poster presentation*.
- J. Fatermans, A.J. den Dekker, K. Müller-Caspary, I. Lobato, and S. Van Aert, *Bayesian analysis of noisy scanning transmission electron microscopy images for single atom detection*, SCANDEM Conference, Lyngby, Denmark, June 2018, *Oral presentation*.
- J. Fatermans, A.J. den Dekker, K. Müller-Caspary, I. Lobato, and S. Van Aert, *The maximum a posteriori probability rule to detect single atoms from low signal-to-noise ratio scanning transmission electron microscopy images*, 19<sup>th</sup> International Microscopy Congress, Sydney, Australia, September 2018.
- S. Van Aert, J. Fatermans, A. De Backer, K.H.W. van den Bos, C.M. O’Leary, K. Müller-Caspary, L. Jones, I. Lobato, A. Béché, A.J. den Dekker, S. Bals, and P.D. Nellist, *Maximising dose efficiency in quantitative STEM to reveal the 3D atomic structure of*

*nanomaterials*, 19<sup>th</sup> International Microscopy Congress, Sydney, Australia, September 2018.

- S. Van Aert, A. De wael, J. Fatermans, I. Lobato, A. De Backer, L. Jones, A.J. den Dekker, and P.D. Nellist, *Strategies for quantifying 3D atomic structures of nanomaterials and their dynamics using dose-efficient ADF STEM*, 5<sup>th</sup> Conference on Frontiers of Aberration Corrected Electron Microscopy, Vaalsbroek, The Netherlands, May 2019.
- S. Van Aert, A. De wael, J. Fatermans, I. Lobato, A. De Backer, L. Jones, A.J. den Dekker, and P.D. Nellist, *Quantifying 3D atomic structures of nanomaterials and their dynamics using model-based scanning transmission electron microscopy*, Spring Meeting of the European Materials Research Society, Nice, France, May 2019.
- J. Fatermans, A.J. den Dekker, C.M. O’Leary, P.D. Nellist, and S. Van Aert, *Atom column detection from STEM images using the maximum a posteriori probability rule*, Microscopy Conference, Berlin, Germany, September 2019, *Oral presentation*.
- J. Fatermans, A.J. den Dekker, S. Van Aert, *Atom detection from electron microscopy images*, Royal Belgian Society for Microscopy Annual Meeting, Louvain-la-Neuve, Belgium, September 2019, *Poster presentation*.

# Acknowledgements - Dankwoord

Vier jaar geleden voegde ik mij na mijn studies Fysica aan de Universiteit Gent bij onderzoeksgroep EMAT aan de Universiteit Antwerpen. Het leek mij een geweldige kans om een doctoraat te kunnen uitvoeren bij een van de meest toonaangevende onderzoeksgroepen op het gebied van elektronenmicroscopie. De voorbije vier jaar zijn voorbijgevlogen en nu is het moment daar om enkele mensen persoonlijk te bedanken zonder wie dit doctoraat niet mogelijk was geweest.

In eerste instantie zou ik graag mijn promotoren Sandra en Arjan enorm willen bedanken, want zonder hen had ik niet de kans gehad om een doctoraat te kunnen starten. Dank je voor jullie fijne begeleiding, voor jullie enthousiasme, voor het delen van zoveel kennis en voor de vele inhoudelijke verbeteringen aan mijn werk. Door jullie oog voor detail was ik altijd zeker dat presentaties en publicaties tot in de puntjes in orde waren. Het vertrouwen dat jullie in mij stelden werkte heel motiverend en dat waardeer ik enorm.

I would like to thank all (ex-)members of Sandra's research group within EMAT for the valuable discussions during group meetings. I will not name everyone separately since especially during the last year the group has grown exponentially with a lot of new members who have joined. By being part of Sandra's research group I also had the opportunity to attend the ATOM workshops, which I enjoyed a lot, and during which I was able to share and improve my research results. De Friday Lectures in EMAT waren voor mij een ontzettend nuttige gelegenheid om de interessante kennis die beschikbaar is binnen de groep met elkaar te delen. Ik wil dan ook alle (oud-)groepsleden van EMAT die ik heb leren kennen gedurende de afgelopen jaren hiervoor bedanken. Thank you all EMAT members. In het bijzonder wil ik Liesbet nog bedanken voor het maken van een mooie cover. Doordat ik elke woensdag werkte vanop imec-Vision Lab kon ik ook kennis vergaren over onderzoek buiten dat van elektronenmicroscopie. I would like to thank all members of imec-Vision Lab for making this possible.

I would also like to thank professor Peter Nellist and Colum of the University of Oxford, Knut, Thomas, Ivan, and my office colleague Nicolas for providing me with excellent simulated or experimental images which allowed me to test my ideas in practice. Thank you all for the valuable collaboration.

Tot slot wil ik graag mijn vrienden, zus en ouders bedanken. Bedankt voor jullie onvoorwaardelijke steun en interesse in wat ik doe. Zonder jullie was ik niet kunnen uitgroeien tot de persoon die ik nu ben. Als laatste wil ik graag nog Barbara bedanken. Zonder jou had ik dit doctoraat nooit tot een goed einde kunnen brengen. Ik kijk uit naar de toekomst en ben benieuwd naar wat die in petto heeft!

Jarmo Fatermans